University of Southampton

National Oceanography Centre

Gulf Stream transport and pathway variability: the importance of air-sea fluxes

Thesis for the degree of Doctor of Philosophy

Author:

Zoe Jacobs

Supervisors:

Jeremy Grist, Bob Marsh,

Simon Josey and Bablu Sinha

1st June 2018

Abstract

UNIVERSITY OF SOUTHAMPTON

FACULTY OF NATURAL AND ENVIRONMENTAL SCIENCES

National Oceanography Centre

Doctor of Philosophy

Gulf Stream transport and pathway variability: the importance of air-sea fluxes

by Zoe Jacobs

Understanding the various mechanisms that control path and transport variability of the Gulf Stream (GS) is important due to its major role in the global redistribution of heat. This work provides evidence that localised surface heat fluxes can induce changes in the path and strength of the GS.

Interannual path and transport variability of the GS are calculated here using different methods in a range of observational products, which are compared to high resolution (eddy-resolving) ocean model output. It is shown that changes in the baroclinic transport, i.e. the density-driven component, are crucial in controlling total GS transport variability. Furthermore, observational and model evidence was found that intense air-sea fluxes during severe winters alters the cross-stream density structure and in turn the GS transport compared to the previous year. The investigation found that these years were also associated with deeper mixed layers, strengthened meridional temperature gradients (to the north and south of the GS core) and an intensified westward component of the southern recirculation.

Lagrangian analysis is performed to examine GS pathway variability. Distinctive characteristics of the recirculating and Subpolar Gyre (SPG)-bound pathways are revealed. In particular, a more direct, faster, subsurface pathway to the SPG is revealed than has been found previously. By demonstrating that this pathway had increased throughput to this region during the 1990s, it is possible for the first time to reconcile the 1990s SPG warming with a Lagrangian approach. The influx of warm water during this decade is related to air-sea fluxes associated with the North Atlantic Oscillation (NAO). Additionally, near-surface pathways are significantly correlated to the wind stress curl over the STG.

Acknowledgements

This thesis was funded by the Graduate School of the University of Southampton and the National Oceanography Centre, Southampton. I am grateful for all the funding received.

To everyone that has supported me along the way, I cannot thank you enough. A particular thank you to my team of supervisors, for all your help and time. I have learnt so much working with each of you and appreciate all the advice and support over the last four years. Thank you for all the commenting and editing, for helping me battle with Matlab and Fortran, and for encouraging me to present my work at various conferences. I am also grateful for all the help, advice and support from Joel Hirschi. To everyone else at the National Oceanography Centre, and in particular from the Marine Systems Modelling Group, thank you for the inspiration and advice over the years. In particular, a huge thank you to Jeff, who helped me get to grips with the computer system and continued to help me overcome various computing dramas over the years.

Thanks to Andrew Coward and the NEMO developers that have generated the high-resolution model runs used in this thesis. I appreciate all the hard work that has gone into NEMO and have learnt a lot during the weekly meetings. Further thanks go to B. Blanke and N. Grima who have developed the Ariane software used in this thesis. I am grateful for the time spent on the GOBLIN project with Katya Popova and co. as it provided me with invaluable experience using Ariane.

To my fantastic officemates Matt and Helen, who have been with me since day 1, for the companionship during the tough days in the fish bowl, for helping me get through all the PhD crises and for all the tea breaks and creme eggs. Also, to Jess and Sam who joined us in 256/28 more recently, thanks for keeping me smiling during this challenging year. A huge thank you to the rest of the PhD community at the National Oceanography Centre, Southampton. In particular, to Freya, Jesse, Cris and Victor who have been a massive part of my PhD life.

Finally, the biggest thank you to James, Mum, Dad, Rob, Livvy, Cee, Sue, Bob, Will and the rest of my amazing friends and family for getting me through the last four years in one piece, I could not have done it without you.

Academic Thesis: Declaration Of Authorship

I, Zoe Jacobs, declare that this thesis and the work presented in it are my own and has been generated by me as the result of my own original research.

I confirm that:

1. This work was done wholly or mainly while in candidature for a research degree at this University;

.

2. Where any part of this thesis has previously been submitted for a degree or any other qualification at this University or any other institution, this has been clearly stated;

3. Where I have consulted the published work of others, this is always clearly attributed;

4. Where I have quoted from the work of others, the source is always given. With the exception of such quotations, this thesis is entirely my own work;

5. I have acknowledged all main sources of help;

6. Where the thesis is based on work done by myself jointly with others, I have made clear exactly what was done by others and what I have contributed myself;

7. Either none of this work has been published before submission, or parts of this work have been published as:

Signed:_____

Date:_____

Contents

List of Tables

List of Figures

Chapter 1

Introduction

1.1 The Gulf Stream System and its variability

1.1.1 The Gulf Stream - a general description

The Gulf Stream (GS) is the Western Boundary Current (WBC) of the Subtropical Gyre (STG) of the North Atlantic that facilitates the transport of warm, saline water from the subtropics to much higher latitudes by rapid advection (*Rossby*, 1996). It begins as the Florida Current as it flows along the east coast of North America until it reaches Cape Hatteras, at about 75^oW, where it then turns northeast and heads towards the Grand Banks as the GS proper (*Schmitz Jr*, 1996), see Figure 1.1. A high spatial and temporal variability of the GS path exists and is amplified when the narrow GS reaches the abrupt topography of Cape Hatteras (*Lillibridge and Mariano*, 2012).

Near Cape Hatteras, GS speeds are between 1.2-1.5 m s^{-1} (*Molinari*, 2004; *Gawarkiewicz et al.*, 2012) but can be as high as 2.5 m s^{-1} (*Lillibridge and Mariano*, 2012). The mean transport upstream of Cape Hatteras, i.e. the Florida Current, was observed to be $32.2Sv$ from 1982-1998 with an annual (interannual) variation of up to $5Sv$ ($4Sv$) (*Baringer and Larsen*, 2001). Downstream of this at 73^oW, peak transport of the separated Gulf Stream reaches an average maximum of $93Sv$ (*Halkin and Rossby*, 1985) but can reach up to $150Sv$ between 55^oW and 60^oW (*Knauss*, 1969; *Richardson*, 1985; *Hogg*, 1992; *Rossby*, 1996) before decreasing due to recirculation and mesoscale activity (*Schmitz Jr*, 1996; *Chaudhuri et al.*, 2011).

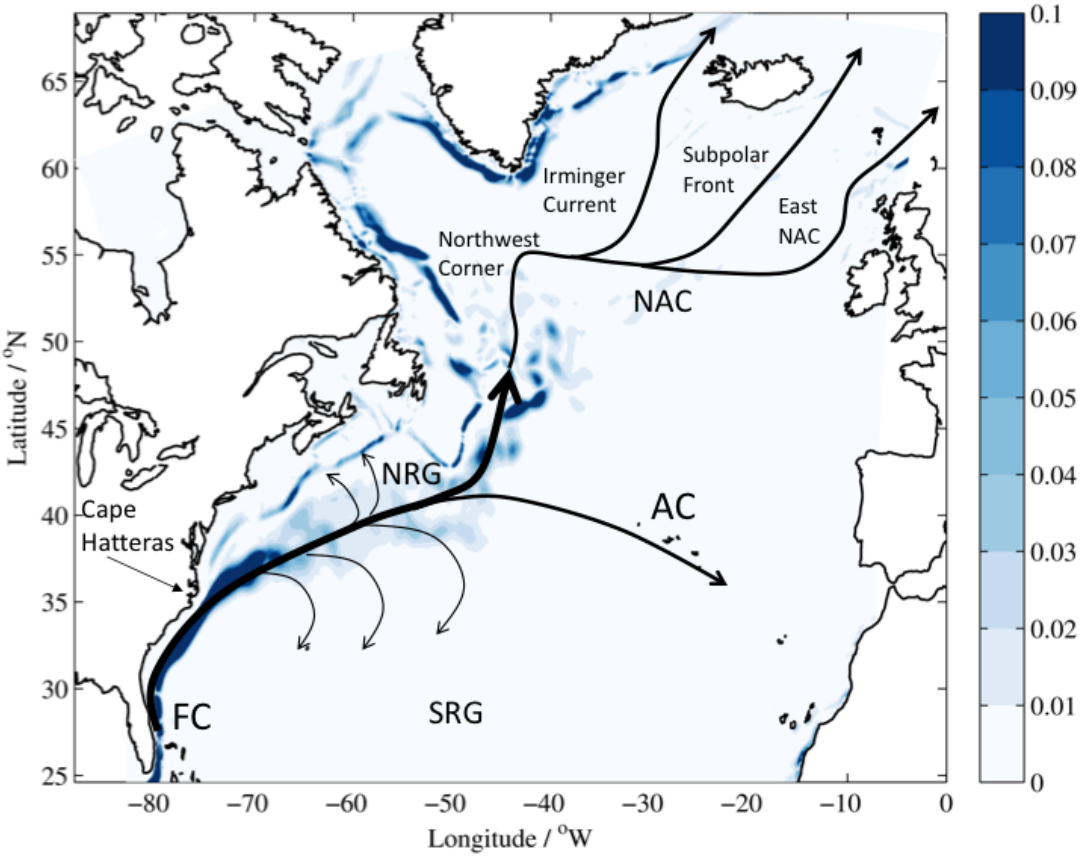

Figure 1.1: Schematic of the Gulf Stream and its pathways (North Atlantic Current (NAC), Northern Recirculation Gyre (NRG), Southern Recirculation Gyre (SRG), Azores Current (AC) and Florida Current (FC)) with the mean surface velocity (m s^{-1}) in ORCA12 from 1980-2010.

The intensification of the transport between Cape Hatteras and 55^oW, with an increase from $50Sv$ to $100Sv$, is associated with the barotropic component, while the baroclinic transport remains constant at about $50Sv$ (*Schmitz Jr*, 1996).

On interannual timescales, the transport can vary by more than 10% (*Rossby et al.*, 2010). Decadal variability also exists with a weaker GS observed during the 1960s followed by a period of greater transport during the 1980s-90s (*Sato and Rossby*, 1995; *Curry and McCartney*, 2001). Specifically, over 25 years an increase of $25 - 33\%$ is recorded (*Curry and McCartney*, 2001). However, on shorter timescales greater variability exists when the shifting path, eddies and recirculations are considered (*Rossby et al.*, 2010). The weakening observed during the 2000s by *Ezer et al.* (2013) using altimetry is disputed by *Rossby et al.* (2013) who find that changes in the density gradients/structure of the entire water column

are important, as opposed to just the surface, and find no evidence of declining transport. The importance of analysing the whole water column is also highlighted by *Meinen and Luther* (2016).

GS transport also varies seasonally with the greatest differences observed in the upper $50m$ of the water column (*Rossby et al.*, 2010). The seasonal wind variation causes the strongest transport to occur in winter and the weakest to occur in autumn (*Worthington*, 1977; *Kelly and Gille*, 1990; *Hogg and Johns*, 1995). However, the high mesoscale variability of the GS has led to inconsistent results across studies analysing GS velocity and transport (*Richardson*, 1985; *Lillibridge and Mariano*, 2012). Inconsistencies also arise depending on the type of transport being measured, i.e. the barotropic element is related to wind stress fluctuations while the baroclinic element is related to buoyancy forcing that causes steric changes to the thermal structure of the water column (*Wang and Koblinsky*, 1996).

Additionally, the GS path shifts meridionally on seasonal timescales by about 0.25^o soon after separation from Cape Hatteras (*Tracey and Watts*, 1986) with a maximum seasonal shift found between 73^oW and 64^oW (*Kelly et al.*, 1999). On average, it is found further north in autumn, reaching a maximum in August, and further south during the spring, reaching a minimum in March (*Fuglister*, 1972; *Tracey and Watts*, 1986; *Drinkwater et al.*, 1994; *Lee and Cornillon*, 1995; *Rayner et al.*, 2011). However, this can be out of phase by up to 6 months, which is due to the select measurement of either the barotropic or baroclinic component (*Lillibridge and Mariano*, 2012). For example, *Kelly and Gille* (1990) observed the GS in a more northerly position in winter and spring and in a more southerly position in summer and autumn.

On interannual timescales, the GS path can change its position by up to 1^o when the GS is defined using the maximum Sea Surface Temperature (SST) gradient (*Drinkwater et al.*, 1994), velocities from Acoustic Doppler Current Profiler (ADCP) data (*Rossby and Benway*, 2000) and the maximum Sea Surface Height (SSH) gradient (*Lillibridge and Mariano*, 2012; *Pérez-Hernández and Joyce*, 2014). For example, during the 1990s the GS was found $100 - 200km$ further north compared to the 1960s (*Taylor and Gangopadhyay*, 2001; *Kwon et al.*, 2010) and has

been found further to the south since 2004 (*Ezer et al.*, 2013). This decadal variability was found to exist west of 65^oW with more interannual (4-5 years) variability occurring to the east of this (*Gangopadhyay et al.*, 2016).

The high variability of the GS path is dominated by eastward propagating meanders that interact with the westward propagating eddy field, which can cause difficulties when measuring the main GS core (*Krauss et al.*, 1990; *Rossby*, 1996; *Lillibridge and Mariano*, 2012). Meanders can exceed $100km$ in length and have periods of between 2 and 60 days (*Tracey and Watts*, 1986; *Peña-Molino and Joyce*, 2008). Once they have grown to a large amplitude they can break off to form eddies, which trap water from the opposite gyre, i.e. warm core rings to the north and cold core rings to the south (*Halkin and Rossby*, 1985; *Rossby*, 1999). The occurrence of eddies increases further downstream, and east of 55^oW the GS is dominated by mesoscale activity (*Krauss et al.*, 1990). Enhanced Eddy Kinetic Energy (EKE) occurs along the major current paths due to baroclinic instability and anomalous values can be related to a shift in the main path of the current (*Volkov*, 2005; *Chaudhuri et al.*, 2009; *Hakkinen and Rhines*, 2009; *Sasaki and Schneider*, 2011).

1.1.2 North Atlantic Current

Near 50^oW by the Newfoundland ridge, the GS transport decreases as it branches into the North Atlantic Current (NAC) (*Schmitz Jr*, 1996), which has multiple convoluted pathways due to greater eddy variability in this region (*Bower and von Appen*, 2008; *Read et al.*, 2010). Nonetheless, the NAC transports up to $40Sv$ into the Newfoundland basin (*Rossby*, 1996). A large anticyclonic meander, also referred to as the Mann eddy, at about 52^oN in the "northwest corner" region southeast of Newfoundland, is the point where the GS becomes the NAC (*Rossby*, 1996). The warm, salty water transported by the GS and NAC flows into the eastern Subpolar Gyre (SPG) via three main channels at speeds of about 0.2 m s^{-1}; the Irminger Current to the west of Iceland, the subpolar front through the Iceland basin (*Fratantoni*, 2001; *Hakkinen and Rhines*, 2009) and one through the Rockall trough (East NAC), Figure 1.1. These surface waters cool as they travel northward and are preconditioned for the formation of deep waters seen in much

of the global ocean (*Bower and von Appen*, 2008).

1.1.3 Other Gulf Stream pathways

In addition to the NAC, the GS also splits into the Southern Recirculation (SR), the Northern Recirculation (NR) and the Azores Current (AC) (*Schmitz Jr*, 1996) between 50^oW and 46^oW (*Qiu*, 1994). The eastward flowing AC is a continuation of the wind-driven STG (*Schmitz Jr*, 1996) at 35^oN and separates the warm subtropical water to the south from cooler subpolar water to the north (*Krauss et al.*, 1990). The westward-flowing recirculation gyres are partially eddy-driven and cause the barotropic transport of the GS system to approximately double (*Holland et al.*, 1983; *Schmitz Jr*, 1996).

Using current meter moorings and surface drifters, *Richardson* (1985) estimated the transport of the NR and SR to be approximately $30Sv$ and $40Sv$ respectively. This has been found to vary in relation to the strength of the wind stress with stronger recirculation gyres resulting from higher wind stress values (*Spall*, 1996). The cyclonic NR is found to the north of the main GS, in the Slope Water, beneath the thermocline and extends to the ocean floor (*Hogg*, 1992; *Zhang and Vallis*, 2007). At, 65^oW near the New England seamount, the majority of the NR waters are thought to re-join the GS with most of the SR re-joining the GS further to the west (from Cape Hatteras to 70^oW) (*Hall and Fofonoff*, 1993; *Johns et al.*, 1995). This leads to an increase in the overall GS transport between these longitudes (*Hall and Fofonoff*, 1993).

The surface-intensified, anticyclonic SR covers a region to the south of the GS from $55 - 75^oW$ (*Worthington*, 1976; *Kelly et al.*, 2010) and exists above and below the thermocline (*Hogg*, 1992). The SR is maintained by inertial processes (*Fofonoff*, 1954) and intense cooling to the south of the GS, which creates a region of Potential Vorticity (PV) minima (*Worthington*, 1972; *Cushman-Roisin*, 1987; *Huang*, 1990). The width and strength of the SR varies seasonally with the greatest width and strength observed from summer to autumn before contracting and weakening during the winter and spring (*Wang and Koblinsky*, 1996). However, *Worthington* (1976) found evidence for a stronger SR at the end of the winter,

which is driven by strong air-sea fluxes.

1.2 The Gulf Stream in a dynamical framework

This section is dedicated to describing the dynamics and theory associated with WBCs, using the STG of the North Atlantic as an example. The asymmetry of the large-scale ocean circulation, i.e. wide, gentle flow in the interior and narrow, fast flow along the western boundary, was first inferred by *Sverdrup* (1947) who used the theory of mid-ocean vorticity balance. The importance of friction for western intensification was then explained by *Stommel* (1948) and *Munk* (1950).

Sverdrup balance is described in terms of PV conservation (*Sverdrup*, 1947). Over the ocean, the wind inputs anticyclonic (negative) relative vorticity, which is balanced by a gain of cyclonic (positive) relative vorticity at the western boundary in the GS (*McDowell et al.*, 1982). The convergence in the STG arises due to the Easterly trades south of 30^oN and the midlatitude Westerlies to the north. This wind pattern causes northward and southward Ekman transport respectively, which initiates Ekman pumping across the STG. This squashing of the water column requires a decrease in the planetary vorticity, as the relative vorticity is small in the STG interior, which requires it to move southward leading to the equatorward flow seen across the gyre. The converse is true for the interior of the SPG, i.e. divergence, Ekman suction (vortex stretching) and poleward flow. This argument of negative (positive) wind stress curl resulting in a southward (northward) transport in the STG (SPG) is now commonly regarded as Sverdrup balance. Mathematically, PV balance (Equation 1.1) is derived from the combination of the continuity and momentum balance equations to achieve the linearised barotropic vorticity equation:

$$\beta v = f\frac{\partial w}{\partial z} \tag{1.1}$$

Where β is the linear variation of the Coriolis parameter, f, v is the meridional velocity, w is the vertical velocity and z is the height of the water column. This

clearly states a change in latitude is required after the stretching of the water column to maintain PV balance. The vertical velocity arises from the Ekman pumping (in the STG) and is related to the curl of the wind stress (τ):

$$w = \frac{1}{\rho f} curl\tau = \frac{\partial}{\partial x}(\frac{\tau^y}{\rho f}) - \frac{\partial}{\partial y}(\frac{\tau^x}{\rho f}) \tag{1.2}$$

Where ρ is the density, τ is the wind stress (meridional and zonal components τ^x and τ^y) and x and y are the zonal and meridional dimensions respectively. This can then be vertically integrated to obtain the Sverdrup transport in the interior, which is proportional to the wind stress curl (*Anderson and Corry*, 1985; *Hogg and Johns*, 1995):

$$\beta V = f\frac{\partial w}{\partial z} \tag{1.3}$$

where V is the meridional transport. Consequently, the line of zero curl τ marks the boundary between two gyres. However, for Sverdrup balance to occur the open streamlines predicted by Sverdrup balance must be closed by a narrow boundary current at the western boundary, which is explained by *Stommel* (1948) and *Munk* (1950).

Both arguments introduce friction (additional to wind) as a mechanism to support a cyclonic vorticity tendency that opposes the anticyclonic tendency due to large-scale wind stress curl across the STG. Specifically, friction is added to the bottom by *Stommel* (1948) and along the side walls and between the currents by *Munk* (1950), which both resulted in return flow along the western boundary. However, it is somewhat unrealistic that the wind-driven flow can reach the bottom of the STG in order for bottom friction to introduce cyclonic vorticity. Munk's solution avoids this restriction and still manages to produce the northward return flow (the GS) on the western boundary. As discussed previously, the flow in the interior must flow equatorward in the STG to reduce its planetary vorticity due to squashing of the water column from Ekman pumping. In order for this water to return to a higher latitude, it must increase its PV via changes in the relative vorticity (as

the planetary vorticity is already contained in Sverdrup balance). Munk's model introduces friction along both the sidewalls (i.e. the coastline), which reduces the current velocity to zero at the walls. From the eastern sidewall, this leads to an injection of additional negative (anticyclonic) relative vorticity, (as $dv/dx < 0$), which means it is difficult for the current to return to the interior. Conversely, along the western sidewall, there is an injection of positive (cyclonic) relative vorticity (as $dv/dx > 0$), which enables the water to travel northwards in order to increase its Coriolis parameter, f. Recalling that relative velocity = dv/dx - du/dy, the changes in the first term must be positive for anticyclonic tendency. Therefore, frictional boundary currents are always found on the western boundary in both STGs and SPGs in both hemispheres in order to obtain PV balance.

To reduce the accumulation of high PV water the thickness (h) of the water column must increase as:

$$PV = \frac{rV + f}{h} \tag{1.4}$$

where rV is the relative vorticity (*Cushman-Roisin*, 1987). This creates a storage region and a deeper thermocline in the Sargasso Sea, which sets up a high pressure centre that drives the anticyclonic SR (*Cushman-Roisin*, 1987). Surface buoyancy forcing, and subsequent cooling, also induces a downstream decrease in the PV, manifest as strong formation of Eighteen Degree Water (EDW) (*Hall and Fofonoff*, 1993; *Marchese*, 1999). The SR acts as a storage region for these waters until heat fluxes readjust the PV required for the water to re-enter the ocean interior (*Cushman-Roisin*, 1987).

1.3 Controls on Gulf Stream variability

As mentioned in section 1.1, considerable variability of GS transport and path shift exists on a range of timescales. Previous literature has linked its variability to natural oscillations, e.g. the North Atlantic Oscillation (NAO) and the El Nino Southern Oscillation (ENSO), circulation changes, e.g. in the Deep Western

Boundary Current (DWBC) and the recirculation gyres of the GS, or surface fluxes e.g. fluctuations in the wind stress field and buoyancy fluxes. The controls on GS transport and GS path shift variability will now each be discussed in turn.

1.3.1 Transport

Table 1.1 lists the main mechanisms that have been found to influence the transport of the GS, which will now be discussed.

Table 1.1: Mechanisms found to induce variations in GS transport in the literature.

Mechanism	Citations
North Atlantic Oscillation	(*Gangopadhyay and Watts*, 1992; *Sato and Rossby*, 1995; *Baringer and Larsen*, 2001; *Curry and McCartney*, 2001; *Flatau et al.*, 2003; *Visbeck et al.*, 2003; *Molinari*, 2004; *De Coëtlogon et al.*, 2006; *DiNezio et al.*, 2009; *Hakkinen and Rhines*, 2009; *Kwon et al.*, 2010; *Meinen et al.*, 2010; *Reverdin*, 2010; *Rossby et al.*, 2010; *Chaudhuri et al.*, 2011; *Rhein et al.*, 2011; *Sasaki and Schneider*, 2011; *Lillibridge and Mariano*, 2012)
Recirculation Gyres	(*Huang*, 1990; *Kelly et al.*, 1996; *Lillibridge and Mariano*, 2012)
Rossby Waves	(*Sturges and Hong*, 2001)
Momentum fluxes	(*Xue et al.*, 1995; *Xue and Bane Jr*, 1997; *Kelly et al.*, 1999; *Hakkinen and Rhines*, 2009; *Sasaki and Schneider*, 2011; *Lillibridge and Mariano*, 2012)
Buoyancy fluxes	(*Worthington*, 1977; *Kelly et al.*, 1996; *Moat et al.*, 2016)

The NAO index is the difference between two atmospheric pressure centres; the Icelandic Low and the Azores High (*Visbeck et al.*, 2003). Stronger Westerlies occur during a positive NAO index, which initiates greater (less) heat loss over the SPG (STG), while the opposite occurs during the negative NAO phase (*Hurrell et al.*, 1995). This is the dominant mode of atmospheric variability in the North Atlantic and can cause significant impacts to the ocean's properties and circulation, notably to the GS (*Visbeck et al.*, 2003).

There is some disagreement on how the NAO impacts the transport of the GS, with some studies finding an increased transport following a period of negative

NAO (*Gangopadhyay and Watts*, 1992; *Baringer and Larsen*, 2001; *DiNezio et al.*, 2009; *Rossby et al.*, 2010) and others finding an increased transport after a period of positive NAO (*Sato and Rossby*, 1995; *Curry and McCartney*, 2001; *De Coëtlogon et al.*, 2006; *Kwon et al.*, 2010; *Lillibridge and Mariano*, 2012). These discrepancies could be due to a number of reasons. First, it could suggest that the NAO does not have a dominant influence on controlling GS transport fluctuations, which may be due to the other mechanisms listed in Table 1.1. It could be related to the different methods used to define the GS or calculate its transport, the resolution of the dataset used, or it may be due to different sections of the GS under analysis. For example, during a period of low NAO, *Chaudhuri et al.* (2011) found that a greater GS transport was induced upstream of Cape Hatteras, i.e. in the Florida Current, but a reduced transport was found to occur further downstream after separation at Cape Hatteras. The NAO-induced variation in transport was found to be $1.4Sv$ upstream of Cape Hatteras and in excess of $20Sv$ further downstream (*Chaudhuri et al.*, 2011).

Upstream of Cape Hatteras in the Florida Current, the changes in transport can be related to changes in the wind stress, and therefore the wind stress curl variability. For example, during years of positive NAO, from $20 - 30^oN$ there is actually a positive wind stress curl anomaly, which reduces the transport observed in the Florida Current (*Baringer and Larsen*, 2001; *DiNezio et al.*, 2009; *Meinen et al.*, 2010). This is consistent with the theory discussed in Chapter 1.2, i.e. greater southward transport, which must return north in the GS, when curl τ is more negative and vice versa. The anti-correlation between the transport and the NAO is also reproduced in the ROMS model (*Chaudhuri et al.*, 2011).

Downstream of Cape Hatteras in the separated GS, the NAO index is found to be correlated with the transport at about a 3-year lag (*Chaudhuri et al.*, 2011). This is primarily related to changes in the SPG. For example, during a positive NAO winter the intensified Westerlies lead to cooling over the Labrador Sea, which induces deep convection (*Hurrell et al.*, 1995). This causes a greater Labrador Sea Water (LSW) outflow and a stronger DWBC (deep branch), which leads to an intensification of the Atlantic Meridional Overturning Circulation (AMOC) and, by

continuity, a stronger GS (upper branch) (*Flatau et al.*, 2003; *De Coëtlogon et al.*, 2006; *Robson et al.*, 2012). Consequently, periods of positive NAO coincide with anomalously high GS transports (e.g. from 1970-mid-1990s) with anomalously low transports associated with periods of negative NAO (e.g. 1950s and 1960s) (*Sato and Rossby*, 1995; *Curry and McCartney*, 2001).

In addition to the more widespread changes to buoyancy and momentum fluxes induced by the NAO index, it has been argued that strong, localised air-sea heat fluxes over the STG have been found to influence the GS (*Worthington*, 1977). These strong losses are often initiated during widespread outbreaks of cold, continental air from the northeast of North America extending over the GS region (*Grossman and Betts*, 1990; *Xue et al.*, 1995; *Joyce et al.*, 2009; *Kelly et al.*, 2010; *Ma et al.*, 2015) and occur more frequently during negative NAO years (*Walsh et al.*, 2001). These losses are often the largest seen globally (*Bane and Osgood*, 1989; *Kwon et al.*, 2010) with extreme values sometimes exceeding 1000 W m^{-2} during an outbreak (*Kelly et al.*, 2010; *Silverthorne and Toole*, 2013). This surface heat loss initiates strong convection in the Sargasso Sea, which can lead to Mixed Layer Depths (MLD) of up to $500m$ (*Silverthorne and Toole*, 2013; *Buckley et al.*, 2014). As the surface water warms, the vertically homogenous layer is preserved as Subtropical Mode Water (STMW) beneath the restratified surface layer (*Leetmaa*, 1977; *Dong and Kelly*, 2004; *Mensa et al.*, 2013; *Silverthorne and Toole*, 2013). EDW was first identified by *Worthington* (1958) in the Sargasso Sea who found a uniform temperature and salinity of 17.9^oC and 36.5 psu respectively. Spatial and interannual variability of EDW is correlated to the NAO, which suggests that changes in air-sea forcing are important in its formation (*Joyce et al.*, 2000). The deepening of the thermocline, associated with EDW formation, combined with an increase in meridional temperature gradients across the GS at depth will have a significant influence on its baroclinic transport, given the thermal wind relation (*Leetmaa*, 1977; *Sato and Rossby*, 1995; *Kelly et al.*, 1996; *Dong et al.*, 2007). For example, following a series of Cold Air Outbreaks (CAO) *Worthington* (1977) found an intensification in the separated GS transport, which is discussed further in Chapter 1.4.

There is also a view that GS variability is primarily associated with large wintertime air-sea momentum fluxes (*Xue et al.*, 1995; *Xue and Bane Jr*, 1997; *Kelly et al.*, 1999). In particular, the role of wind stress curl variability has been found to be a major factor in driving changes to the transport of the GS (*Anderson and Corry*, 1985; *Hogg and Johns*, 1995; *Kelly et al.*, 1996; *Sturges and Hong*, 2001; *De Coëtlogon et al.*, 2006; *DiNezio et al.*, 2009). For example, a stronger (i.e. more negative) wind stress curl in the STG causes an intensification to the gyre, and therefore the GS (*Chaudhuri et al.*, 2011). Wind stress curl variability is also closely linked to the NAO, as was mentioned earlier, with the positive phase of the NAO causing a more negative wind stress curl over most of the STG and a stronger separated GS transport (*Meinen et al.*, 2010). This contrasts with the anomalously positive wind stress curl from $20 - 30^o N$ that reduces the transport of the Florida Current (*DiNezio et al.*, 2009). In addition to this, wind stress variability leads to the formation of Rossby waves that propagate westwards across the basin towards the GS (*Frankignoul et al.*, 1997). The influx of Rossby waves is found to influence the sea level along the east coast of North America, which can lead to low frequency barotropic transport variability (*Sturges and Hong*, 2001).

Furthermore, the occurrence of CAOs during winter have been found to induce a reduction in the transport of the pre-separated GS (*Moat et al.*, 2016), which contrasts with the intensification of the separated GS found by *Worthington* (1977). Here, the momentum fluxes are found to be imperative in initiating the change in transport. They found that the anomalous northerly wind, from the CAOs, reduces the Ekman transport, which flows northward at $26.5^o N$, and initiates a reduction in the transport at 5-day timescales. For example, during the winter of 2009-10 a 30% reduction was observed during these events (*Moat et al.*, 2016). Yet, *De Coëtlogon et al.* (2006) have emphasized that wind forcing cannot be the sole influence on GS transport, which implies that, in addition to unforced basin-scale circulation changes, an important role is also played by buoyancy forcing.

Finally, changes in the recirculation gyres have also been found to induce changes in the transport of the GS (*Lillibridge and Mariano*, 2012). Specifically, a stronger SR or NR has been found to intensify the overall GS transport by up to 20% (*Kelly*

et al., 1996) and is related to intense cooling events over the Sargasso Sea (CAOs) (*Huang*, 1990).

1.3.2 Path

Path shifts of the GS are important to monitor as the warm and saline nature of the water mass could have an adverse effect on local ecosystems and fisheries (*Drinkwater et al.*, 1994; *Molinari*, 2004; *Gawarkiewicz et al.*, 2012). For example, in late 2011 the GS appeared to reach around $200km$ north of its mean position at 68^oW, which is the northernmost position it has reached at this longitude since altimetry records in began in 1992 (*Gawarkiewicz et al.*, 2012). This led to anomalous deep ocean temperatures of up to 6^oC recorded by lobster traps (*Gawarkiewicz et al.*, 2012). This specific example was due to a series of meanders, which are known to initiate GS path shifts of more than $100km$ on short timescales (*Molinari*, 2004).

Potential controls on path shift all vary on temporal (several months to several years) and spatial scales ($20km$ to $1000km$) (*Peña-Molino and Joyce*, 2008; *Lillibridge and Mariano*, 2012). The larger lateral path shifts have been attributed to fluctuations in the basin-scale ocean circulation (e.g. in the DWBC) or changes in the surface forcing (e.g. the NAO). The main mechanisms attributed to GS path shift are outlined in Table 1.2 and will be discussed here.

In addition to causing GS transport variability, the NAO is known to induce north-south shifts to the GS (*Taylor and Stephens*, 1998; *Joyce et al.*, 2000). The pattern of the winter NAO index, i.e. negative from the late-1950s to early-1970s and positive during the 1980s and 1990s (*Chaudhuri et al.*, 2011), correlates with the more southward path during negative NAO periods and more a more northward path during positive NAO periods (*Taylor and Gangopadhyay*, 2001; *Kwon et al.*, 2010; *Gangopadhyay et al.*, 2016). Additionally, the negative NAO phase is found to be more prominent during El Niño events relative to La Niña events (*Kwon et al.*, 2010).

During a positive NAO phase, there are stronger mid-latitude westerly winds and stronger easterly trade winds, which induce an enhanced northward Ekman trans-

Table 1.2: Mechanisms found to induce variations in GS path in the literature.

Mechanism	Citations
North Atlantic Oscillation	(*Taylor and Stephens*, 1998; *Joyce et al.*, 2000; *Rossby and Benway*, 2000; *Frankignoul et al.*, 2001; *Taylor and Gangopadhyay*, 2001; *Hameed and Piontkovski*, 2004; *Volkov*, 2005; *De Coëtlogon et al.*, 2006; *Kwon et al.*, 2010; *Rossby et al.*, 2010; *Kwon and Joyce*, 2013; *Lillibridge and Mariano*, 2012; *Pérez-Hernández and Joyce*, 2014; *Gangopadhyay et al.*, 2016; *Sanchez-Franks et al.*, 2016)
El Niño Southern Oscilation	(*Kwon et al.*, 2010; *Pérez-Hernández and Joyce*, 2014; *Sanchez-Franks et al.*, 2016)
Wind Stress	(*Veronis*, 1973; *Gangopadhyay and Watts*, 1992; *White and Heywood*, 1995; *Kelly et al.*, 1996; *Sasaki and Schneider*, 2011)
Rossby Waves	(*Gangopadhyay and Watts*, 1992; *Taylor and Gangopadhyay*, 2001; *Hameed and Piontkovski*, 2004; *DiNezio et al.*, 2009; *Pérez-Hernández and Joyce*, 2014)
Recirculation Gyres	(*Hogg*, 1992; *Jiang et al.*, 1995; *Kelly et al.*, 1996; *Wang and Koblinsky*, 1996; *Frankignoul et al.*, 2001; *Zhang and Vallis*, 2006, 2007)
Deep Western Boundary Current	(*Thompson and Schmitz Jr*, 1989; *Ezer and Mellor*, 1992; *Pickart and Smethie Jr*, 1993; *Gerdes and Köberle*, 1995; *Spall*, 1996; *Bower and Hunt*, 2000; *Joyce et al.*, 2000; *Frankignoul et al.*, 2001; *Zhang and Vallis*, 2006, 2007; *Zhang*, 2008; *Peña-Molino and Joyce*, 2008; *Yeager and Jochum*, 2009; *Kwon et al.*, 2010; *Lillibridge and Mariano*, 2012; *Pérez-Hernández and Joyce*, 2014)
Labrador Sea Water	(*Hameed and Piontkovski*, 2004; *Lillibridge and Mariano*, 2012; *Pérez-Hernández and Joyce*, 2014; *Sanchez-Franks et al.*, 2016; *Bisagni et al.*, 2017)

port south of 40^oN (*Visbeck et al.*, 2003). This, combined with a northward shift in the latitude of zero wind stress curl, leads to a northward shift in the GS path (*Taylor and Stephens*, 1998; *Joyce et al.*, 2000; *Taylor and Gangopadhyay*, 2001; *Kwon et al.*, 2010; *Rossby et al.*, 2010; *Sasaki and Schneider*, 2011; *Gawarkiewicz et al.*, 2012). Contrastingly, the winds are weaker during negative NAO phases, which leads to weaker Ekman transport and a more southward GS (*Chaudhuri et al.*, 2011). However, *Hameed and Piontkovski* (2004) found evidence that the position of the Icelandic Low is more important than the NAO index with a more eastward Icelandic Low inducing a more southward GS path. This relationship is

also identified by *Sanchez-Franks et al.* (2016) who found that the combination of a more westward and anomalously strong Iceland Low led to a more northward GS 2-3 years later. The importance of the Icelandic Low is due to its proximity to the Labrador Sea as changes in the wind from the low-pressure center will initiate SST changes in this region (*Hameed and Piontkovski*, 2004; *Sanchez-Franks et al.*, 2016).

The combined influence of anomalous wind and buoyancy forcing over the Labrador Sea induces deep convection and a greater export of LSW (*Hurrell et al.*, 1995). The consequent strengthening of the DWBC and Slope Water Current then acts to push the GS into a more southward position at a lag time of 1-3 years (*Thompson and Schmitz Jr*, 1989; *Schmeits and Dijkstra*, 2001; *Peña-Molino and Joyce*, 2008; *Sanchez-Franks et al.*, 2016; *Bisagni et al.*, 2017). A regional primitive equation model found that without a DWBC, the GS separated $250km$ further to the north than if a DWBC of $10Sv$ were present (*Spall*, 1996). The stronger Slope Water Current induced by a greater export of LSW can also be used as a preceding indicator of GS shift with a colder Slope Water preceding a southward GS shift (*Rossby and Gottlieb*, 1998; *Sanchez-Franks et al.*, 2016). Given this relationship, *Sanchez-Franks et al.* (2016) created a forecast of the position of the GS with a lead time of 1 year using the positon and strength of the Icelandic Low combined with the Southern Oscillation Index (a measure of the strength of the Walker circulation). The forecasted position was found to be significantly correlated with the observations from 1994-2014, which highlights the considerable impact of these mechanisms.

In addition to the production of LSW leading to a lagged response, the adjustment of the Ekman transport leads to a lagged response between the NAO and the coincidental GS path shift (*Visbeck et al.*, 2003). This lag is found to vary between 1 year (*Frankignoul et al.*, 2001) and 2 years (*Taylor and Stephens*, 1998; *Hameed and Piontkovski*, 2004; *Lillibridge and Mariano*, 2012). Furthermore, the time it takes for Rossby waves to cross the ocean basin also elicits a lag (*Gangopadhyay and Watts*, 1992). Westward travelling Rossby waves are initiated by fluctuations in the NAO index and when they reflect off the East coast of North America they act

to push the thermocline up to the surface (*Hameed and Piontkovski*, 2004). This initiates the detachment of the GS from the coast and thereby acts as a control on the latitude of GS separation (*Hameed and Piontkovski*, 2004). This is also revealed in a two-layer wind driven model (*Veronis*, 1973; *Gangopadhyay and Watts*, 1992), which shows that changes in the wind stress, and the subsequent initiation of Rossby waves, induces changes in the path of the GS that are consistent with observations. The influx of LSW also leads to a stronger NR, which can induce a more southward GS path (*Hogg*, 1992; *Zhang*, 2008; *Joyce and Zhang*, 2010) while an intensified SR also leads to a more southward GS (*Jiang et al.*, 1995; *Spall*, 1996).

A more direct control on GS and NAC path shift is the position of the line of zero wind stress curl. Sverdrup dynamics implies that if the wind stress was entirely zonal, there would be no meridional flow across the line of zero wind stress curl so the location of the NAC is predicted to be related to the position of this line, which represents the boundary between the STG and SPG (*White and Heywood*, 1995). For example, using altimetric data, interannual variability in the position of NAC branches (from 1986-1988 and 1992-1994) was found to be associated with shifts in the position of the line of zero wind stress curl during the winter (when it is most defined with large wind stress values) (*White and Heywood*, 1995).

Although each of these mechanisms has been found to cause shifts in the GS path, their influence may not be equally weighted. For example, the NAO has been widely studied and the mechanisms associated with GS path shift are understood. In contrast, the El Nino Southern Oscillation is not as widely studied and further work is required to understand exactly how it contributes to GS path shift. The interconnectivity of these mechanisms is apparent and they can influence the GS on various timescales, which adds complexity to the issue of what exactly controls the position and transport of the GS.

1.4 Climatic importance of the Gulf Stream

There is a keen interest in the variability of the GS due to its major role in the global redistribution of heat (*Lillibridge and Mariano*, 2012). There is a large sensible and latent heat flux from the GS to the overlying atmosphere in winter, of up to 100 W m^{-2} and 200 W m^{-2} monthly mean values respectively (*Kelly et al.*, 2010), due to the large temperature difference at the interface (*Minobe et al.*, 2010; *Davis et al.*, 2013). However, the latent heat fluxes are found to be more important in this region (*Joyce et al.*, 2009; *Kwon et al.*, 2010). These considerable heat fluxes also turn northward with the GS path at about 50^oW as it travels towards the Northwest Corner (*Joyce et al.*, 2009).

Additionally, the sharp SST front of the GS (up to 10^oC over $200km$ (*Kelly et al.*, 2010)) maintains surface baroclinicity via differential heating, which initiates intense atmospheric cyclogenesis over the current (*Hoskins and Valdes*, 1990; *Nakamura et al.*, 2004, 2008). This enables it to strongly influence the North Atlantic storm track (*Joyce et al.*, 2000; *Frankignoul et al.*, 2001; *Joyce et al.*, 2009; *Brayshaw et al.*, 2011; *Kwon and Joyce*, 2013; *Hand et al.*, 2014; *Parfitt et al.*, 2016). For example, during years where PV is low over the Sargasso Sea the GS is found further north while the maximum frequency of storms in the North Atlantic is found 2^o further north (*Joyce et al.*, 2000). In addition to this, the mean pattern of upper tropospheric clouds is related to the subsurface ocean front of the GS (*Joyce et al.*, 2009). Specifically, the strong SST gradient across the GS leads to surface wind convergence, which anchors a narrow precipitation band across the path (*Minobe et al.*, 2008; *Vannière et al.*, 2017). Resolution is important here as the sharper SST gradient in reanalyses (ERA-Interim) with a finer horizontal resolution was found to increase the heat fluxes and precipitation over the GS by up to 30% (*Parfitt et al.*, 2016).

The considerable heat flux from the GS has been thought to ameliorate the climate of Western Europe to create milder winters than other global landmasses at the same latitude (*Rossby*, 1996). For example, the temperature of western Europe is up to 15^oC warmer than these landmasses during the winter, which

is due to a combination of the atmosphere and ocean driving air-sea heat flux variability (*Yamamoto et al.*, 2015). Over North America, the Rockies interact with the jet stream to create northwesterly winds that move cold, dry air over the northeast of North America and southwesterly winds that move warm, humid air towards Europe (*Seager et al.*, 2002). However, this heat is not enough to support mild winters in Europe, with the extra heat coming from the GS (*Riser and Lozier*, 2013). Both factors are found to be important with the atmosphere dominating on short timescales (i.e. less than interannual) and the ocean dominating on longer timescales (i.e. interannual to decadal) (*Bjerknes*, 1964). For example, *Yamamoto et al.* (2015) used atmospheric Lagrangian trajectories to determine along-track air-sea heat exchange near western Europe. They found that basin-wide changes in SST can affect the accumulated heat flux of particles but short-term changes in the AMOC are unlikely to affect the winters of western Europe unless combined with atmospheric changes.

Hence, the high heat flux from the GS may provide some predictability for the North Atlantic storm track and winter conditions in Europe, which highlights the need to understand the processes controlling the GS.

The most important contribution to winter surface heat flux variability is from 3-10 day storms (*Alexander and Scott*, 1997) as they contribute significantly to the overall heat exchange in the GS region (*Ma et al.*, 2015). Each winter sees about 10-20 CAOs with about 5 extreme flux days, defined as having an air-sea temperature difference of more than 20^oC (*Grossman and Betts*, 1990). Their occurrence has been related to the NAO (*Walsh et al.*, 2001) and the East Atlantic Pattern (EAP) (*Ma et al.*, 2015).

Recognizing the importance of buoyancy forcing for the wider GS system, *Worthington* (1977) proposed a mechanism termed anti-cyclogenesis, whereby the STG is strengthened via a deepening of the thermocline on the southern flank of the GS. The clearest example of anti-cyclogenesis was observed by *Worthington* (1977) after the severe winter of 1976/77, when CAOs led to large heat losses over the western STG. This led to anomalously deep mixed layers and a high renewal of EDW to the south of the GS, which strengthened the subsurface meridional temperature

gradients across the current. He found that this increased upper baroclinic GS transport by around 50% compared to corresponding transport estimates after the much milder winter of 1974/75. Similarly, *Halliwell and Mooers* (1979) also found an intensified transport, by 25%, a northward shift in the current and increased eddy shedding during this winter.

The effects of winter 1976-77 were also investigated by *Leetmaa* (1977) who revealed a thermocline depth of $800m$ at $34^oN, 71^oW$, which is close to where *Worthington* (1977) measured an increase in transport. The extensive renewal of EDW during this winter follows a series of years (1972-75) when EDW formation was anomalously low, coincident with mild winters over northeast North America (*Talley and Raymer*, 1982; *Worthington*, 1977). This severe winter, therefore, led to an associated increase in transport, compared to the previous decade, of $+40Sv$ (*Worthington*, 1977). Contrastingly, *Rossby et al.* (1995) found that the opposite relationship exists with decreasing transport from a weaker SST gradient across the GS associated with anomalous heat loss west of 62^oW. However, only 2.5 years of satellite data were used to obtain this relationship across all months, rather than just winter months. This may be too short a period as *Worthington* (1977)'s results suggest that it is a particularly severe winter that could elicit an intensification of the GS.

In addition to the strengthening of the main current (of up to 60%) following winter cooling, *Huang* (1990) found an accompanying increase in both the NR and SR using a two-layer model. To the south, the destruction of high PV from intense cooling at the surface creates a barotropic high pressure centre and drives recirculation (*Worthington*, 1976). However, geostrophic adjustment is vital to achieve this *Huang* (1990). In contrast, a study by *Zheng et al.* (1984) proposed that cooling over the Sargasso Sea is not the sole driving force for an increase in GS transport. They suggest that this mechanism is reinforced by the heat loss observed in the Slope Water, i.e. the combination of isotherms upwelling to the north of the GS and downwelling to the south.

1.5 The Gulf Stream in Ocean Models

WBCs are composed of nonlinear frontal structures and energetic mesoscale eddy fields, which makes it difficult to model accurately (*Pierini*, 2015). In particular, the correct separation from the coast at Cape Hatteras is influenced by a combination of factors including the horizontal resolution, boundary conditions, parameterisations and coastline of the model, surface forcing, the strength of the DWBC and occurrence of eddies (*Ezer*, 2016; *Schoonover et al.*, 2017).

Early modelling studies failed to simulate the separation point or volume transport correctly, which is mostly due to the coarse resolution of climate models (*Dengg et al.*, 1996). Specifically, the GS was found to separate too far north and have an anomalously weak transport (*De Coëtlogon et al.*, 2006; *Saba et al.*, 2016). Consequently, a horizontal resolution of $1/10^o$ or finer is required to model an accurate separation and to resolve mesoscale activity (*Bryan et al.*, 2007; *Yeager and Jochum*, 2009; *Kwon et al.*, 2010). The increased resolution enables a combination of factors to improve, e.g. stronger buoyancy forcing over the Labrador Sea, which allows a stronger DWBC that forces the GS into a more southward position (*Yeager and Jochum*, 2009). Furthermore, coarse resolution models may underestimate sea level differences and, therefore, GS transport as they are unable to adequately resolve the coastline and the bottom topography (*Ezer*, 2017; *Schoonover et al.*, 2017). *Chassignet and Xu* (2017) went even further and investigated the effects of increasing the resolution from $1/12^o$ to $1/50^o$. They found that the $1/50^o$ resolution model produces more realistic GS penetration into the basin and with depth, and recirculation gyre variability compared to observations.

An incorrect separation, i.e. an anomalously northward GS, prohibits the model from reproducing the NR and leads to a warm SST bias, which has climatic implications (*De Coëtlogon et al.*, 2006; *Zhang and Vallis*, 2007; *Saba et al.*, 2016). For example, in climate models that have a coarser horizontal resolution than 1^o, a large cold bias exists near Newfoundland due to an anomalously southward NAC, which leads to atmospheric blocking events over Greenland (*Scaife et al.*, 2011). A stronger atmosphere-ocean coupling is revealed with an improved resolution,

which greatly improves the blocking frequency in this region by reducing the cold bias (*Scaife et al.*, 2011). Additionally, blocking occurs less frequently and storm track activity is weaker when the GS SST is smoothed (*O'Reilly et al.*, 2016) with the opposite being true during periods of high eddy heat flux over the GS region (*O'Reilly et al.*, 2017).

1.6 Lagrangian perspectives on the downstream destination of Gulf Stream Waters

Thus far, the variability of the GS and how it is modelled has been discussed in a Eulerian sense. However, many studies have measured the speed or investigated the various pathways of the GS and NAC using observational surface drifters or by modelling synthetic drifters (*Brambilla and Talley*, 2006; *Hakkinen and Rhines*, 2009; *Burkholder and Lozier*, 2011; *Rypina et al.*, 2011; *Burkholder and Lozier*, 2014; *Foukal and Lozier*, 2016). Notably, the interconnectivity between the STG and SPG has received much attention in the literature as the Lagrangian estimates are not consistent with the Eulerian equivalent. For example, *Johns et al.* (1995) found that, of the $65Sv$ of GS transport recorded at Cape Hatteras, $20Sv$ continue northeast as the NAC into the SPG. However, this estimate has been disputed by many Lagrangian studies (*Brambilla and Talley*, 2006; *Burkholder and Lozier*, 2011) that found little intergyre exchange at the surface.

The absence of a prominent conduit between the two gyres near the surface is evident in both observational and modelling studies. For example, only 1/273 surface drifters reached the Nordic Seas that flowed through a box (from 78^oW to 48^oW, 35^oN to 47^oN) near the GS region during the period 1992-2002 (*Brambilla and Talley*, 2006). This drifter had a lifetime of 495 days, which is substantially longer than the mean surface drifter lifetime of 271 days (*Brambilla and Talley*, 2006). In addition to the short mean lifetime of drifters, the southward Ekman transport is also found to reduce the number of drifters reaching the SPG by $5-6\%$ (*Brambilla and Talley*, 2006). In spite of this, longer drifter lifetimes and reduced Ekman transport is still not enough to reproduce the $20Sv$ of upper GS transport that travels to the SPG as found by *Johns et al.* (1995). However, *Hakkinen and*

Rhines (2009) observed an increase in the number of drifters that reached the SPG from 2001-2007, which coincides with the warming of the Nordic Seas during this period. They related this expansion of drifters to a meridional tilt in the line of zero wind stress curl, which has been related to the NAO. This observation implies that surface forcing may be important in controlling the amount of intergyre connectivity at the surface.

However, greater intergyre exchange has been found to exist in sub-surface pathways beneath the climatological mixed layer on timeacales ranging from 2-7 years (*Burkholder and Lozier*, 2011, 2014; *Foukal and Lozier*, 2016). Using the eddy-resolving model of the North Atlantic, FLAME, *Burkholder and Lozier* (2011) found that up to 29% of trajectories launched in the STG reach the SPG when they are not constrained to the surface (compared to 2.3% at 15 m). The optimum release depth for intergyre connectivity was found to be $700m$ as the trajectories follow the isopycnal that they are released on, which in this case, is beneath the Ekman layer (*Burkholder and Lozier*, 2011). These shoaling density surfaces allow floats to cross the boundary into the SPG as those launched on shallow isopycnals are too light, which results in them recirculating within the STG. This highlights the need to use the three-dimensional flow field when investigating GS pathways.

Near the surface of the GS there is a strong PV gradient that acts as a transport barrier (*Lozier and Riser*, 1990). This weakens with depth, which enables more cross-gyre mixing than at the surface (*Rypina et al.*, 2011). However, there is evidence for intergyre exchange on timescales of less than two years when trajectories are released in the main GS path, as opposed to within the STG interior, at the surface (*Rypina et al.*, 2011). These trajectories were found to travel on the shoreward side of the GS, i.e. in the northern flank, which eliminates the need to cross a PV barrier and enables a direct pathway between the two gyres (*Rypina et al.*, 2011).

In spite of having to take into consideration drifter lifetimes, the trajectory release location and surface constraints (i.e the existence of an eddy field and Ekman transport), interannual variability in the throughput of subtropical waters to the SPG is still observed. Using a transport index based on the sea level pressure

at the centre of the STG and SPG, a peak in NAC transport was observed during the 1990s, with an increase of $25-33\%$ seen from 1970-95 (*Curry and McCartney*, 2001). This is thought to be associated with a sustained period of the positive NAO index (*Curry and McCartney*, 2001; *Flatau et al.*, 2003). At the surface, an expansion of drifters to the north was also found to occur since 2001, which is thought to be related to a tilt in the line of zero wind stress curl, as mentioned previously, (*Hakkinen and Rhines*, 2009) and increased EKE from the slowdown of the SPG as it contracted to the west (*Bower and von Appen*, 2008). However, it has been argued that this increase may mainly be due to more drifters being initiated on the onshore side of the GS core (*Rypina et al.*, 2011).

Nevertheless, the warming of the SPG that occurred during the 1990s (*Häkkinen and Rhines*, 2004; *Grist et al.*, 2010) could have been caused by anomalous Ocean Heat Transport (OHT) into the region (*Marsh et al.*, 2008). In the SPG, *Grist et al.* (2010) found that OHT at the southern boundary (42^oN) plays a dominant role in driving ocean heat content anomalies with air-sea interaction only being a dominant factor in a just few years over the period 1962-2001. However, the largest OHT anomalies occur when heat convergence and surface heat flux anomalies coincide, e.g. in the late 1990s (*Grist et al.*, 2010). This could highlight the importance of subsurface pathways into this region from the STG.

Consequently, further work is required to reconcile the Eulerian studies, that showed increased gyre (and AMOC) transport in the 1990s, with the Lagrangian studies, which apparently show no significant increase in intergyre transport.

1.7 The scope of this thesis

The scientific scope of this thesis is based on the importance of air-sea fluxes controlling GS path and transport variability. The work presented in this thesis is predominantly model-based with some comparison to observations in the first research chapter (Chapter 3). The high resolution, eddy-resolving ORCA12 hindcast from the ocean model Nucleus for European Modelling of the Ocean (NEMO) is used to quantify transport and pathway variability of the GS on different timescales

in both a Eulerian and Lagrangian framework.

The first research chapter introduces the thesis by quantifying the path and transport variability of the GS. Two methods are used to define the GS path using the SST field in the Advanced Very High Resolution Radiometer (AVHRR), which are compared to ORCA12. The latitudinal variability of the GS is then investigated on monthly and interannual timescales in order to assess the accuracy of these methods. The barotropic and baroclinic transport is also calculated at 70^oW in the observational product Global Ocean Data Assimilation System (GODAS) and compared to ORCA12. It is thus demonstrated how a changing density structure across the GS can lead to changes in transport. This evidence is placed in the context of work by *Worthington* (1977) who put forward the theory that intense air-sea heat fluxes led to GS intensification after a severe winter in North America. This is investigated in the observational dataset EN4 during two severe winters, i.e. 1976/77 and 2013/14, to assess whether considerable heat fluxes can induce changes in the baroclinic GS transport.

Having provided evidence that changes in the density structure across the GS are important in determining transport variability, the second research chapter utilises the GS transport calculated in ORCA12 to explore the role of localised buoyancy forcing in facilitating said density changes. The use of this model hindcast enables a thorough investigation into the mechanisms associated with this variability. The end of winter, year-to-year changes in transport are analysed in relation to the mean winter surface heat flux, the end of winter MLD, changes in the meridional temperature gradients and the variation in the strength of the southern recirculation. There has not before been a model-based study that examines the contributions coming from the north (*Zheng et al.*, 1984) and the south of the GS (*Worthington*, 1977), which aims to investigate previously studied mechanisms over a lengthy period (33 years).

The third research chapter examines the nature and causes of variability in the downstream destination of advected GS water in the ORCA12 hindcast. Using trajectory analysis, the downstream destination of GS water, i.e. the SPG, the SR, the NR or the AC, is quantified at different release depths and on seasonal

and interannual timescales. This novel approach will also build upon the work that investigates intergyre connectivity (*Brambilla and Talley*, 2006; *Burkholder and Lozier*, 2011; *Rypina et al.*, 2011; *Foukal and Lozier*, 2016) by attempting to establish a more direct pathway between the two gyres via the GS on timescales of less than a year. Furthermore, the near-surface throughput of GS water to the SPG and the SR, the most favoured pathways, is analysed in relation to localised air-sea fluxes on monthly timescales. At the subsurface, the decadal variability of throughput to the SPG is also examined in relation to large-scale air-sea fluxes. This also provides a Lagrangian framework for the increased intergyre connectivity observed in the early 1990s by Eulerian-based studies (*Marsh et al.*, 2008; *Grist et al.*, 2010; *Robson et al.*, 2012).

Together, these chapters provide a novel scientific contribution to the mechanisms controlling GS variability on a range of timescales. They also highlight the importance of air-sea fluxes in controlling the variability of the GS transport and its pathways.

Chapter 2

Methods

This chapter describes the model, software and datasets used in this thesis and then outlines the methods used in each chapter. First, the NEMO model is described in section 2.1, Ariane software is detailed in section 2.2 and the datasets and methodologies for each research chapter are explained in sections 2.3, 2.4 and 2.5.

2.1 The NEMO model

This thesis utilises the high resolution, global, ocean model NEMO (*Madec et al.*, 2015), using the eddy-resolving ORCA12 configuration setup of the DRAKKAR project (*Duchez et al.*, 2014; *Blaker et al.*, 2015; *Marzocchi et al.*, 2015), which spans 1978-2010. The model is discretised on a C-grid and this hindcast has a horizontal resolution of approximately $1/12^o$, which corresponds to about $9.25km$ at the equator, $7km$ at Cape Hatteras and $1.6km$ in the Ross Sea. It has 75 vertical levels with finer grid spacing near the surface, i.e. less than $1m$ at the surface compared to $250m$ at $5500m$ with 22 levels in the upper $100m$.

In order to prevent numerical instability where the meridians converge in the northern hemisphere, the model is tri-polar with two North Poles, i.e. in Canada and Russia, and one at the South Pole (*Madec and Imbard*, 1996). North of 20^oN, the grid is quasi-isotropic bipolar and south of 20^oN it is isotropic Mercator. Additionally, the bottom topography is represented as partial steps with a free-slip lateral friction condition applied at the lateral boundaries. The Louvain la Neuve

(LIM2) sea-ice model is used to represent sea ice in the simulation (*Timmermann et al.*, 2005).

The run is initialised using the World Ocean Atlas 2005 climatological fields (*Antonov et al.*, 2006; *Locarnini et al.*, 2006). The simulation includes DFS4.1 surface forcing (*Brodeau et al.*, 2010), with 6-hourly mean $10m$ winds, $2m$ temperature, $2m$ humidity, and monthly mean precipitation fields. Linear interpolation is used to integrate these fields into the model and the output fields are stored as 5-day means from 1978-2010. The surface salinity is relaxed towards the climatology to avoid excessive drifting in the global salinity.

The region of focus in this thesis is the North Atlantic and this region in the model will now be validated using observations. The realism of the modelled surface velocities (i.e. level 1 in ORCA12) with the altimetric sea surface currents distributed by AVISO (http://www.aviso.altimetry.fr/duacs/) is illustrated in Figure 2.1a, which shows a representative model-data comparison during April 2005 (Figure 2.1b). A strong agreement exists between the two 5-day mean surface velocity fields with high values seen in the GS region. Some specific differences are apparent, which are likely due to the higher resolution in the model, i.e. the separated GS is narrower and positioned further south in ORCA12. Nevertheless, the model represents realistic levels of mesoscale variability (in the form of meanders and eddies), and a broadly correct location and strength for the NAC and AC. This is further illustrated by *Marzocchi et al.* (2015). It is worth noting here that due to unpredictable non-linearities in the GS's response to forcing, mismatches in the SST and corresponding flux fields will exist between the model and observations. Finally, we note that the model successfully represents GS separation from the coast throughout the hindcast, which is a common problem in models of resolution lower than $1/10^o$ (*Chassignet and Garraffo*, 2001), see Chapter 1.2. These coarser resolution models tend to have a GS that separates from the coast too far north (*Dengg et al.*, 1996).

In addition to the model-data comparison of velocity fields, Figure 2.1c reveals the monthly surface heat flux anomalies in the western STG region in the ORCA12 hindcast and two observational datasets; NCEP/NCAR (*Kalnay et al.*, 1996) and

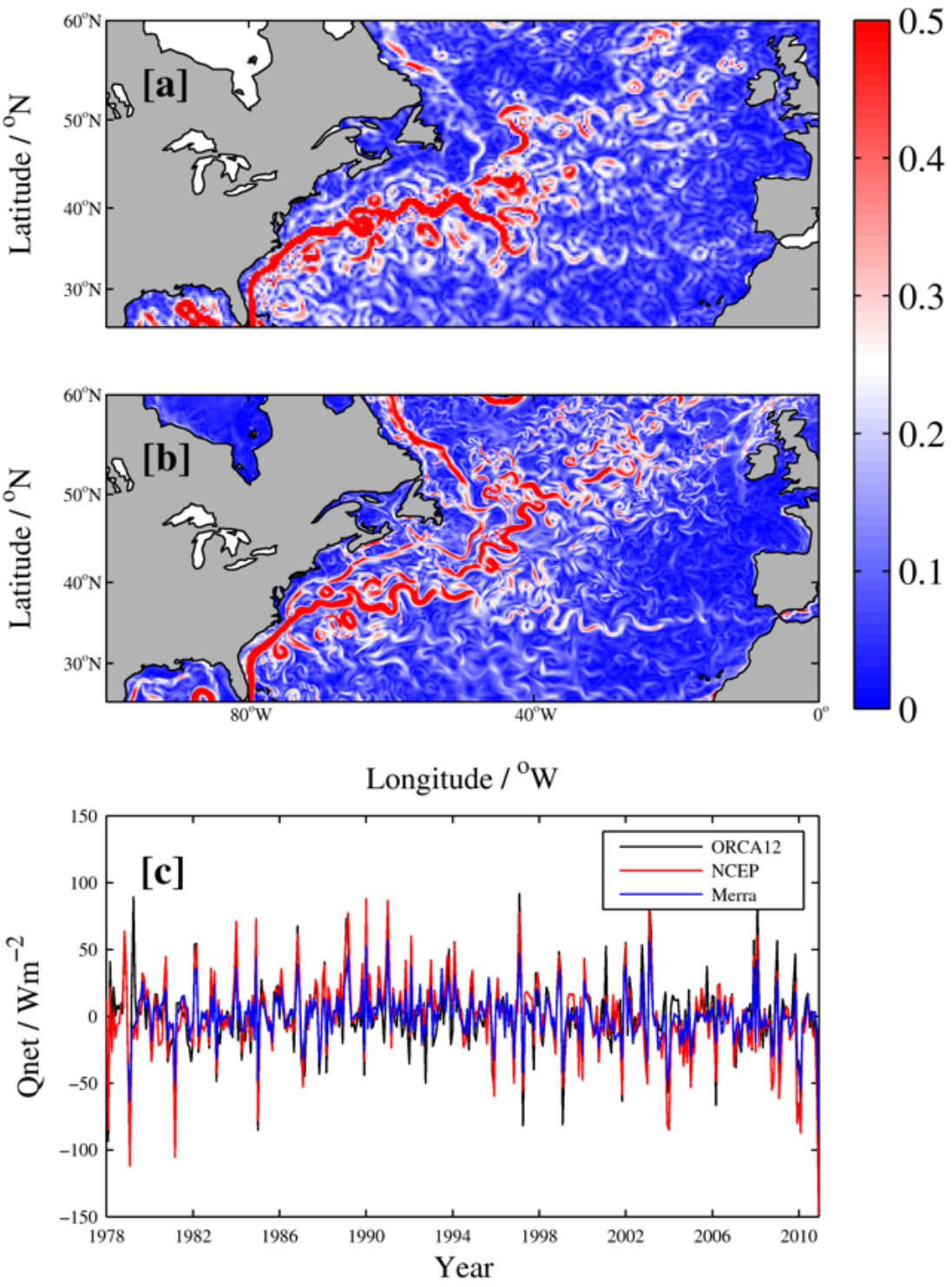

Figure 2.1: Example of mean 5-day surface currents (m s^{-1}) in the GS region from AVISO [a] and ORCA12 [b] during April 2005 and monthly surface heat flux anomalies in ORCA12, NCEP/NCAR and Merra averaged over the region $25 - 25^{o}N$, $50 - 80^{o}W$.

Merra (*Rienecker et al.*, 2011). Overall, the ORCA12 surface heat flux forcing agrees well with the observational datasets. Although the magnitude of the anom-

alies in ORCA12 are more comparable with those in NCEP/NCAR (*Kalnay et al.*, 1996), which is why this dataset is used in Chapter 4.

2.2 Ariane

In order to investigate variability in GS pathways in Chapter 4 and Chapter 5, the particle tracking software Ariane, an offline volume-preserving Lagrangian scheme is used (*Blanke and Raynaud*, 1997). This package is available online at http://stockage.univ-brest.fr/ grima/Ariane/. The software is used with the 5-day mean velocity fields of ORCA12, using multiple point particles (*Popova et al.*, 2013). The particles are advected in the model velocity field where they characterise and quantify selected features of ocean circulation from a Lagrangian perspective.

The three-dimensional velocity field is interpolated at each time step, which enables the advection of each particle in the direction of the current. This software uses a C-type grid to analyse trajectories from model outputs (*Arakawa*, 1972) and has been found to be fast and accurate at calculating successive streamline segments (*Blanke and Raynaud*, 1997). The algorithm computes three-dimensional streamlines exactly in order to calculate the true trajectory of each particle assuming a stationary velocity field. The three components of velocity, zonal, meridional and vertical, are known for the 6 faces of each grid box and the flow is non-divergent as $\frac{\partial u}{\partial x} + \frac{\partial v}{\partial y} + \frac{\partial w}{\partial z} = 0$. This enables the particle position to be calculated at each grid cell edge. For each direction, the crossing time is independently calculated and the minimum represents the exact crossing time and enables the final position to be calculated. Detailed calculations are given by *Blanke and Raynaud* (1997). Additionally, the temperature, salinity and density are recorded as the particles travel in the velocity field according to the Eulerian evolution of the model output.

2.3 Path and transport variability of the Gulf Stream: methodology

A combination of observational products and a high-resolution ocean model hindcast are used to explore the latitudinal path shift and transport variability of the GS over the last few decades. The following sections provide details on how each dataset is used to either define the GS path (section 2.3.1) or calculate the GS transport (Chapter 2.3.2).

2.3.1 GS path definitions

In order to define the GS path, two methods are employed; the location of the maximum SST gradient and the 21^oC isotherm at the surface. Of the many definitions used to define the GS path in the literature (Chapter 1), these definitions are being utilised as the SST field can be obtained accurately since the beginning of the satellite record. The optimally interpolated monthly SST from AVHRR (*Reynolds et al.*, 2007) is used alongside the monthly SST from ORCA12 with a description of each given in Table 2.1.

Table 2.1: Description of SST datasets utilised in this chapter in order to assess the latitudinal variability of the GS. Type refers to either observational (O) or model hindcast (M), note that the SST is the top layer temperature in the model.

Datset	Type	Period	Resolution	Citation	Section
AVHRR	O	1982-2014	0.25^o	(*Reynolds et al.*, 2007)	3.2.1, 3.4.3
ORCA12	M	1978-2010	0.083^o	(*Madec et al.*, 2015)	3.2.2, 3.3.3

The fine horizontal resolution ($1/4^o$) of the AVHRR dataset (Table 2.1) enables an accurate estimate of the location of the GS north wall, which is characterised by sharp temperature gradients. Here, the SST gradients are calculated in the North Atlantic, from $25 - 50^oN$, $80 - 50^oW$, for each month from 1982-2014 using:

$$SSTgradient = \sqrt{(\frac{dT}{dx})^2 + (\frac{dT}{dy})^2} \tag{2.1}$$

where T is the SST and x and y are the distance (m) in the longitudinal and

latitudinal dimensions respectively. The maximum SST gradient at each longitude is then taken as the location of the GS path (*Krauss et al.*, 1990; *Drinkwater et al.*, 1994; *Kwon and Joyce*, 2013) and is analysed in Chapter 3.2.1. Additionally, the location of the 21^oC isotherm at each longitude is used to define the GS path. The 15^oC isotherm is commonly used at the subsurface ($200m$) to define the GS path (*Joyce et al.*, 2000; *Frankignoul et al.*, 2001; *Joyce and Zhang*, 2010; *Chaudhuri et al.*, 2011; *Davis et al.*, 2013; *Kwon and Joyce*, 2013; *Pérez-Hernández and Joyce*, 2014). As the surface temperature gradients are correlated with those at $200m$ (*Krauss et al.*, 1990), a surface isotherm can also be used to define the GS path. 21^oC is selected as it captures the GS effectively and was found to represent the SST of the GS (*Rasmussen et al.*, 2005; *Gawarkiewicz et al.*, 2012).

As well as comparing the two methods used to define the GS path, these methods are also applied to the high-resolution, ocean model hindcast ORCA12 (Table 2.1) in order to provide an indication of the extent that the model captures recent GS path variability (Chapter 3.2.2).

2.3.2 GS transport

GS transport is calculated at 70^oW using an observational product, GODAS, and a model hindcast, ORCA12, which are described in Table 2.2. This longitude was selected due to the current having a narrow core at this location compared to further downstream (*Krauss et al.*, 1990). GODAS is a model forced by the momentum flux, heat flux and fresh water flux from the NCEP atmospheric Reanalysis 2 that assimilates observational temperature and synthetic salinity profiles every month, with the sea level being assimilated since 2007. The following fields will be examined from GODAS: temperature, salinity and zonal currents.

At 70^oW, there is less interference from mesoscale activity compared to further downstream (*Krauss et al.*, 1990), which makes it an ideal longitude to measure the transport of the main GS core. GODAS is one of few observational products that includes a) the full depth velocity field as well as b) the temperature and salinity fields. The former enables the calculation of the full depth transport, while the latter permits the calculation of the density-derived transport. The difference

between the two equals the barotropic transport, which facilitates the comparison between this and the baroclinic (density-derived) transport. This allows further evaluation of their contributions to seasonal and interannual GS transport variability. This analysis is repeated using the ORCA12 hindcast and is validated using the results from GODAS.

Table 2.2: Description of datasets utilised in this chapter in order to assess the transport variability of the GS. Type refers to either observational (O) or model hindcast (M).

Datset	Type	Period	Resolution	Levels	Citation	Section
GODAS	O	1980-pres	0.33^o	40	(*Behringer and Xue*, 2004)	3.3
EN4	O	1900-pres	1^o	42	(*Good et al.*, 2013)	3.4
ORCA12	M	1978-2010	0.083^o	75	(*Madec et al.*, 2015)	3.5

In addition to this, GS baroclinic transport is calculated in EN4 in order to investigate the potential influences of intense buoyancy fluxes during two severe winters. EN4 is utilised as it includes data of both severe winters, 1976/77 and 2013/14, which is not the case in GODAS or ORCA12 (Table 2.2).

GODAS

The monthly transport of the GS at 70^oW is calculated in GODAS from 1980-2015 using two methods. The first calculates the total depth-integrated transport from $34 - 42^oN$ using the zonal velocity field, u, as follows:

$$U_g = \int_{-H}^{0} \int_{34N}^{42N} u dy dz \tag{2.2}$$

where U_g is the zonal transport, H is the height of the water column and y and z are the meridional and vertical distances (m) respectively. The second method computes the baroclinic component of the geostrophic velocity using the thermal wind equation. The temperature and salinity fields are used to calculate the meridional density gradients, which enables the currents to be obtained using the bottom as the reference depth of no motion. The velocity shear is calculated as follows:

$$\frac{du_g}{dz} = \frac{g}{\rho f}\frac{d\rho}{dy} \tag{2.3}$$

where u_g is the zonal velocity to be calculated, g is the gravitational acceleration (9.81 m s^{-2}), ρ is the density (calculated from temperature and salinity fields using the equation of state), f is the Coriolis parameter and dy and dz are the meridional and vertical grid box dimensions respectively. The velocity shear is then vertically integrated to calculate the baroclinic component of the geostrophic velocity at each level. This is then integrated into the baroclinic transport using equation 2.2. The difference between the full depth transport and the baroclinic transport is assumed to be the barotropic transport. The variability of these components is examined in order to quantify the contributions to the total transport on seasonal and interannual timescales. Due to the fact that baroclinic transport is primarily associated with the density structure and barotropic primarily with the large-scale wind driven circulation, insight will be provided on the importance of buoyancy and momentum fluxes on GS transport variability.

EN4

EN4 is an obervational product that contains global subsurface temperature and salinity profiles, which are quality controlled (*Good et al.*, 2013), see Table 2.2. The baroclinic transport of the GS is calculated from EN4 data to analyse and compare the two severe winters of 1976/77 and 2013/14 as it covers both of these time periods, unlike the other datasets used in this chapter. Results from these two winters are presented as they have both been identified as particularly severe winters (*Worthington*, 1977; *Grist et al.*, 2016). This enables the illustration of the effect of intense air-sea fluxes on the baroclinic transport of the GS.

Using the temperature and salinity fields the transport is calculated using the same method as the previous section (equation 2.3). The total transport cannot be calculated, as this dataset does not contain velocity fields. The transport is calculated in the main GS core at 70^oW (as in GODAS) from 30^oN to the coast and further to the east in the NAC at 30^oW from 30^oN to 54^oN using equation 2.3.

The transport variability at these two longitudes are compared as representative of the regions impacted during the two severe winters in question. Furthermore, the geostrophic transport at 70^oW and 30^oW is also calculated using a reference depth of $1000m$ in order to analyse the changes in the upper transport.

The temperature field from EN4 and the Surface Heat Flux (Qnet) and Sea Level Pressure (SLP) fields from NCEP/NCAR reanalysis (*Kalnay et al.*, 1996) are also employed to investigate the characteristics of the two severe winters.

ORCA12

The main limitation of using observational datasets to calculate the baroclinic component of geostrophic velocity and transport is the need to use a reference level, i.e. a relative depth of no motion. In the GODAS and EN4 calculations, this is taken to be the ocean bottom or 1000m. This method is also used in ORCA12 (using equations 2.2 and 2.3) to replicate the work done using the observational products. However, in ORCA12 it is also possible to remove this limitation by calculating the geostrophic velocity over the entire depth of the ocean using the SSH field as the absolute value of the pressure is known. This enables the calculation of the GV from the surface to the sea floor. The pressure at each level, P, is then calculated using the hydrostatic equation:

$$P = \int_{-z}^{\eta} g \frac{\rho}{\rho_0} dz \tag{2.4}$$

where g is the gravitational acceleration (9.81 m s^{-2}), $\frac{\rho}{\rho_0}$, is the density anomaly referenced to 1035 kg m^{-3}, η is the SSH relative to the surface geoid and z is the height of each grid box. This is then combined with the equation for zonal geostrophic velocity (u_g) in equation 2.5, to produce equation 2.6:

$$u_g = -\frac{1}{f\rho} \frac{\partial P}{\partial y} \tag{2.5}$$

$$u_g = -\frac{1}{f}\frac{\partial}{\partial y}\int_{-P}^{Pref}\frac{\rho}{\rho_0}dP - \frac{g}{f}\frac{\partial \eta}{\partial y} \tag{2.6}$$

where f is the Coriolis parameter, ρ is the density, P is the pressure, y is the meridional dimension of each grid box, g is the gravitational constant and η is the SSH. The first part of the right-hand side of equation 2.6 is the baroclinic component of the geostrophic velocity, which uses the dynamic height method to calculate the slope of a constant geopotential surface relative to a constant pressure. The second part of the right hand side of equation 2.6 is the barotropic component, associated with the sea surface slope. The total current, obtained using the velocities prescribed by the model, is compared to the geostrophic current (i.e. baroclinic and barotropic components) to ensure that the remainder, the ageostrophic current, is small. The ageostrophic component arises from frictional and inertial processes but also due to the direct influence of the wind at the surface, which results in the Ekman transport. However, as it is the zonal current being investigated, the contributions from Ekman transport are assumed to be small. Evidence for this is shown in Figure 3.31 where the ageostrophic component (i.e. Ekman and non-linear terms) accounts for about 10% of the total transport at this longitude.

Having calculated the total geostrophic velocity (u_g), the depth-integrated transport is then calculated employing four different methods, which are described in Table 2.3, using the geostrophic velocity estimated in Equation 2.6. Only the zonal component of the GS is considered, so a reduced flow may reflect the current becoming temporarily more meridional with the passing of a meander. The high resolution of this hindcast enables the frequent occurrence of meanders and eddies and variable positions of the westward recirculations to the north and south of the main GS core. Consequently, the accurate estimation of GS transport is challenging. Here, it is calculated using two sets of latitudinal limits (30^oN-coast and $34 - 38^oN$) and focusing on either all geostrophic velocity or eastward-only geostrophic velocity as follows:

$$U_{g1} = \int_{-H}^{0} \int_{30N}^{c} u_g \Pi dy dz; \tag{2.7}$$

$\Pi = 0$ for $u_g < 0$; $\Pi = 1$ for $u_g > 0$

$$U_{g2} = \int_{-H}^{0} \int_{30N}^{c} u_g dy dz \tag{2.8}$$

$$U_{g3} = \int_{-H}^{0} \int_{34N}^{38N} u_g \Pi dy dz \tag{2.9}$$

$\Pi = 0$ for $u_g < 0$; $\Pi = 1$ for $u_g > 0$

$$U_{g4} = \int_{-H}^{0} \int_{34N}^{38N} u_g dy dz \tag{2.10}$$

where U_g is the zonal transport, H is the height of the water column, u_g is the zonal velocity and y and z are the meridional and vertical dimensions respectively.

Table 2.3: Methods used to calculate the geostrophic transport of the GS in the ORCA12 hindcast.

Method	Lat lims	Velocity component	Equation
1	30^oN-coast	Eastward only	2.7
2	30^oN-coast	Eastward and westward	2.8
3	$34^oN - 38^oN$	Eastward only	2.9
4	$34^oN - 38^oN$	Eastward and westward	2.10

2.4 The role of air-sea heat fluxes in driving interannual variations of Gulf Stream transport: methodology

The high resolution, global, ocean model hindcast ORCA12 (section 2.1) is utilised to explore the extent to which winter surface heat fluxes have led to spring GS intensification over the last few decades. The use of ORCA12 permits a thorough investigation of GS forcing mechanisms, in particular the contributions from the north and from the south of the GS core. The model diagnostic techniques are

outlined in section 2.4.1 and the Lagrangian experimental setup (in Ariane, section 2.2) is described in section 2.4.2.

2.4.1 Diagnostics, datasets and transport calculations

From the ORCA12 hindcast, the following fields are analysed: mean winter (JFM) net surface heat flux (Qnet), which is diagnosed from the model surface fields, winter mean wind stress curl and early spring (April) mixed layer depth (MLD), defined as the depth where the temperature differs by 0.1^oC from the surface (*Silverthorne and Toole*, 2013), over the domain $20-50^oN$, $85-30^oW$ in the North Atlantic. Additional to the model forcing, we analyse the winter mean SLP field, $2m$ air temperature, and $2m$ wind speed from the NCEP/NCAR atmospheric reanalysis (2.5^o x 2.5^o horizontal resolution), all over the same period as the ORCA12 hindcast (1978-2010) (*Kalnay et al.*, 1996).

The temperature and meridional temperature gradient profiles in April are examined along a transect at 70^oW. The GS still has a narrow core at 70^oW, which makes it ideal to measure the geostrophic transport with minimal mesoscale interference, e.g. from meanders or eddies, which are commonplace further east. The transport is also found to be largely geostrophic at this location (Chapter 3.5 and Figure 3.31), so it is certain that the entire transport variability is captured. Additionally, it is close to where *Worthington* (1977) found an intensification of the current after the severe winter of 1976/77. As outlined in section 2.3.2, using the model eliminates the need to employ a reference level for a depth of no motion as the SSH field, and therefore the absolute value of the pressure is known. Equations 2.4-2.6 are used to calculate the geostrophic velocity and Equation 2.7 is used to calculate the total eastward, depth-integrated GS transport from 30^oN to the coast (Table 2.3). This method is used as it is found to capture the entire GS transport variability whilst eliminating westward flows from the southern recirculation and the Slope Water Current. However, the transport may be overestimated with the passing of an eddy as only the eastward flow (and not the return flow) is counted.

As discussed previously, we examine the influence of the winter Qnet on the density fields and baroclinic transport of the GS. Using the thermal wind relation,

we relate horizontal density gradients to the vertical shear of velocity, and anomalies thereof - i.e. a strengthening of the density gradients across the GS leads to an increase in the current shear. Integrating upwards, this translates into an intensification of the baroclinic transport.

In order to separate transport changes that are due to changes in the SSH field (barotropic) and in the density field (baroclinic), the pressure gradient associated with each can be examined. However, some change in the SSH will be related to the expansion/contraction of the water column due to changes in density, i.e. the steric height. If the change in steric height is exactly equal to the SSH then this translates to a transport change that is entirely driven by the density gradient. In general, part of the SSH change will not be explained by the change in steric height, e.g. it could be associated with wind-driven mass convergence. In order to evaluate this, the surface steric height is calculated using 4000 m as a reference depth of no motion, i.e. calculated from the bottom up rather than the top down as in Equation 2.4. $4000m$ is used as it is the deepest depth that remains clear of bottom topography along the section until about 38^oN. This uses the assumption that density changes below this depth create negligible transport changes on the timescales of interest here. Specifically, the variation in the missing transport from $4000m$ is found to be much smaller (about 10%, $+/-5Sv$) than the overall transport changes ($+/-40-60Sv$).

In addition to this, the potential vorticity (PV) in April is calculated along a transect at 54^oW using TEOS-10 software (*McDougall and Barker*, 2011), which utilises the temperature and salinity fields from the ORCA12 hindcast. This is used to quantify stratification changes, via mixed layer deepening, along this longitude.

2.4.2 Lagrangian experimental setup

In order to investigate variability in GS pathways, we use the particle tracking software Ariane (see section 2.2). This is used with the 5-day mean velocity fields of ORCA12, using multiple point particles (*Popova et al.*, 2013). The particles are advected in the model velocity field where they characterise and quantify selected features of the ocean circulation from a Lagrangian perspective.

For each experiment, 400 particles are uniformly distributed within a single $1/12^o$ grid box (i.e. 20x20) at a particular depth and released into the GS upstream of separation from Cape Hatteras. This is close to the maximum number that can be released successfully within a single grid box, which ensures all particles are immediately entrained into the GS. The specific release point is at 26^oN, 80^oW (Figure 4.1), at depths of 1m, 10m, 50m, 100m, 200m and 300m, a total of 2400 particles. Particles are released at the beginning of April and are tracked forward in time for 3 months. This provides enough time for the particles to reach the bifurcation point of the GS, where they may recirculate to the south or continue north as the NAC, with possible flows entering the AC or the NR (*Schmitz Jr*, 1996). A total of 30 experiments are conducted, one for each year from 1980-2010 (starting from 1980 to avoid spurious results related to model spin-up).

2.5 The importance of air-sea fluxes on the variability of GS pathways from a Lagrangian perspective: methodology

This chapter utilises the eddy-resolving ORCA12 configuration of the global, ocean circulation model NEMO, which is used in conjunction with the particle-tracking software Ariane. Both the model and the software are described in detail in sections 2.1 and 2.2 respectively. They are employed to explore and quantify the variability of GS pathways with depth and on a range of timescales from seasonal to decadal. These pathways are also examined in relation to both localised and more widespread air-sea fluxes. The experimental setup is described in section 2.5.1 with the definition and diagnostic of GS pathways outlined in section 2.5.2.

2.5.1 Experimental setup

A total of 30 experiments are performed, one for each year from 1980-2009 (starting from 1980 to avoid spurious results related to model spin-up). For each experiment, particles are released at the beginning of each month (12 releases) and at 6 different depths throughout the water column; $1m$, $10m$, $50m$, $100m$, $200m$ and $300m$ (6

releases) resulting in a total of 72 releases per experiment. The releases at $1m$ will not be used in this study due to issues experienced at the surface, i.e. particles are killed when reaching the non-linear free surface. The location of each release depth is shown in Figure 2.2. Each experiment is run for a total of 2 years to ensure that every monthly release has a minimum run time of 1 year, i.e. January releases run for 2 years while December releases run for 13 months. 400 particles are initiated in a single grid box (where they are uniformly distributed, i.e. 20x20) at 26^oN, 79.6^oW (Figure 2.3) for each individual release (i.e. per month and per release depth, which results in $400 * 12 * 6$ particles for each experiment). The experiment design is distinct from other studies (*Burkholder and Lozier*, 2011; *Foukal and Lozier*, 2016) in that all particles directly enter the GS before separation from the coast at Cape Hatteras. This ensures that the experiment captures variability of the GS rather than other currents.

2.5.2 Downstream destination of Gulf Stream water

In order to quantify the variability in the downstream destination of GS water, certain regions are defined where GS water has entered via one of the main pathways after bifurcation. For example, it can continue northeast as the NAC into the SPG, east as the AC or recirculate to the south or to the north (*Schmitz Jr*, 1996). In order to quantify this, certain regions are defined that particles reside in after travelling in one of these pathways after a given time period (Figure 2.3). Particles entering the SPG via the NAC are defined as crossing 50^oN, those residing in the SR are defined as being south of 40^oN and west of 35^oW, particles that have recirculated to the north are found north of 40^oN and west of 55^oW while those that have continued east in the AC are found south of 50^oN and east of 35^oW. It is worth noting here that this region covers an area much greater than the AC and is indicative of the wider STG recirculation, in addition to particles travelling in the AC. Finally, if particles are found in the region from $40 - 50^oN$, $55 - 35^oW$ they are defined as still being in the main current (Cur) i.e. they are yet to bifurcate. The defined regions are also summarized in Table 2.4.

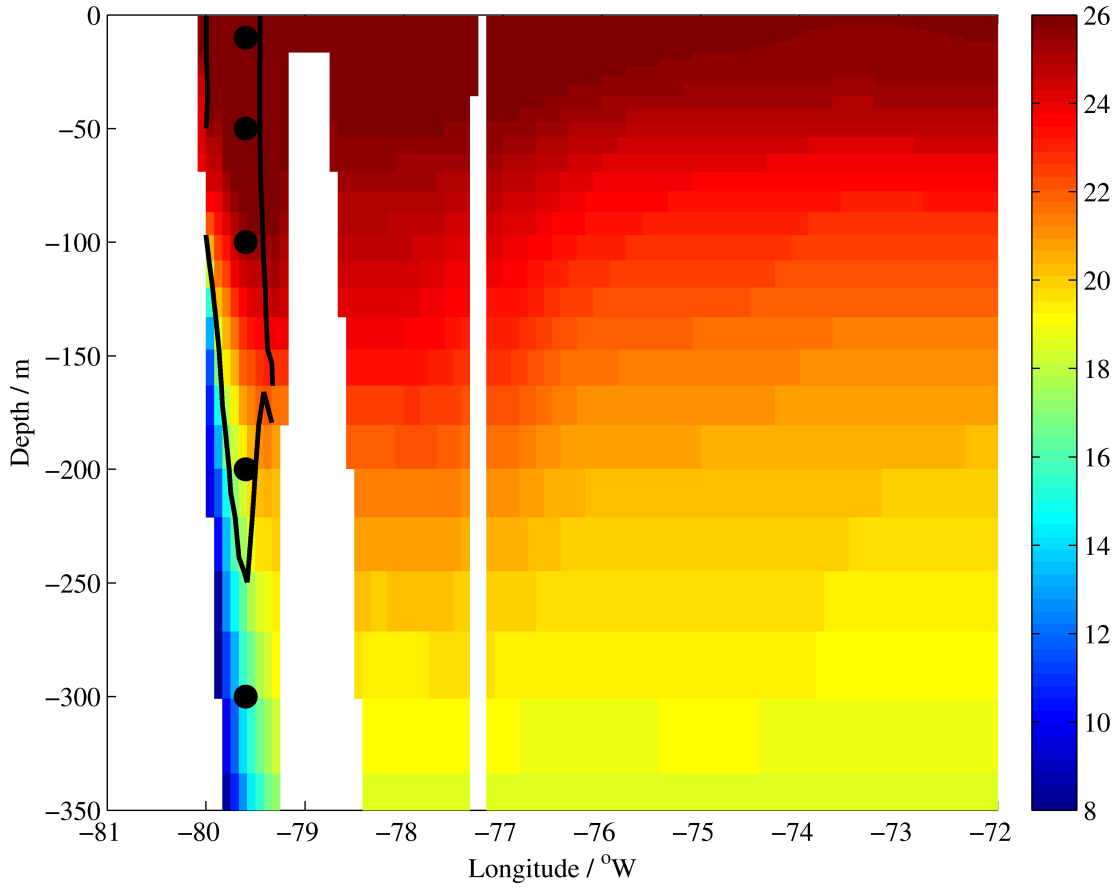

Figure 2.2: Mean temperature (^oC) in the Florida Straits across 26^oN in the ORCA12 hindcast from 1978-2010, with the mean 1m s^{-1} meridional velocity contour overlaid. The markers represent the release depth locations at $10m$, $50m$, $100m$, $200m$ and $300m$.

Table 2.4: Latitudinal and longitudinal limits for the following regions; the Subpolar Gyre (SPG), the Southern Recirculation (SR), the Northern Recirculation (NR), the Azores Current (AC) and the main current (Cur).

Region	Latitude	Longitude
SPG	$> 50^oN$	All
SR	$< 40^oN$	Coast to 35^oW
NR	$> 40^oN$	Coast to 55^oW
AC	$< 50^oN$	35^oW to coast
Cur	$40 - 50^oN$	55 to 35^oW

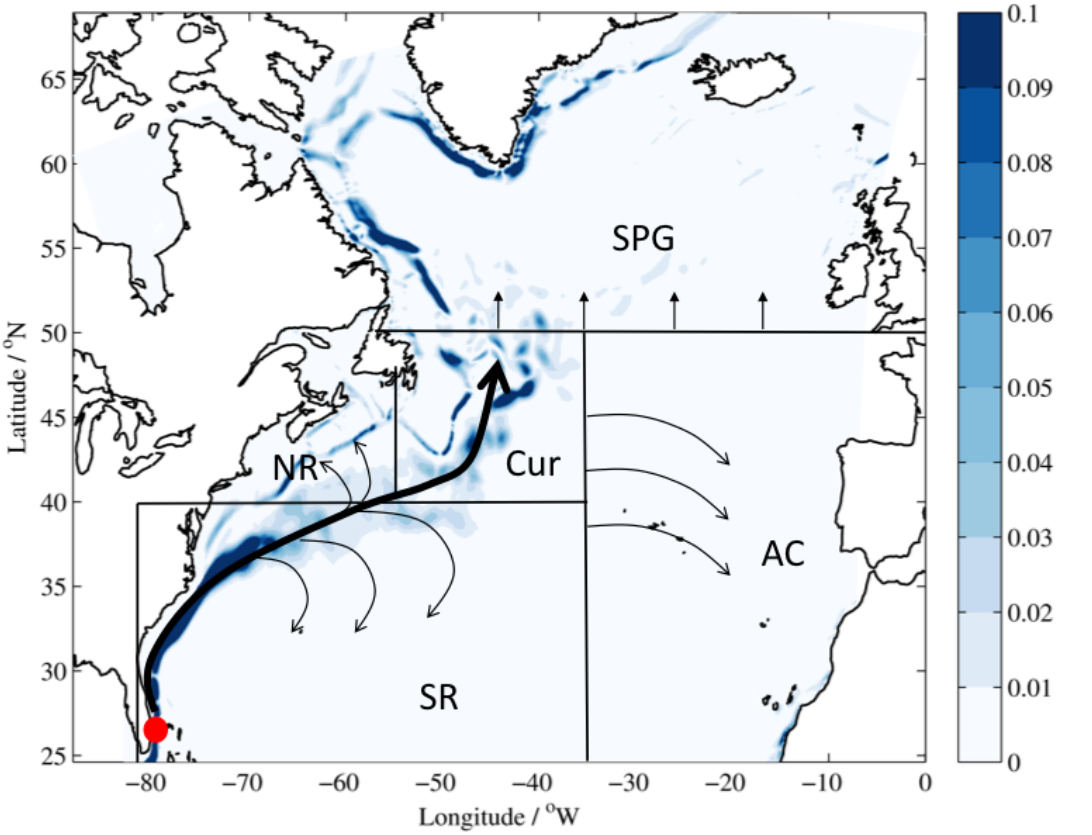

Figure 2.3: Mean surface velocities (m s^{-1}) in the North Atlantic from 1980-2010 in the ORCA12 hindcast. The red marker represents the release location for trajectories in the Florida Straits with the following regions defined; the Subpolar Gyre (SPG), the Southern Recirculation (SR), the Northern Recirculation (NR), the Azores Current (AC) and the main current (Cur).

Chapter 3

Path and transport variability of the Gulf Stream

3.1 Introduction

Close to separation from the coast at Cape Hatteras, the GS path has been found to shift by up to 1^o on interannual timescales (*Lillibridge and Mariano*, 2012). The transport of the GS is also known to vary by more than 10% interannually (*Rossby et al.*, 2010) and as much as 25% over a 25-year period (*Curry and McCartney*, 2001). Disagreements in the variability of both the path and transport arise from differences with distance from the coast at which observations were taken and also with the method used to measure the GS front (Chapter 1.3). In order to investigate this, two methods are used to define the GS front using the same high-resolution dataset, AVHRR, the maximum SST gradient and the 21^oC isotherm at the surface. This enables the comparison of how the GS shifts latitudinally at different locations along its path using two methods within the same dataset. These methods are also utilised in the eddy-resolving ocean model hindcast ORCA12 in order to quantify GS path shift variability over the last few decades, which is also compared with the observations.

The transport variability of the GS on interannual timescales is also investigated at 70^oW using the observational dataset, GODAS, and also in ORCA12. At this location, the GS is more of a distinct jet compared to further east where mesoscale variability dominates (*Krauss et al.*, 1990). This enables a more accurate analysis of GS transport variability. The full-depth velocity field in GODAS enables the

separation of the barotropic and baroclinic transport components with the latter calculated using the density field. This will provide further understanding into the mechanisms influencing the GS transport on seasonal and interannual timescales and inform our analysis of GS transport variability in Chapter 4.

Many mechanisms have been found to influence the transport variability of the GS and are discussed in detail in Chapter 1.3. The variability of the baroclinic component is found to be important when examining the interannual variability of GS transport. This suggests that surface buoyancy fluxes are a crucial factor in inducing transport changes of the GS, which has been found in prior studies (*Worthington*, 1977; *Kelly et al.*, 1996). In particular, severe winters in North America have been found to cause an intensification of the GS (*Worthington*, 1977). A stronger anti-cyclonic circulation was induced by a higher pressure centre in the western STG (*Worthington*, 1976). Worthington's anti-cyclogenesis mechanism was found to be operating during the winter of 1976/77 whereby a series of Cold Air Outbreaks (CAOs) led to deeper mixed layers south of the GS and a strengthening of the transport near 72^oW (*Worthington*, 1977). Here, changes of the GS path and baroclinic transport during two severe winters in North America, 1976/77 and 2013/14, will be quantified in EN4. This will then be related to the density structure and the net air-sea heat flux (Qnet) over the North Atlantic. These winters are selected as they are known to have been particularly severe (*Worthington*, 1977; *Grist et al.*, 2016) and therefore have the most potential to influence the baroclinic transport.

The datasets and methods used have been described in Chapter 2.3, with the results presented here as follows; Chapter 3.2 quantifies the latitudinal variability of the GS path at different longitudes using two GS definitions in AVHRR and ORCA12, GODAS transport variability (total and baroclonic) is then analysed in Chapter 3.3, Chapter 3.4 investigates the impact of two severe winters on the baroclinic transport and path of the GS in EN4 and, finally, the GS transport variability (total and baroclonic) in ORCA12 is presented in Chapter 3.5.

3.2 Latitudinal variability of the Gulf Stream

This section quantifies the latitudinal variability of the GS on interannual timescales, both as an annual average and for individual months. Utilising the SST field, two definitions of the GS are used. Comparisons are drawn between these two methods and between different datasets, which consists of one observational dataset (AVHRR) and one model hindcast (ORCA12) that have different horizontal resolution (Table 2.1). The interannual variability of GS path shift is also analysed at different locations along the separated current, i.e. from $75 - 50^oW$.

3.2.1 Observations

Here, the interannual variability of the latitude of the GS is calculated from the AVHRR SST dataset. Two methods are utilised in order to quantify their effectiveness of capturing the latitudinal variability of the GS at different longitudes along the GS path.

The two methods employed to define the GS path are the maximum SST gradient and the surface 21^oC isotherm and are used to analyse the latitudinal variability along the GS path from $75 - 50^oW$. These were selected as the SST field can be obtained accurately since the beginning of the satellite record. The maximum SST gradient has proven to be an effective indicator of the GS path (*Drinkwater et al.*, 1994) as have subsurface isotherms (*Tracey and Watts*, 1986; *Joyce and Zhang*, 2010; *Chaudhuri et al.*, 2011; *Davis et al.*, 2013). Thereby, we can assume that a surface isotherm is also an appropriate GS path definition. The annual SST field in AVHRR is used to investigate the year-to-year variation of the GS position from 1982-2013 and is shown in Figure 3.1. Using both methods, the mean latitude of the GS is found increasingly further to the north with decreasing longitude, i.e. from 75^oW to 60^oW. However, further to the east at 50^oW, the mean latitude is only further to the north when using the maximum SST gradient.

Just after separation from the coast at 75^oW, the GS path has a small latitudinal range of approximately 1^o when using the maximum SST gradient and just 0.5^o when using the 21^oC isotherm (Figure 3.1a). This is close to where *Tracey and*

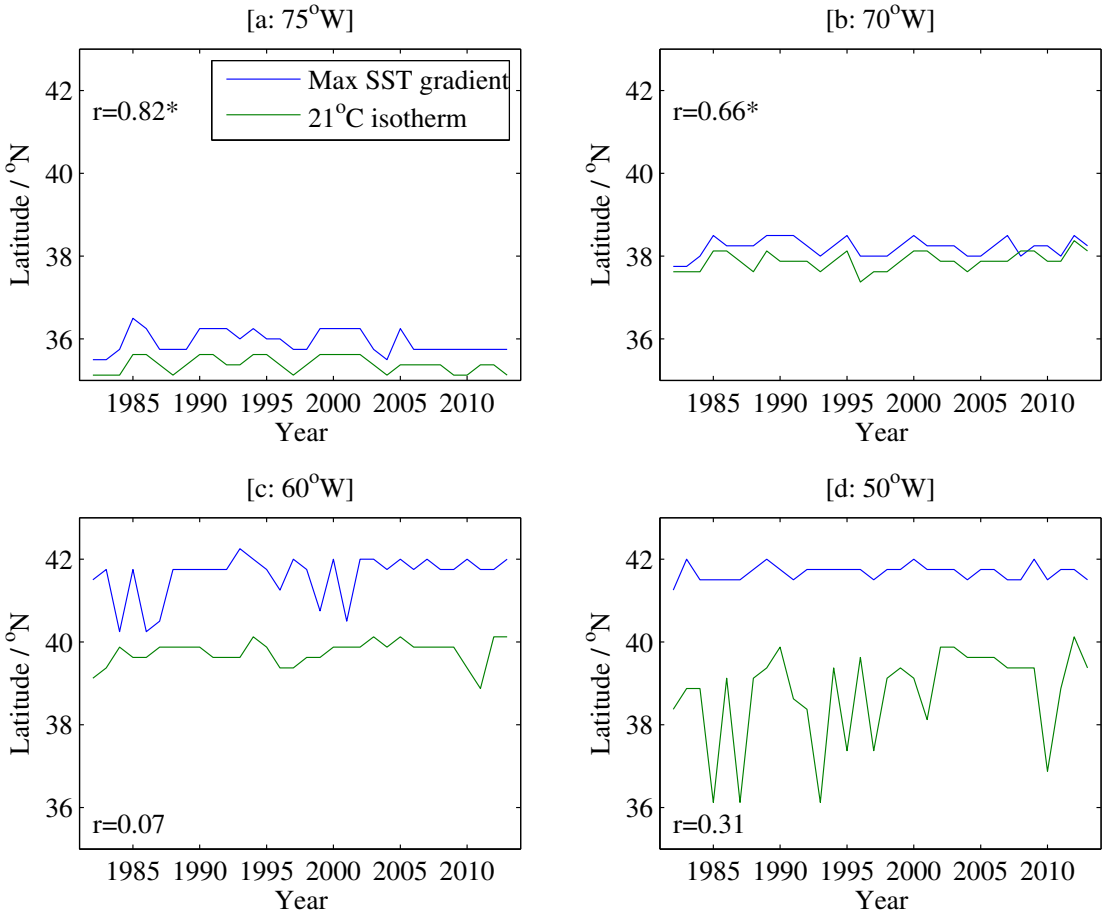

Figure 3.1: Latitude (^oN) of the GS using the maximum SST gradient and 21^oC isotherm to define the GS path at 75^oW [a], 70^oW [b], 60^oW [c] and 50^oW [d] using the annual SST field in AVHRR from 1982-2013. The r value on each panel is the correlation coefficient between the two methods at each longitude with an asterisk denoting statistical significance at the 99% confidence interval.

Watts (1986) found a relatively small variation, $20km$, in GS path shift compared to that seen further east, $145km$ by 72^oW. They used inverted echo sounders to locate the thermocline of the GS and, therefore, the 15^oC isotherm at $200m$, outlined by *Watts and Johns* (1982). This also concurs with a maximum shift of 0.5^o found by *Drinkwater et al.* (1994), who also employed the maximum SST gradient GS definition in AVHRR. Additionally, at this longitude, the GS is found to have a more northward position when using the maximum SST gradient to define its path with a range of $35.5-36.5^oN$ compared to $35.13-35.63^oN$ when using the 21^oC isotherm. Although some differences exist between the two methods, a high positive correlation (r=0.82) exists between them. This suggests that, at 75^oW, the latitudinal variability of the GS is captured well by both methods on interannual

timescales. In order to calculate the statistical significance of this correlation the degrees of freedom (dof) are determined using the following equation by *Bretherton et al.* (1999):

$$dof = T\frac{1 - r_1 r_2}{1 + r_1 r_2} \tag{3.1}$$

where T is the length of each timeseries, r_1 and r_2 are the correlation coefficients of each timeseries when correlated with themselves when lag=1, thereby accounting for autocorrelation. The significance level is then determined by referring to a dof table. Using this method, the positive correlation (r=0.82) identified between the two methods at 75^{o}W is deemed to be significant to the 99.9% confidence interval.

At 70^oW, the average latitudinal position is now at 37.9^oN when using the 21^oC isotherm and slightly further north at 38.2^oN when using the maximum SST gradient (Figure 3.1b). The correlation coefficient between the two methods is slightly lower (r=0.66) than that seen at 75^oW but the difference between the two is smaller, notably since about 2000. The northward migration of the 21^oC isotherm is consistent with the observed warming in the North Atlantic (*Straneo and Heimbach*, 2013) since about 1995. Nevertheless, the correlation is also significant at the 99.9% level. The interannual variation over the 32-year period is similar to that observed at 75^oW, which again, agrees with *Tracey and Watts* (1986) that GS shift is coherent across a range of longitudes further to the west.

Further east at 60^oW, a greater discrepancy exists between the two GS path definitions with average latitudes of 41.6^oN and 39.74^oN for the maximum SST gradient and 21^oC isotherm respectively (Figure 3.1c). However, a greater range of interannual variability occurs when using the maximum SST gradient (2^o) compared to the 21^oC isotherm (1.25^o). An insignificant correlation (r=0.07) between the two methods also exists at this longitude. The greater variability and more northward path that exists when using the maximum SST gradient suggests that the variation in slope water temperature is important at this location.

The greatest differences in latitudinal variability between the two methods occurs at 50^oW, which sees a range of $< 1^o$ when using the maximum SST gradient,

compared with 4^o when using the 21^oC isotherm (Figure 3.1d). The mean location of the GS at this longitude is similar to that seen at 60^oW at 41.7^oN. The estimated location of the 21^oC isotherm, and therefore the GS by this definition, can reach as far south as 36^oN, which leads to an insignificant r value at this longitude. This suggests that, at this longitude, the main GS path at the surface is not always as warm as 21^oC with certain years, e.g. 1985, 1987 and 1993, being, potentially, much cooler than this as the latitude of the isotherm is located much further to the south.

The more northerly extent of the GS when using the maximum SST gradient for all longitudes under investigation here implies that the 21^oC isotherm is more closely matched to the GS core with the former more closely representing the GS north wall. An example of the annually averaged SST field with the position of the GS path using both methods is shown in Figure 3.2a. It illustrates the high similarity between the two methods between the coast and about 63^oW with the maximum SST gradient being found further north to the east of this. It should also be noted that in this particular year, 2013, the 21^oC isotherm is found further to the north at 50^oW. This indicates a greater similarity between the two methods compared to other years, which is discussed above.

As an annual average, the interannual variability in the shift of the GS path is fairly limited as this eliminates much of the mesoscale variability seen in this region. There is evidence that there is greater variability on interannual timescales when using the mean monthly field rather than the mean annual field. For example, the mean SST during April 2014 is shown in Figure 3.2b, which shows evidence of meanders and eddies along the GS path. It also reveals the estimated location of the GS when using the maximum SST gradient and the 21^oC isotherm methods. Here, they are found to agree west of about $70 - 65^oW$ where they then diverge, which is due to the 21^oC isotherm being found much further south during this time of year. Immediately after separation from the coast at Cape Hatteras there is a large meander, which could suggest that the GS was in a northward position during 2014. The occurrence of large meanders at 68^oW was also recorded during the end of 2011 by *Gawarkiewicz et al.* (2012). They found that an unusual tilt in the

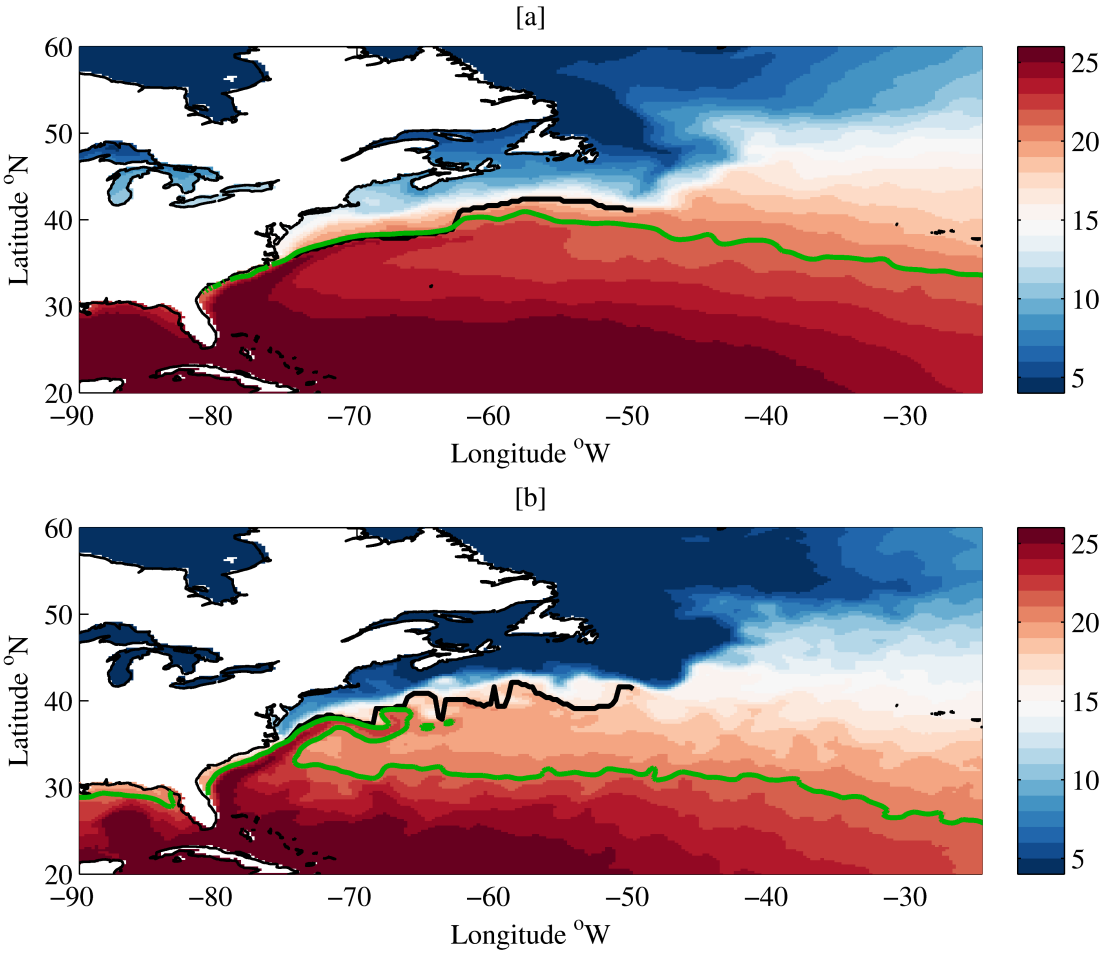

Figure 3.2: Mean SST (^oC) of the North Atlantic in 2013 [a] and April 2014 [b] in AVHRR. The black line is an estimate of the GS path using the maximum SST gradient while the green line represents the GS path using the 21^oC isotherm.

current caused it to come within $12km$ of the Mid-Atlantic Bight shelf break, i.e. $200km$ further north of its mean position at this location. This led to an increase in deep ocean temperatures of $> 6^oC$ (recorded by lobster traps), which could have profound impacts on the ecosystem (*Gawarkiewicz et al.*, 2012).

On the crest of the meander in April 2014, at 73^oW, there is a good agreement between the two methods used to define the GS when investigating the interannual variability of its path during the same month (Figure 3.3a). Even though the GS is consistently further north by about 1^o when using the maximum SST gradient, the peaks and troughs, referring to more northward and more southward positions respectively, are significantly correlated (r=0.8) to the 99.9% confidence interval (see equation 3.1). Further evidence for this is seen in Figure 3.3b, which shows

that the magnitude of GS latitude anomalies from year to year is very similar when using both methods. However, the latitudinal difference between the two methods appears to be reducing in recent years, i.e. since 2007, which could indicate a warming of the GS at this location. As suggested previously, there is greater interannual variability seen on monthly timescales, which highlights the considerable mesoscale variability of the GS. The latitudinal range, for both methods, is about 2^o, which is more than double that seen at 75^oW and 70^oW when looking at the annual SST field. There is also some evidence that the GS was undergoing a northward shift since 2011 with its two northernmost locations occurring in April 2012 and 2014. Furthermore, in April 2014 the GS was the furthest north it has been throughout the satellite record when defined by both methods used here. Specifically, it was located at nearly 37.5^oN when using the 21^oC isotherm and 38^oN when using the maximum SST gradient. This corresponds to an anomalously northward GS of about 1^o in both methods (Figure 3.3b), which is statistically significant to the 95% confidence interval.

In summary, two methods have been used to define the GS path from $75-50^oW$ using the AVHRR SST field; the maximum SST gradient and the 21^oC isotherm. When analysing the latitudinal variability of the GS on interannual timescales a greater correlation exists between the two methods further to the west, i.e. at 75^oW and 70^oW, compared with east of 63^oW. Regardless of this, the maximum SST gradient was consistently found to be further northwards of the 21^oC isotherm at all longitudes, as it captures the GS north wall as opposed to the main GS core. Greater variability was observed using the monthly SST field rather than the annual average, which highlights the considerable level of mesoscale activity in the GS. Both methods agree that the GS path has undergone a significant northward shift in recent years with the northernmost position observed in April 2014 ($+1^o$) when using both definitions.

3.2.2 Model

This section investigates the interannual variability of the latitude of the GS using the SST field in the ORCA12 hindcast using the same two methods as the pre-

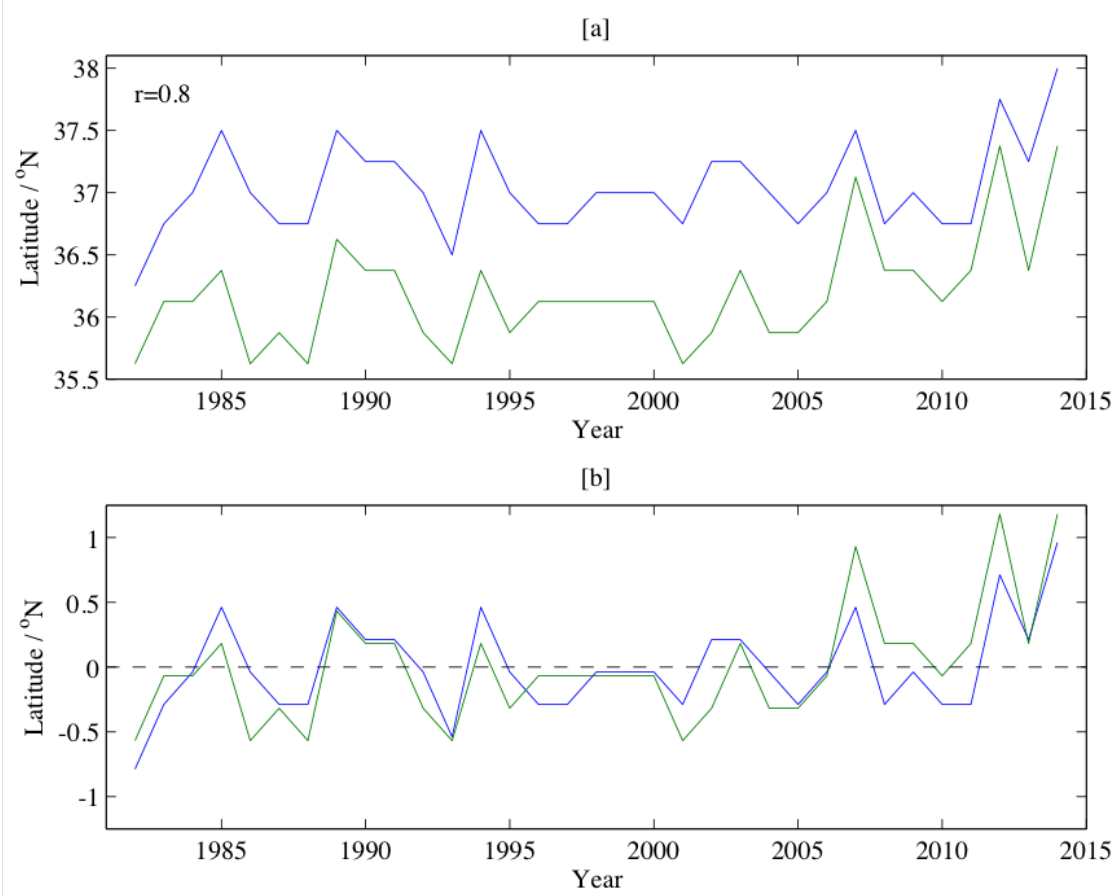

Figure 3.3: Latitude (^oN) [a] and anomalous latitude (^oN) [b] of the estimated path of the GS in April at 73^oW in AVHRR from 1982-2014 using the maximum SST gradient (blue) and the 21^oC isotherm (green). The r value on each panel is the correlation coefficient between the two methods at each longitude and is statistically significant at the 95% confidence interval.

vious section. Comparisons are drawn between the two definitions of the GS and also between the model and the observations to examine the realism of GS path variations in the hindcast.

Using the high resolution, eddy-resolving ORCA12 hindcast, the same GS definitions were applied to the annual SST field from $75 - 50^oW$ (Figure 3.4). A similar pattern is revealed to that seen in the observations (Figure 3.1) with an increasing GS latitude seen from $75 - 60^oW$ and large differences between the methods at 50^oW.

Figure 3.4a shows that the mean latitude of the GS after separation at 75^oW is just north of 35^oN, when using both methods, which is slightly further south than that seen in the observations (Figure 3.1). The latitudinal variability on

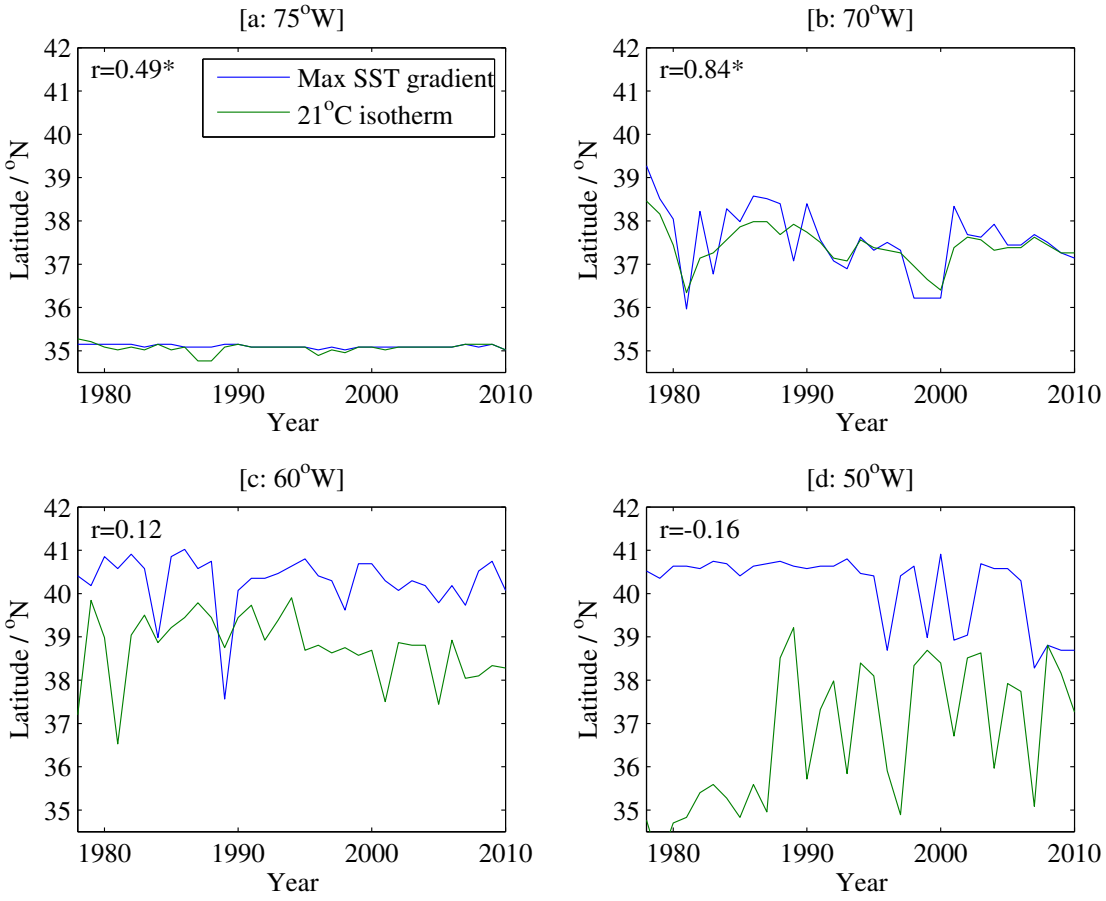

Figure 3.4: Latitude (^oN) of the GS using the maximum SST gradient and 21^oC isotherm to define the Gulf Stream path at 75^oW [a], 70^oW [b], 60^oW [c] and 50^oW [d] using the annual SST field in ORCA12 from 1978-2010. The r value is the correlation coefficient between the two methods at each longitude with an asterisk denoting statistical significance at the 99% confidence interval.

interannual timescales is also less than 0.2^o, which provides evidence for a constant GS separation throughout the hindcast. r=0.49 at this longitude, and is significant to the 99% level, but the variability is mostly occurring with the 21^oC isotherm rather than the fairly constant maximum SST gradient.

The variability is much greater at 70^oW with a 3.3^o range seen for the maximum SST gradient and a 2.1^o range for the 21^oC isotherm (Figure 3.4b). This is greater than that seen in observations ($< 1^o$), which could reflect the finer resolution in the model ($1/12^o$ compared with $1/4^o$). Latitudinal shifts are visible for both methods at this longitude with evidence that the GS was further north during the late 1980s and early 1990s before shifting to the south in the late 1990s. Even though the agreement between the methods is greatest at this longitude with a significant

correlation coefficient of 0.84 at the 99.9% level, the maximum SST gradient still exhibits greater year-to-year variability.

A similar trend is also revealed at 60^oW when using the 21^oC isotherm but this is not as prominent when using the maximum SST gradient definition (Figure 3.4c). This GS path shift is in agreement with prior findings, i.e. more northward path during the 1980s and 1990s (*Taylor and Gangopadhyay*, 2001) and could be related to any of the mechanisms described in Chapter 1.3. However, there is evidence that the path shift in this hindcast could be related to the NAO, which was positive in the late-1980s to the early-1990s and coincides with the period of a more northward GS path seen in Figure 3.4b and 3.4c. During the positive phase of the NAO, strengthened Westerlies over midlatitudes lead to an enhanced southward Ekman transport south of 40^oN (*Visbeck et al.*, 2003) and a northward shift in the latitude of zero wind stress curl (*Sasaki and Schneider*, 2011). These combined effects induce a northward shift in the GS (*Taylor and Stephens*, 1998; *Joyce et al.*, 2000; *Kwon et al.*, 2010; *Rossby et al.*, 2010). This will be discussed further in Chapter 5. The agreement between the two GS definitions is insignificant at this longitude, r=0.12, which is also in accordance with that seen in the observations (Figure 3.1c).

At 50^oW (Fig. 3.4d), this variability is no longer visible with little agreement between the two methods, i.e. r=0.16. However, greater year-to-year variability exists in later years, i.e. after 1987 when using the 21^oC isotherm and after 1995 when using the maximum SST gradient. The greater agreement between the two methods west of about 68^oW when using the annual SST field can be seen in Figure 3.5a, which uses 2010 as an example. A breakdown in the correspondence between the two methods is also evident to the east of this with the maximum SST gradient generally found to the north of the 21^oC isotherm.

A direct comparison between the model and observations using both methods from $75 - 50^oW$ is shown in Figure 3.6. Overall, there is poor correspondence between observed and modelled interannual changes in the GS path. This could be due to a combination of factors including differences in resolution or the difficulties associated with modelling the GS (Chapter 1.5) e.g. accurate separation

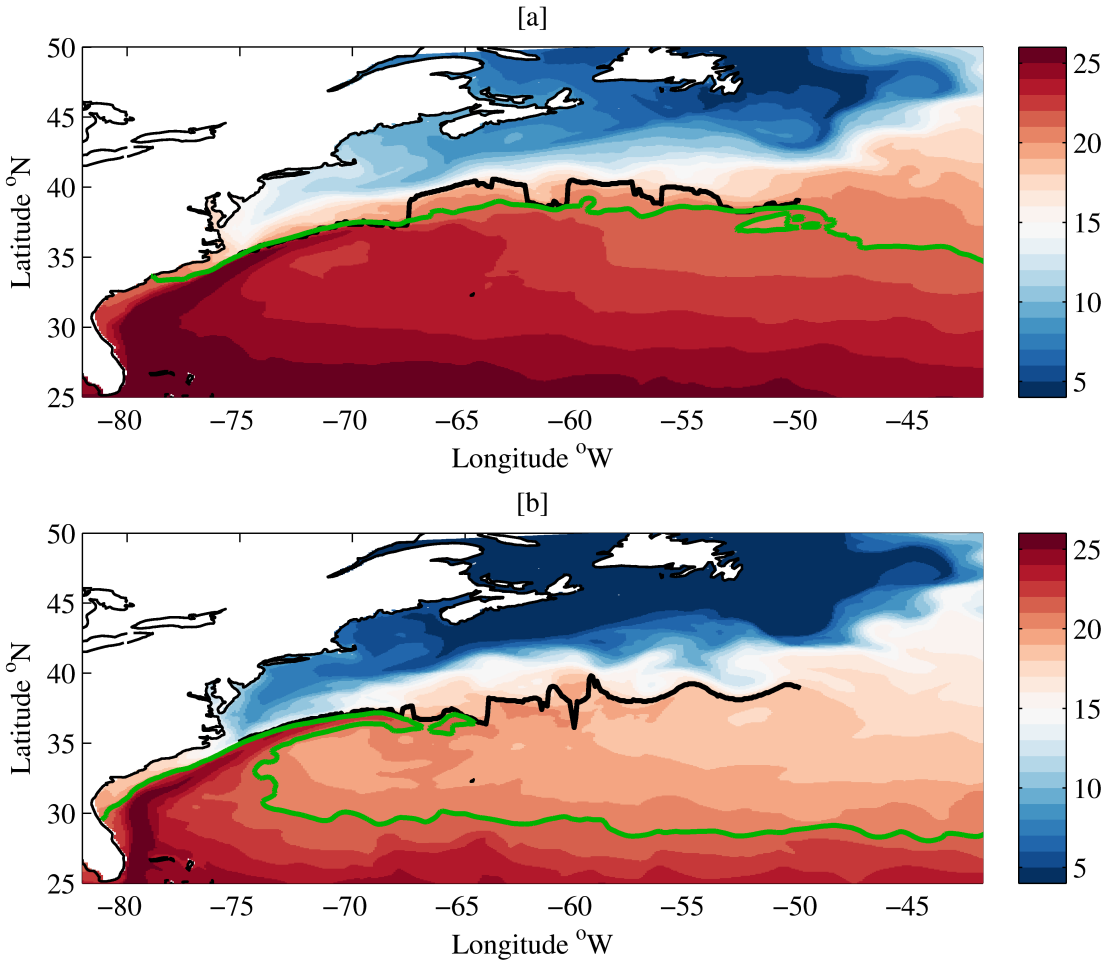

Figure 3.5: Mean SST (^oC) of the North Atlantic in 2010 [a] and April 2014 [b] in ORCA12. The black line is an estimate of the GS path using the maximum SST gradient while the green line represents the GS path using the 21^oC isotherm.

and mesoscale activity. At 75^oW, near separation from the coast at Cape Hatteras, the agreement between AVHRR and ORCA12 is greater when using the 21^oC isotherm (Figure 3.6b) as opposed to the maximum SST gradient (Figure 3.6a). The GS is also consistently further north in the observations at this longitude using both definitions, which is accentuated when using the maximum SST gradient. This could suggest that, in reality, there is a greater GS path shift near separation, which has been found to be fairly constant in ORCA12. This could be due to a stronger Slope Water current, which is known to induce a southward shift in the GS path (*Peña-Molino and Joyce*, 2008), and could be a model limitation as this is not present in the observations. For example, in this particular hindcast, pulses of water from the Labrador Sea have been found to travel in the Slope Water current,

which forces the GS into a more southward separation from the surface to about $500m$ in comm. with *New* (2017).

At 70^oW (Figures 3.6c and 3.6d), 60^oW (Figures 3.6e and 3.6f) and 50^oW (Figures 3.6g and 3.6h), the agreement between AVHRR and ORCA12 is consistently greater when using the 21^oC isotherm with the best agreement, and only significant correlation (at the 99% level), found at 50^oW, r=0.45. Using the maximum SST gradient, the GS is generally found further south in the model, which could also be related to the strong Slope Water current found in ORCA12. Differences in both methods could also be related to the finer resolution of ORCA12, which enables greater variability in the mesoscale eddy field. However, this should be much reduced using the annual average SST field.

Due to the high level of mesoscale variability in the GS region in ORCA12, it is too difficult to measure the monthly variability of the path accurately using the temperature field. This is mostly due to the occurrence of warm and cold rings along the entire length of the separated GS. In order to eliminate some of this variability, the SST field has been averaged over March, April and May, which is still able to capture the greater variability experienced on monthly timescales. To ensure consistency with AVHRR, the interannual variability of the GS latitude using both methods at 73^oW is revealed in Figure 3.7a using this 3-monthly averaged SST field. A very high , and significant, correlation exists between the two methods (r=0.92) at the 99.9% level with the maximum SST gradient only slightly further north than the 21^oC isotherm. The similarity between the two methods at this longitude is further highlighted in Figure 3.5b, which reveals that the 21^oC isotherm follows the maximum SST gradient until about 65^oW during this particular spring. This pattern matches that seen in AVHRR in Figure 3.2b. A greater range is also revealed (2^o), compared with that seen at 75^oW (0.2^o), when using the 3-monthly average rather than the annual SST field, which resembles that seen in AVHRR (Figure 3.3), although this could also be related to 73^oW being further east than 75^oW as a greater latitudinal range was discovered at 70^oW. The increased latitude towards the end of the hindcast, i.e. since about 2000, is also consistent with the more northward GS observed in AVHRR on monthly timescales. Specifically, the

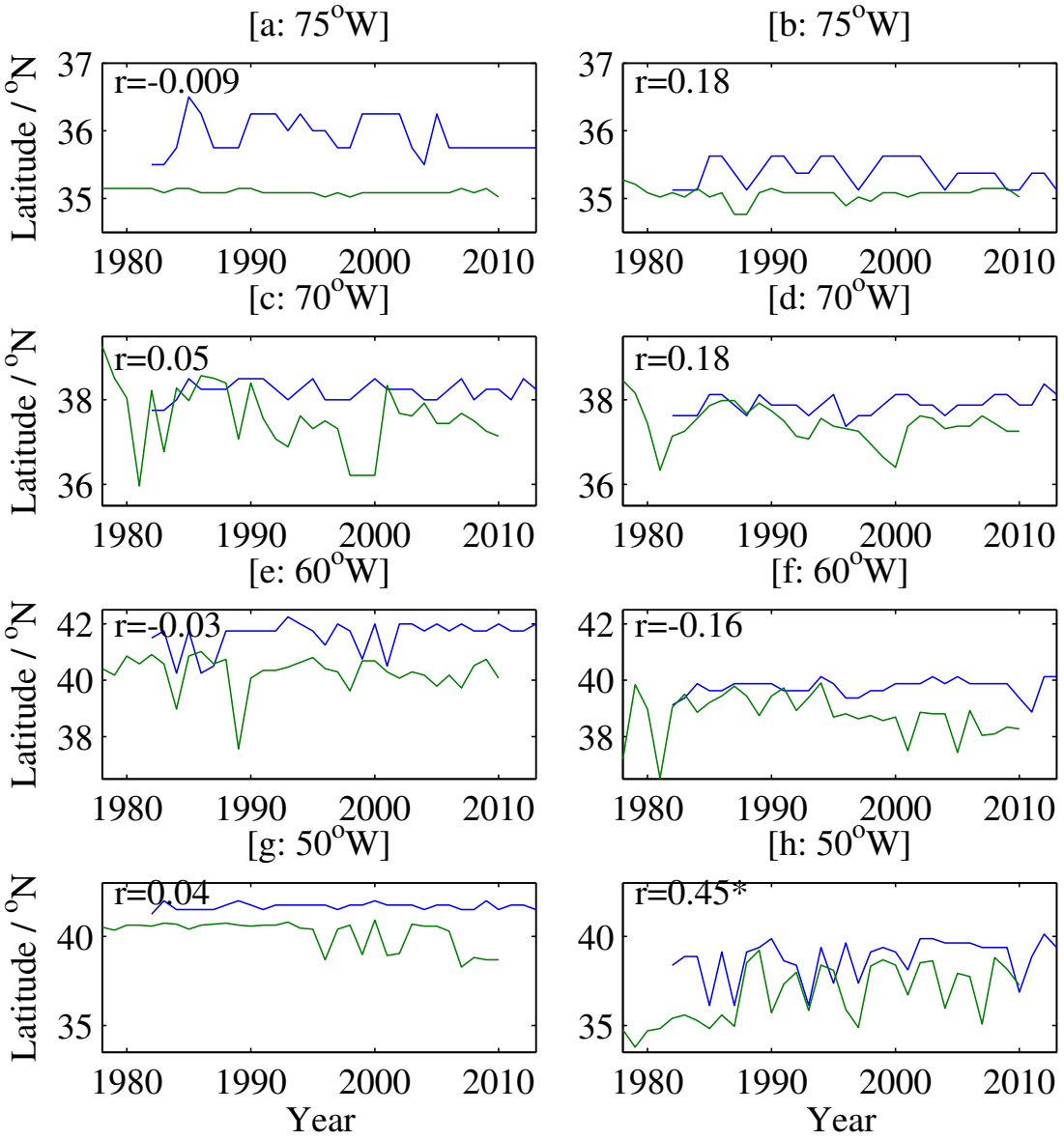

Figure 3.6: Latitude (^oN) of the GS using the maximum SST gradient in the left column [a, c, e and g] and the surface 21^oC isotherm in the right column [b, d, f, h] using AVHRR (blue) and ORCA12 (green) at 75^oW [a, b], 70^oW [c, d], 60^oW [e, f] and 50^oW [g, h] using the annual SST field in AVHRR from 1982-2013 and ORCA12 from 1978-2010. The r value on each panel is the correlation coefficient between the two methods at each longitude with an asterisk denoting statistical significance at the 99% confidence interval.

GS is found up to 2^o further north between the late-1990s and late-2000s (Figure 3.7b).

This section has used the maximum SST gradient and the 21^oC isotherm at the surface to define the separated GS path from $75 - 50^oW$ using the ORCA12

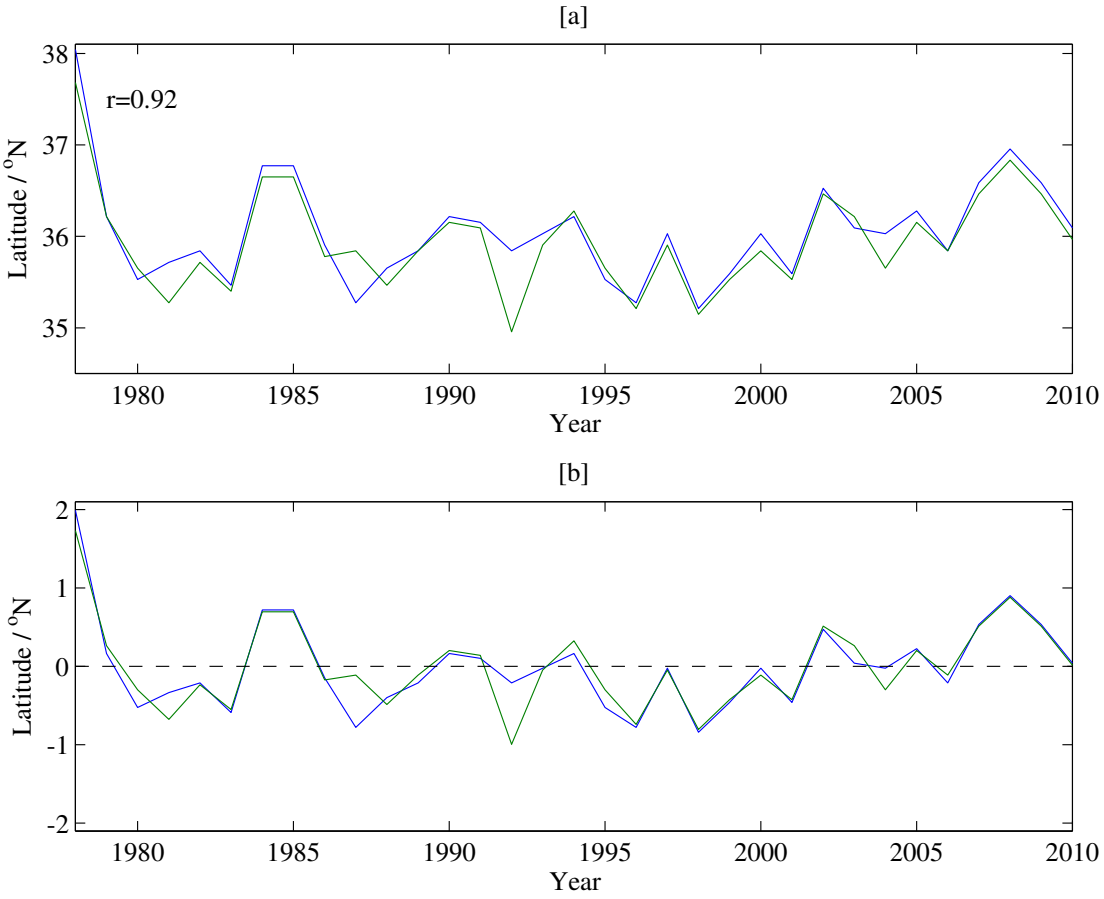

Figure 3.7: Latitude (^oN) [a] and anomalous latitude (^oN) [b] of the estimated path of the GS at 73^oW in ORCA12 from 1982-2014 when averaged from March-May using the maximum SST gradient (blue) and the 21^oC isotherm (green). The r value is the correlation coefficient between the two methods at each longitude, which is statistically significant at the 99.9% confidence interval.

hindcast. Like that observed in AVHRR, more significant correlations exist between the methods further to the west, in this case at 70^oW (r=0.84). A more northward GS path is also revealed, at this longitude and at 60^oW, during the late-1980s and early-1990s, which agrees with prior findings (*Taylor and Gangopadhyay*, 2001). As found in AVHRR, the maximum SST gradient is generally found further north of the 21^oC isotherm, which is more obvious further to the east, i.e. from $60 - 50^oW$. When directly comparing the observations with the model, the GS was consistently found further south in the model across all longitudes. This may be due to a stronger Slope Water current modelled in the ORCA12 hindcast, which is known to push the GS into a more southward position (*Peña-Molino and Joyce*, 2008). For example, the mean upper (0-250 m) westward transport of the Slope Water

current at 70^oW from 1992-2004 is $-5Sv$ (not shown). This is greater than the $-3.5Sv$ observed by *Rossby et al.* (2005). However, it could also be due to pulses of water from the Labrador Sea travelling around the Grand Banks and acting to push the GS into a more southward separation in comm. with *New* (2017).

At all longitudes there is greater agreement between the model and observations when using the 21^oC isotherm, which could indicate that this is the best method to define the GS when using the annual SST field. However, overall there is poor correspondence between the observed and modelled interannual variability of the GS path. This may produce contrasting results when quantifying GS path shift in observations and models. Contrastingly, when using monthly, in AVHRR, or 3-monthly averaged, in ORCA12, SST fields, the 21^oC isotherm is no longer an effective method in capturing the GS path further to the east due to the seasonal cycle of SST. This results in the maximum SST gradient being the most accurate method to measure the GS path east of about 70^oW in both the observations and the model. However, the correlation between the two methods further to the west at 73^oW is high in AVHRR and ORCA12. To summarise, the maximum SST gradient and the 21^oC isotherm can both be used to investigate GS path variability from $75 - 70^oW$ but the 21^oC isotherm is ineffective on monthly timescales to the east of this.

3.3 Transport variability of the Gulf Stream: observations

This section investigates the depth-integrated transport of the GS at 70^oW using the zonal velocity field (total transport) and the density field (baroclinic transport) in GODAS. The residual is also calculated, which is taken as the barotropic component. The variability of these components is examined in order to quantify the contributions to the total transport on seasonal and interannual timescales. This will provide insight into the relative importance of buoyancy and momentum fluxes on GS transport variability. The transport is also analysed in relation to its contribution from the southern and northern components, which are used to examine the path shift of the GS over the last few decades and relate to findings

in Chapter 3.2.

The zonal velocity is vertically integrated across 70^oW from $34-42^oN$, which gives the transport of the GS at this longitude and is shown in Figure 3.8. Figure 3.8a reveals the total transport between these two latitudes (black line) and also separates out a more northern component from $38-42^oN$ (blue line) and a more southern component from $34-38^oN$ (red line). A clear seasonal cycle is evident with peaks in the total transport occurring during the winter. It has previously been stated that this is mostly related to the seasonal cycle of the wind stress (*Hogg and Johns*, 1995). This leads to a seasonal cycle of up to $40Sv$ with a winter peak of $40-70Sv$ and a summer minimum of $30Sv$.

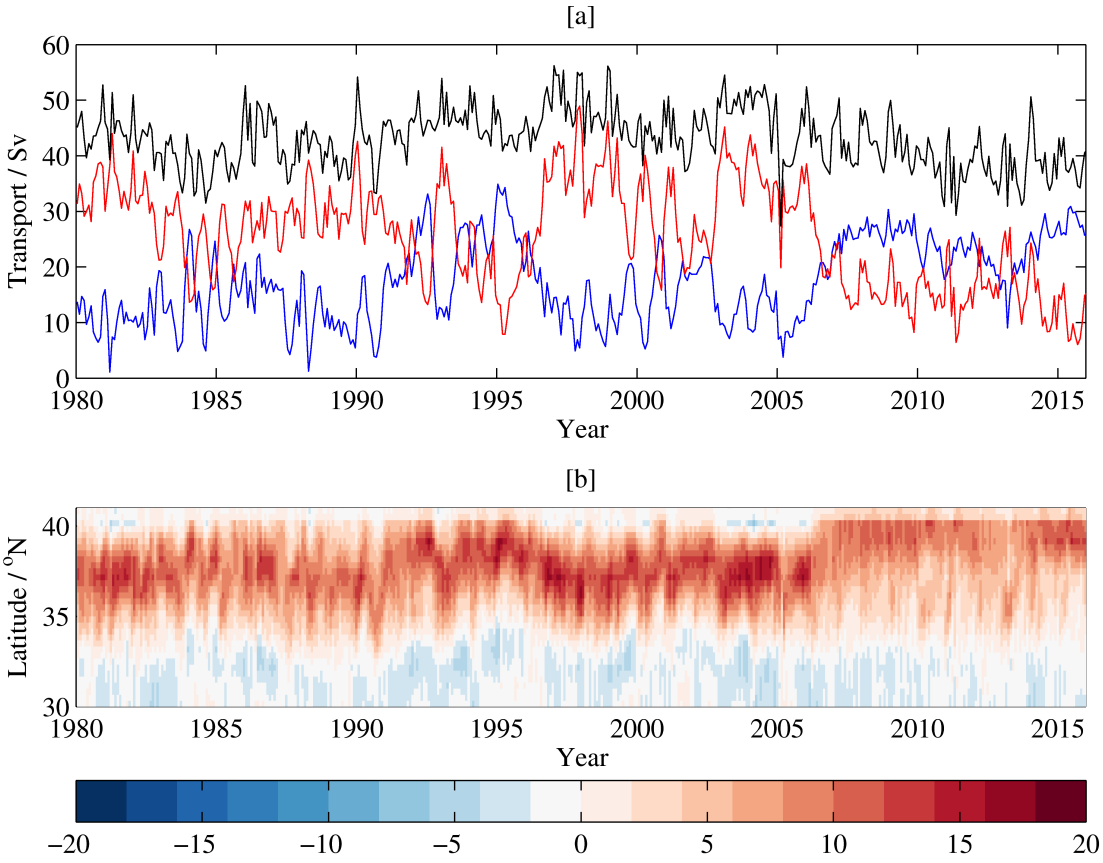

Figure 3.8: [a] Full depth transport (Sv) of the GS at 70^oW from $34-38^oN$ (red), $38-42^oN$ (blue) and $34-42^oN$ (black) from 1980-2015 using GODAS. [b] Full depth transport (Sv) per 1^o (normalised from $1/3^o$) in the GS at 70^oW from $30-42^oN$ from 1980-2015 in GODAS. Both are calculated using the zonal velocity field.

The separation of the GS into its northern and southern components provides further information on its transport but also on the location of the main GS core.

During the early to mid-1980s the transport was fairly constant, apart from the seasonal cycle, with nearly equal contributions from the north and south components. From about 1987-1991, the majority of the total transport occurs from $34 - 38^oN$, which can be seen in Figure 3.8a and indicates a more southern GS position during this period. The following period, i.e. the early to mid-1990s, sees a northward shift in the main GS core with most of the transport coming from the northern component. This is consistent with estimates of GS path shift observed in AVHRR (Figure 3.3). Furthermore, in some years, e.g. 1995, less than $5Sv$ comes from $34 - 38^oN$, which provides further evidence that the GS is in an anomalously northward position during these years. A southward shift is visible after this with transport in the northward component dropping from $30Sv$ during the 1990s to $10Sv$ in the early 2000s. This is then followed by a more northward path since 2006, which causes most of the transport to occur from $38 - 42^oN$. However, the transport is not as strong during this period compared with during the mid-1990s or mid-2000s with maximum values of $10 - 12Sv$ as opposed to $15 - 18Sv$ per 1^o (Figure 3.8b). In spite of this, the total transport remains high during the winter with contributions from the south. Again, this is likely related to the seasonal wind field. However, since March 2007 sea level data began to be assimilated into the GODAS, which may have caused this change (Climate Data Guide - www.climatedataguide.ucar.edu).

In order to isolate the baroclinic component, the GS transport is calculated at 70^oW using the thermal wind equation, using the ocean bottom as the depth of no motion, after calculating the density field. This is in outlined in section 2.3.3. The resulting baroclinic transport is shown in Figure 3.9a, which is, again, separated into its northern ($38 - 42^oN$) and southern ($34 - 38^oN$) components. The total transport ranges from $30 - 65Sv$ with a period of higher transport from 1996-2006, which is followed by a period of declining transport since 2007. The strengthened transport during the late-1990s and early-2000s is mostly due to an increase in transport from $34 - 38^oN$ with up to 81% coming from the southern component. This is in contrast with the period of declining transport, which is due to the combined effects of a northward shift in the current inducing a greater transport from $38 - 42^oN$ and a reduced transport in this region. For example, the maximum

transport since 2006 is $10-12Sv$ per degree while the maximum during the 1990s and early-2000s is consistently $15-18Sv$ per degree (Figure 3.9b). This may also be related to the change in the dataset since March 2007 as mentioned above.

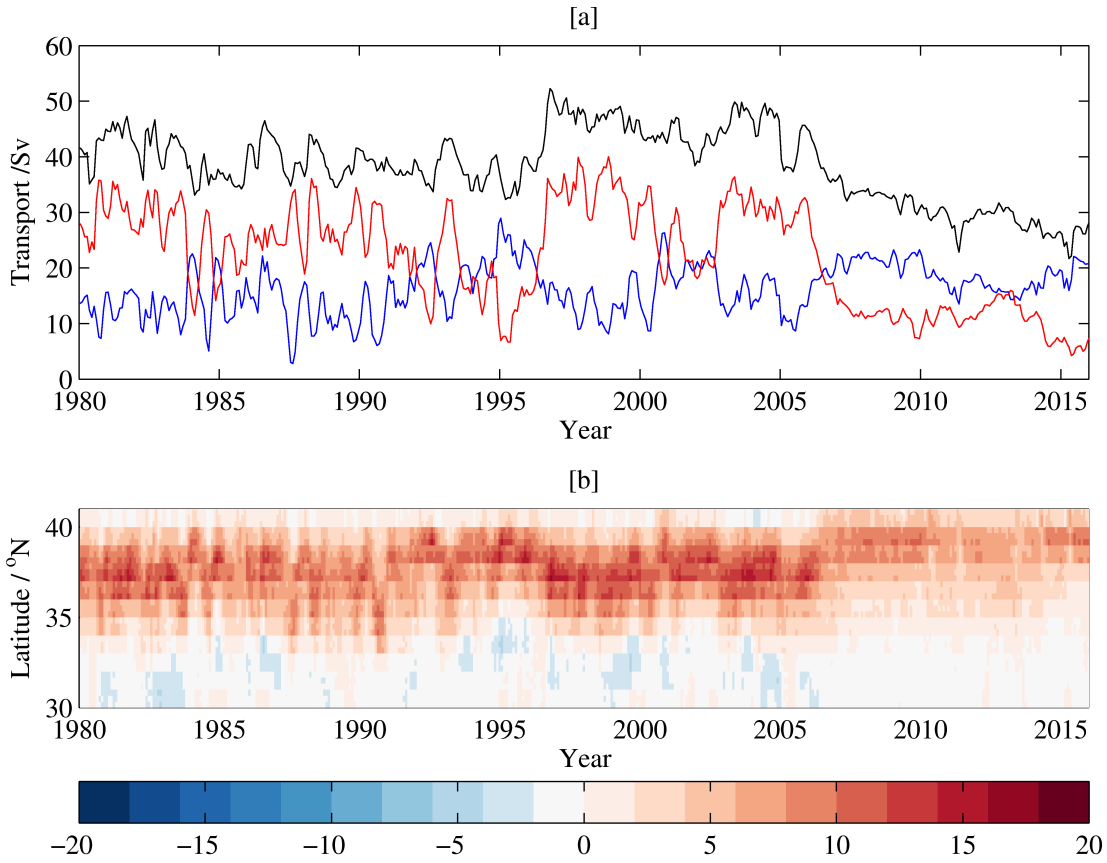

Figure 3.9: [a] Full depth baroclinic transport (Sv) of the GS at 70^oW from $34-42^oN$ (red), $38-42^oN$ (blue) and $34-42^oN$ (black) from 1980-2015 using GODAS. [b] Full depth baroclinic transport (Sv) per 1^o (normalised from $1/3^o$) in the GS at 70^oW from $30-42^oN$ from 1980-2015 in GODAS. Both are calculated using the thermal wind relation after obtaining the density field using temperature and salinity with the ocean bottom set as the depth of no motion.

In order to distinguish whether the abrupt change in GODAS was an actual change in the GS or due to the assimilation of sea level data, the mean and standard deviation of the baroclinic transport (from Figure 3.9) for the 8-year periods before and after the abrupt change, 1998-2006 and 2008-2016, are shown in Figure 3.10. The anomaly in the mean transport between the two periods exceeds the standard deviation from $39-41^o$N, which implies that the northward shift that occurred during the introduction of sea level data was unprecedented and may have infact been due to the step change in the assimilated observations. The mean location of

the GS core during this period is around 39^{o}N compared to 37^{o}N during the pre-2007 period. The mean position of the GS was found to be around 38^{o}N at 70^{o}W in AVHRR (Figure 3.1b) and combined with evidence of the GS shifting north in recent years (Figure 3.3), suggests that the post-2007 position of 39^o may be more realistic.

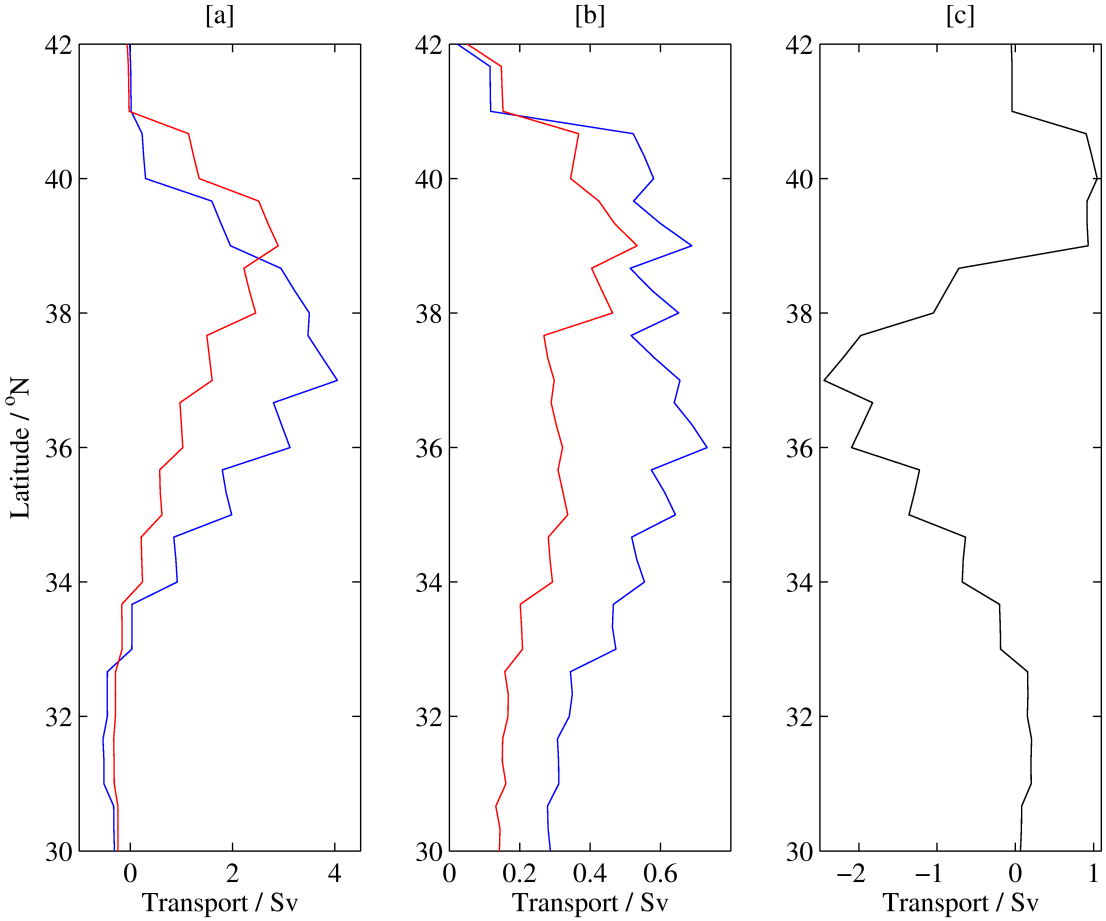

Figure 3.10: [a] Mean baroclinic transport (Sv per 1/12^o) in the GS at 70^oW from 1998-2006 (blue) and 2008-2016 (red), [b] standard deviation of the baroclinic transport (Sv) during the same periods and [c] the difference between the mean transport (Sv) during 1998-2006 and 2008-2016.

Regardless of this, the transport changes observed here, of strengthening during the 1990s followed by weakening since the mid-2000s, is in agreement with prior findings (*Sato and Rossby*, 1995; *Curry and McCartney*, 2001; *Ezer et al.*, 2013). In addition, there is also some agreement on the position of the GS with studies also finding the GS to be in a more northward position during the 1990s (*Taylor and Gangopadhyay*, 2001; *Kwon et al.*, 2010). This is also consistent with findings in Chapter 3.2.1 using the AVHRR SST field. To confirm this, the latitude of the maximum baroclinic transport (Figure 3.9b) for each April is used as an index for the GS position at 70^oW. Despite the different range (associated with different resolutions) both approaches show a northward shift in the GS path after 2005. This is significantly correlated (r=0.42) with the estimated latitude of the GS using the 21^oC isotherm in AVHRR at 73^oW (Figure 3.11a). However, after linearly detrending both of the timeseries, the correlation is no longer significant (Figure 3.11b).

The fact that the baroclinic transport is often greater than the total transport suggests that the reference depth, i.e. the ocean bottom, is not zero as assumed. This could be due to westward velocities associated with the DWBC, which would lead to an overestimation of the baroclinic transport. However, in terms of the overall trend, there is a high correspondence between the total transport (Figure 3.8) and the baroclinic transport (Figure 3.9). This implies that much of the total GS transport variability is associated with baroclinic transport variability, i.e. density changes, as opposed to variability in the primarily wind-driven barotropic transport. Furthermore, Figure 3.12 reveals that the upper $(0-1000m)$, i.e. where the effects of density changes are most prominent and where any potential DWBC-related errors are avoided, baroclinic transport is significantly correlated to the upper total transport (r=0.61). This supports the finding that changes in the baroclinic GS transport dominate the changes observed in the total GS transport. However, there are some periods where this is not the case, i.e. 1991-1996 and 2006-2016. For example, the decline in baroclinic transport by $25Sv$ since 2006 is greater than the $15Sv$ reduction in the total transport, which could imply that the GS is becoming more barotropic, or even ageostrophic, in recent years. A deepening of the GS would have consequences for the reference depth of 1km as it

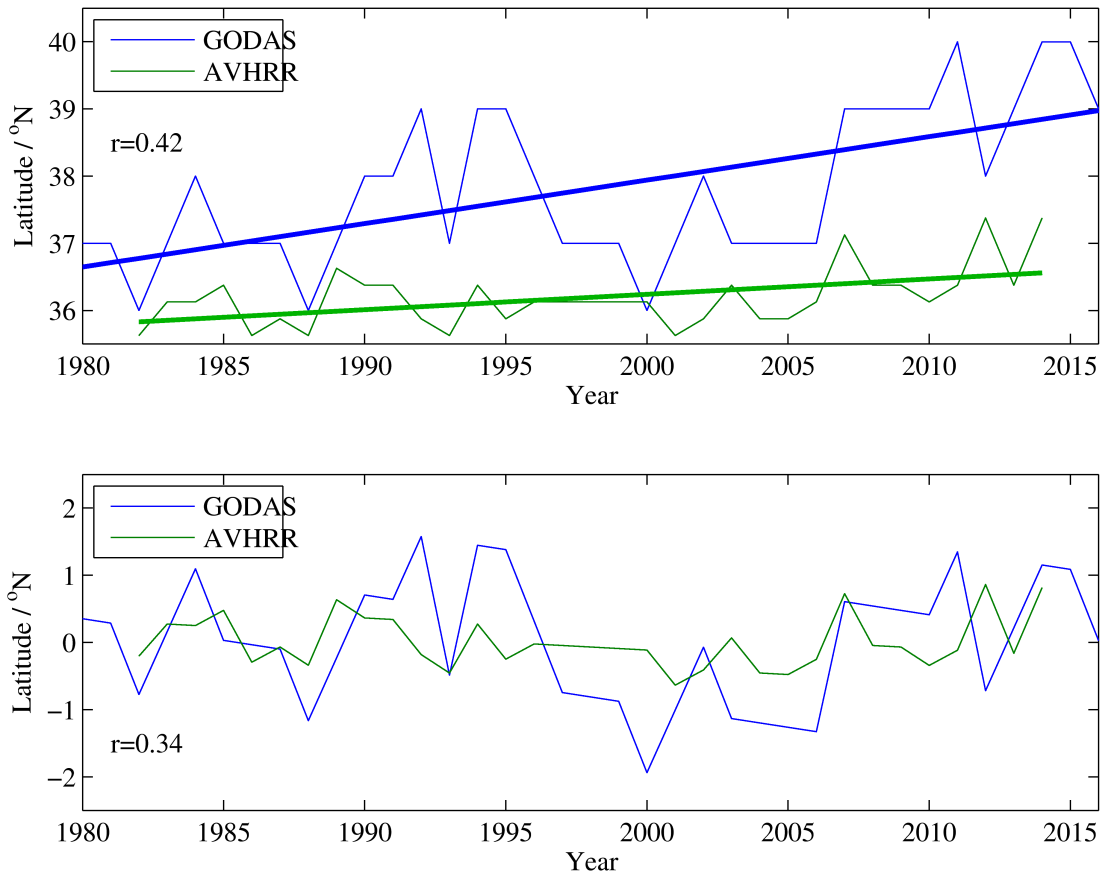

Figure 3.11: Top: Latitude (^oN) of the estimated path of the GS at 70^oW in GODAS in April from 1982-2014 (using the location of the maximum baroclinic transport) and at 73^oW in AVHRR using the 21^oC surface isotherm as in Figure 3.3. The correlation coefficient is represented by r, which is statistically significant at 95% Bottom: as above but detrended, r is insignificant.

would not be deep enough to capture the geostrophic GS transport. However, this hypothesis can be eliminated as the GS was not found to be deepening since 2006 (not shown).

Despite this, the correlation coefficient remains significant throughout the period 1980-2016, which highlights the importance of density changes driven by buoyancy fluxes. However, it should be noted that density changes may also occur via advection. Evidence on the importance of buoyancy forcing in inducing changes in baroclinic GS transport has been found in the literature (*Worthington*, 1977). Specifically, an intensification of the GS in 1977 was found to be related to the severe winter of 1976/77, in the northeast of North America, that induced widespread heat loss over the Sargasso Sea (*Worthington*, 1977). The effects on the GS during

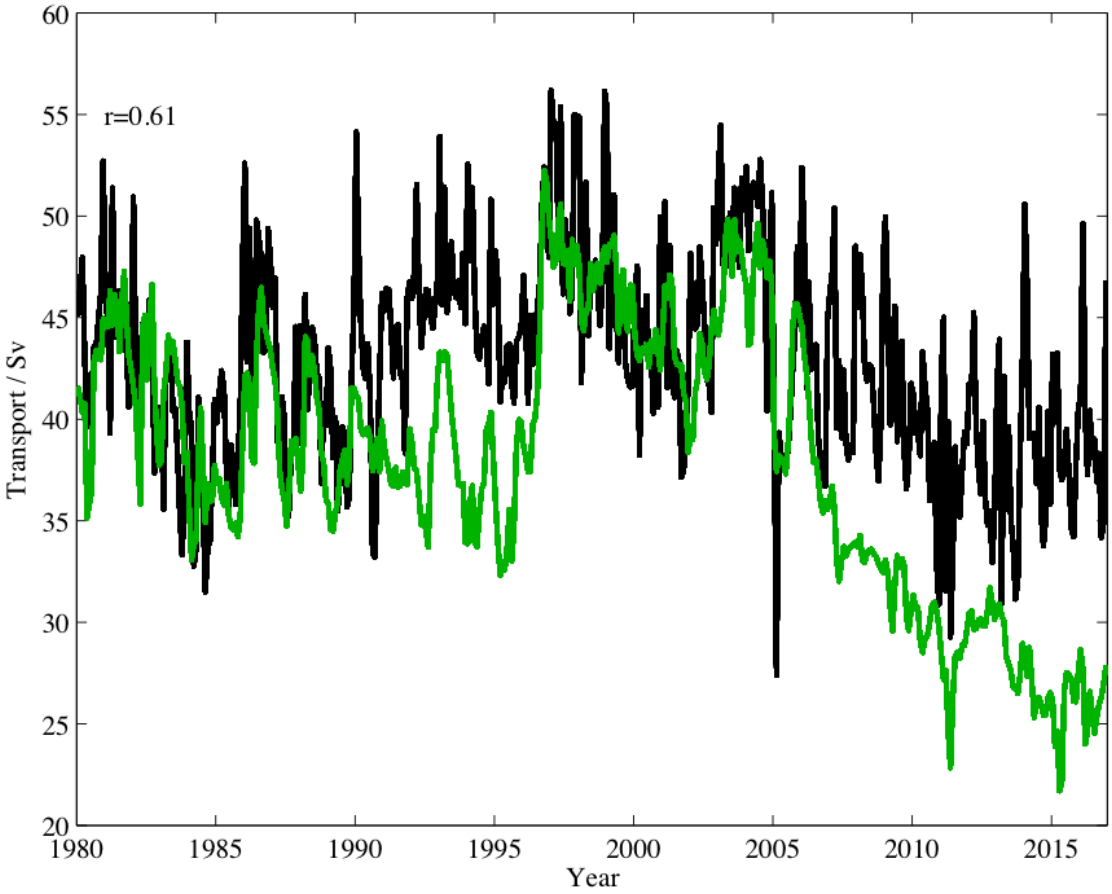

Figure 3.12: Upper $(0-1000m)$ total (black) and baroclinic (green) transport (Sv) of the GS at 70^oW from $34-42^oN$ (black) from 1980-2016 using GODAS. The baroclinic component is calculated using the thermal wind equation, here using 1000 m as a depth of no motion.

this winter will be investigated in the next section alongside the more recent severe winter of 2013/14. Additionally, the ORCA12 hindcast will be used in Chapter 4 to investigate the importance of buoyancy fluxes on GS transport variability with the potential mechanisms also explored.

3.4 The severe winters of 1976/77 and 2013/14

3.4.1 Transport variability of the Gulf Stream using EN4

The techniques applied to assess the interannual variability of the GS path and its transport are now used to quantify the impacts of two severe winters on the GS. The severe winter of 1976/77 was investigated by *Worthington* (1977) who found

an intensification of the GS occurred after a succession of CAOs, which he referred to as the anti-cyclogenesis mechanism. This winter is re-evaluated here alongside the more recent severe winter of 2013/14 to assess the extent of changes in surface heat loss and baroclinic transport. The baroclinic currents and upper $(0 - 1000m)$ transport of the GS are estimated in the EN4 dataset, using the temperature and salinity fields and $1000m$ as the depth of no motion, from 1970-2014 at 70^oW and 30^oW (equation 2.3 and 2.2), which are shown alongside temperature transects. The atmospheric context, i.e. Qnet and sea level pressure (SLP), is also evaluated for each winter.

Before investigating the potential influence of intense air-sea fluxes on the GS, the full depth baroclinic transport, calculated using the density field (Chapter 2.3.3), at 70^oW is revealed in Figure 3.13. The transport is, again, separated into its northern $(38 - 42^oN)$ and southern $(34 - 38^oN)$ components, which reveals that the total transport is mostly due to the southern contribution (Figure 3.13a). In contrast to that observed in GODAS (Figure 3.9b), Figure 3.13b shows that the main GS core is fairly stable in terms of its latitudinal path shift. This is most likely due to the coarser horizontal resolution (1^o) compared with GODAS $(1/3^o)$. Additionally, the two products will lead to different results as the GODAS is constrained by the model equations while the smoothed EN4 dataset is independent of these dynamics. Despite this, the mean baroclinic transport is $56.2Sv$, which is similar to that seen in GODAS $(44.4Sv)$. Furthermore, the upper baroclinic transport in EN4 is significantly correlated, $r = 0.44$, with GODAS during February, which indicates a high correspondence between the two observational products. The general pattern of weaker transport during the 1980s, stronger transport during the 1990s and then a weakening during the late 2000s (*Sato and Rossby*, 1995; *Curry and McCartney*, 2001; *Ezer et al.*, 2013) is also reproduced here and is in agreement with GODAS.

3.4.2 Anti-cyclogenesis mechanism

The anti-cyclogenesis mechanism described by *Worthington* (1977) implies that, during a particularly severe winter over North America, the successive CAO events

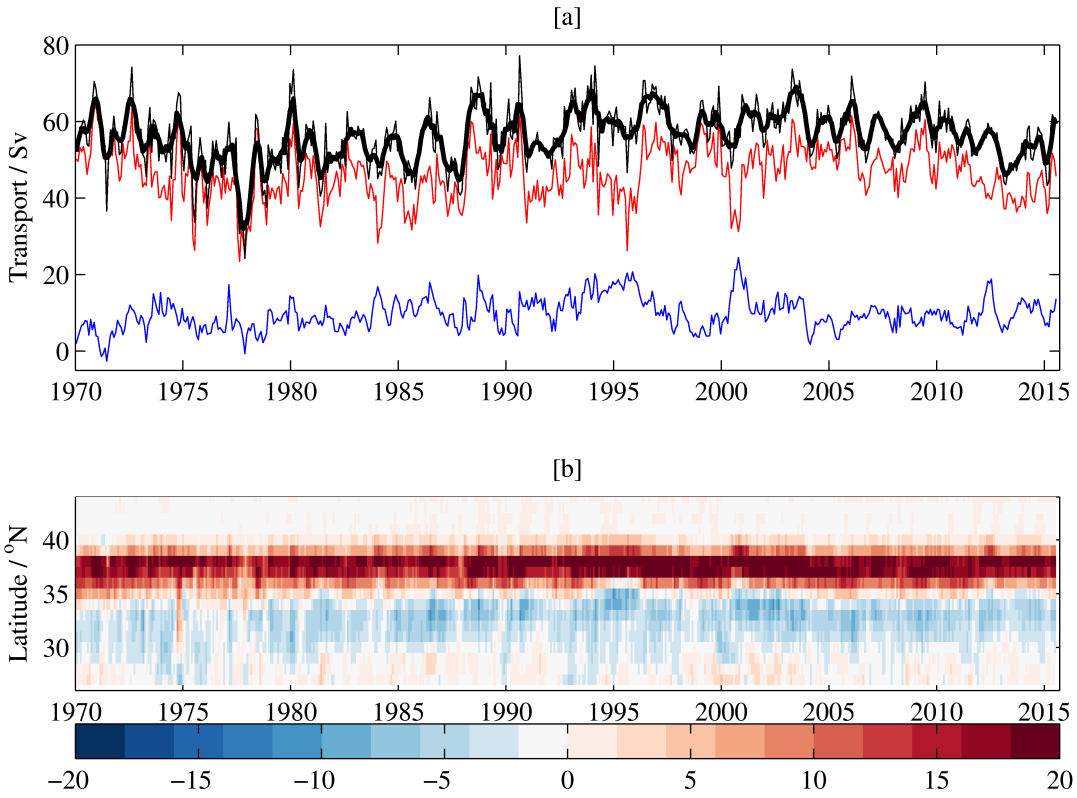

Figure 3.13: [a] Full depth baroclinic transport (Sv) of the GS at 70^oW from $34-38^oN$ (red), $38-42^oN$ (blue) and $34-42^oN$ (black) from 1970-2014 using EN4. Smoothed total transport is shown by the bold black line. [b] Full depth baroclinic transport (Sv) per 1^o in the GS at 70^oW from $30-42^oN$ from 1970-2014 in EN4. Both are calculated using the thermal wind relation after obtaining the density field using temperature and salinity, using the ocean bottom at the depth of no motion.

will induce a considerable heat loss over the Sargasso Sea. This then leads to deeper mixed layers over the region via deep convection, which induces an intensification of the GS via a strengthening of the meridional temperature gradients. In order to visualise this, examples of temperature cross-sections at 70^oW for two contrasting winters are displayed in Figure 3.14. During the winter of 1991/92 (Figure 3.14a) the depth of the thermocline (maximum vertical gradient of potential temperature) is approximately 400-500 m but the depth of the mixed layer is shallow as the water is not well-mixed. This is in contrast with Figure 3.14b, which reveals that a much deeper mixed layer exists during the winter of 1993/94 at around 500 m. This led to stronger meridional temperature gradients to this depth from $36-38^oN$, which, via thermal wind balance, translated into a greater zonal current shear during 1994 (Figure 3.14d) compared to 1992 (Figure 3.14c). This supported a greater upper

$(0-1000m)$ baroclinic transport of $60Sv$, compared to just $35Sv$ in 1992. However, it should also be noted that we see changes in the thermocline to depths of greater than 900 m, with a greater vertical temperature gradient visible from about 600-800 m in 1994. This may have also had an impact on the horizonal temperature gradient and, therefore, the baroclinic transport of the GS. Changes at this depth are more likely to be due to changes in the wind stress as opposed to surface buoyancy fluxes, as they are occurring beneath the mixed layer. For example, a greater wind stress will lead to increased Ekman transport and convergence (from a more negative wind stress curl) over this region, which causes greater Ekman pumping. This increases the (negative) vertical velocity at the base of the Ekman layer, which results in enhanced downwelling and a deeper thermocline. The overall changes in GS transport are likely due to a combination of changes in momentum and buoyancy fluxes but here we highlight the importance of the latter in causing changes in the MLD as seen in Figure 3.14.

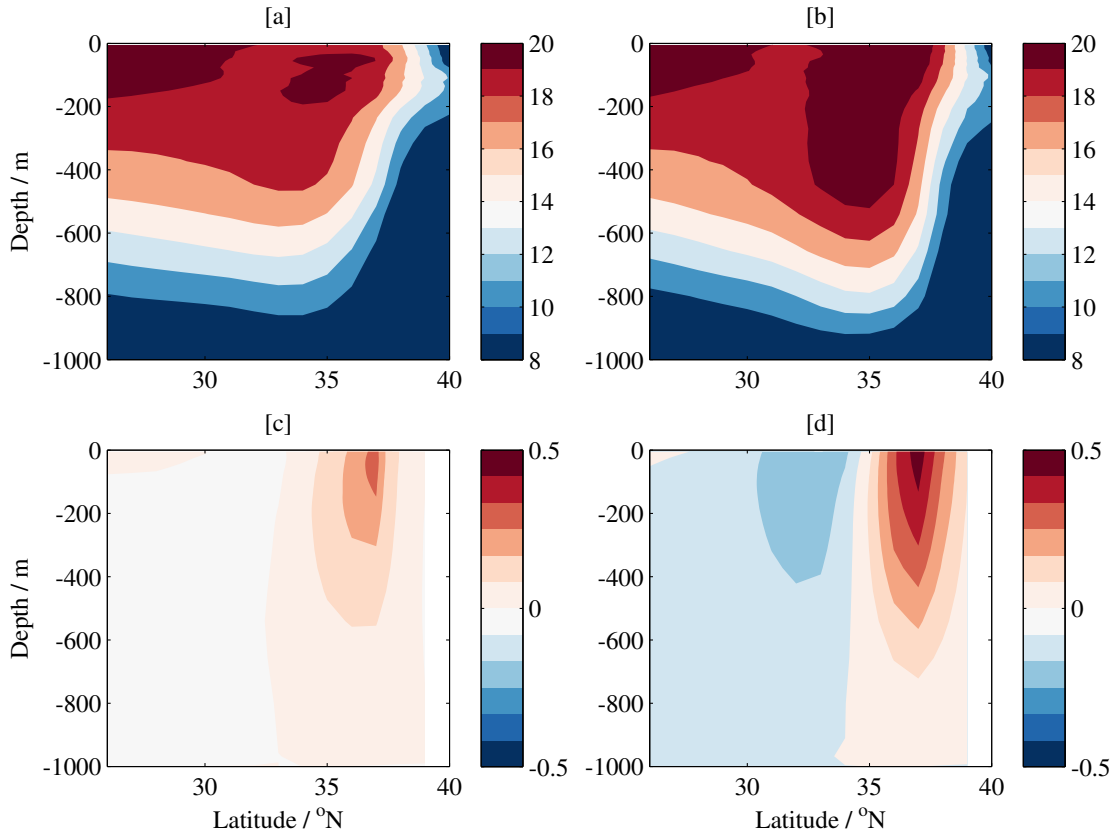

Figure 3.14: Temperature (^oC) in February 1992 [a] and February 1994 [b] and zonal currents m s^{-1} in February 1992 [c] and February 1994 [d] along 70^oW from $26-40^o$N in EN4.

3.4.3 Winter of 1976/77

70^oW is close to where *Worthington* (1977) observed an increased baroclinic GS transport during the severe winter of 1976/77. Figure 3.15a shows the temperature along this section during February 1977 with the temperature anomaly for this month seen in Figure 3.15b. A deep mixed layer is evident (500m) at 34^oN, i.e. to the immediate south of the GS, which implies strong buoyancy fluxes were operating during this winter. However, there is also evidence of a deeper thermocline, which may imply that a large wind stress curl is causing greater downwelling. The warmer water existing throughout the GS during a severe winter could be due advection of warmer water in the GS or may be as a result of the northward shift in the GS path.

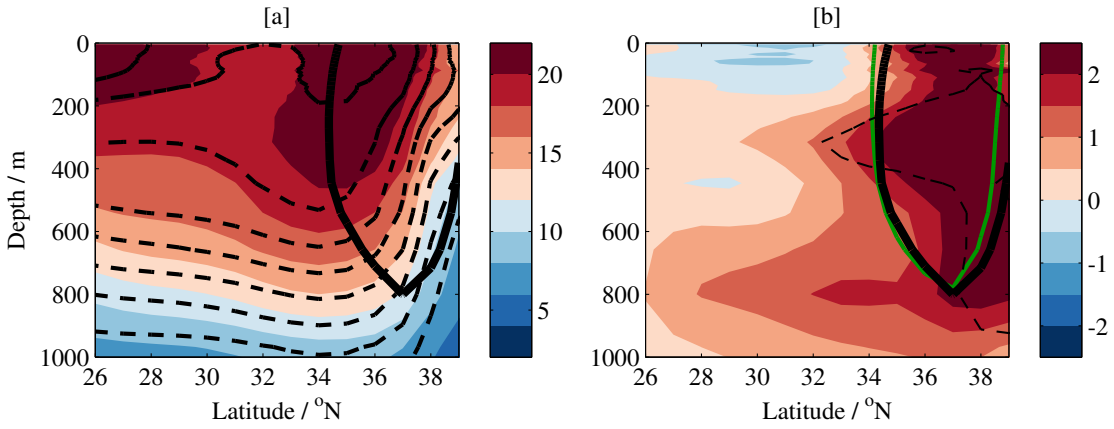

Figure 3.15: Temperature (^{o}C) along 70^oW from $26-39^oN$ in February 1977 [a] and the corresponding temperature anomaly (^oC) from the period 1970-79 [b] in EN4. The bold black line is the 0.1 m s^{-1} geostrophic velocity contour in February 1977 while the green line represents the same contour averaged over 1970-79. The dashed black lines in panel [a] represent the decadal mean isotherms and the dashed black lines in panel [b] represent 2 standard deviations.

The mean and anomalous geostrophic velocities for February 1977 along the same section are revealed in Figure 3.16a and Figure 3.16b respectively. A positive anomaly can be seen on the northern flank of the GS (from $36-39^oN$), which was supported by sharper meridional temperature gradients observed in Figure 3.15a. Additionally, a northward shift in the GS path of up to 1^o is apparent during February 1977 (black line) compared to the decadal mean (green line), which may have also contributed to the positive GV anomaly in Figure 3.16b. This is further

highlighted in Figure 3.16c, which reveals the position of the mean GS core for each February during the 1970s. The black line (1977) is found further north than all other years during this decade and is therefore a clear and significant shift of the GS.

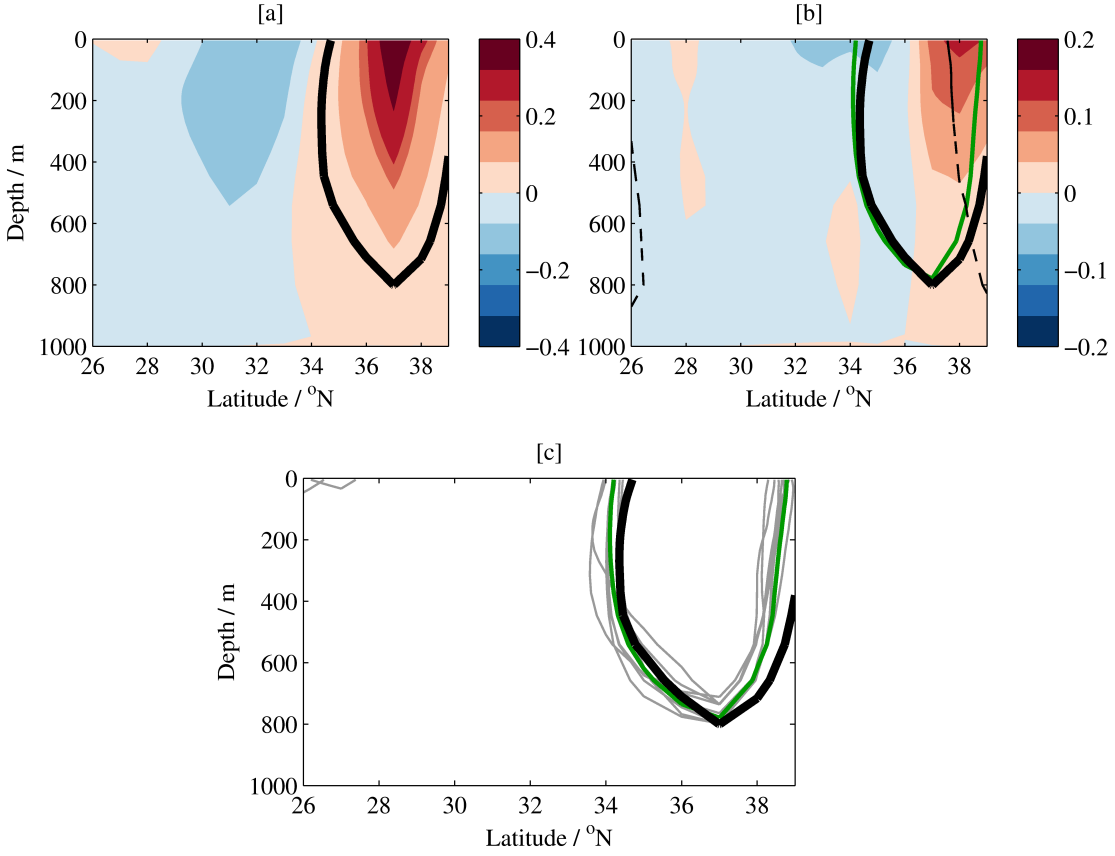

Figure 3.16: Geostrophic current (m s^{-1}) along 70^oW from $26-39^oN$ in February 1977 [a] and the corresponding velocity anomaly (m s^{-1}) from the period 1970-79 [b] in EN4. The bold black line is the 0.1 m s^{-1} geostrophic velocity contour in February 1977 while the green line represents the same contour averaged from 1970-79. The dashed black lines represent 2 standard deviations. [c] the grey lines reveal the location of the 0.1 m s^{-1} geostrophic velocity contour for each February from 1970-79, the green line is the decadal mean and the bold black line is 1977 (as in panel b).

The temperature section to the immediate south of the GS (i.e. at 34^oN, 70^oW) in February from 1970-2014 is shown in Figure 3.17. At this location, the depth of $20-21^oC$ water reaches about $200m$ on average but there are some years where it can be non-existent during this month e.g. in 2010 and 2011. However, during 1977 it reaches $450m$, almost double the average. The only time that this is exceeded in February is in 1994, which was the example used of a strengthened GS in Figure

3.14. This provides further evidence for an anomalously deep mixed layer and thermocline during the winter of 1976/77, associated with a greater formation of Subtropical Mode Water (STMW).

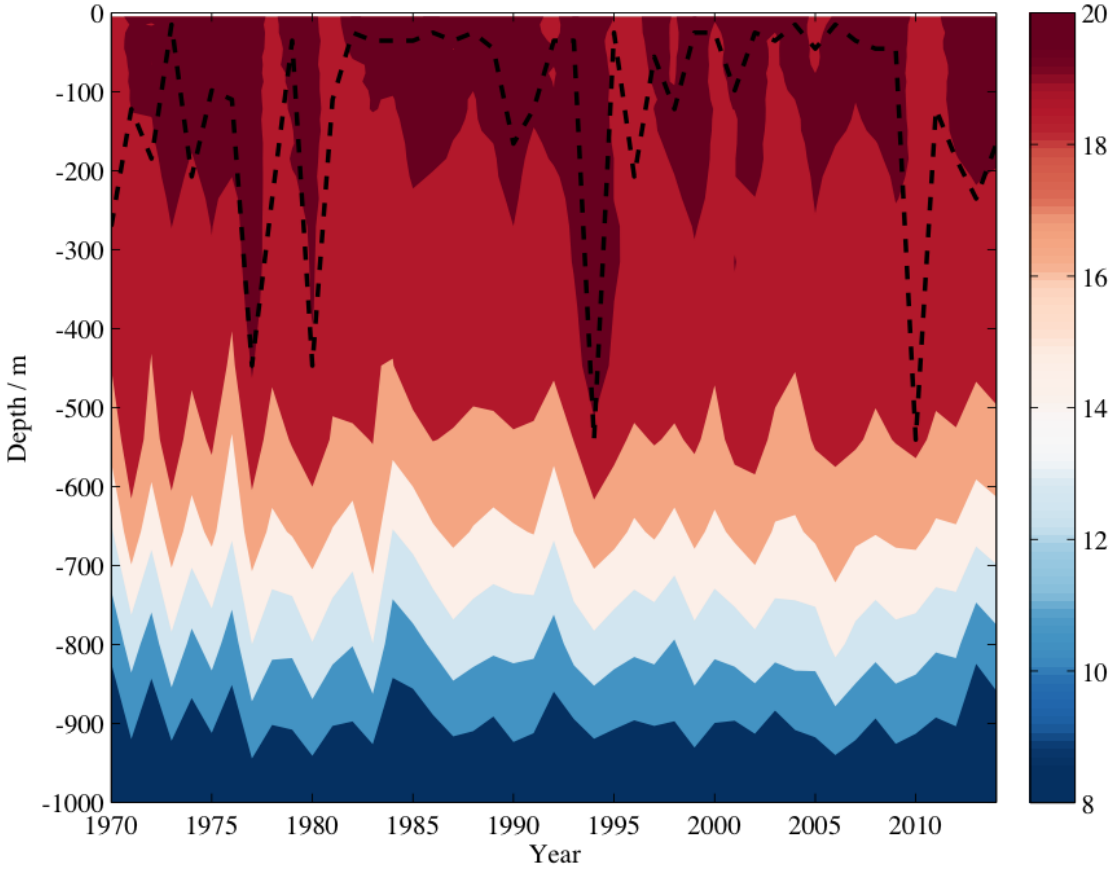

Figure 3.17: Temperature (^oC) at 34^oN, 70^oW in February from 1970-2014 in EN4. The dashed line represents the depth of the mixed layer, defined as the depth where the temperature is greater than 0.5^oC different from the surface.

The upper $(0 - 1000m)$ baroclinic transport of the GS during February from 1970-2014 is displayed in Figure 3.18. The greatest upper transport recorded at 70^oW $(49Sv)$ during the 1970s was in 1977 with an anomaly of 25% greater than the decadal average. However, since the 1970s the transport at these locations has exceeded the values recorded in 1977 many times. For example, during 1994 a maximum transport of $60Sv$ was recorded at 70^oW. Consequently, this implies that although the intensified GS in 1977 was anomalous during the 1970s, it does not stand out as a particularly anomalous year over the last 45 years. There is also further evidence for a more northward path, as seen in Figure 3.15b, with an increased contribution to the total transport increase coming from the northward

component. Furthermore, *Worthington* (1977) found that the high formation of STMW during the winter of 1976/77 followed multiple winters of relatively low STMW formation. He hypothesised that this led to a considerable increase in transport, of up to 50%, compared to the previous year. This is also found here with an increase of 60.5% from February 1976 to February 1977, which is the greatest transport increase observed from 1970-2014.

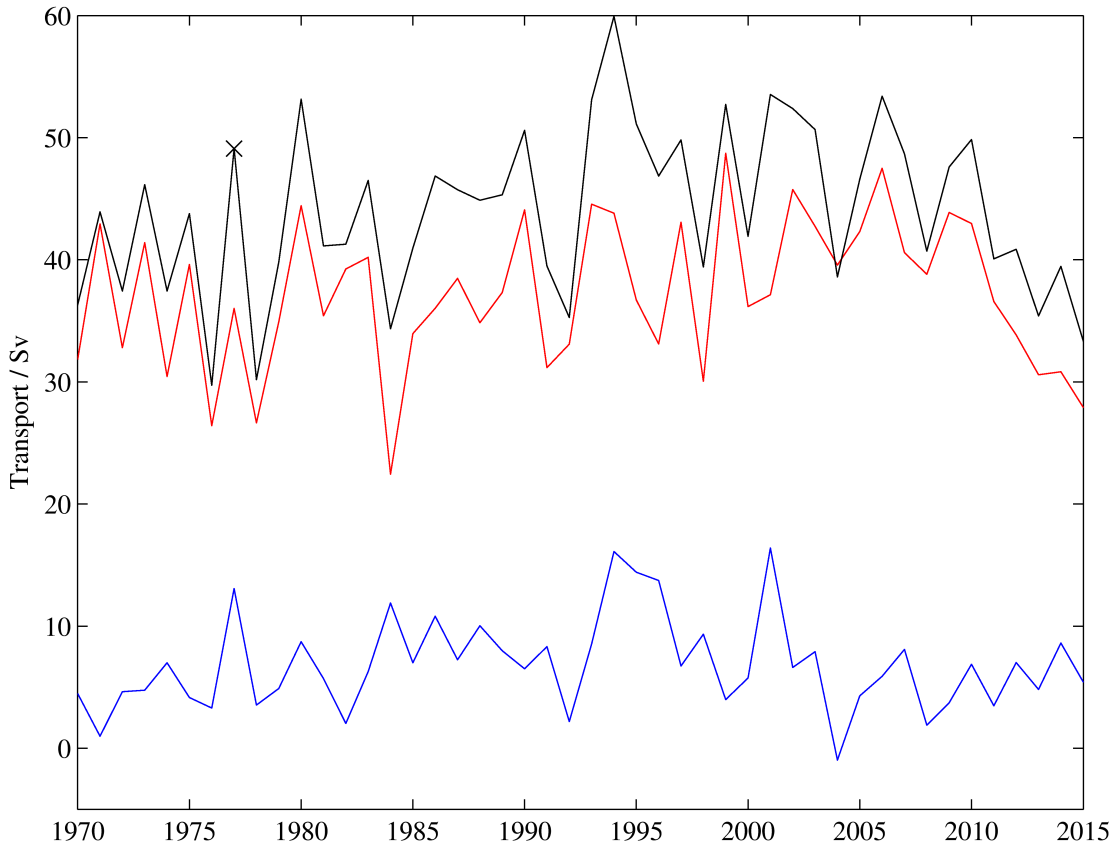

Figure 3.18: Upper $(0 - 1000m)$ baroclinic transport (Sv) of the GS at 70^oW from $34 - 38^oN$ (red), $38 - 42^oN$ (blue) and $34 - 42^oN$ (black) in February from 1970-2014. The black cross denotes February 1977.

Finally, to investigate the nature of the severe winter of 1976/77, Figure 3.19 shows the Qnet anomaly during December (Figure 3.19a), January (Figure 3.19b), February (Figure 3.19c) and March (Figure 3.19d). It reveals that a series of CAOs may have occurred from December to February with the prevailing meteorological conditions causing them to flow to the southeast over the Sargasso Sea. This led to a large anomalous heat loss of up to 200 W m^{-2} in this region, which was more widespread in December and February and more restricted to the western STG in January. This was likely conducive for the high STMW formation and subsequent

intensification of the baroclinic GS found by *Worthington* (1977) during this winter.

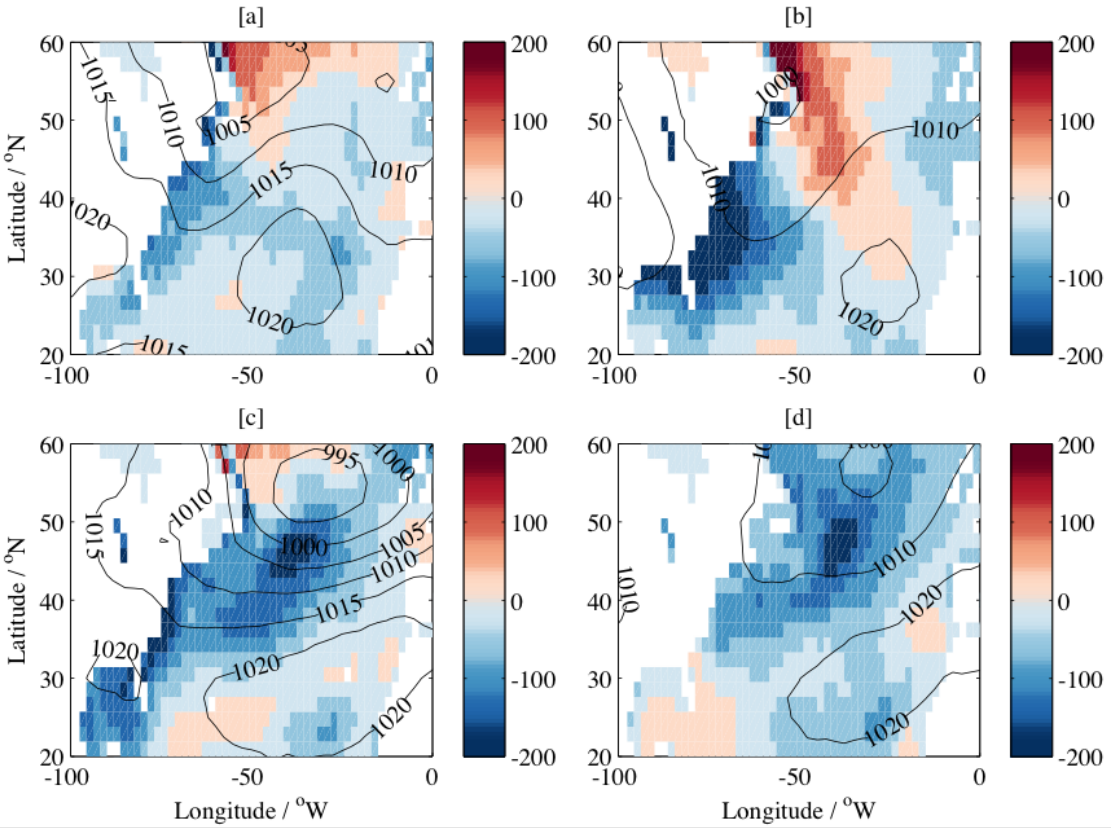

Figure 3.19: Qnet anomaly (W m^{-2}) over the North Atlantic in December [a], January [b], February [c] and March [d] during the winter of 1976/77 (using 1971-1980 as a reference period) in NCEP/NCAR reanalysis. Black lines represent the corresponding SLP (hPa) for each month.

The increase in the transport observed here is in the upper baroclinic component, assuming a level of no motion at $1000m$. The current velocities are not available in EN4 so comparisons cannot be made with the total transport, as is possible in GODAS. However, in GODAS, the upper $(0 - 1000m)$ baroclinic transport is significantly correlated with the upper total transport, r = 0.61 (Figure 3.12). This connection provides evidence to suggest that changes in the total transport are represented by changes in the baroclinic transport at 70^oW.

3.4.4 Winter of 2013/14

During the more recent severe winter of 2013/14, there were no major changes to the main GS core along 70^oW. However, further east at 30^oW, significant

anomalies are observed in both the temperature and geostrophic velocity. This is now the NAC rather than the GS and has a large zonal component from $40-50^oW$. The full-depth baroclinic transport at 30^oW is revealed in Figure 3.20, which is separated into its northern $(30-42^oN)$ and southern $(43-54^oN)$ components. It reveals that the total transport is mostly due to the northern contribution (Figure 3.20a) and is reduced in some years due to a negative transport from the southern component. The southern component is mostly westward transport but with an eastward transport observed at about 32^oN, the Azores Current, which is seen to vary interannually. Regardless of this, the mean total transport is $13.7Sv$, $19.5Sv$ from the north and -5.8 Sv from the south. There is also some evidence of a weaker transport during the 1980s that increases during the 1990s, which is in agreement with GS transport variability at 70^oW (Figure 3.13) but on a smaller scale.

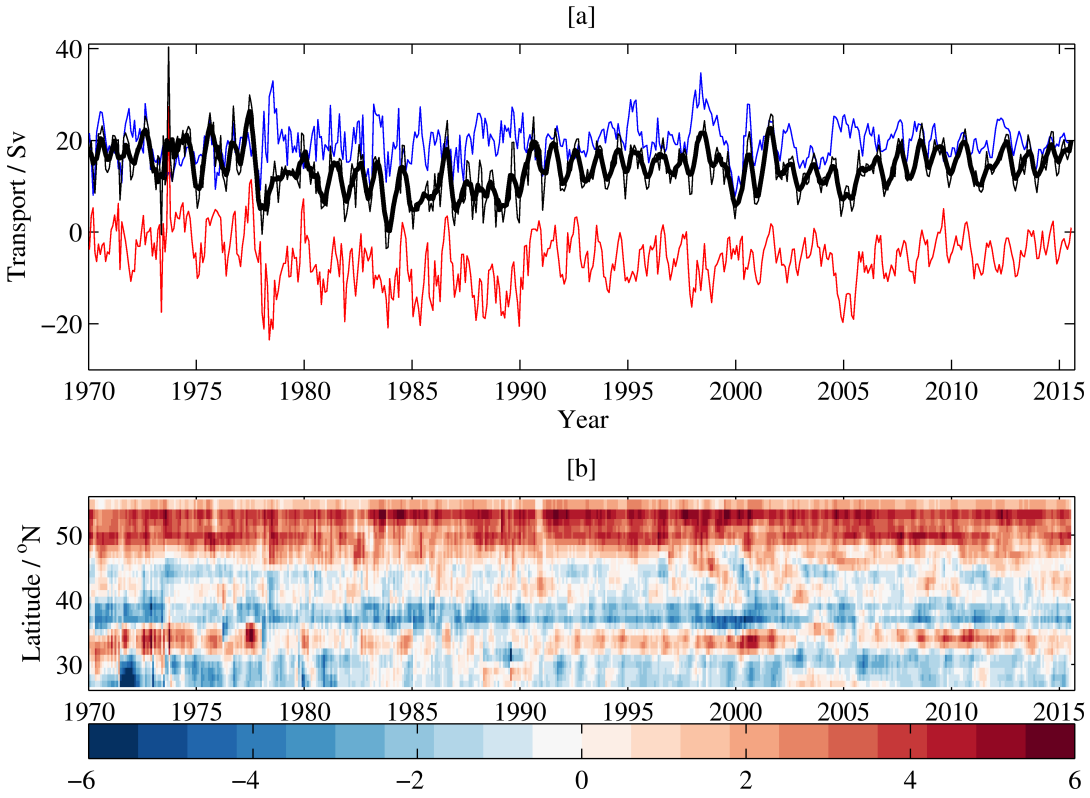

Figure 3.20: [a] Full depth baroclinic transport (Sv) of the NAC at 30^oW from $30-42^oN$ (red), $43-54^oN$ (blue) and $30-54^oN$ (black) from 1970-2015 using EN4. Smoothed (using a matlab function) total transport is shown by the bold black line. [b] Full depth baroclinic transport (Sv) per 1^o in the NAC at 30^oW from $30-54^oN$ from 1970-2014 in EN4. Both are calculated using the thermal wind relation after obtaining the density field using temperature and salinity, using the ocean bottom as the depth of no motion.

The temperature and geostrophic velocity during the winter of 2013/14 are now examined along 30°W in the region of the NAC, which reveals greater changes compared to the GS at 70°W. Figure 3.21a shows the temperature along 30^oW during March 2014 with the temperature anomaly for this period seen in Figure 3.21b. In contrast to that seen along 70^oW in Figure 3.14, at 30^oW the geostrophic velocity contour now denotes the AC from $30-35^oN$ and the NAC from $40-53^oN$. A significant anomaly of up to -2.5^oC exists throughout the NAC and extends to depths of greater than $1000m$. This is due to the isotherms outcropping further to the south during this winter (compared to decadal mean, Figure 3.21a) and may have led to deeper mixed layers and increased meridional temperature gradients that may have also shifted southwards.

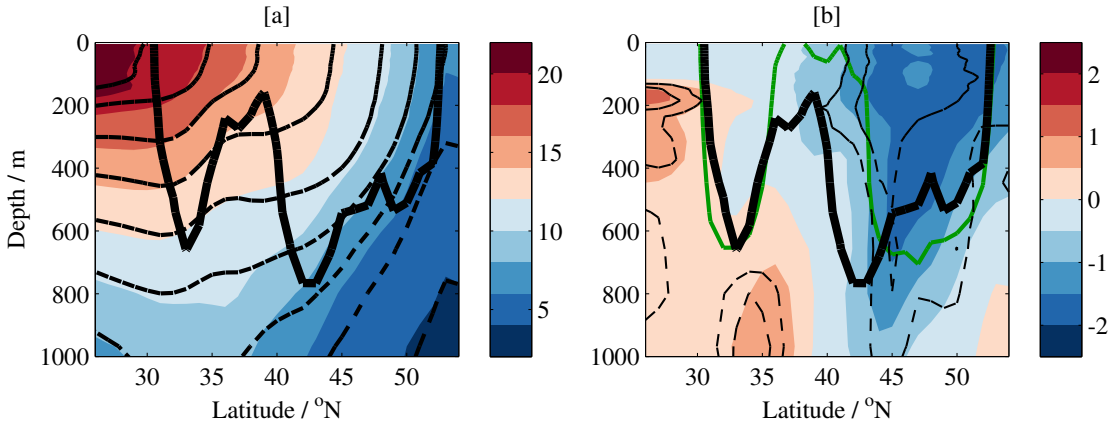

Figure 3.21: Temperature (^oC) along 30^oW from $26-54^oN$ in March 2014 [a] and the corresponding temperature anomaly (^oC) from the period 2004-13 [b] in EN4. The bold black line is the 0.01 m s^{-1} geostrophic velocity contour in March 2014 while the green line represents the same contour averaged from 2004-13. The dashed black lines in panel [a] represent the decadal mean isotherms and the dashed black lines in panel [b] represents 2:3 standard deviations.

The mean and anomalous geostrophic velocity for March 2014 along the same section are revealed in Figure 3.22a and Figure 3.22b respectively. A negative anomaly of up to 0.02 m s^{-1} can be seen in the Azores Current and on the northern flank of the NAC from about $45-52^oN$. This opposes a positive anomaly of up to 0.03 m s^{-1} observed on the southern flank of the NAC from $35-45^oN$, which is likely due to a shift in the path of the current by up to 3^o, i.e. the southern limit is now 40^oN (black line) rather than 43^oN for the decadal mean (green line). The southward shift led to the current almost joining up with the Azores Current

at depths shallower than 200 m, which are seen as two separate currents in the decadal mean.

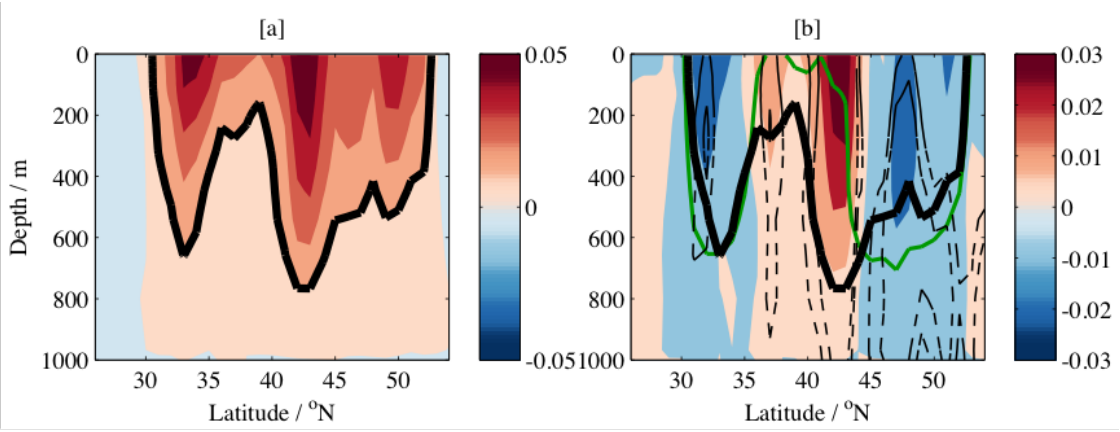

Figure 3.22: Geostrophic current (m s^{-1}) along 30^oW from $26-54^oN$ in March 2014 [a] and the corresponding velocity anomaly (m s^{-1}) from the period 2013-14 [b] in EN4. The bold black line is the 0.01 m s^{-1} geostrophic velocity contour in March 2014 while the green line represents the same contour averaged from 2013-14. The dashed black lines represent 2:3 standard deviations.

The temperature section on the southern flank of the NAC (i.e. at 44^oN, 30^oW) in March from 1970-2014 is shown in Figure 3.23. Here, the depth of $13-14^oC$ water (warmer subpolar mode water temperatures can be from $10-15^oC$, *McCartney and Talley* (1982)) reaches about $300m$ on average but it can be non-existent in some years. This was the case during the late 1980s but since then, the formation of $13-14^oC$ water has been renewed in March at this location for every year until 2014. There is even evidence to suggest that it was deepening, i.e. $200m$ in 1989 and $350m$ in 2010. The upturn of isotherms at the end of the time series illustrates winter 2013/14 formation of the most anomalously cool mode water in the central SPG for 17 years.

The upper $(0-1000m)$ baroclinic transport of the NAC during March from 1970-2015 is displayed in Figure 3.24, along with the north and south components as seen in Figure 3.20a. The effect on baroclinic transport at 30^oW in March 2014 ($23.5Sv$) is negligible, with a positive anomaly of just 7% from the decadal average. This is most likely due to an increased width of the NAC during this year as the positive anomaly is compensated for by a negative anomaly on the northern flank. This is also evident in Figure 3.24, which reveals an increase and a decrease in the

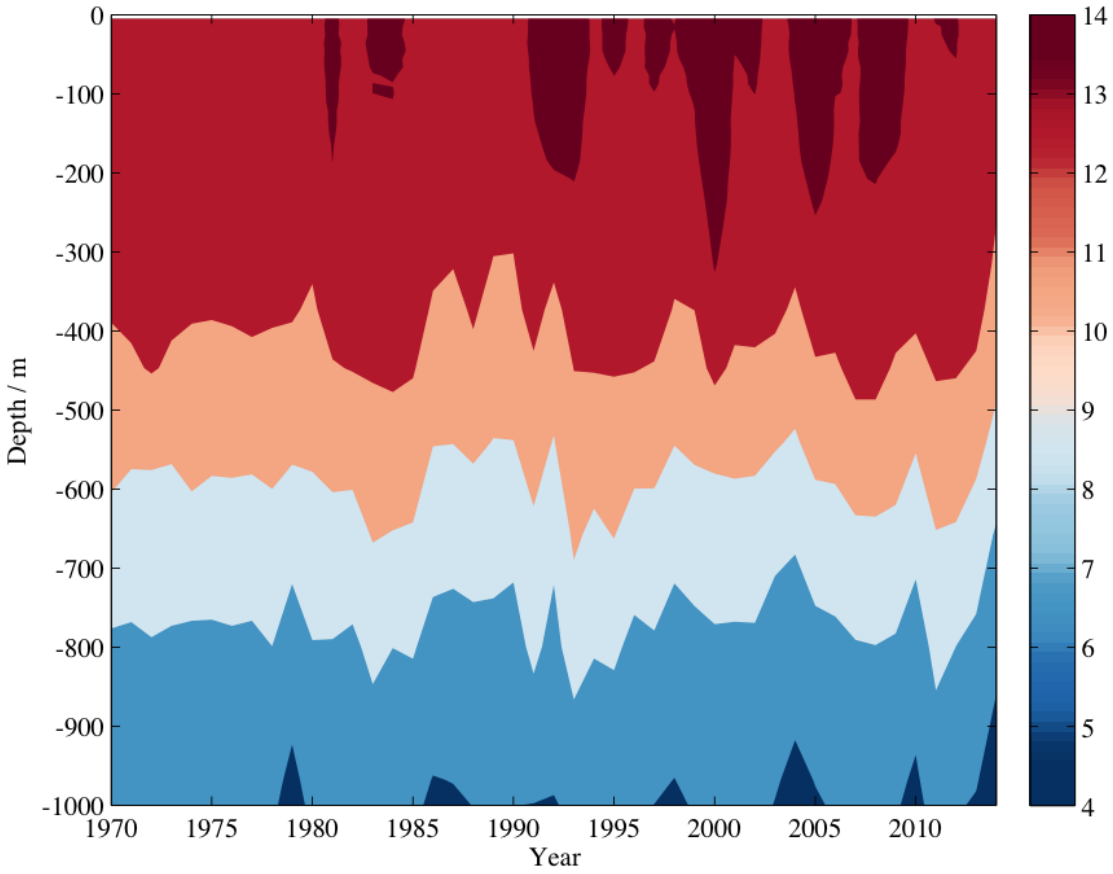

Figure 3.23: Temperature (^oC) at 44^oN, 30^oW in February from 1970-2014 in EN4.

transport on the southern and northern components respectively.

For this winter to have such different effects to that seen in 1976/77, the atmospheric setup must have differed substantially. Figure 3.25 shows the Qnet anomaly during December (Figure 3.25a), January (Figure 3.25b), February (Figure 3.25c) and March (Figure 3.25d) during the winter of 2013/14. It reveals that, like in 1976/77, a series of CAOs occurred but, this year, during the months of December and February. They also appeared to leave the continent at different locations with the atmospheric circulation causing them to flow over the SPG as opposed to the western STG. They led to a widespread anomalous heat loss in this region of up to 200 W m^{-2}, which had minimal impact on the geostrophic transport of the NAC but may have induced a change in the structure and path of the current.

To summarise, this section has investigated the influence of two severe winters on the path and transport of the GS. During the winter of 1976/77 an influence on

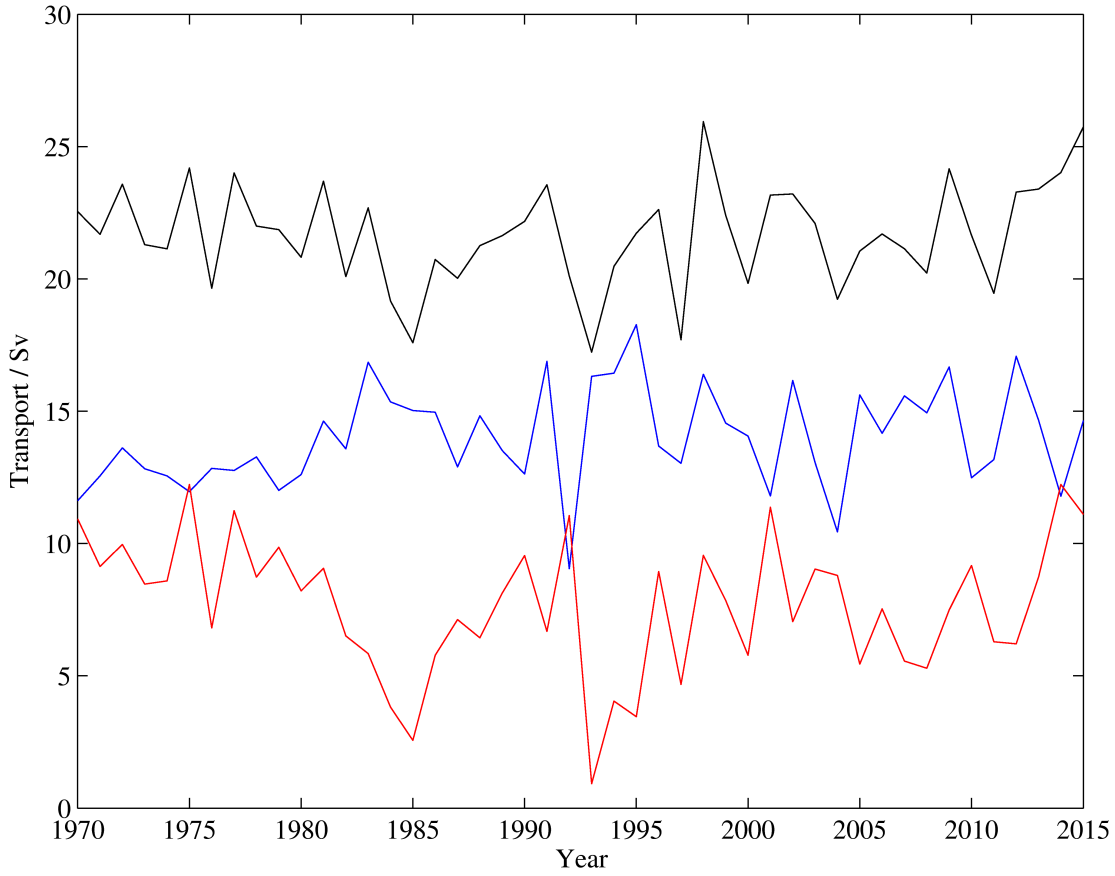

Figure 3.24: Upper $(0-1000m)$ eastward transport (Sv) of the NAC at 30^oW from $30-42^oN$ (red), $43-54^oN$ (blue) and $30-54^oN$ (black) in March from 1970-2015 in EN4.

baroclinic transport is evident, with a series of CAOs causing a large formation of STMW and an intensification and northward shift of the main GS core at 70^oW. This led to the greatest upper $(0-1000m)$ baroclinic transport recorded at 70^oW throughout the 1970s but was frequently exceeded since then. However, the increase in transport (from 1976-77) compared to the previous year was the greatest seen throughout the period 1970-2014 in March.

In contrast to this, the CAOs recorded during the winter of 2013/14 travelled over the SPG, as opposed to the western STG, which led to the greatest cold anomaly seen in this region since 1986. This has been referred to as the cold blob of the North Atlantic (*Grist et al.*, 2016; *Duchez et al.*, 2016). It caused anomalously deep mixed layers and a potential change in structure of the NAC at 30^oW. Although this was a very severe winter that caused considerable damage from flooding and strong winds in the UK, there was a limited influence on the overall transport of

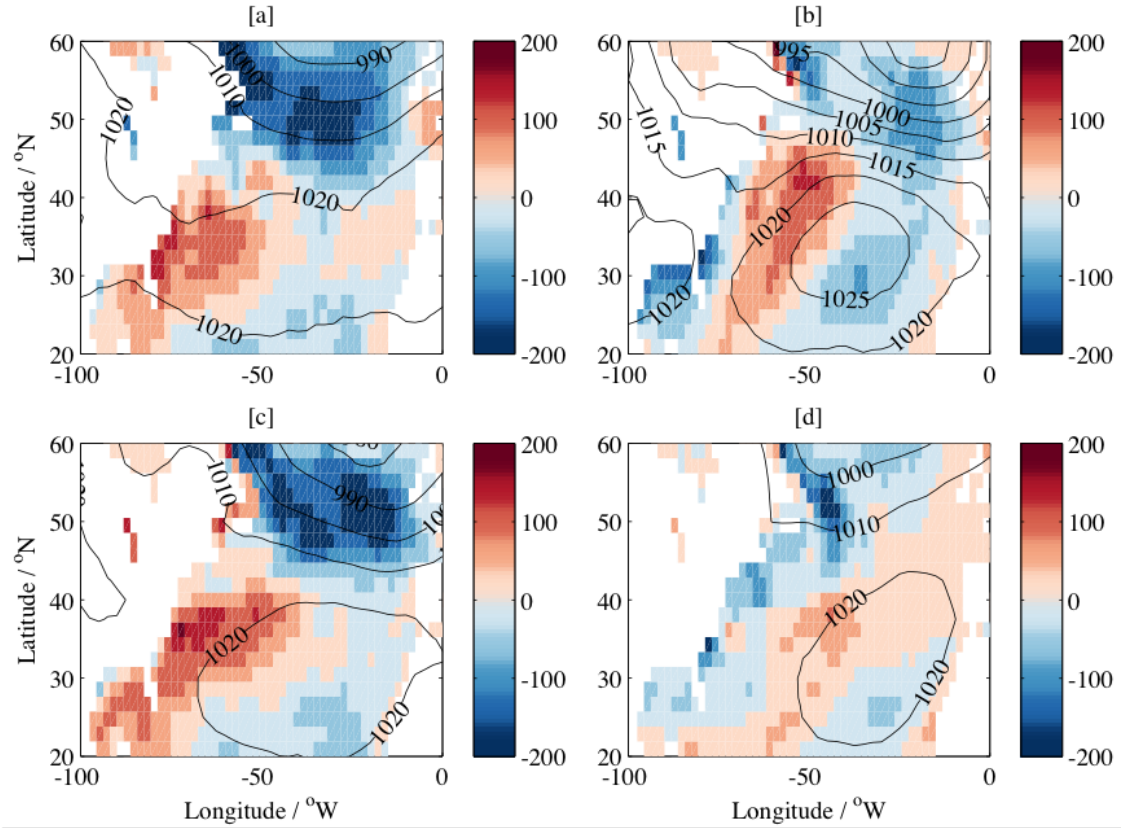

Figure 3.25: Qnet anomaly (W m^{-2}, negative values indicative of stronger heat loss) over the North Atlantic in December [a], January [b], February [c] and March [d] during the winter of 2013/14, with respect to 2004-13, in NCEP/NCAR reanalysis. Black lines represent the corresponding SLP (hPa) for each month.

the GS/NAC. Therefore, baroclinic transport in the main GS core was largely unaffected during this winter but significant effects were felt elsewhere, namely in the upper water column of the central SPG.

The effect of intense heat loss over the Sargasso Sea on GS transport is further investigated in Chapter 4. The ORCA12 hindcast is analysed in order to assess the impact of buoyancy forcing on the GS transport and its Lagrangian pathways. The next section outlines the methods used to estimate the GS transport in ORCA12 and the challenges associated with this.

3.5 Transport variability of the Gulf Stream: model hindcast

This section calculates the transport of the GS at 70°W, i.e. where we see a narrow core, in ORCA12 using two methods. First, the total and baroclinic transport at 70^oW will be calculated in the same way as in GODAS (section 3.3) in order to separate the importance of the baroclinic component on interannual timescales. There is considerable difficulty surrounding the accurate estimation of GS transport due to the regular occurrence of meanders and eddies along the path, and the westward-flowing recirculation gyres to the north and to the south (see Chapter 1.1). This section then goes on to calculate the geostrophic velocity of the GS using the dynamic height method (outlined in Chapter 2.4.3), which also includes the SSH, eliminating the need for a reference depth. Using this geostrophic velocity field, it then compares four methods used to calculate the GS transport at 70^oW, which are compared to the observations. These methods involve enforcing latitudinal limits and taking into account eastward-only velocities (Table 2.3). Additionally, the total (i.e. derived from the model's zonal velocity field) and the geostrophic transport is examined along two transects, 70^oW and 60^oW, with the residual, i.e. the ageostrophic transport, identified for each.

The zonal model velocity is vertically integrated across 70^oW from $34 - 42^oN$, which gives the transport of the GS at this longitude and is shown in Figure 3.26. Figure 3.26a reveals the total transport between these two latitudes (black line) and also separates out a more northern component from $38 - 42^oN$ (blue line) and a more southern component from $34 - 38^oN$ (red line). The pattern of total transport is distinctly different from that seen in Figure 3.8a, when using GODAS. In the observations, the total transport is never negative but there are a few months where either the north or south component dips below the $0Sv$ line. Contrastingly, in ORCA12, the total transport drops below $0Sv$ on several occasions and can be due to both the north and south components, which themselves are negative as often as they are positive. This further highlights the difficulty in measuring the GS transport in this hindcast, as the westward recirculations can dominate on a regular basis. For example, 1998-99 sees a transport of up to $100Sv$ in the

more southern component, with a more southerly GS path clearly evident in Figure 3.26b. However, due to a negative transport of up to $60Sv$ from $38-42^oN$, the total transport is reduced and could be due to a stronger Slope Water current or eddy activity. This is unrepresentative as the large transport from $34-38^oN$ is clearly representing a more southern path as opposed to a reduction in the transport.

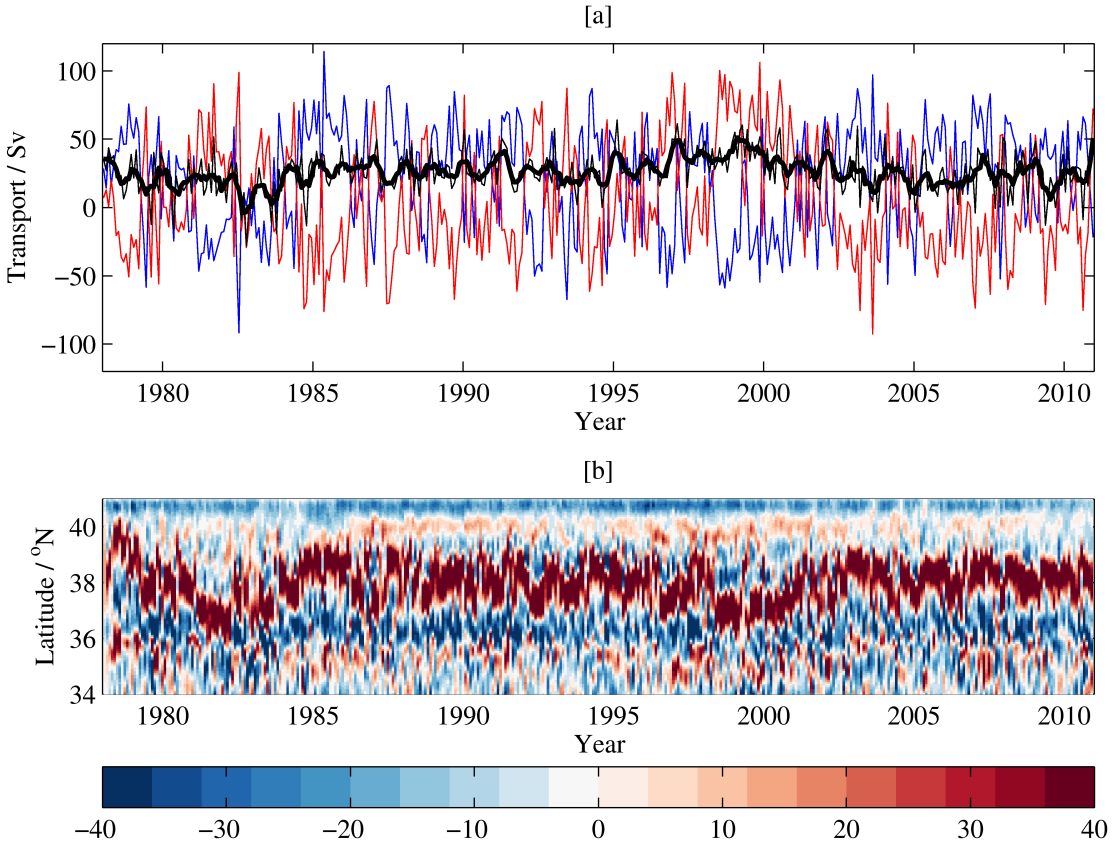

Figure 3.26: [a] Full depth transport (Sv) of the GS at 70^oW from $34-38^oN$ (red), $38-42^oN$ (blue) and $34-42^o$N (black) from 1978-2010 using the ORCA12 hindcast. Smoothed (using a matlab function) total transport is shown by the bold black line. [b] Full depth transport (Sv) per 1^o (normalised from $1/12^o$) in the GS at 70^oW from $30-42^oN$ from 1978-2010 in ORCA12. Both are calculated using the zonal velocity field.

The corresponding full-depth baroclinic transport is shown in Figure 3.27. Unlike that seen for the total transport in Figure 3.26a, the baroclinic transport is always positive from $34-42^oN$. However, the contributions to the north and south are frequently westward (negative) but not as frequently, or as negative, as that seen in Figure 3.26a. The mean transport ($40Sv$) is similar to that seen in the total transport but the range from both components is much smaller ($-20Sv$ to $60Sv$) than the total transport ($-100Sv$ to $100Sv$). This highlights the barotropic

nature of the recirculations and eddies associated with this region. However, the interannual variability of the baroclinic transport is similar to the total transport with the greatest transport seen in the late-1990s followed by a decline over the 2000s. This implies, consistent with observations (Fig. 3.12) that, in the model, density changes in the GS region are important in controlling the overall variability in the transport of the GS on interannual timescales.

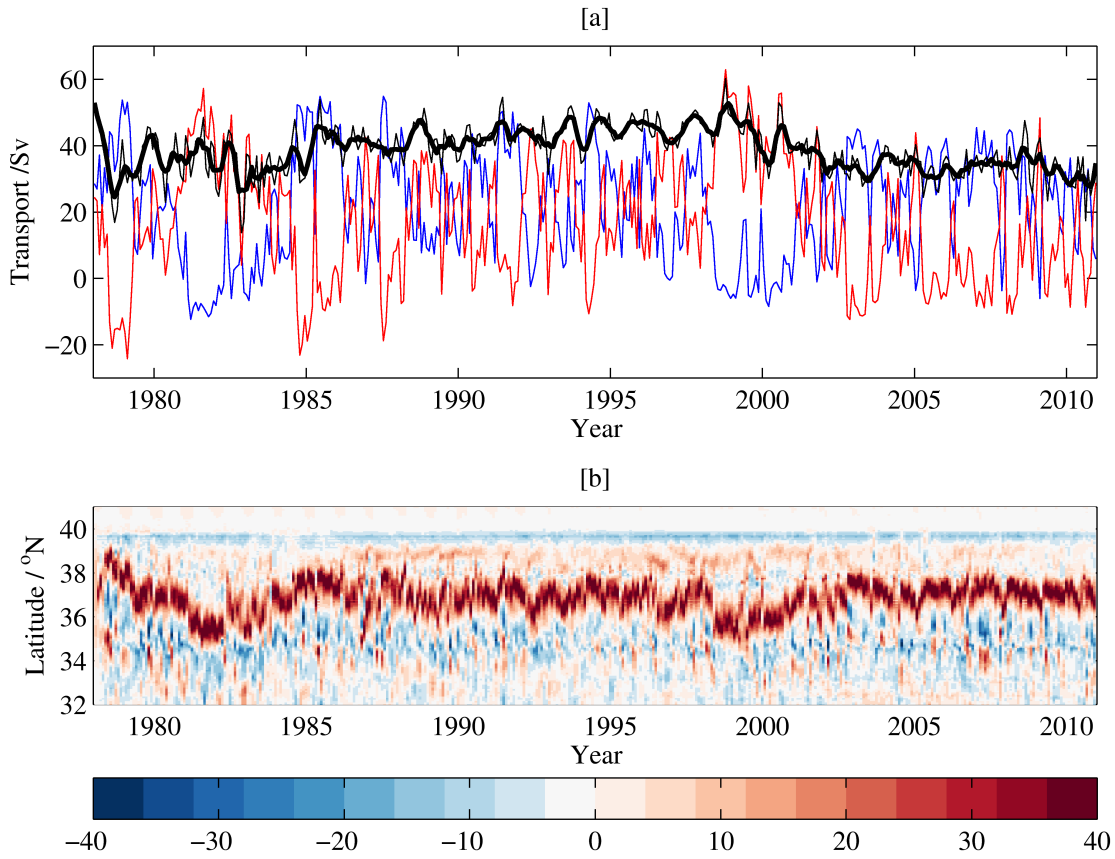

Figure 3.27: [a] Full depth baroclinic transport (Sv) of the GS at 70^oW from$34-38^oN$ (red), $38-42^oN$ (blue) and $34-42^oN$ (black) from 1978-2010 using the ORCA12 hindcast. Smoothed (using a matlab function) baroclinic transport is shown by the bold black line. [b] Full depth transport (Sv) per 1^o (normalised from $1/12^o$) in the GS at 70^oW from $30-42^oN$ from 1978-2010 in ORCA12. Both are calculated using the thermal wind relation after obtaining the density field using temperature and salinity, using the ocean bottom as the depth of no motion.

Specifically, Figure 3.28 reveals that the upper $(0-1000m)$, i.e. where the effects of density changes are most prominent, baroclinic transport is significantly correlated to the upper total transport (r=0.86). This supports the finding that changes in the baroclinic GS transport dominate the changes observed in the total GS transport in the ORCA12 hindcast, which is also true in GODAS (Figure 3.12).

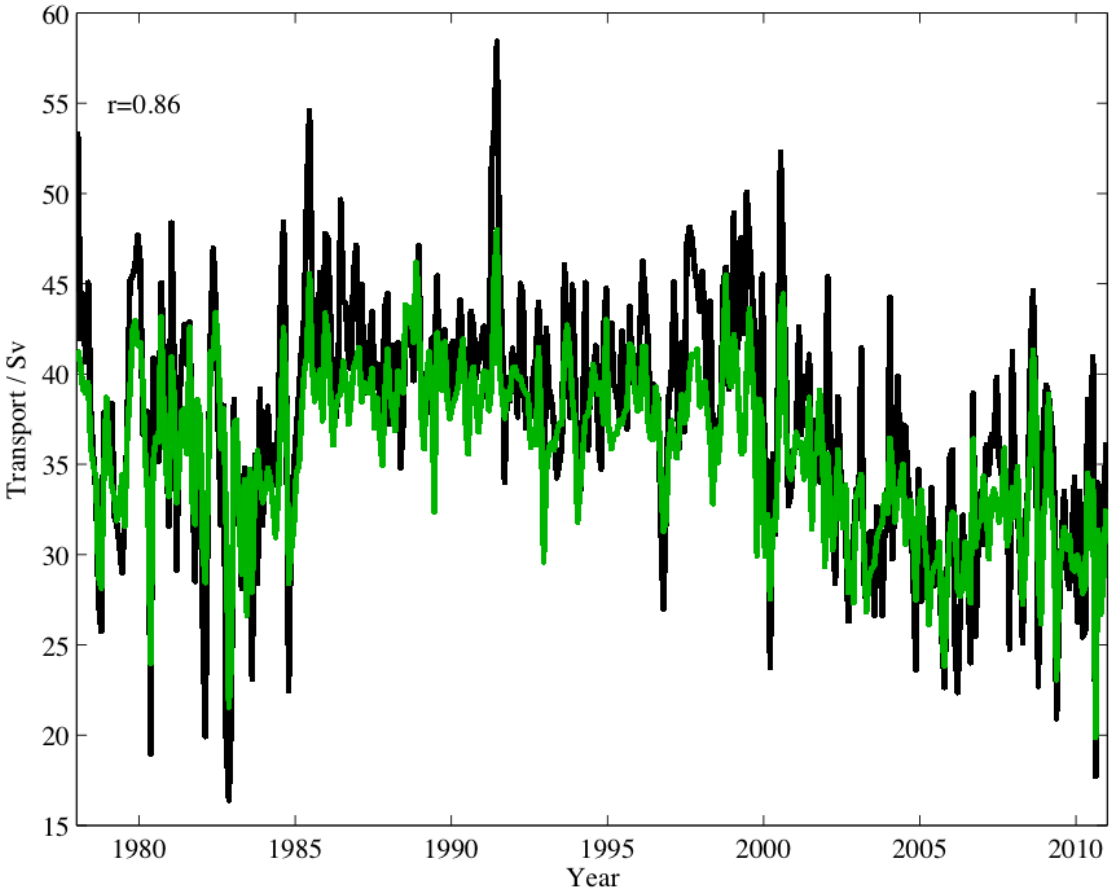

Figure 3.28: Upper $(0-1000m)$ total (black) and baroclinic (green) transport (Sv) of the GS at 70^oW from $34-42^oN$ (black) from 1978-2010 using ORCA12. The correlation coefficient, r, is statistically significant at the 95% confidence interval.

As in section 3.3 and Figure 3.101 the latitude of the maximum baroclinic transport is used to define the location of the GS in ORCA12. The spring average (MAM) is shown alongside the GS position calculated using the model surface 21^oC isotherm (calculated earlier - Figure 3.7) over the same period in Figure 3.29. The two are significantly correlated (r = 0.51) to the 95% confidence interval (obtained using the dof method (*Bretherton et al.*, 1999)) with a more southern GS during the late 1990s and a more northward GS during the 2000s found using each method. This is consistent with that observed in GODAS (section 3.3) and AVHRR (section 3.2). It could also provide a more accurate method to estimate GS path variability in ORCA12 as it eliminates the need to account for temporal variations in temperature.

In addition to the strong recirculation gyres, the high resolution of the ORCA12

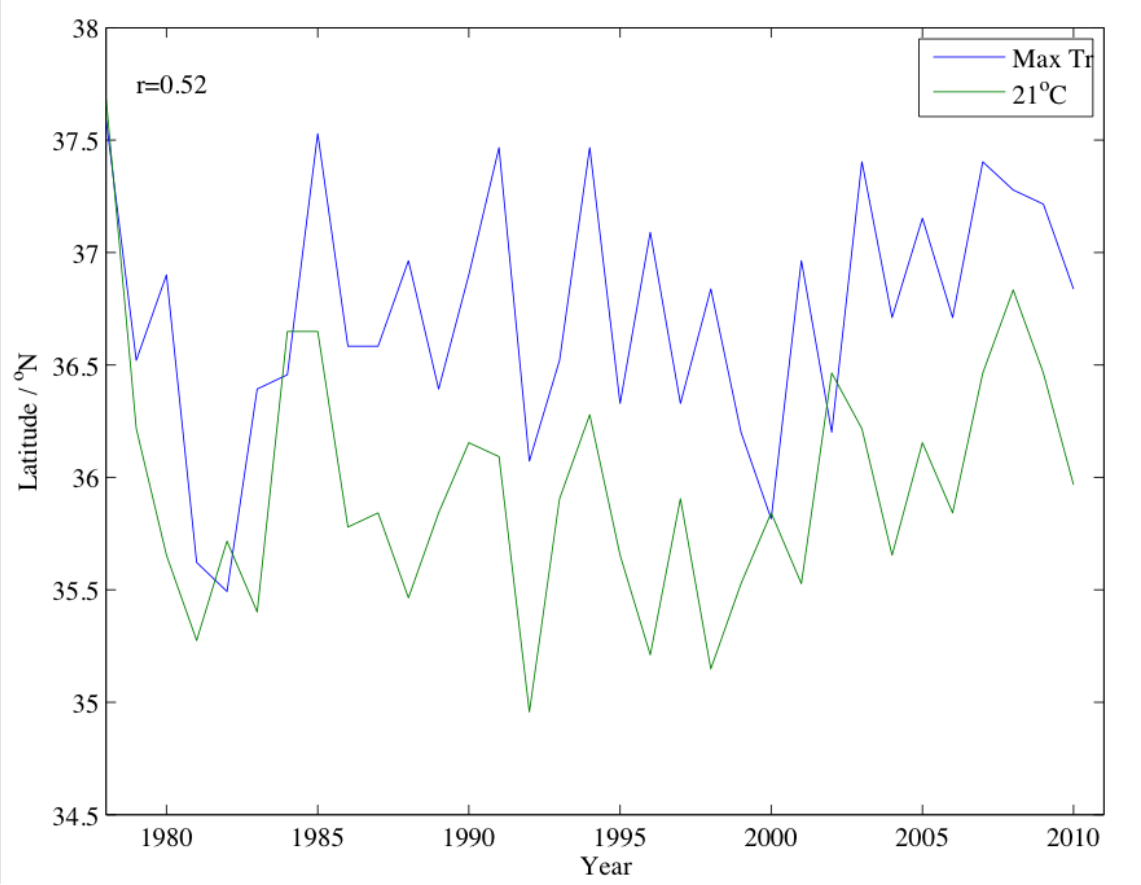

Figure 3.29: Latitude (^oN) of the estimated path of the GS at 70^oW in ORCA12 averaged from April-May from 1978-2010 (Max Tr - using the location of the maximum baroclinic transport) and at 73^oW in ORCA12 using the 21^oC surface isotherm as in Figure 3.7. The correlation coefficient, r, is statistically significant at the 95% confidence interval.

hindcast enables a greater level of mesoscale activity, which leads to a convoluted path along most of the GS. Specifically, the ORCA12 hindcast was found to have larger EKE, on average, further to the west in the GS region compared to that seen in ARGO observations, which use Lagrangian data to estimate EKE (Le Boyer, 2017 - www.sites.google.com/site/arnaudleboyer/home/slope-current-variability-forced-by-mesoscale-turbulence). This illustrates the challenge of accurately measuring GS transport.

In order to assess this further, four different methods are employed to calculate GS transport at 70^oW. Figure 3.30a shows the eastward-only transport at 70^oW from 30^{o}N-coast and Figure 3.30b is the total transport between these locations. A considerable discrepancy exists between the total and eastward-only transports.

A large mean transport of $129 + / - 19Sv$ is found when examining eastward-only velocities, which is greater than the observed mean transport of $40Sv$ in GODAS (Figure 3.8) and $93Sv$ observed by *Halkin and Rossby* (1985). Only considering eastward velocity leads to an overestimate of the transport as the westward return flow of eddies is ignored. However, when taking into account westward velocity, in addition to eastward velocity, the mean total transport is just $7 + / - 10Sv$ (Figure 3.30b), which is unrepresentative of the true GS. In addition to this, the total transport is regularly negative throughout the hindcast, which is also incorrect at this location. This is due to two westward counter-currents on each side of the main GS core, the Slope Water current to the north and the southern recirculation to the south. In particular, the Slope Water current is anomalously strong in the ORCA12 hindcast ($5Sv$ compared to $3.5Sv$ by *Rossby et al.* (2005) as mentioned earlier), which may be causing the negative transport at this location.

In order to eliminate the contributions from these westward flows, latitudinal limits of $34 - 38^oN$ were utilised to calculate the eastward transport (Figure 3.30c) and total transport (Figure 3.30d) of the GS at 70^oW. The mean eastward transport is now reduced to $92 + / - 17Sv$, which is more closely matched to the observations (*Halkin and Rossby*, 1985). However, due to the considerable path shift of the GS the current may not always be confined within the latitudinal limits prescribed here, which could lead to inaccuracies in estimating its transport. Contrastingly, the mean total transport is increased to $23 + / - 17Sv$ when considering the latitudinal limits. This has significantly improved the estimated transport but there are still multiple occurrences of negative transports. Again, this is related to shifts in the GS path, which also affect the location of the westward counter-currents. Overall, the difficulty of defining latitudinal limits makes it nearly impossible to obtain an accurate transport at this location for every month.

Figure 3.31 reveals the total transport (i.e. derived from the zonal velocity field) and the geostrophic transport (i.e. derived from geostrophic balance) of the GS at 70^oW (Figure 3.31a) and 60^oW (Figure 3.31b) in the ORCA12 hindcast using the same method as Figure 3.30a. The residual between the two, i.e. the ageostrophic transport, for each of these longitudes is revealed in Figures 3.31c

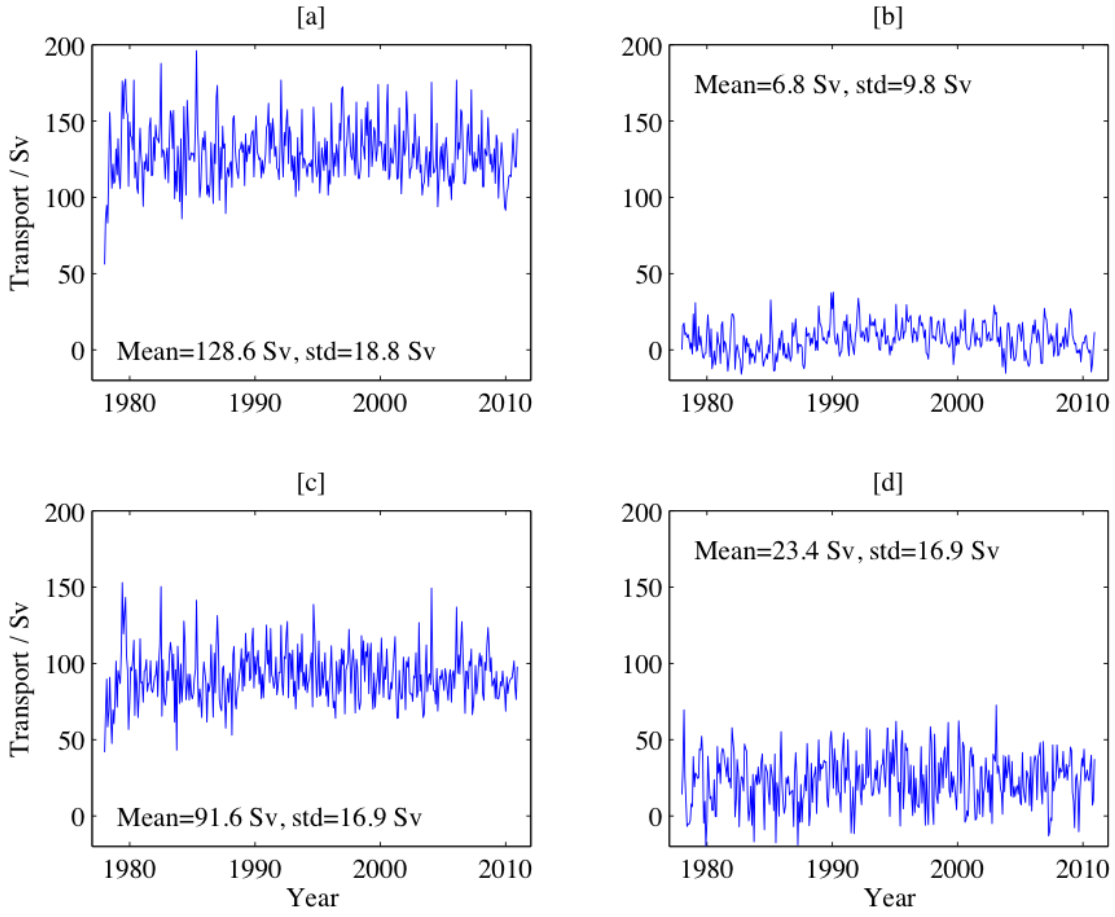

Figure 3.30: Eastward-only geostrophic transport (Sv) of the GS from 30^oN to the coast at 70^oW [a], total geostrophic transport (Sv) of the GS from 30^oN to the coast at 70^oW [b], eastward-only geostrophic transport (Sv) of the GS from $34-38^oN$ at 70^oW [c], total geostrophic transport (Sv) of the GS from $34-38^oN$ at 70^oW [d] in ORCA12 from 1978-2010.

and 3.31d, which is associated with the frictional and inertial terms in momentum balance. At 70^oW, the average transport at this location is much larger than that seen in the observations (Figure 3.8), which is likely due to a larger latitudinal extent ($30-42^oN$ compared to $34-42^oN$) and the finer resolution of the model ($1/12^o$ compared to $1/3^o$). The finer resolution enables eddies and meanders to be properly resolved, which increases the GS transport substantially due to the high level of mesoscale variability in this region (Chapter 1.1). The method used, i.e. eastward-only velocity and from 30°N-coast, will also increase the transport as was found in Figure 3.30. The ageostrophic transport at this location (Figure 3.31d) is primarily negative (westward), which could suggest that the GS is frictionally decelerated near the boundary, but remains within about 10% of the total transport

values.

At 60^oW, the average total transport is slightly larger, $147Sv$, and a greater variability exists over the 33-year hindcast. For example, an increasing transport can be seen from the mid-1980s to the mid-1990s, which is followed by a declining transport since the mid-1990s. This trend is also found by *Curry and McCartney* (2001), but is absent at 70^oW. Additionally, the ageostrophic component is less than that seen at 70^oW, as this longitude is further from frictional influences near the boundary.

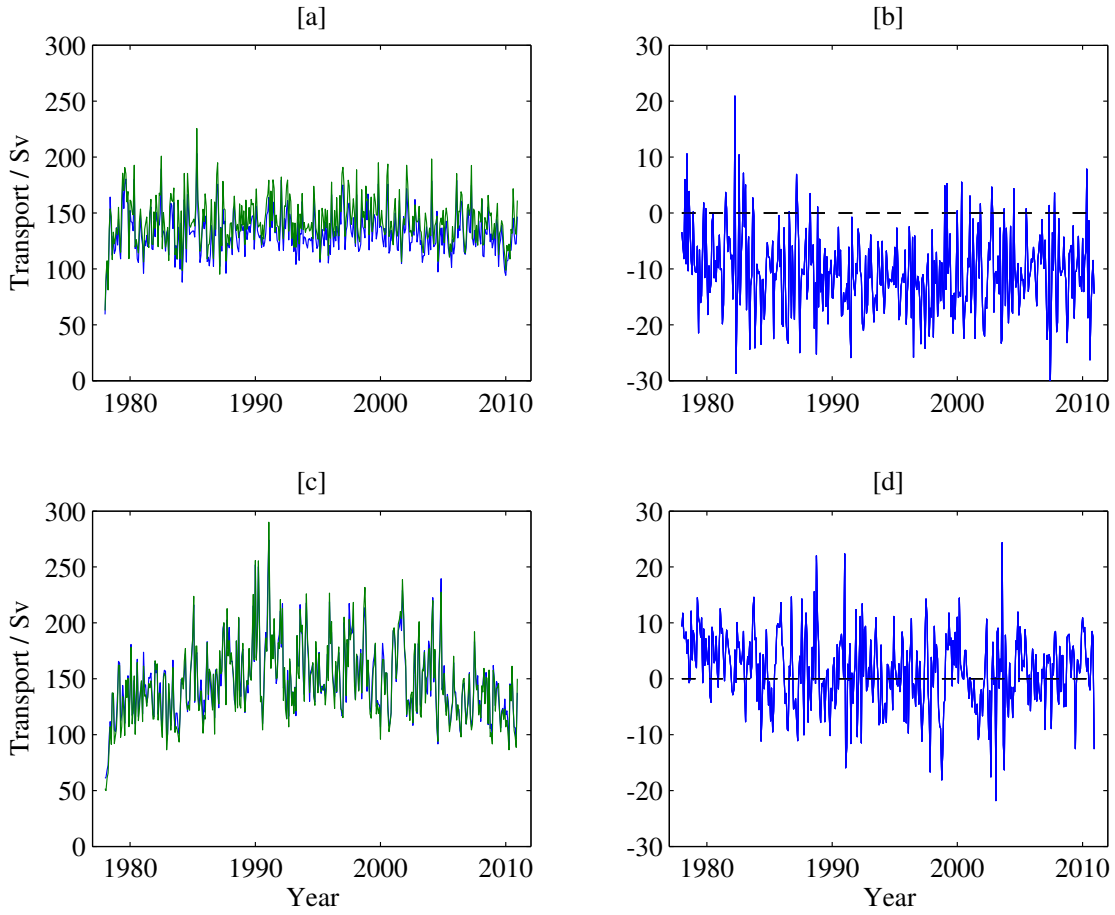

Figure 3.31: Geostrophic transport (Sv) (blue) and total transport (Sv) (green) of the Gulf Stream from 30^oN to the coast at 70^oW [a] and 60^oW [c] in ORCA12 form 1978-2010. The ageostrophic transport (Sv) of the GS, i.e. total minus geostrophic transport, at 70^oW [b] and 60^oW [d] in ORCA12 from 1978-2010.

This section first examined the total and baroclinic transport variability of the GS at 70^oW in the ORCA12 hindcast. The total transport was found to be negative in some months, which was due to strong westward velocities in either the north or south components. This highlights the difficulty in measuring the GS transport in this hindcast as the westward recirculations can dominate on a regular basis. However, the close correspondence between the variability of the baroclinic and total upper transport (r=0.86) implies that density changes are imperative in controlling GS transport changes on interannual timescales. The GS transport at this location was then calculated using four different methods. The eastward-only method yields an average transport much greater than that seen in the observations but using the total transport is anomalously low, and often even negative. This is due to two strong westward counter-currents, i.e. the southern recirculation and the

Slope Water current. However, using latitudinal constraints to try to avoid this is also inaccurate due to the considerable path shift of the GS and its recirculations at this location. The total eastward transport captures all variations in the GS transport and is seen to decrease further downstream, i.e. from $70 - 60^oW$.

3.6 Discussion

The latitudinal path shift and the transport variability of the GS have been investigated using different definitions of the GS in multiple observational products and in a model hindcast. The main findings will each be discussed in turn but the key points are as follows:

1. The 21^{o}C isotherm is a more accurate GS path definition using the annual SST field while the maximum SST gradient is more effective east of 70^{o}W in the monthly SST field in AVHRR and ORCA12. However, there is a poor correspondence between the observed and modelled GS path.

2. The variability of the upper (0-1000m) baroclinic transport is significantly correlated to the total transport variability, in both GODAS and ORCA12, which implies that density changes are imperative in controlling interannual transport variations of the GS at 70^{o}W.

3. Changes in density strongly impacted the dominant baroclinic transport (hence total transport) during the severe winter of 1976/77, whereby a considerable heat loss led to a high STMW formation and the greatest increase of GS baroclinic transport in February from the previous February at 70^{o}W over the period 1970-2014.

4. No major change in baroclinic transport was evident during the severe winter of 2013/14 but a change in the structure of the NAC at 30^{o}W was induced by considerable heat loss over the central SPG.

5. Due to the challenging nature of estimating the GS transport in ORCA12, the eastward-only method with no latitudinal constraints is the only method that captures all GS transport variability at 70^{o}W.

In order to examine the latitudinal variability of the GS, two methods are used to define the GS path at the surface from $75 - 50^oW$; the maximum SST gradient and the 21^oC isotherm. The former was found to capture the GS north wall while the latter better represented the GS core, which led to the maximum SST gradient definition being consistently further north. Additionally, both methods were found further to the south in the ORCA12 hindcast, compared with AVHRR, which may be due to a stronger Slope Water current that is known to lead to a more southern GS position (*Peña-Molino and Joyce*, 2008). In spite of this, there is greater agreement between the model and observations when using the 21^oC isotherm, which could indicate that this is the best method to define the GS when using the annual SST field (Figure 3.6). However, due to the seasonal cycle of SST, the 21^oC isotherm is ineffective at capturing the latitudinal variability of the GS path to the east of about $70 - 65^oW$ in both ORCA12 and AVHRR. Consequently, the maximum SST gradient is the most accurate GS path definition, east of 70^oW, on monthly timescales. Additionally, the pattern of GS shift seen in prior findings, i.e. more northward during the late-1980s and early-1990s (*Taylor and Gangopadhyay*, 2001), is also reproduced here.

The total and baroclinic transport of the GS at 70^oW were calculated from 1980-2015 using GODAS. A period of strong transport is revealed from the mid-1990s, which is followed by a decline since the mid-2000s. This is in agreement with previous studies (*Sato and Rossby*, 1995; *Curry and McCartney*, 2001; *Ezer et al.*, 2013). The investigation of the variability of GS transport from the southern ($34-38^oN$) and northern ($38-42^oN$) components further informs on GS path shift. For example, the majority of the transport comes from the northward component in the early to mid-1990s, providing evidence for a more northern GS (Figure 3.9). This also agrees with prior findings (*Taylor and Gangopadhyay*, 2001; *Kwon et al.*, 2010) and is significantly correlated with findings in AVHRR (Figure 3.11). Once the barotropic transport component is removed, the seasonal cycle disappears, which enables the interannual variability to be examined more easily. The upper ($0 - 1000m$) total transport and baroclinic transport are significantly correlated (Figure 3.12), which provides evidence that much of the GS transport variability is related to upper ocean density changes.

The techniques used to investigate the latitudinal and transport variability of the GS were then utilised to quantify the effects of two severe winters, 1976/77 and 2013/14, on the GS. As discussed in Chapter 1, *Worthington* (1977) put forward the anti-cyclogenesis mechanism as a theory for GS intensification following a winter of intense air-sea fluxes. These fluxes occur when there are widespread CAOs from northeast North America and can induce a considerable heat loss over the Sargasso Sea (*Xue et al.*, 1995; *Kelly et al.*, 2010). During the winter of 1976/77 a series of CAOs led to anomalously deep mixed layers and a high renewal of STMW (*Leetmaa*, 1977; *Worthington*, 1977). This strengthened the cross-stream temperature gradients across the GS at 72^oW, which increased vertical current shear and depth-integrated baroclinic transport in the upper $1000m$ by about 50% (*Worthington*, 1977).

The effects of this severe winter are reaffirmed here with a northward shift of the GS also apparent at 70^oW (Figure 3.15). The series of CAOs were found to cause a strengthened GS transport in the main GS core at 70^oW that was the largest seen for that decade. Furthermore, the increase in transport from the previous winter, 60.5%, was the largest observed over the period 1970-2014, which closely matches the finding of *Worthington* (1977). However, transports of a similar magnitude and other considerable transport increases occurred multiple times from 1980-2014, which could suggest that buoyancy-forced changes of GS transport are frequently substantial. This mechanism will be investigated in the next chapter using the ORCA12 hindcast.

The more recent severe winter of 2013/14 led to extremely cold and snowy conditions in North America (*Palmer*, 2014) and caused the stormiest winter on record in the UK (*Matthews et al.*, 2014). However, the CAOs were found to exit the continent further north than that seen during the winter of 1976/77, which led to an anomalously strong heat loss over the central SPG, notably along 30^oW. This was also confirmed by *Grist et al.* (2016) who found that sensible heat fluxes dominated to the west while latent heat fluxes were strongest in the east. This led to the largest cold anomaly observed in this region since 1986, which instigated a structural change in the NAC at 30^oW (Figure 3.22). The intense Qnet provides

evidence that the low ocean heat content and deep mixed layers found in the eastern SPG were primarily related to air-sea exchange rather than changes in ocean heat transport (*Grist et al.*, 2016). This is a rare event as the latter is known to dominate in this region (*Grist et al.*, 2010; *Robson et al.*, 2012). The lasting effects of this winter are related to the anomalously dense volume of Subpolar Mode Water (SPMW) in this region, persistent through 2014/15 (*Grist et al.*, 2016). This coincided with the largest baroclinic transport in the NAC since 1998 during early 2015 and further work is required to establish a connection between the two.

Before investigating the changes to GS transport induced by air-sea fluxes further, the total and baroclinic transport was calculated at 70^oW in the ORCA12 hindcast. Like that observed in GODAS, the interannual variability in the upper total transport is significantly correlated (r=0.86) to the upper baroclinic transport (Figure 3.28). This further highlights the importance of density changes in setting transport changes in the GS. In order to avoid using a reference level, the availability of the SSH field enables the absolute (barotropic + baroclinic) geostrophic velocity to be calculated. However, the considerable mesoscale variability in the GS at this location, which has been found to be greater than that seen in observations (Le Boyer, 2017 - www.sites.google.com/site/arnaudleboyer/home/slope-current-variability-forced-by-mesoscale-turbulence), and the path shift of the GS and its recirculations lead to difficulty in accurately assessing the GS transport on monthly timescales. Four methods were employed to estimate the total transport of the GS at 70^oW, which include using all and eastward-only velocities and shifting the latitudinal boundaries. The total transport, i.e. from eastward and westward velocities, is often negative due to large contributions from the westward recirculations i.e. the Slope Water current and southern recirculation. The latitudinal shift of these counter-currents, along with the main GS core, also prevents the use of latitudinal constraints when estimating the GS transport at this location. Therefore, the total eastward transport is the method that captures the total GS transport variability and will be used in Chapter 4 to enable a more thorough investigation into the effect of strong buoyancy forcing on GS transport variability.

Chapter 4

The role of air-sea heat fluxes in driving interannual variations of Gulf Stream transport

4.1 Introduction

There is a keen interest in the variability of the GS due to the complex dynamical and thermodynamical interaction between the atmosphere and the ocean in this region (*Kelly et al.*, 2010), which plays a major role in the global redistribution of heat (*Lillibridge and Mariano*, 2012). There is a large sensible and latent heat flux from the GS to the overlying atmosphere in winter, of up to 100 W m^{-2} and 200 W m^{-2} monthly mean values respectively (*Kelly et al.*, 2010), due to the large temperature and humidity difference at the interface (*Minobe et al.*, 2010; *Davis et al.*, 2013). Additionally, the sharp SST front of the GS leads to differential heating and large horizontal gradients in the atmospheric boundary layer, which maintains tropospheric baroclinicity and initiates intense cyclogenesis over the current (*Hoskins and Valdes*, 1990; *Nakamura et al.*, 2004). This enables it to strongly influence the North Atlantic storm track (*Joyce et al.*, 2000; *Brayshaw et al.*, 2011; *Kwon and Joyce*, 2013). However, it can also be argued that the atmospheric boundary layer can weaken the GS front. For example, the cold air mass that provided a strong cooling to the south of the GS during the winter of 1977 (*Worthington*, 1977), see Chapter 3.4, would weaken the front by negative feedback. Due to the second law of thermodynamics, the tendency of the SST front is to weaken so for frontogenesis to occur, a dynamical mechanism is required e.g. Ekman convergence or advection

of temperature by non-linear momentum terms.

In terms of the drivers of interannual variability in the GS, it has been argued that strong air-sea heat fluxes over the GS influence the current itself (*Worthington*, 1977). Evidence for this was found in Chapter 3, where the baroclinic transport variability in the GS at 70^oW was found to vary in close accordance with the total transport, i.e. baroclinic and barotropic components, in both observations and in ORCA12. This implies that density changes are important in controlling the GS transport on interannual timescales and could highlight the importance of buoyancy forcing. However, buoyancy forcing is only one of a number of processes that can change the density structure. For example, the wind will have an influence on the sloping of isopycnals via a change in the wind stress curl. As was explained in the previous chapter, a more negative wind stress curl increases Ekman pumping over this region, which enhances downwelling and acts to deepen the thermocline. In addition to surface forcing, changes in advection, inertial and other ageostrophic flows may also lead to changes in the density structure. Regardless of this, here we highlight the importance of buoyancy forcing in inducing transport variations of the GS.

Strong buoyancy forcing and, subsequently, strong heat losses are often induced during widespread outbreaks of cold, continental air from the northeast of North America extending over the GS region (*Grossman and Betts*, 1990; *Joyce et al.*, 2009; *Kelly et al.*, 2010; *Ma et al.*, 2015). These losses are often the largest seen globally (*Bane and Osgood*, 1989; *Kwon et al.*, 2010) with extreme values sometimes exceeding 1000 W m^{-2} during an outbreak (*Silverthorne and Toole*, 2013). This surface heat loss initiates strong convection in the Sargasso Sea, which can lead to MLDs of up to 500 m (*Buckley et al.*, 2014). Re-stratification then preserves beneath the surface the Eighteen Degree Water (EDW) formed in the early spring (*Leetmaa*, 1977; *Dong and Kelly*, 2004; *Mensa et al.*, 2013; *Silverthorne and Toole*, 2013). This deepening of the mixed layer combined with an increase in meridional temperature gradients across the GS will have a significant influence on its baroclinic transport, given the thermal wind relation (*Leetmaa*, 1977; *Sato and Rossby*, 1995; *Kelly et al.*, 1996; *Dong et al.*, 2007), see Chapter 3.

There is also a view that GS variability is primarily associated with large wintertime air-sea momentum fluxes (*Xue et al.*, 1995; *Xue and Bane Jr*, 1997; *Kelly et al.*, 1999). In particular, the role of wind stress curl variability has been found to be a major factor in driving changes to the transport of the GS (*Anderson and Corry*, 1985; *Hogg and Johns*, 1995; *Kelly et al.*, 1996; *Sturges and Hong*, 2001; *De Coëtlogon et al.*, 2006; *DiNezio et al.*, 2009). For example, a stronger (i.e. more negative) wind stress curl in the STG causes an intensification to the gyre, and therefore the GS (*Chaudhuri et al.*, 2011; *Häkkinen et al.*, 2011). Wind stress curl variability is also closely linked to the NAO with a positive phase of the NAO causing a more negative wind stress curl and stronger GS transport (*DiNezio et al.*, 2009; *Meinen et al.*, 2010). Yet, *De Coëtlogon et al.* (2006) has emphasized that wind forcing cannot be the sole influence on GS transport, which implies that, in addition to unforced basin-scale circulation changes, an important role is also played by buoyancy forcing.

Recognizing the importance of buoyancy forcing for the wider GS system, *Worthington* (1972) proposed a mechanism termed anti-cyclogenesis, whereby the STG is strengthened via a deepening of the thermocline on the southern flank of the GS. The clearest example of anti-cyclogenesis was observed by *Worthington* (1977) after the severe winter of 1976/77, when cold air outbreaks led to large heat losses over the western STG. This led to anomalously deep mixed layers and a high renewal of mode water to the south of the GS, which strengthened the meridional temperature gradients across the current. He found that this increased baroclinic GS transport (relative to $2000m$) by around 50% compared to corresponding transport estimates after the much milder winters of 1974/75 and 1975/76. This was reaffirmed using EN4 in Chapter 3.4.

The effects of winter 1976-77 were also investigated by *Leetmaa* (1977) who revealed a thermocline depth of 800 m at $34^oN, 71^oW$, which is close to where *Worthington* (1977) measured an increase in transport. The extensive renewal of EDW during this winter followed a series of years when EDW formation was anomalously low, coincident with mild winters over northeast North America (*Worthington*, 1977). This severe winter, therefore, caused an increased transport, compared

to the previous decade, of about $40Sv$ (*Worthington*, 1977).

In addition to the strengthening of the main current (of up to 60%) following winter cooling, *Huang* (1990) found an accompanying increase in both the NR and SR (see Figure 4.1) using a two-layer model. In contrast, a study by *Zheng et al.* (1984) proposed that cooling over the Sargasso Sea is not the sole driving force for an increase in GS transport. They suggest that this mechanism is reinforced by the heat loss observed in the Slope Water, i.e. the combination of isotherms upwelling to the north of the GS and downwelling to the south.

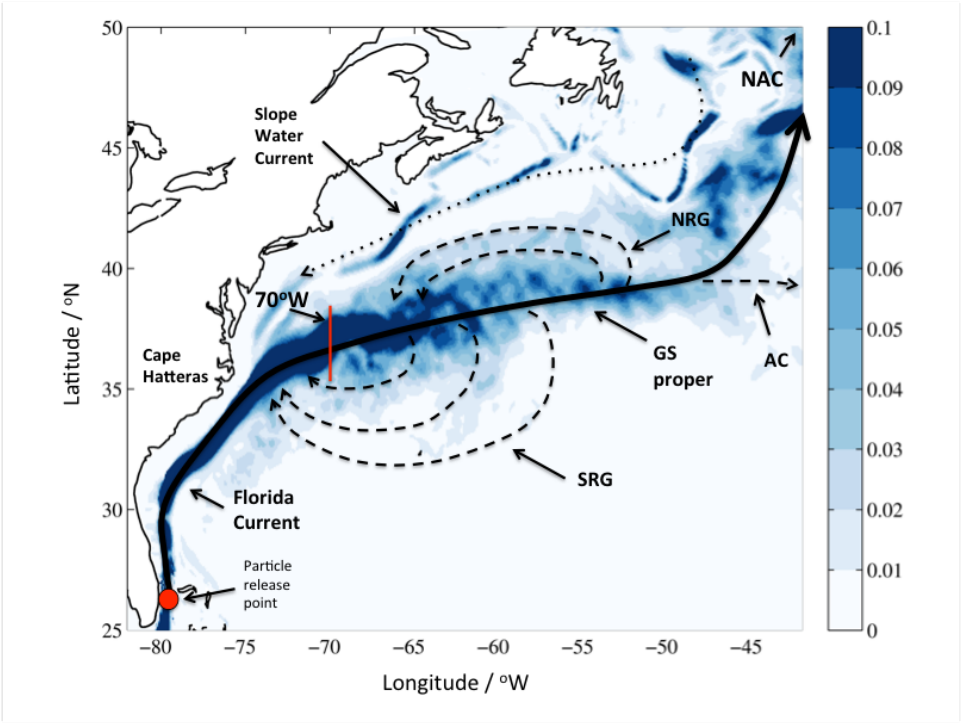

Figure 4.1: Mean surface currents (m s^{-1}) in the Gulf Stream region from ORCA12 simulation in April over the period 1978-2010. The bold black line denotes the estimated GS path before becoming the North Atlantic Current further northeast, the dashed black lines represent part of the Southern Recirculation, the Northern Circulation and the Azores Current, and the dotted line estimates the position of the slope water current. The red circle is where particles are released in the Lagrangian experiments and the red line marks 70^oW.

This chapter will explore the extent to which winter surface heat fluxes have led to spring GS intensification over the last three decades and in particular to examine the contributions coming from the north, (*Zheng et al.*, 1984), and from the south, (*Worthington*, 1977), of the GS core. Here, it is the full-depth geostrophic

transport that is calculated, which follows on from Chapter 3.5, in order to quantify the importance of the SSH gradient and the three-dimensional pressure gradient. The analysis is conducted using the high resolution ORCA12 hindcast over the period 1978-2010. With continuous high-resolution coverage in both time and space, multi-timescale GS variability is more realistic than previously available in historical observations or coarser resolution models. This permits a more thorough investigation of GS forcing mechanisms. The model and diagnostic techniques are outlined in Chapter 2.4 and here, findings are presented that highlight the relative importance of mechanisms outlined above (*Worthington* (1977); *Zheng et al.* (1984) and *Huang* (1990)).

4.2 Results

4.2.1 Geostrophic transport variability

The geostrophic currents of the GS at 70^{o}W are calculated in the same way as Chapter 3.5 (outlined in Chapter 2.3.2 and equations 2.4-2.7). Interannual variability of GS geostrophic transport in April at this longitude is evident in Figure 4.2a. April is chosen as this is when the winter heat flux leaves its imprint on the thermal structure of the ocean, i.e. after the accumulated winter buoyancy forcing. After this, the imprint is progressively eroded by restratification. Excluding 1978, the range in April transport exceeds 70 Sv with a maximum of 175 Sv in 2007 and a minimum of 105 Sv in 1993. This variability is of the same order as observed by *Worthington* (1977), who found a range of about 40 Sv in the early-mid 1970s. The large absolute transport values in Figure 4.2a are due to selective use of eastward velocities - see Eqn. 2.7. Much of the eastward transport is in fact compensated by westward transport in energetic mesoscale eddies. However, the eastward-only velocities were found to be most effective in capturing GS transport variability due to the existence of strong westward counter-currents (Chapter 3.5).

The five years of greatest (weakest) transports are marked in red (blue) in Figure 4.2a and will henceforth be referred to as strong (weak) years, see Table 4.1. Figure 4.2b shows the increase or decrease in geostrophic transport between consec-

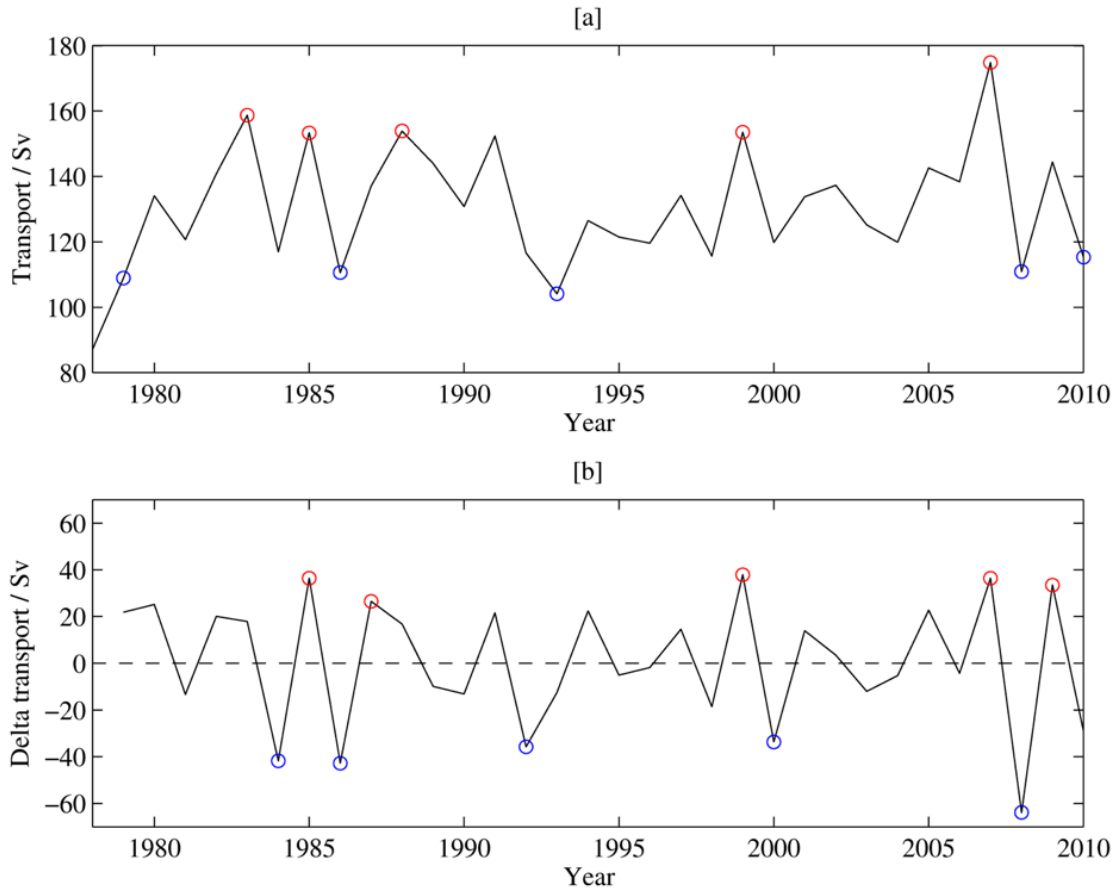

Figure 4.2: [a] Total eastward geostrophic transport of the Gulf Stream at 70^oW in April from 1978-2010 in ORCA12 with red markers representing the five largest transports modelled in this period and the blue markers representing the five lowest transports modelled in this period and [b] year-to-year changes of the geostrophic transport (measured in [a]) referred to as delta transport i.e. $T = Ti - Ti^{-1}$, where T is the transport and i is the year). Here the red markers represent the five highest increases in transport from the previous year and the blue markers represent the five highest decreases in transport from the previous year.

utive Aprils, i.e. April(year) minus April(year-1). The greatest increases/decreases in transport are $+40Sv$ over 1984-85 (about 35%) and -$60Sv$ (about 38%) over 2007-08. As in Figure 4.2a, red (blue) markers represent years of largest increase (decrease) in transport from the previous year, which are subsequently referred to as strengthened (weakened) years, see Table 4.1. Transport variability was also examined in March and May (not shown) with increased/decreased transport in strengthened/weakened years (April) also accompanied by increases/decreases in March and/or May in 8/10 years. Furthermore, Figure 4.3 shows the mean Qnet averaged over the winter (JFM), extended winter (DJFMA) and annually. It shows

that the winter Qnet is representative of interannual variability with the greatest average heat losses occurring from January-March. This implies that the index selected to define the winter Qnet is not sensitive to a potential shift in the seasonal cycle and that April is a logical month to analyse GS transport changes associated with winter forcing.

Table 4.1: List of strong, weak, strengthened and weakened years, defined in section 4.2.1

Strong years	Weak years	Strengthened years	Weakened years
1983	1979	1985	1984
1985	1986	1987	1986
1988	1993	1999	1992
1999	2008	2007	2000
2007	2010	2009	2008

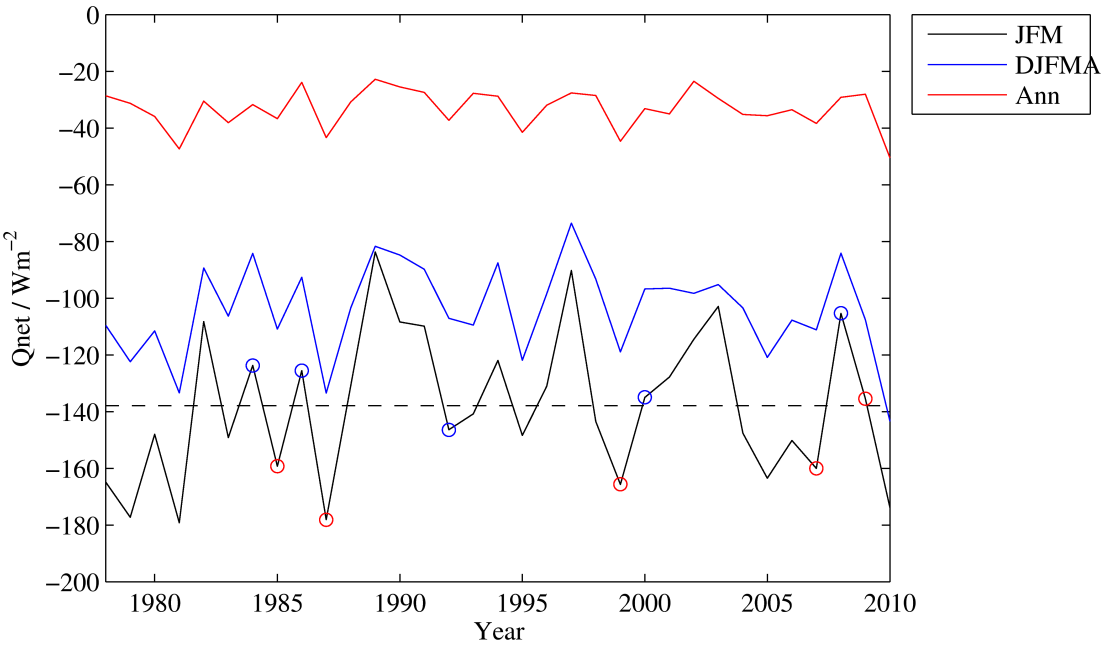

Figure 4.3: Mean surface heat flux (Qnet) from January-March (JFM - black), from December-April (DJFMA - blue) and as an annual average (Ann - red) over a region from $25-35^{o}$N and coast to 50^{o} from 1978-2010 in the ORCA12 run. The dashed black line represents the mean winter (JFM) Qnet.

As outlined in Chapter 2.4.3, two components are required to calculate GS transport; the SSH and the three-dimensional pressure gradient. The SSH slopes down from south to north, inducing a large eastward GS transport. This is opposed by the pressure gradient that is controlled by isopycnals sloping upwards from

south to north, which acts to reduce the large eastward transport relative to the surface flow. These two components are difficult to separate as changes in the water column's pressure, and therefore density, gradients will induce changes in its steric height, which will also cause a change in the SSH. In order to establish how much GS geostrophic transport variability (in Figure 4.2a) is due to density changes, i.e. changes in the three-dimensional pressure field, the steric height of the water column is calculated and is used as a proxy for SSH. The model SSH includes changes in the barotropic component, i.e. due to convergence from changes in the wind stress and other minor processes, and changes in the baroclinic component, i.e. thermal expansion/contraction due to changes in the temperature of the water column. The SSH proxy is used to calculate the geostrophic transport (see Chapter 2.4), which is compared to the original geostrophic transport, i.e. using the model SSH. If the new transport (using proxy SSH) is similar to the original transport (using model SSH) this proves that the majority of the transport change from year-to-year is due to density changes, i.e. changes to the steric height of the water column. The geostrophic GS transport is calculated at each latitude from $30 - 37.5^o$N along 70^oW, using the proxy and real transports, in April from 1978-2010. The correlation coefficient (r) between the two transports as a function of latitude, from $30 - 37.5^oN$, is shown in Figure 4.4a. It reveals that a positive correlation, which is statistically significant (not shown), exists at every latitude. This confirms that the SSH, and therefore the geostrophic transport, along 70^oW is mostly explained by the steric changes associated with density with only a minor role being played by processes such as convergence/divergence of mass associated with wind stress variability that induce changes in the barotropic flow. The mean GS transport and mean delta transport, from 34.75^o-36^oN, calculated using both methods are shown in Figures 4.4b and 4.4c. This region is the location of the main GS core and has a mean correlation of 0.71. The transports are of the same order of magnitude with both methods exhibiting a similar pattern of interannual variability. This further emphasises that changes in the model SSH are mostly explained by steric changes in the water column.

Additionally, the total change (from the previous year) in eastward transport (as in Figure 4.2b) using the SSH proxy is calculated along 70^oW from 1978-2010.

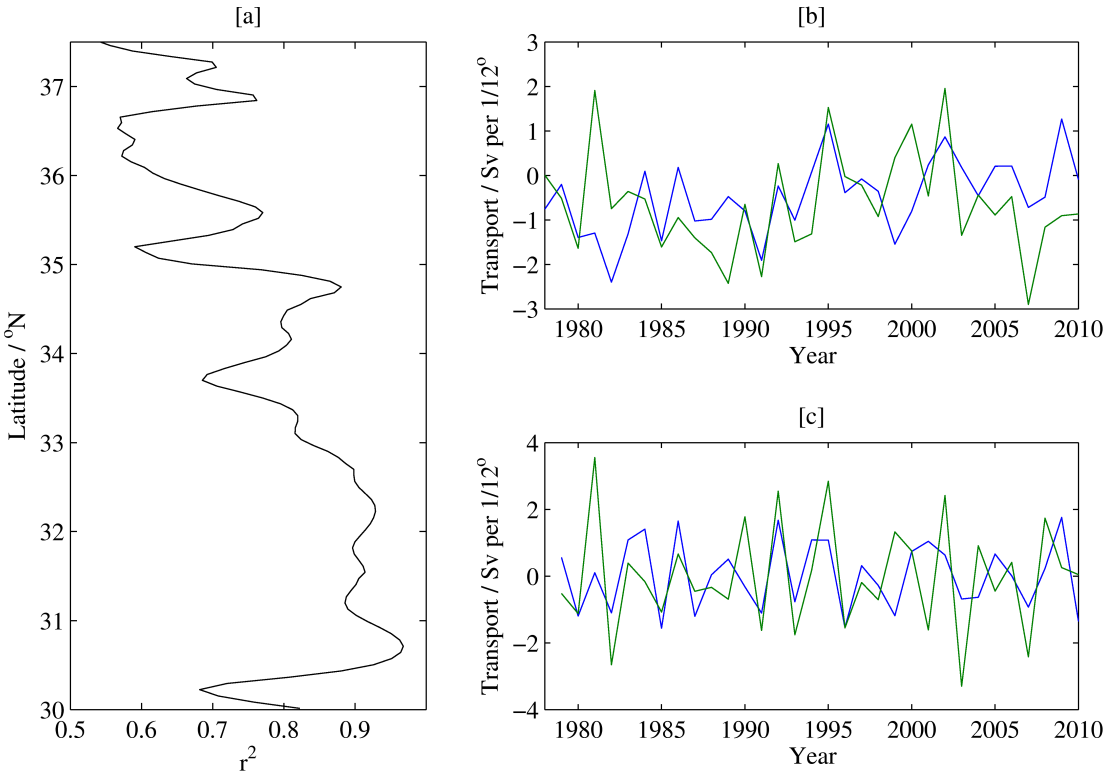

Figure 4.4: Correlation coefficient (r) of the two GS geostrophic transport calculations (i.e. using SSH and the steric height as an SSH proxy) at each latitude from $30 - 37.5^{o}N$ along 70^{o}W [a], mean GS geostrophic transport per $1/12^{o}$ from 34.5-36^{o}N [b] and the year-to-year change in this transport [c] using the model SSH (green) and the SSH proxy (blue) using the ORCA12 hindcast in April from 1978-2010.

This is shown as a percentage of the original method (using model SSH) in Figure 4.5, i.e. (proxy transport change / real transport change) * 100. The variation between about 40 to 140% is likely due to differences outside of the main GS region as the interannual variability in delta transport was found to be similar between the two methods from 34.75^{o}-36^{o}N (Figure 4.4c). Despite this, taking the average across the timeseries, it reveals that more than 88% of the transport changes are due to changes in the density gradient, i.e. most of the SSH changes are explained by steric changes associated with density. This means that if you take any year at random, it is expected that more than 88% of the eastward transport change between that year and the next is because of the density gradient change. Additionally, for the westward transport changes (not shown), the mean for the timeseries is more than 86%. This confirms that the majority of the interannual variability in GS transport at 70^{o}W, in April, is due to density changes in the

water column. This is consistent with findings in Chapter 3, i.e. total transport is significantly correlated with baroclinic transport in the upper 1000m (Figure 3.28). These density changes could be due to strong winter heat losses, which occur during severe winters (*Worthington*, 1977), and are investigated in relation to geostrophic transport changes in the next section.

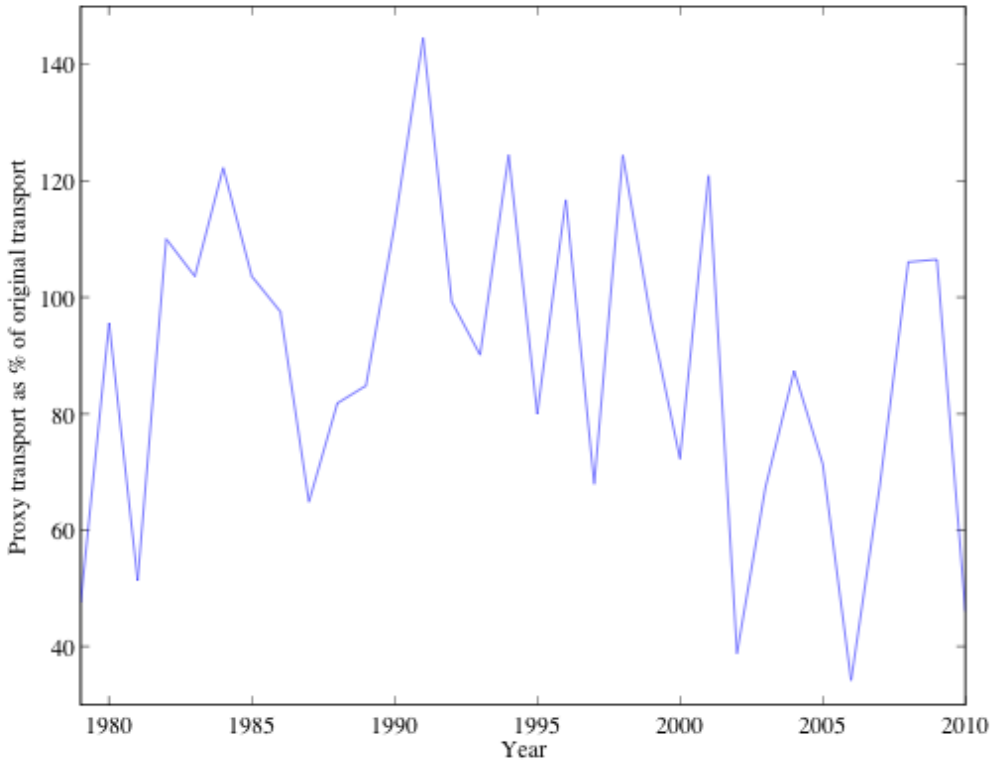

Figure 4.5: The proxy eastward transport change (using the SSH proxy) as a % of the true eastward transport change (using the model SSH) from the previous year along 70^oW in April from 1978-2010 in ORCA12.

4.2.2 Surface Heat Flux and Mixed Layer Depth

Figure 4.6a shows the mean winter Qnet from 1978-2010 in the ORCA12 hindcast, which reveals large heat losses over the GS region. Figure 4.6b is a composite of the winter Qnet for the strong years minus the weak years (defined in Chapter 4.2.1). A negative anomaly of up to -50 W m^{-2} is seen to the south of the GS from $72 - 55^oW$, which indicates that a larger heat loss has occurred in this region in the winters preceding the years of strong GS transport compared to the years of, relatively, weak GS transport. It should be noted that if an anomalous Qnet

over the course of a given year significantly changes the thermal structure (and thus transport) across the GS, then the Qnet will change the structure from that existing at the beginning of the year, (rather than some mean state). Consequently, as well as examining composites of strong versus weak transport years we also examine composites of the greatest strengthened minus the greatest weakened years. This is consistent with the analysis of (*Worthington*, 1977) who noted that the severe winter of 1976/77 led to an increase in transport (50%) relative to an earlier winter. This increased transport was also reproduced in Chapter 3.4 using EN4.

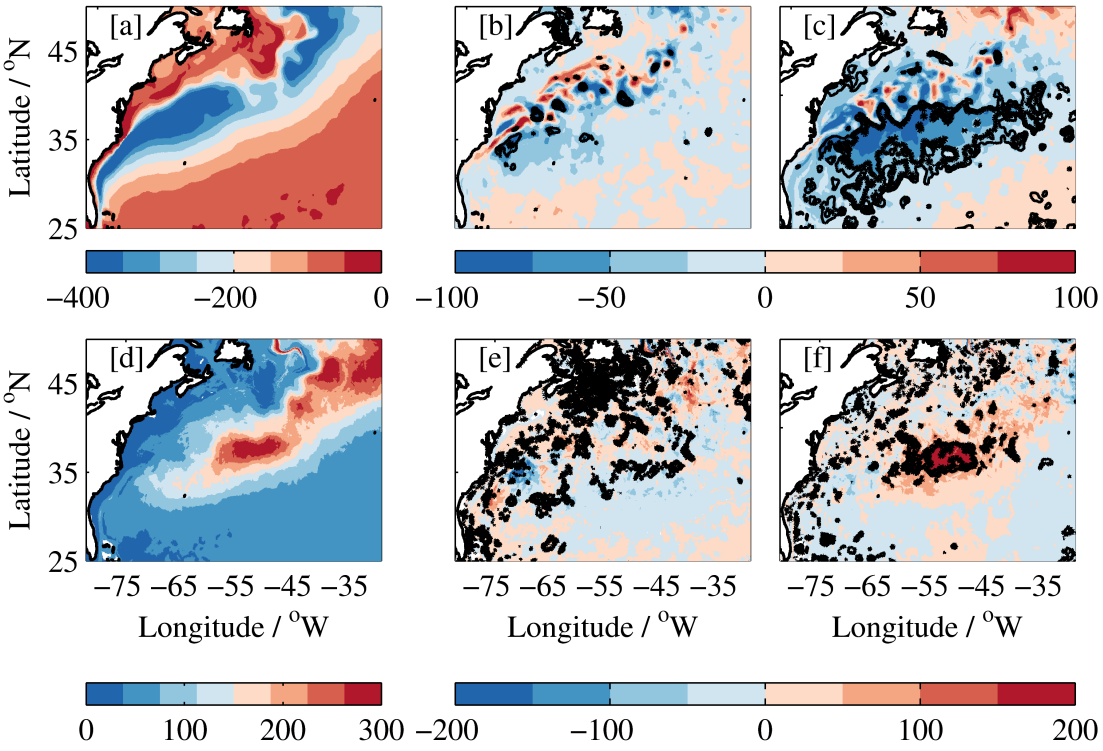

Figure 4.6: Mean winter (JFM) surface heat flux (W m^{-2}) [a], winter surface heat flux composite for the strong minus weak years [b] and the strengthened minus weakened years [c] of the ORCA12 run, the mean April mixed layer depth (m) [d], April MLD composite for the strong minus weak years [e], and the strengthened minus weakened years [f]. Black contours denote the $90-95\%$ confidence intervals.

The Qnet composite for strengthened minus weakened years (Figure 4.6c) reveals a larger, i.e. more negative, Qnet anomaly that covers the entire western STG region. Monte Carlo analysis was undertaken to quantify the statistical significance of this result by calculating 10,000 random composite anomalies, i.e. finding the anomaly between 2 sets of average Qnet over 5 random years (from 1978-2010). The significance of the actual composite anomaly (strengthened minus weakened

years) is then determined by defining the 90% and 95% confidence intervals. This method will be used throughout the rest of the chapter.

Much of this Qnet anomaly is statistically significant with the greatest heat loss, i.e. in the years of greatest transport increase, occurring in a region immediately to the south of the GS path with values of more than -100 W m^{-2}. The fact that the relationship is stronger when focusing on the change in transport for consecutive years highlights the importance of the pre-existing ocean state that the buoyancy flux acts upon. It also reaffirms the findings in Chapter 3.4 and by *Worthington* (1977). Additionally, Figure 4.3 reveals that an anomalous Qnet anomaly exists in 4/5 strengthened years with a positive Qnet anomaly in 4/5 weakening years.

The mean April MLD from 1978-2010 in ORCA12 is also shown in Figure 4.6d, which indicates that deep mixed layers exist in a region to the south of the GS from about $60 - 45^oW$. This is the site for EDW formation and is susceptible to deep mixed layers as this is where the 18^oC isotherm outcrops at the surface during late winter/early spring (*Joyce et al.*, 2000). The composite for the strong minus weak years, shown in Figure 4.6e, reveals patches of positive anomalies (deepening) of up to $100m$ in the Sargasso Sea from $75 - 40^oW$. However, there is a lack of any coherent anomaly pattern. In contrast, a statistically significant positive anomaly of more than $200m$, corresponding to mixed layer deepening, can be seen in Figure 4.6f, which is a MLD composite of the strengthened minus weakened years. This deepening is centred on a region further east, i.e. from $30 - 40^oN$, $64 - 40^oW$, which is the main site for EDW formation. The deeper mixing that is taking place in this region in years of strengthened GS transport leads to MLDs more than 200 m deeper than in years of weakened GS transport. Again, this implies that the pre-winter ocean condition influences how much anomalously strong surface heat fluxes deepen the MLD and strengthen geostrophic transport in the upper ocean. Furthermore, the composites showing the change in Qnet or MLD from the previous year (not shown) reveal greater anomalies but still covering the same area.

Following Worthington's anti-cyclogenesis mechanism, deepening of the mixed layer during strengthened years is expected near 70^oW. However, an asymmetric

dipole exists with MLD deepening in strengthened years occurring further east, as discussed above, and a smaller MLD shoaling in the west. This agrees with *Qiu and Huang* (1995), who found that winter mixed layers were generally shallower than $200m$ to the west of 60^oW. A possible explanation is that there is an increased upper ocean heat content through heat advection by the GS, leading to early re-stratification. This could cause deeper mixed layers to be capped further to the west (*Dong and Kelly*, 2004; *Dong et al.*, 2007) and implies that the oceanic impact of severe winters can be damped by an elevated ocean heat content. The correlation between heat loss and MLD properties may thus break down, which is commonly found to occur further west (*Warren*, 1972; *Talley and Raymer*, 1982; *Yasuda and Hanawa*, 1997; *Dong et al.*, 2007). In order to examine this further, selected temperature profiles will be examined in the next section.

4.2.3 Temperature Variability

Stronger, more significant relationships have been found between MLD, Qnet and transport in strengthened/weakened years (as opposed to strong/weak years), so we hereafter examine only these years. This is due to expectations that the Qnet will change the thermal structure from that at the previous end-of-winter state to the current end-of-winter state, as mentioned in the previous section. Figure 4.7a is a composite of the meridional temperature section along 70^oW in April for the strengthened years minus the weakened years with the corresponding mean field revealed in Figure 4.7c. In order to avoid spurious temperature anomalies associated with the shift in the GS path and associated mesoscale variability, the composite is calculated relative to the GS core in each month, which is defined as the latitude of the maximum surface velocity at 70^oW.

In the difference between strengthened and weakened years, a cold anomaly with values of up to -4^oC is revealed to the north of the GS core in the Slope Water and a smaller, but still significant, negative anomaly of up to -3^oC is seen to the south of the GS core at depths greater than $300m$. This signal is symmetric for the two cases, i.e. with respect to the climatological mean, a warm anomaly during the weakened years and a cold anomaly for the strengthened years (not shown). A

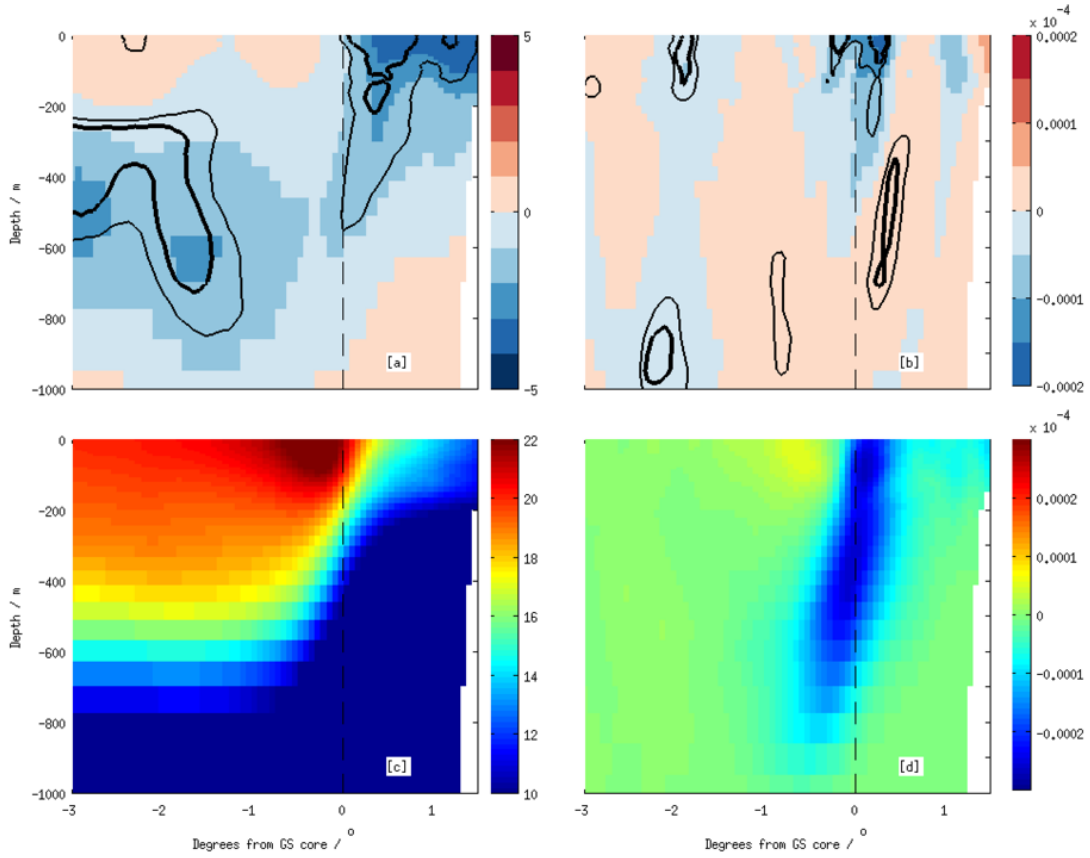

Figure 4.7: Composited differences (strengthened minus weakened years) in a) April temperature (^oC) and b) April meridional temperature gradient (^{o}C m^{-1}), both calculated relative to the Gulf Stream core (here defined as the location of the maximum surface velocity) along 70^oW of the ORCA12 run. Black contours denote the $90-95\%$ confidence intervals and straight dashed line represents the location of the core of the Gulf Stream. c) Mean April temperature (^oC) and d) mean April meridional temperature gradient (^{o}C m^{-1}) also calculated relative to the Gulf Stream core, along 70^oW in the ORCA12 hindcast for the period 1980-2010.

warm anomaly of up to 1^oC is also found in the upper ($200m$) region of the Sargasso Sea between 0.4^o and 3.0^o south of the GS core. This implies that when the GS transport is intensified relative to the previous year, there is large heat loss to the north (cold anomaly), which suggests that the warmer isotherms outcrop further to the south in these years (see the mean field in Figure 4.7c). In addition to this, there is also a, potentially, deep mixed layer to the south (cold anomaly) that appears to be capped by a layer of slightly warmer water (warm anomaly). This capping seen to the south could be due to heat advection processes as suggested by *Dong et al.* (2007). Further investigation of the evolution of the vertical temperature

profiles at 34^oN, 70^oW between September 1986 and April 1987 (a strengthened year) supports this (Figure 4.8a). The most uniform temperature profile can be seen in February, with considerable re-stratification occurring by April, when warm advection is likely causing capped mixed layers to occur further west. In contrast to 70^{o}W, mixed conditions persist late into spring further to the east at 54^oW in Figure 4.8b.

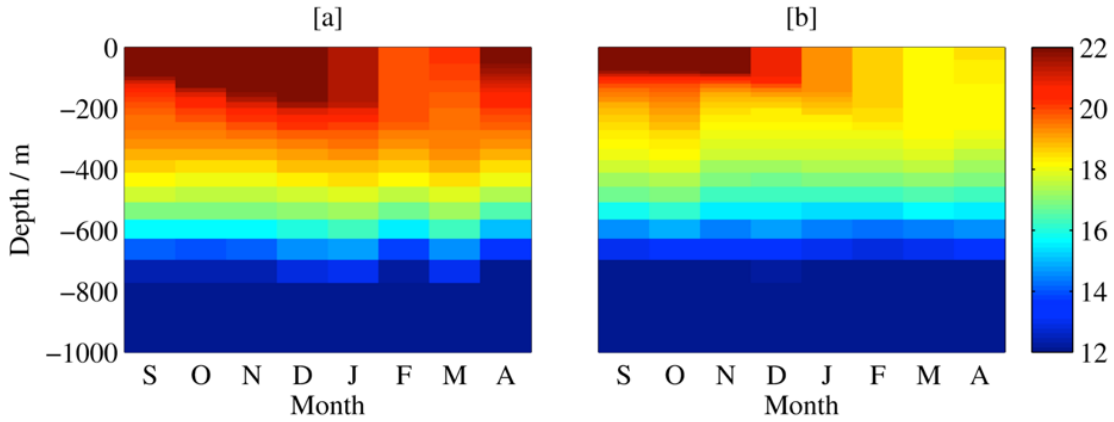

Figure 4.8: Temperature profiles (^oC) at 34^oN from September 1986 to April 1987 (a strengthened year) at 70^oW in the ORCA12 run [a] and 54^oW [b].

The changes in the temperature structure could be either associated with the anomalous Qnet (Fig. 4.6c) or anomalous ocean heat transport convergence. For example, using observations from the 1992-1999 period, *Dong et al.* (2007) conclude that OHT rather than surface fluxes determine the thermal structure of the region's upper ocean. This question is investigated by calculating the anomalous heat flux into the upper ocean from both components over the 12 months leading up to the April of the 5 strengthened years. This calculation has been carried out for a) the region of cooling down to $1000m$ south of the GS and b) the cooling region in the top $400m$ north of the GS (Table 4.2). South of the GS, in the mean, strengthened years are preceded by net cooling from surface fluxes and warming from OHT convergence. This implies that it is the surface heat fluxes rather than the OHT convergence that contribute to the low temperature to the south of the GS. However, we note one strengthened year in particular, 1999, where anomalous OHT convergence acted strongly to cool the region (and in general the anomalies are less than a standard deviation from the mean). In spite of this,

on average, the OHT acted to warm the southern box during the strengthened years, which supports the argument that these years are sometimes characterised by warm advection that caps the mixed layer. Immediately north of the GS, anomalous ocean heat transport convergence can either act to warm or cool the top $400m$ in each of the strengthened years. However, in the mean the average effect in strengthened years is to warm this region while the mean effect of the anomalous surface fluxes is to cool.

Table 4.2: Anomalous heat flux and ocean heat transport convergence (J) (top) and the standard deviation (bottom) in the 12 months leading up to the April of a strengthened year. Positive values imply anomalous heat flux into the boxes. The Southern box is 70.5^oW to 56.7^oW and 34^o to 36^oN, for the surface to $1000m$. The northern box encompasses north of 38^oN and west of 56.7^oW for the upper $400m$. The western and northern boundaries being the US coast.

	S Box OHT conv.	S box Qnet	N Box OHT conv.	N box Qnet
Anomaly	9.7×10^{19} J	-6.7×10^{19} J	2.0×10^{19} J	-1.1×10^{19} J
Std dev	8.8×10^{20} J	$1.4 \times 10^{20} J$	4.4×10^{20} J	7.3×10^{19} J

The composite of the differences in meridional temperature gradients along 70^oW (also relative to the GS core) in April, for strengthened years minus the weakened years, is shown in Figure 4.7b, with the corresponding mean field displayed in Figure 4.7d. A positive difference is associated with increasing temperature to the north and vice versa. Figure 4.7d illustrates the negative temperature gradients on the northern flank of the GS above $400m$ and on the southern flank of the GS from $400 - 900m$. In Figure 4.7b, a negative anomaly is apparent on the northern flank of the GS to depths of $600m$ with the greatest difference occurring in the top $200m$. This suggests that during years of increased transport, from the previous April, there is a steepening of the meridional temperature gradients across the GS core but predominantly on the northern flank due to more southward outcropping of warm isotherms (Figure 4.7c), which could have led to the intensified GS at 70^oW.

This agrees with findings of *Zheng et al.* (1984), who observed that heat loss in the Slope Water causes an uplift of isotherms that outcrop further south and cause an increase in the baroclinic transport. A similar situation was also found by *Dong et al.* (2007), identifying that years with a high transport are associated with

strong thermal wind shear across the current. They also suggest that a warming on the southern flank of the GS could correspond to a strengthened upper southern recirculation. This will be investigated in the following section and may provide a link between the deeper mixed layers found further east and the strengthened GS seen at 70^oW.

In contrast, deepening of the mixed layer during strengthened years (observed in Figure 4.6f) suggests a response in the horizontal temperature gradient further to the east, near 54^oW, which is similar to that observed by (*Worthington*, 1977). At this longitude, the GS no longer has a narrow core and there is greater occurrence of mesoscale activity (*Krauss et al.*, 1990), which makes it difficult to account for latitudinal path shift when examining the temperature and temperature gradients. In spite of this, Figure 4.9 reveals anomalies for both these variables at 54^oW, i.e. centred on the MLD anomaly in Figure 4.6f. A sharper uplift of the isotherms is visible in the GS from about 200-500m during the strengthened years (Figure 4.9a) compared to the weakened years (Figure 4.9c), which has led to the cold anomaly seen in Figure 4.9e throughout the mean GS path. The location of the GS core during each set of years is very similar (except that it extends to a greater depth during the strengthened years), which confirms that this anomaly is related to changes in the isotherms as opposed to a lateral path shift. The greater uplift of isotherms also caused greater meridional temperature gradients in the GS core during the strengthened years (Figure 4.9b), leading to the negative anomaly visible from 37-38^{o}N (Figure 4.9f). The strengthened temperature gradients at depth at 54^oW is consistent with a response to the south similar to that found by *Worthington* (1977), which contrasts with a response to the north at 70^oW, which is more like that found by *Zheng et al.* (1984) (see section 4.1).

In addition to this, we calculate the mean planetary PV in a region to the south of the GS along 54^oW (where deep mixed layers exist), which is shown in Figure 4.10a. PV minima are found in the region to the immediate south of the GS, which is associated with deep mixed layers (Figure 4.6f). The corresponding composite of this (i.e. strengthened minus weakened years) is shown in Figure 4.10b. It reveals that, during the strengthened years, in April (when the upper ocean is re-

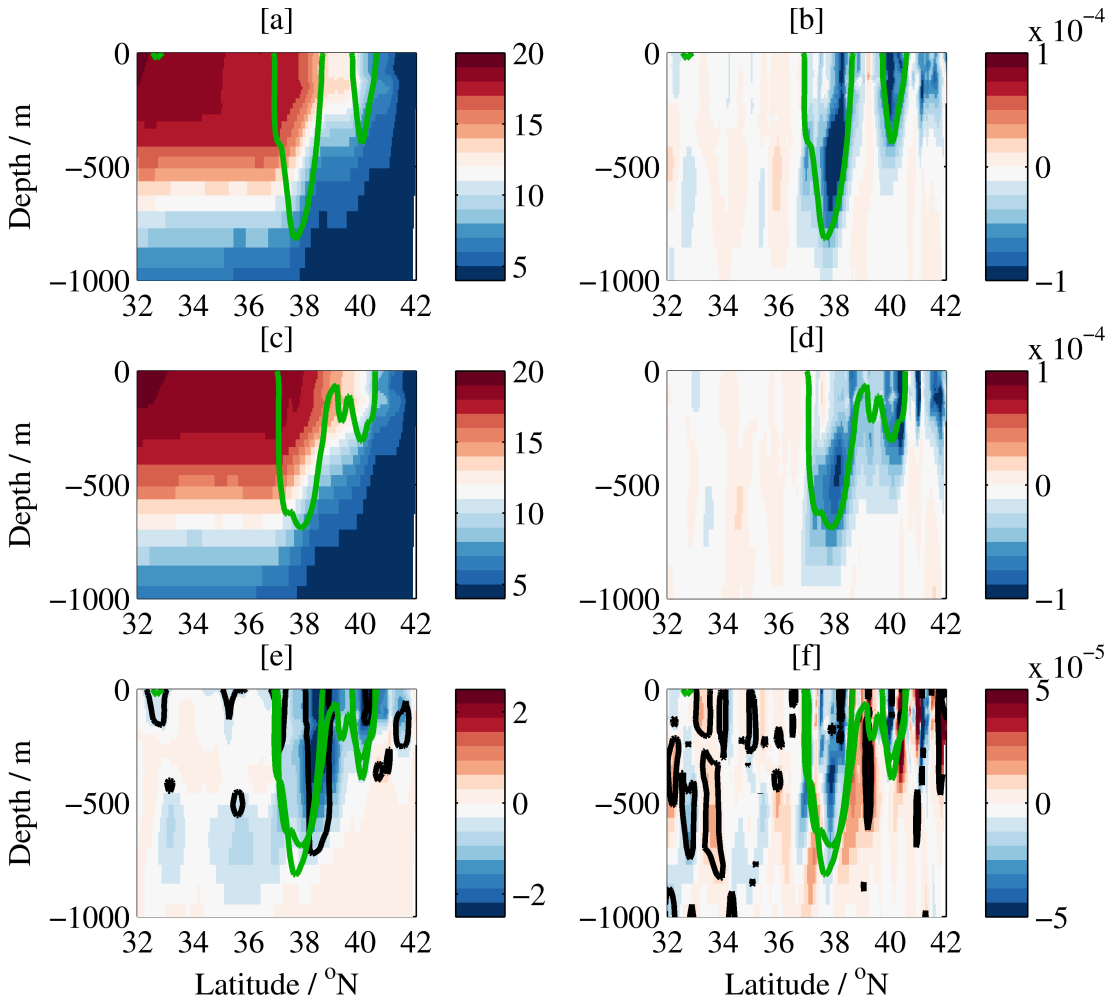

Figure 4.9: Mean April temperature (^oC) along 54^{o}W during the strengthened years [a] and weakened years [c] and the corresponding mean April meridional temperature gradient (^{o}C m^{-1}) during the strengthened years [b] and weakened years [d] in ORCA12. The composite anomaly (strengthened minus weakened years) for temperature (^oC) and meridional temperature gradient (^{o}C m^{-1}) are also revealed in [e] and [f] respectively. Black contours denote the $90-95\%$ confidence intervals and the green lines are the mean 0.5m s^{-1} zonal velocity contours for either the strengthened or weakened years.

stratified), the PV is anomalously negative from $32-38^oN$ and down to, at least, $200m$ depth. This anomaly extends down to about $350m$ closer to the GS (i.e. from $35-38^oN$). The maximum anomaly, of up to -5x10^{-11} m s^{-1}, is found in the top $50m$ and further to the south, which suggests that it is related to surface forcing and may have caused PV minima to occur further to the south during these years. Further analysis reveals that the mean PV in April from $34-38^oN$ in the STMW layer is lower in the strengthened years, which is consistent with stronger

horizontal temperature gradients and baroclinic transport (via thermal wind).

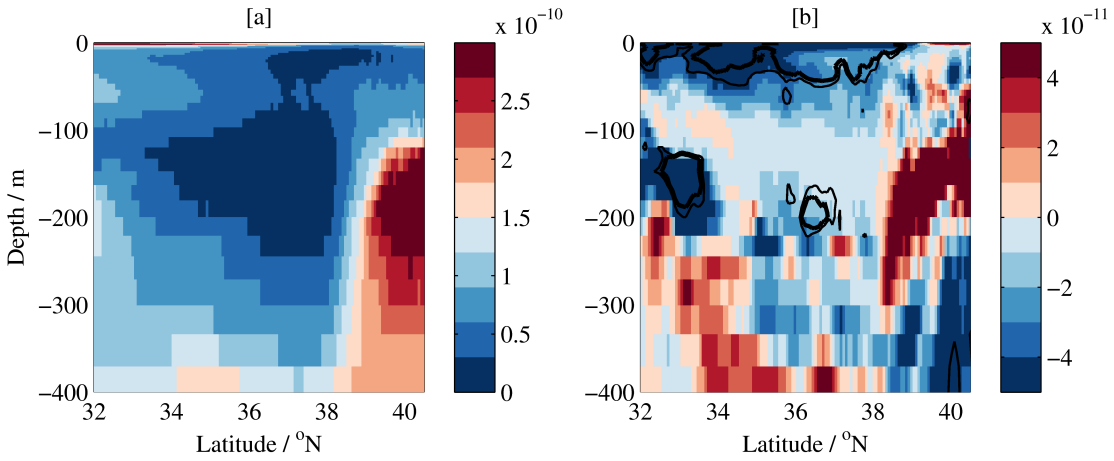

Figure 4.10: Mean April planetary PV (m s^{-1}) from 1978-2010 [a] and the associated composite for the strengthened minus weakened years [b] along 54^oW of the ORCA12 run. Black contours denote the $90-95\%$ confidence intervals.

4.2.4 Lagrangian analysis

In order to examine the variability of the SR during strengthened and weakened years, Lagrangian analysis is undertaken using the particle tracking software Ariane. As outlined in Chapter 2.4.2, particles are released in the Florida Straits near the surface ($10m$) at the beginning of April from 1980-2010 and allowed to flow in the GS for three months. The particles were tracked for 3 months as it was found to be a long enough timescale to track downstream circulation changes after bifurcation, i.e. into the NAC or SR, whilst limiting the number of particles re-entering the GS after recirculation to the south or to the north. Avoiding this was preferential as the focus in this chapter is to examine the immediate pathways after the particles pass through 70^oW and the effect that the increased transport may have on them. Particles are released in April in order to examine GS pathways downstream of 70^oW in order to examine if the increased transport has an impact on them. Figure 4.11c is the composite of the particle density (i.e. the number of particles that have passed through each 1^o grid box) for the strengthened (Figure 4.11a) minus the weakened years (Figure 4.11b) after they have travelled in the GS system for 3 months. The differences reveal that, during the strengthened years, more particles are found to the south of the main GS core between 62^oW and 75^oW with fewer

particles found further to the east. This suggests that during years of intensified GS transport there is a stronger westward flow on the southern flank of the GS, which indicates a stronger southern recirculation. This is consistent with the higher transport seen at 70^oW and the weaker flow continuing eastward into the NAC. Even though more particles are seen south of the GS to the west of 62^oW, east of 62^oW there are fewer. This suggests that there is a tighter southern recirculation cell with an intensified westward component during the strengthened years, which enables a stronger return flow and increases the transport at 70^oW. Additionally, this potentially provides the warm advection necessary for the capping of mixed layers seen further to the west (Figure 4.8a).

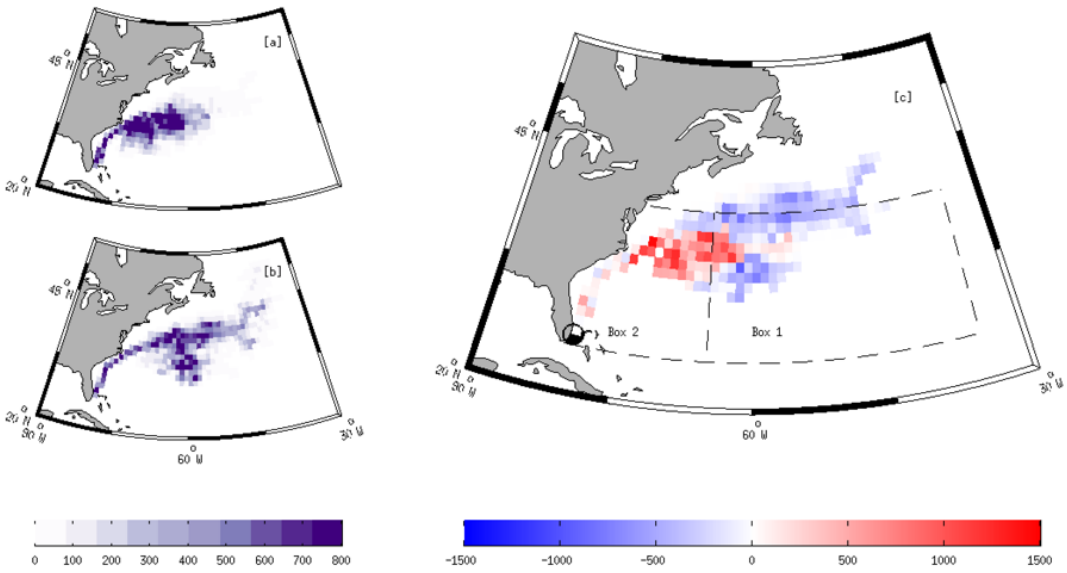

Figure 4.11: ORCA12 Trajectory density (i.e. the number of particles that have passed through a 1^o grid box) for the strengthened years [a] and the weakened years [b] from April-June and the composite anomaly of the strengthened minus the weakened years [c].

In order to quantify the potential changes in the strength of the southern recirculation, three metrics have been calculated based on the location of the particles after 3 months and the direction of flow:

1. the number of particles residing in the SR are calculated, which is defined as Box 1 (from $25^oN - 40^oN$ and $35^oW - coast$);

2. a western SR is defined as Box 2 that has an eastward extent of 65^oW (with the eastern SR defined as being located from $65^oW - 35^oW$);

3. the proportion of particles that flow west during the third month when residing in either the whole SR (Box 1) or the western SR (Box 2) is quantified.

The percentage of particles that fall into Box 1 and Box 2 for each year are averaged over all years, and for the strengthened and weakened years, with the difference taken between the two - see Table 4.3. Nearly all of the particles are located in the SR and more than half are found in the western SR after 3 months during the strengthened years. In contrast to this, during the weakened years, far fewer particles reside in the SR or western SR after 3 months. Specifically, during the strengthened years, 32.1% more particles are found in the SR and 47.7% more particles are found in the western SR than during the weakened years. Both of these anomalies are statistically significant to the 95% confidence level, which was calculated using Monte Carlo analysis, described in section 4.2.2. A graphical representation of this is shown in Figure 4.12a, which illustrates the average location of particles after bifurcation of the GS for all 31 years, the strengthened years, and the weakened years. Of the particles not residing in the SR, the remainder (Rem) is comprised of the NAC, NR, and those still located in the main GS core. This further shows that more particles reside in the SR and fewer in the remainder, after three months in the strengthened years, and the opposite in the weakened years. Figure 4.12b shows the number of particles residing in the western SR after three months for each strengthened year and each strong year. It reveals that 4/5 strengthened years have an above average number of particles travelling to the western SR. Furthermore, only 2/5 strong years exhibit this pattern and are both also strengthened years.

Table 4.3: Percentage of particles found in the SR (1), in the western SR (2) and in the eastern SR for all years, strengthened years and weakened years with the difference taken between the two.

Region	SR (%)	Western SR (%)	Eastern SR (%)
All years	80.31	24.12	28.25
Strengthened years	97.25	52.00	32.75
Weakened years	65.20	4.30	11.15
Difference	32.05 +/- 13.37	47.70 +/- 17.34	21.60 +/- 15.83

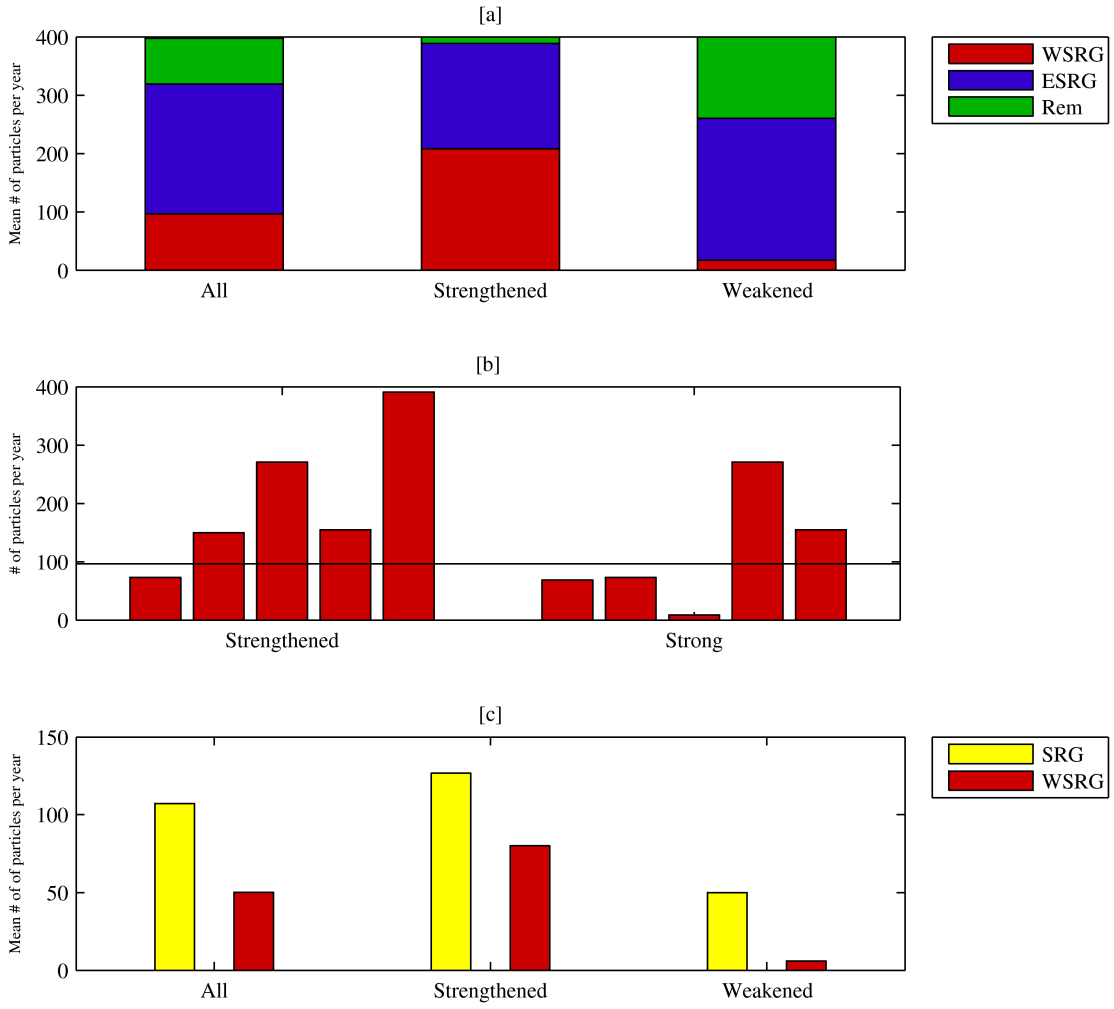

Figure 4.12: The number of particles residing in the western SR, eastern SR, and the remainder (Rem) (which is comprised of the NAC, NR and the remainder left in the main current) after 3 months averaged over all years, strengthened years and weakened years [a], the number of particles reaching the SR during each strengthened year and each strong year (black line represents the mean across all years) [b] and the number of particles travelling west during the third month for particles residing in the SR and western SR [c].

Figure 4.12c shows the number of westward-moving particles in the SR in the third month after release. The sharp increase in westward-moving particles in the western SR during strengthened years confirms that much of the increase in particle numbers found in the western SR (Figure 4.12c) is associated with westward flow and thus with strengthened surface recirculation. It should also be noted that the mean Ekman currents during this time are southward with no clear distinction between strengthened and weakened years (not shown). This shows that the near-surface entrainment of particles into the southern recirculation is not solely controlled by Ekman currents. This stronger recirculation augments transport at 70^oW, contributing to the increase seen there. Additionally, a tighter recirculation implies a strengthening of the anticyclone, which is consistent with *Worthington* (1977).

4.3 Wind Stress Curl

In addition to Qnet, the wind stress curl is also known to influence the transport of WBCs via Sverdrup balance with a greater negative wind stress curl inducing an increased southward interior Sverdrup transport and an increased poleward return flow (GS) at the western boundary (*Sverdrup*, 1947; *Hogg and Johns*, 1995). The composite for winter wind stress curl for the strengthened years minus the weakened years is shown in Figure 4.13. It reveals a negative anomaly, i.e. a more negative wind stress curl of up to $-2x10^{-7}$N m^{-3}, during the strengthened years over much of the western STG south of 35^oN. The greatest and most significant anomaly is found in the western Sargasso Sea close to the southern flank of the GS from $75 - 65^oW$ and may be driving the tight western recirculation seen during the strengthened years (*Chaudhuri et al.*, 2009). This anomaly pattern is quite dissimilar to the pattern of Qnet anomalies shown in Figure 4.6c, which revealed widespread anomalous heat loss as opposed to more focused negative wind stress curl to the west.

To investigate if the two forcing anomaly fields are connected, mean winter wind stress curl and Qnet have been averaged over a box to the south of the GS from $25-35^oN$ and coast-50^oW for each year in the hindcast. This is shown in Figure 4.14,

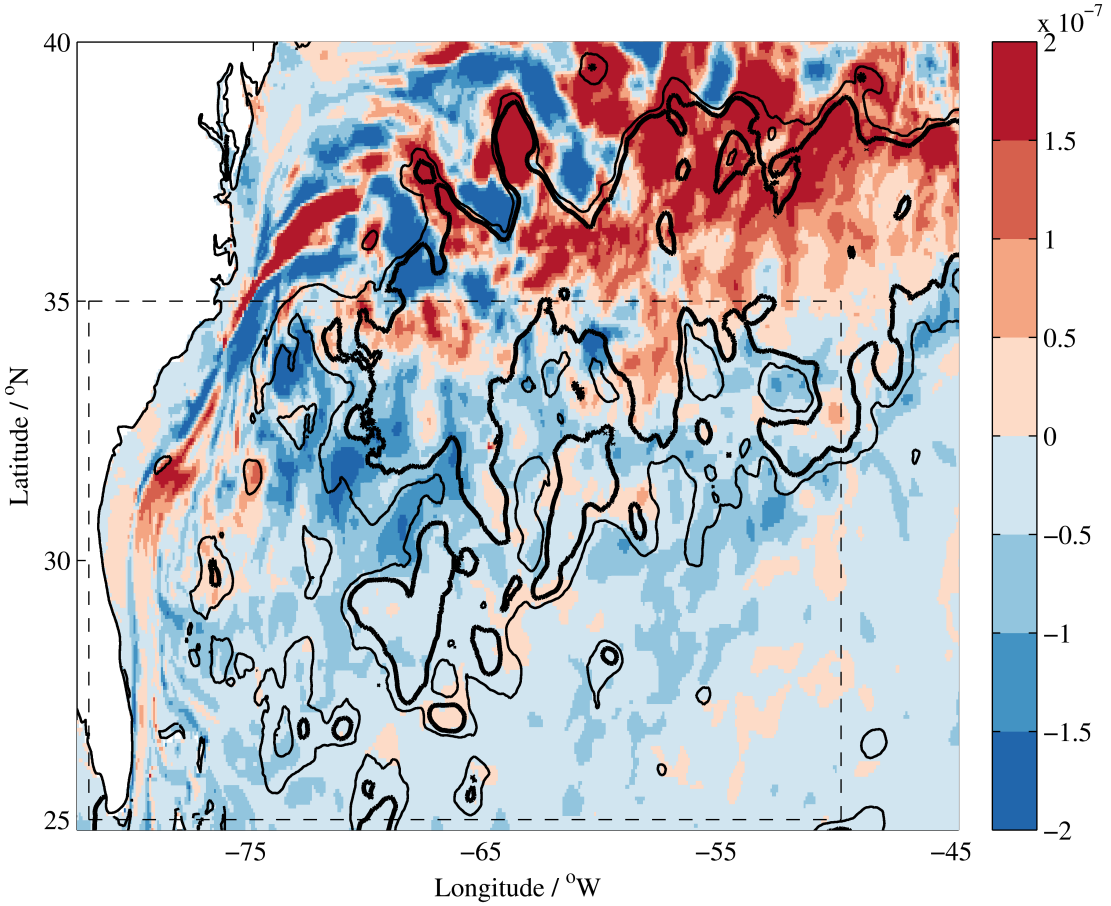

Figure 4.13: Winter wind stress curl (N m^{-3}) composite for the strengthened minus the weakened years in the ORCA12 run. Black contours denote 1-2 standard deviations, dashed line represents the box where the wind stress curl and surface heat flux is averaged for Figure 4.14.

which highlights the strengthened and weakened years. No significant correlation between the two variables exists at this location, but two standout strengthened years are noticeable, which correspond to 1985 and 2007, and exhibit considerably negative Qnet and wind stress curl values. Although one of the other strengthened years (2009) has been forced with near-average winter Qnet and wind stress curl values, the remaining two strengthened years appear to occur immediately after winters with large heat losses that do not coincide with a considerable response in wind stress curl. This indicates that wind stress curl occasionally varies in conjunction with Qnet, to reinforce changes in GS transport, while Qnet can act without a significant wind stress curl response to drive changes in GS transport.

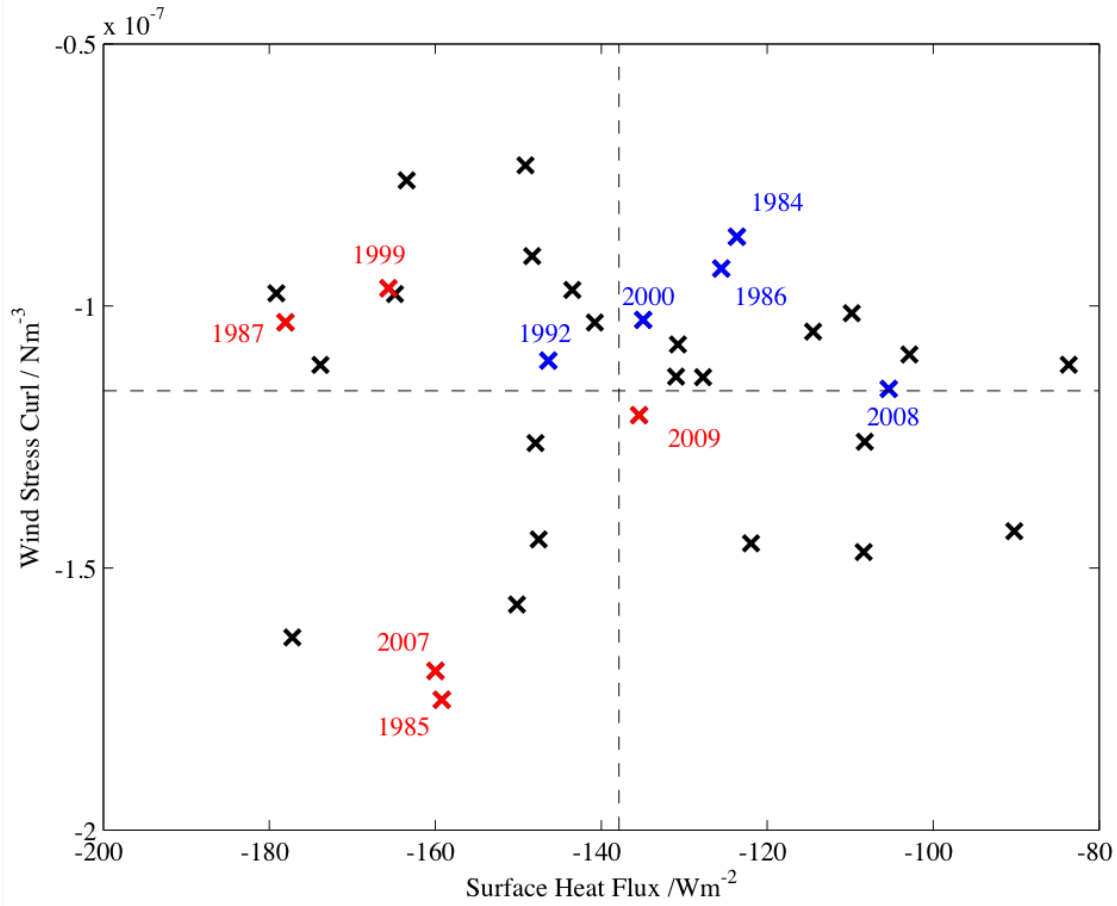

Figure 4.14: Mean winter surface heat flux (W m^{-2}) and wind stress curl (N m^{-3}) averaged over a region to the south of the Gulf Stream from $25 - 35^oN$ and the coast to 50^oW from 1978-2010 with strengthened years being highlighted in red and weakened years highlighted in blue.

4.3.1 Mean Sea Level Pressure

The mean winter (JFM) SLP, $2m$ air temperature and $2m$ wind speed patterns are investigated in order to ascertain if a common set of meteorological conditions prevails during the strengthened or weakened years, which may be strongly influencing Qnet. Figure 4.15 shows these anomalies for the strengthened years minus the weakened years. It reveals lower air temperature of up to 2^oC over the western North Atlantic, which is associated with the flow of polar, continental air shown by both the negative SLP and southward wind anomalies.

This suggests that, during the strengthened years, more frequent and/or more intense low-pressure systems occur over this region. These cyclonic systems, known as cold air outbreaks, initiate a northerly wind that brings cold, dry air south over

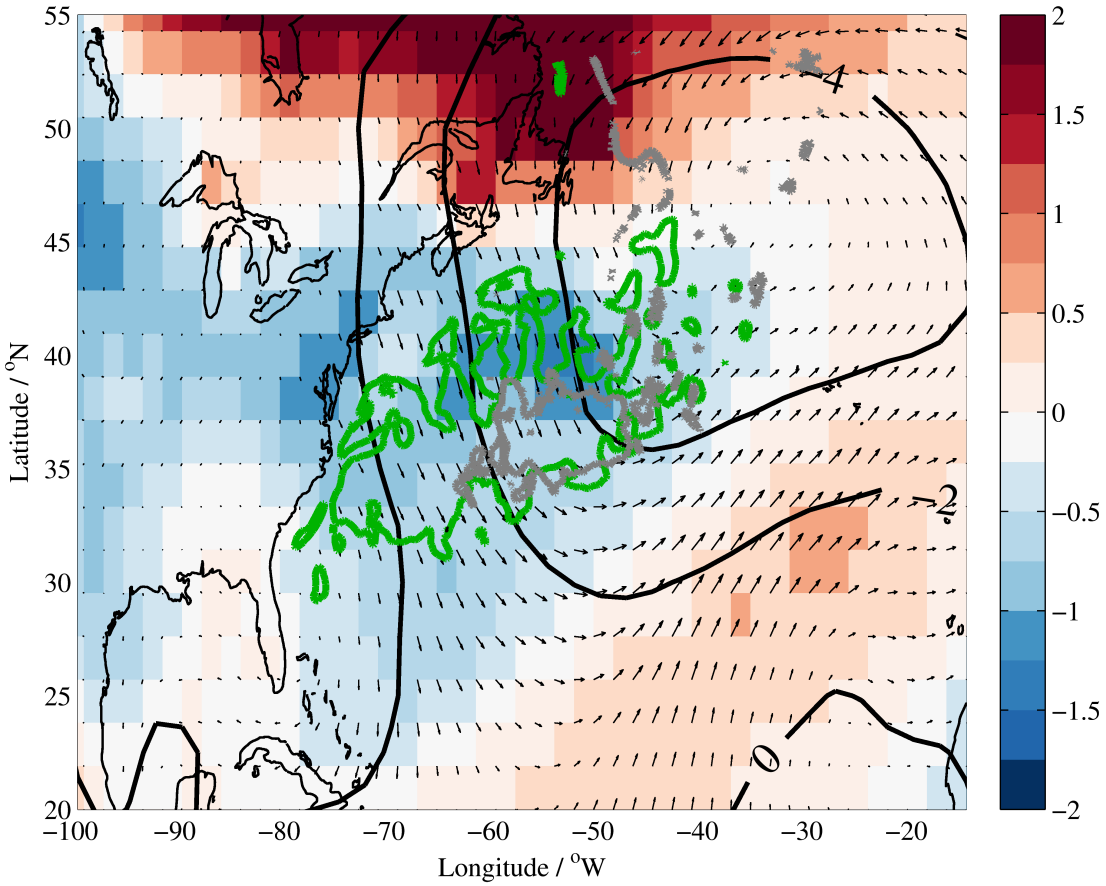

Figure 4.15: Mean winter (JFM) 2 m air temperature (^oC) composite for the strengthened minus the weakened years with contours of the winter (JFM) sea level pressure (mb) composite for the strengthened minus the weakened years. Arrows represent the vectorised winter (JFM) wind velocity (ms^{-1}) anomaly for the strengthened minus the weakened years. The green and grey contours denote the $-50Wm^{-2}$ and 100m anomalies for the Qnet and MLD composites respectively (i.e. from Figure 4.5 and 4.5d).

the GS and, consequently, causes a large Qnet due to the higher temperature difference at the air-sea interface. The contours of anomalous Qnet and MLD, from Figures 4.6c and 4.6f, are shown on this plot, which reveals that the location of greatest heat loss and MLD are located within this region of cold, dry air.

This further highlights the dominant influence of Qnet over wind stress curl in driving GS transport changes, as a stronger subtropical high would also be required to initiate greater wind stress curl forcing south of 35^oN. Although in some years in which the GS strengthens (for example 2007, not shown), such a pattern (i.e. a stronger subtropical high) can occur, supporting the case for both roles of Qnet and wind stress curl, Fig. 4.15 indicates that this is not typically the case.

4.4 Discussion

Results have been presented on the role of intense air-sea heat fluxes in driving fluctuations of GS transport using the high resolution ORCA12 hindcast. Significant relationships have been identified between the transport at 70^{o}W and Qnet and MLD in the western STG, the temperature and meridional temperature gradient with depth along 70^{o}W and 54^{o}W and the southern recirculation. The main findings will each be discussed in turn but the key points are as follows:

1. The majority of GS transport changes at $70^oW (> 88\%)$ are due to density changes as opposed to fluctuations in the barotropic component.

2. Years of strengthened transport from the previous year were preceded by widespread significant winter heat loss, which also initiated deep convection in the Sargasso Sea that resulted in anomalously deep mixed layers further to the east during these years.

3. Anomalous cooling of up to 4^oC occurs in the Slope Water during these years, which led to greater meridional temperature gradients on the northern flank of the GS, while a Worthington-style response is evident at 54^{o}W with strengthened meridional gradients at depth across the GS core.

4. The strengthened transport years are also characterised by a stronger, westward-intensified, southern recirculation gyre, which may be contributing to the increased transport at 70^oW.

5. The winter mean sea level pressure during the strengthened years facilitated the arrival of CAOs over the GS region, which along with other evidence points toward an important role for buoyancy forcing in setting interannual GS transport variations.

Stronger relationships are found with the change in transport at 70^{o}W compared to the previous April, as opposed to the absolute transport. This highlights the importance of the pre-existing ocean state that the buoyancy flux acts upon. Greater increases in spring transport are associated with i.) high winter heat losses

throughout the western STG (Figure 4.6c), ii.) deeper early spring mixed layers to the south of the main GS core and east of 60^oW (Figure 4.6f), which induced a response similar to that observed by (*Worthington*, 1977) of strengthened temperature gradients at greater depths (Figure 4.9), and iii.) stronger meridional temperature gradients to the north of the GS at 70^oW (Figure 4.7b).

The large heat losses in the Slope Water, of up to 4^oC, that led to the strengthening of temperature gradients to the north (Figure 4.7b) agrees with the findings of *Zheng et al.* (1984). This is in contrast to that of *Worthington* (1977), who found an intensification of the GS occurred in conjunction with strengthening temperature gradients to the south from a deeper thermocline after the severe winter of 1976/77. The formation of deeper mixed layers further to the west was found here to be prevented by surface warming, potentially from increased heat advection in the intensified GS. However, the strengthening of temperature gradients in the main GS core at greater depths occurs alongside deeper mixed layers further to the east at 54^oW (Figure 4.9f), which is consistent with a (*Worthington*, 1977).

Lagrangian analysis indicated that an increased, westward-intensified, southern recirculation tends to occur during strengthened years, which is expected to contribute to the increased transport seen at 70^oW (Figure 4.11). It may also be facilitating warm advection in this region, leading to the capping of deeper mixed layers further west, referred to above. The deeper mixed layers found further to the east (from $60 - 50^oW$), than noted by *Worthington* (1977), have the potential to contribute to the increased transport seen at 70^oW via this intensified recirculation.

The influence of wind stress curl in setting GS transport fluctuations at 70^oW was also investigated. Although wind stress curl can act in conjunction with Qnet to produce an intensification of the GS at this location (i.e. in 1985 and 2007), Qnet has also been found to dominate changes in GS transport (i.e. in 1987 and 1999). This, along with the prevailing winter meteorological conditions during the strengthened and weakened years, highlights the dominant role of buoyancy forcing.

As mentioned in Section 4.1, heat fluxes over the GS region may have implications for the North Atlantic storm track and winter conditions over western Europe (*Joyce et al.*, 2009; *Kwon et al.*, 2010). This is beyond the scope of this thesis but

it is of interest to determine how SST anomaly patterns, and therefore widespread variable heat loss, develop in strengthened and weakened years. Specifically, this would have a substantial impact on the baroclinicity of the atmosphere and, consequently, the North Atlantic storm track. Then given the SST tripole's influence on the NAO (*Visbeck et al.*, 2003; *Buchan et al.*, 2014), this could implicate the GS in large-scale climate variability.

To conclude, air-sea heat exchange has been found to often play a dominant role in driving interannual variations in GS transport at 70^oW in the ORCA12 hindcast of the NEMO model. Early spring transport increases of up to 35% (compared to the previous year) were found to occur immediately after severe winters were experienced in North America. These increases are the result of strengthened meridional temperature gradients on the northern flank of the GS and/or an intensified southern recirculation.

Chapter 5

The importance of air-sea fluxes on the variability of GS pathways from a Lagrangian perspective

5.1 Introduction

Chapter 4 introduced the use of Lagrangian methods to identify changes in the GS SR from year to year. Significant interannual variability was found near the surface, which implies that considerable variability exists for other deeper GS pathways. As discussed in Chapter 1, the interconnectivity between the STG and SPG has been studied using both observational drifters and models (*Brambilla and Talley*, 2006; *Hakkinen and Rhines*, 2009; *Burkholder and Lozier*, 2011; *Rypina et al.*, 2011; *Burkholder and Lozier*, 2014; *Foukal and Lozier*, 2016). The Eulerian estimate of $20Sv$ or so of GS water that continues as the NAC (*Johns et al.*, 1995) has been disputed by studies using a Lagrangian framework, which show that few surface trajectories from the STG reach the SPG (*Brambilla and Talley*, 2006; *Burkholder and Lozier*, 2011). However, when the floats are not constrained to the surface, intergyre exchange is revealed through a subsurface pathway on timescales ranging from 2-7 years when initiated in the STG interior (*Burkholder and Lozier*, 2011).

Additionally, there is some evidence for timescales of less than two years when particles are released in the main GS path at the surface (*Rypina et al.*, 2011). This suggests that a more direct intergyre pathway exists via the GS, which is quantified in this chapter. *Rypina et al.* (2011) also found that particles released on the shoreward side of the GS have a greater probability of reaching the SPG.

This could dispute the findings of *Hakkinen and Rhines* (2009) who found that a greater through flow of surface drifters entered the SPG from 2001-2007. This greater through flow could be related to the location of initiated drifters as opposed to dynamical circulation changes.

This chapter employs Lagrangian techniques to investigate the variability of the downstream destination of GS water after bifurcation. After flowing in the main GS core, the current splits into its 4 main components; the NAC, the AC, the SR and the NR (*Schmitz Jr*, 1996), which is discussed in Chapter 1. Using trajectory analysis, we investigate these GS pathways on seasonal and interannual timescales and with different release depths. The previous chapter (Chapter 4) found some evidence for an intensified SR after winters of intense heat loss over the Sargasso Sea. Additionally, *Hakkinen and Rhines* (2009) found that the wind stress curl could have influenced the greater throughput to the SPG since 2001. Here, the influence of both the wind stress curl and Qnet will be examined in relation to the amount of flow in different GS pathways. The mechanisms attributed to seasonal and decadal variability will also be investigated in terms of their relation, whether directly or indirectly, to air-sea interaction over the North Atlantic. Finally, the trajectory density (i.e. the number of trajectories passing through each grid cell), depth, temperature, salinity and age are also examined in order to assess the potential impact from decadal variability in throughput to the SPG.

The experimental setup and methods are described in Chapter 2.5 with the results presented here as follows; section 5.2 analyses the variation in GS pathways with different release depths with the seasonal variability of these pathways being presented in section 5.3. Then, the interannual variability is explored for the near-surface trajectories (section 5.4) and the subsurface trajectories (section 5.5) with surface heat fluxes and oceanic dynamics investigated as possible mechanisms controlling this variability.

5.2 Variability with trajectory release depth

First, the variability of GS pathways is investigated with different release depths ($10 - 300m$) after travelling in the flow field for 4, 8 and 12 months. A near-surface ($10m$) and subsurface ($200m$) release depth are further examined from 1-12 months in order to establish how the downstream destination of GS water varies with depth.

Variability of GS pathways with depth and over time is evident in Figure 5.1, which shows the average location of particles over all releases for each depth after 4 months (Figure 5.1a), 8 months (Figure 5.1b) and 1 year (Figure 5.1c). Figure 5.1d reveals the average proportion of particles residing in the two most populated regions (SR and SPG) after 1-12 months for near-surface trajectories ($10m$) and subsurface trajectories ($200m$). This is also revealed for particles travelling in the NR and AC in Figure 5.1e.

After travelling in the flow field for 1 year (Figure 5.1c) and when released nearest to the surface at 10m, 72% of particles reside in the SR, which makes it the most favourable GS pathway at this release depth. It was found in Chapter 4 that this tendency for near-surface trajectories to travel in the SR is not solely controlled by Ekman currents. This value decreases with deeper releases and is compensated for by a greater proportion of particles travelling to the SPG via the NAC pathway until the $300m$ release. Here, there is a slight reversal in this trend and is likely due to a reduced current speed at this depth. For example, for the $200m$ release, 36% of all particles reach the SPG after 1 year while this value is less than 10% when released near the surface ($10m$). This implies that subsurface trajectories, i.e. those residing on a denser isopycnal, are more likely to reach the SPG, which agrees with previous findings (*Burkholder and Lozier*, 2011, 2014; *Foukal and Lozier*, 2016). However, these studies are associated with longer timescales (4-5 years) to enable eventual entrainment into the GS when released in the western STG. Here, we find evidence for a direct GS pathway on shorter timescales (less than 1 year).

This relationship, i.e. increased flow to the SPG with greater depths, also exists

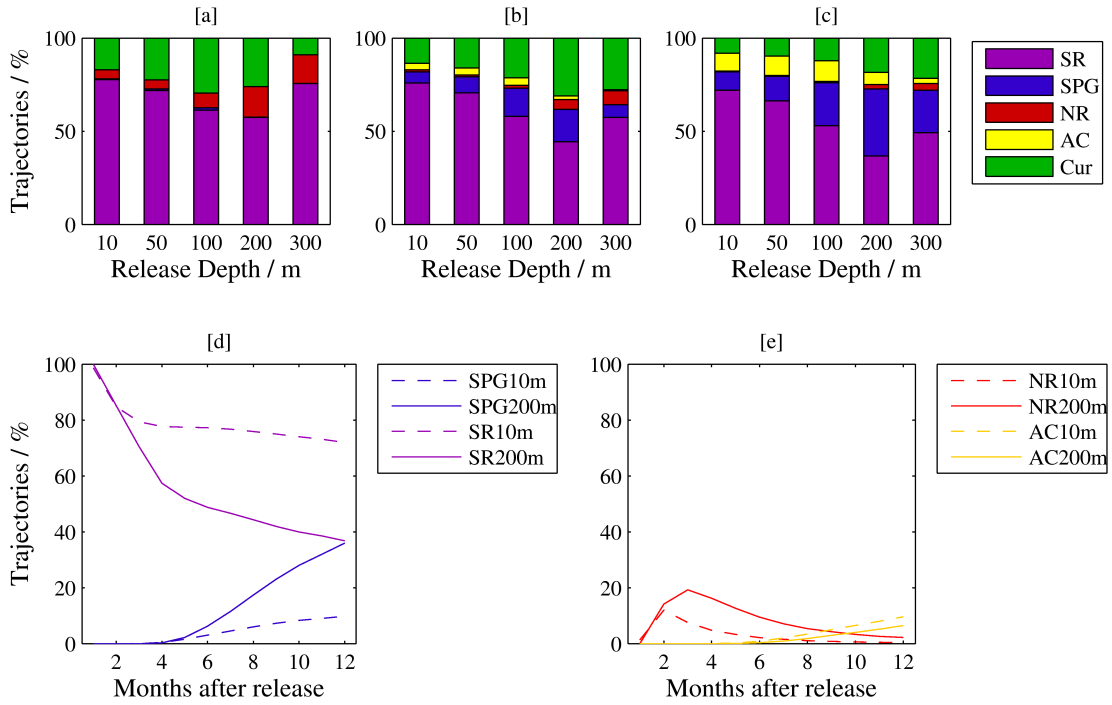

Figure 5.1: Downstream destination of Gulf Stream water after bifurcation (%) at different release depths when initiated in the Florida Straits and allowed to travel for 4 months [a], 8 months [b], and 1 year [c] when averaged over all release months and years. Particles may enter the SPG, the SR, the NR, the AC or remain in the main GS current (Cur). [d] Shows the average percentage of trajectories that reside in the SPG and SR at the $10m$ and $200m$ release depths for 1-12 months after release while [e] focuses on trajectories residing in the NR and AC.

after 8 months (Figure 5.1b), with slightly smaller values of 17% and 6% for the $200m$ and $10m$ releases respectively reaching the SPG. After 4 months (Figure 5.1a) less than 1% of particles cross the boundary into the SPG at all depths. Admittedly, this represents just 1 particle but this value increases until 145 particles reside in this region by after 1 year. This provides confidence in the finding that GS water reaches the SPG on shorter timesales than has been found previously, i.e. 2-5 years (*Burkholder and Lozier*, 2011, 2014; *Foukal and Lozier*, 2016). The majority of particles reside in the SR at all release depths after this time period but there is a considerable contribution (%) that travel in the NR, i.e. particles in the Slope Water, or that remain in the main GS current (Cur), i.e. before bifurcation or continuation into the SPG via the NAC.

However, most particles reside in either the SR or the SPG after all time periods shown in Figure 5.1, which implies that these are the two main GS pathways at

all depths. Figure 5.1d shows that, when released at 10m, nearly all trajectories recirculate to the south with less than 10% reaching the SPG after 1 year, as mentioned above. Contrastingly, when released at 200m the proportion of trajectories reaching the SPG increases from 4 months ($< 1\%$) to 1 year (36%), at which point the proportion of trajectories residing in the SPG matches that in the SR.

At $10m$, the reduction of particles in the NR after 8 months and 1 year suggests that those that were in this region after 4 months were, by then, reentrained into the GS. This is confirmed in Figure 5.1e, which shows that particles (1%) can reach the NR after just 1 month when released near the surface. This proportion increases to more than 12% after 2 months before declining steadily after this, which provides evidence of their re-entrainment into the main GS. A larger percentage of particles also enter this region when released at a greater depth (up to 19% after 3 months), which agrees with previous findings that the bifurcation of the GS into the NR occurs at deeper levels within the water column (*Hogg*, 1992). Finally, a greater proportion of particles reside in the AC after more time has lapsed and for shallower release depths. For example, the minimum time taken to reach the AC is 5 months when released at $10m$ and 6 months when released at $200m$. This reaches a maximum of 9.6% and 6.5% after 1 year for $10m$ and $200m$ respectively. A visual representation of the proportion of trajectories residing in each region when released near the surface ($10m$) and at the subsurface ($200m$) after 4, 8 and 12 months is shown in Figure 5.2.

To summarise, results show that a direct subsurface pathway exists between the STG and the SPG via the GS on timescales as short as 4 months. The existence of a subsurface pathway agrees with prior findings (*Burkholder and Lozier*, 2011, 2014; *Foukal and Lozier*, 2016). For example, *Burkholder and Lozier* (2011) found that the maximum number of particles reaching the SPG occurred when released at 700m from the STG interior. Here, it is clear that GS water can reach the SPG on much shorter timescales than has been found in previous Lagrangian model studies. Specifically, intergyre exchange has been identified on much longer timescales ranging from 2-7 years (*Burkholder and Lozier*, 2011; *Foukal and Lozier*, 2016). However, these trajectories were released within the interior of the STG as

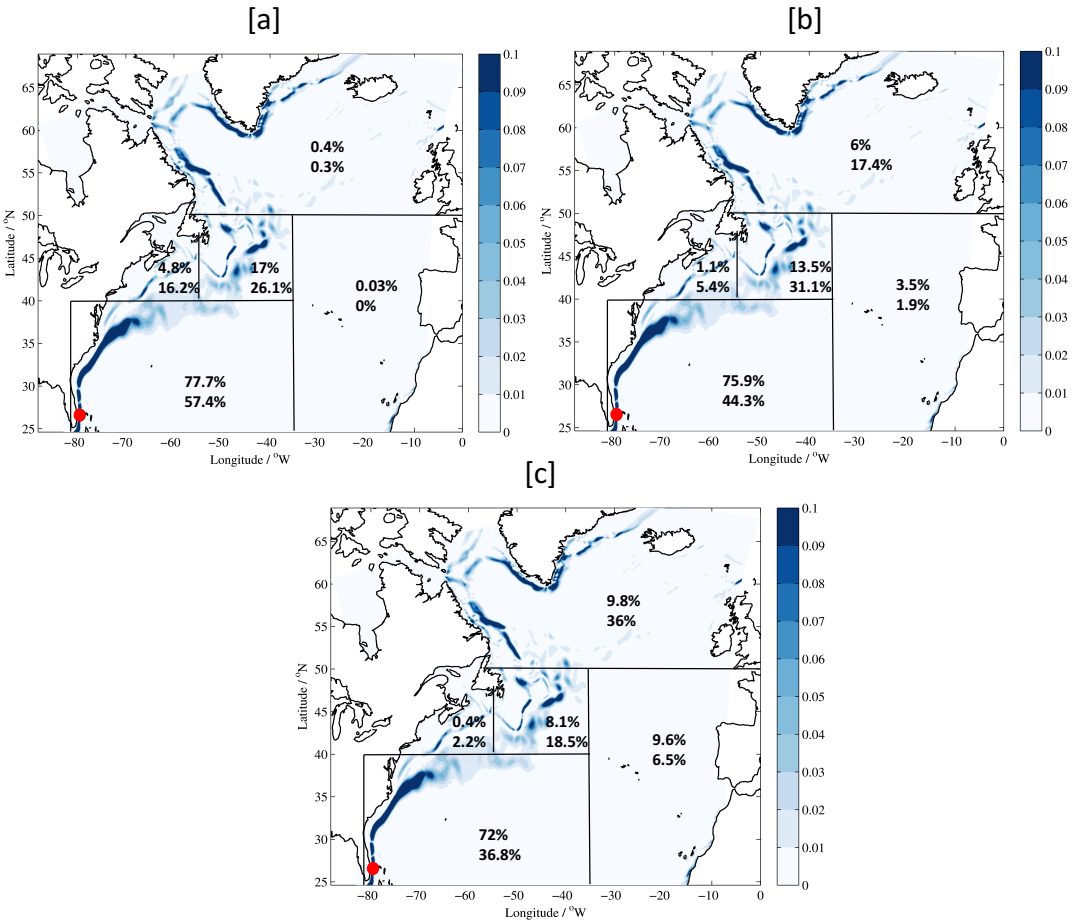

Figure 5.2: Mean surface speeds (m s^{-1}) in the North Atlantic from 1980-2010 in the ORCA12 hindcast with the percentage of trajectories residing in each region when released at $10m$ (top value) and $200m$ (bottom value) when released in the Florida Straits (red marker) and travelling in the flow field for [a] 4 months, [b] 8 months and [c] 12 months.

opposed to directly in the GS core as was done here. For trajectories released at a similar location in the GS, Foukal (personal communication, 29/06/17) found that the mean age of trajectories reaching the SPG was around 1.75 years with a minimum age of about 6 months recorded. This is closer to the findings presented here but still not as rapid as the direct pathway identified at 4 months.

5.3 Seasonal Variability

This section investigates how the downstream destination of GS water varies on seasonal timescales at each release depth; i.e. at $10m$, $50m$, $100m$, $200m$ and

$300m$. The seasonal variability in the starting density and MLD are also examined as potential mechanisms for influencing the proportion of trajectories travelling to the SPG.

5.3.1 Variability of Gulf Stream pathways

To assess whether any seasonal variation exists for the downstream destination of GS water, the proportion of particles residing in each region 12 months after release is averaged over each release month. These results are displayed for each of the release depths (Figure 5.3). Considering first the $10m$ releases (Figure 5.3a), there is a slight variation in the percentage of particles flowing in the AC with less than 1% residing in the NR for all release months at this depth. However, the results reveal that a seasonal cycle exists in the proportion of trajectories that travel to the SR and to the SPG, which vary in anti-phase with each other. A period of less flow to the SR occurs during autumn and winter, with a minimum in October (55%), which increases throughout spring and summer and reaches a maximum in July (84%). This is almost directly compensated for by the seasonal cycle in trajectories residing in the SPG with a corresponding maximum in October (21%) and minimum in July (3%). This cycle also exists at $50m$ (Figure 5.3b) and $100m$ (Figure 5.3c) but the peaks and troughs are shifted in time. At $50m$ there is a lower percentage of trajectories residing in the SR during the summer and autumn (with a minimum of 50%, again, in October) and a high percentage in winter and spring (with a maximum of 81% in March). This is compared with a maximum flow into the SPG in October (23%) and a minimum in March (5%). This cycle is further shifted in time at $100m$ with the maximum flow to the SR occurring from late-autumn to early spring (a maximum of 71% in January) with a lower throughflow during late-spring to early-autumn (a minimum of 37% in August). Again, the opposite occurs for trajectories reaching the SPG with a maximum in July (36%) and a minimum in January (11%).

At greater depths, the seasonal variability is minimal as it is deeper than the wind-driven and surface flux-driven layer (*Wang and Koblinsky*, 1996). However, changes in the seasonal wind field can influence the depth of the thermocline via

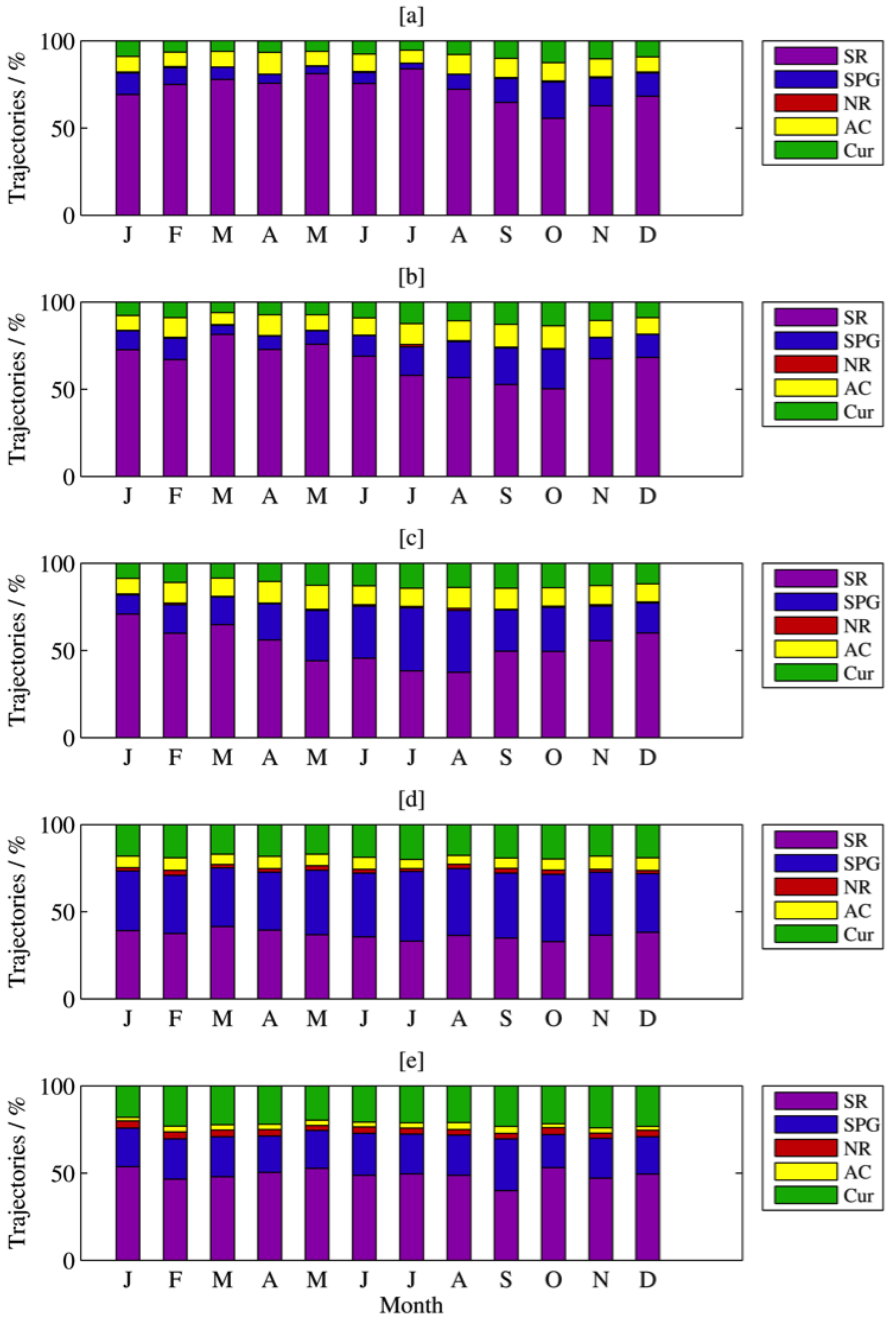

Figure 5.3: Downstream destination of Gulf Stream water after bifurcation (%) at different release months when initiated in the Florida Straits and allowed to travel for 12 months when released at $10m$ [a], $50m$ [b], $100m$ [c], $200m$ [d] and $300m$ [e] when averaged over all years from 1980-2009. Particles may enter the SPG, the SR, the NR, the AC or remain in the main Gulf Stream current (Cur).

Ekman pumping or Ekman suction. As has been discussed previously in this thesis, e.g. section 3.4.2, greater wind stress over this region will cause Ekman pumping, which increases the vertical velocity at the base of the Ekman layer and enhances downwelling. This leads to a deeper thermocline, which may affect the starting density of particles. For example, the $200m$ release was found to be the depth where

the highest proportion of trajectories flow into the SPG (section 5.2), which has a seasonal variation of $34 - 39\%$. However, the seasonal cycle at $100m$ reveals that a similar throughput is achieved when trajectories are released in July (36%) and August (35%). The largest seasonal cycle occurs at this depth, which could suggest it is close to the seasonal thermocline. This would affect the starting density of the trajectories, which was found to be important in the previous section with those residing on a denser isopycnal more likely to reach the SPG. This is shown in Figure 5.4 with the seasonal cycle of the average starting density revealed for each release depth. For $200m$ and $300m$ a seasonal cycle is absent, which contrasts with that seen for the shallower release depths. At $100m$ the greatest throughput to the SPG (from June to August) coincides with the densest starting densities, which could reflect the fluctuation in thermocline depth. For example, during the winter, when the surface forcing is at its greatest (*Silverthorne and Toole*, 2013; *Buckley et al.*, 2014), the thermocline and mixed layer are at their deepest (potentially deeper than 100m). In contrast, during the summer, the surface forcing is weaker and the MLD and thermocline depth are shallower, which leads to a denser isopycnal existing at 100m compared to that during the winter. This provides further evidence that trajectories residing on a denser isopycnal are more likely to reach the SPG, as found in the previous section.

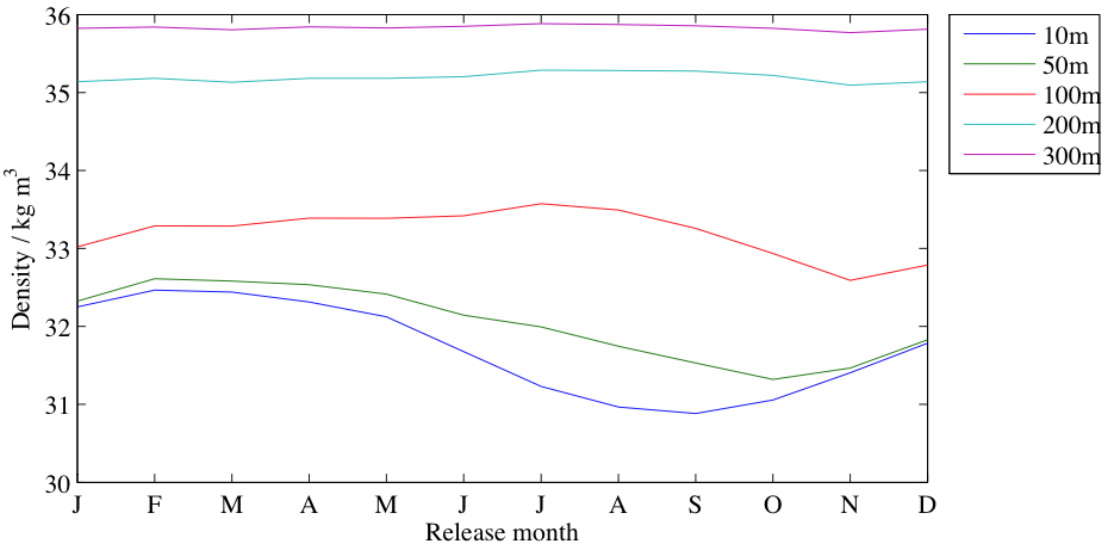

Figure 5.4: Density (kg m^3) in the Florida Straits at 26^oN and averaged over each month from 1980-2010 for each release depth.

Contrastingly, at $10m$ and $50m$ the cycle in seasonal density at the release location in the Florida Straits does not coincide with the cycle in throughput to the SPG seen in Figure 5.3a and Figure 5.3b. This could suggest that, as they are closer to the surface, other processes are important in determining the proportion of GS water travelling to the SPG further downstream. This could include the seasonal variation in the wind stress curl and Qnet, seasonal fluctuations in the Ekman transport or changes to the PV barrier. These are investigated in section 5.4 and 5.5 in relation to the interannual variability of GS pathways.

It is also worth noting here that the seasonal cycle still exists when the defined boundaries of each region are altered by up to 4^o. This is revealed at $10m$ in Figure 5.5, which shows how the proportion of trajectories residing in the SPG (Figure 5.5a), SR (Figure 5.5b), AC (Figure 5.5c) and NR (Figure 5.5d) varies when one of the regional boundaries is altered. For each region, the same seasonal variability is still apparent but with the percentage of trajectories consistently greater or lower for e.g. a more southward or northward southern limit respectively for trajectories travelling to the SPG. This confirms that the variability seen here is due to variability in the pathways of the GS as opposed to the variability in the defined boundaries, e.g. as the SPG expands and contracts on seasonal and interannual timescales (*Lohmann et al.*, 2009).

To summarise, a seasonal cycle was found to exist in the proportion of trajectories travelling to the SPG and SR at depths of up to $100m$. Beneath this, minimal seasonal variation is found. When released at $10m$, the greatest throughput to the SPG occurs from September-November, which is compensated for by fewer particles travelling to the SR. At $50m$ and $100m$ the seasonal cycle is shifted with the greatest throughput to the SPG occurring from August-October and May-August respectively. The greatest seasonal variation occurs at $100m$, which is related to the starting density of trajectories in the Florida Straits with the densest period, on average, coinciding with the greatest throughput to the SPG. This is related to the seasonal variation in MLD with the densest waters occurring at $100m$ when the MLD is shallower than this. This provides further evidence to that found in the previous section that greater throughput to the SPG occurs on

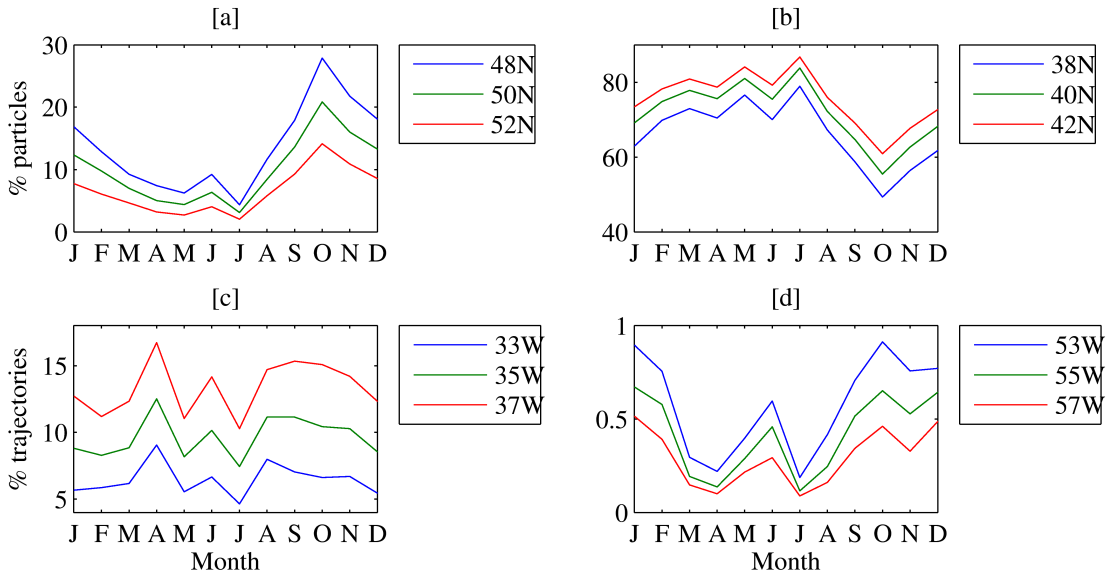

Figure 5.5: Downstream destination of Gulf Stream water after bifurcation (%) at different release months when initiated in the Florida Straits and allowed to travel for 12 months when released at $10m$ and allowing a 4^o variation in the southern boundary for trajectories travelling to the SPG [a], the northern boundary for trajectories travelling to the SR [b], the western boundary for trajectories travelling to the AC [c] and the eastern boundary for trajectories travelling to the NR [d].

a denser isopycnal.

5.4 Near-surface interannual variability

In this section, the interannual variability of the downstream destination of GS water of near-surface trajectories ($10m$) will be analysed. Chapter 4 identified a strengthened SR during years of intense air-sea interaction during the winter. Some of these years were also associated with an anomalously strong wind stress curl over the Sargasso Sea region. In order to establish the mechanisms controlling the interannual variability of certain GS pathways, the winter Qnet and wind stress curl over the Sargasso Sea and the Ekman transport at 50^oN will be correlated with the proportion of trajectories travelling to the SPG and SR on monthly timescales.

5.4.1 Variability of Gulf Stream pathways

To assess the amount of interannual variability in the downstream destination of GS water, the percentage of trajectories residing in each region after 1 year is averaged over each year for releases at $10m$ and is shown in Figure 5.6. There is evidence of multi-year variability in the percentage of trajectories that reside in the SR after 1 year with periods of higher throughput, e.g. from 2006-2010, and periods of lower throughput, e.g. from 1998-2005. This could be related to interannual variation in surface forcing and will be explored in section 5.4.2. The maximum flow into the SR occurs in 2009 where it reaches 90% with a minimum of 56% being recorded in 1986. These extreme values are offset by low percentages for trajectories travelling in the SPG, AC and remaining in the main current in 2009 with the opposite being true for 1986. This is in contrast to what was found for the seasonal variability (section 5.3) where the variations in throughput to the SR were almost exactly counterbalanced by the throughput to the SPG. This implies that the variation on interannual timescales dominates the variability seen in the percentage of trajectories that flow in the AC. For example, the maximum percentage is recorded as 18% in 1986 while the minimum is 4% in 1983. This compares with less than a 5% amplitude of seasonal variation (Figure 5.3).

5.4.2 Correlations with surface heat flux, wind stress, wind stress curl and Ekman transport

Near the surface there is a greater amount of variability when considering individual monthly releases, as opposed to averaging over a whole year (12 monthly releases). This is revealed in Figure 5.7, which shows the interannual variability for each monthly release for the trajectories residing in either the SR or SPG after a year. The percentage of trajectories residing in the SR can vary by as much as 90% from year-to-year, e.g. September 1999-2000, but it can also vary by as little as 52% over the entire 30-year period, e.g. in July. This is also highlighted in Table 5.1, which reveals the lowest standard deviation in July and one of the greatest in September. The proportion of trajectories entering the SPG also has a greater variability in the release months from September-March, with the standard deviation being greater

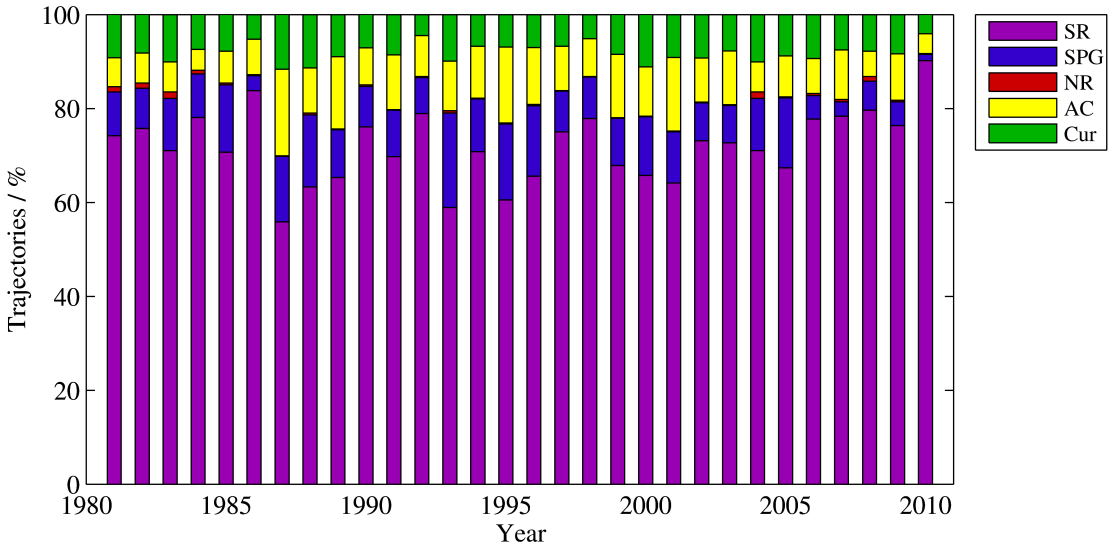

Figure 5.6: Downstream destination of Gulf Stream water after bifurcation (%) at different release years when initiated in the Florida Straits and allowed to travel for 12 months when released at $10m$ and averaged over all months. Particles may enter the SPG, the SR, the NR, the AC or remain in the main Gulf Stream current (Cur).

than the mean for 9/12 months. The greater variability over this period could suggest that variability could be related to the strong air-sea interaction that occurs in this region during the winter.

Table 5.1: Monthly mean (%) and standard deviation (%) of the percentage of trajectories residing in the SPG and SR when released at $10m$ and allowed to travel in the flow field for 12 months.

Month	SPG mean	SPG std	SR mean	SR std
Jan	13.34	12.97	67.27	24.73
Feb	10.41	12.35	73.47	22.35
Mar	7.70	11.63	76.59	21.78
Apr	5.33	5.97	74.62	20.59
May	4.71	6.93	79.87	21.59
Jun	6.96	8.57	73.82	22.91
Jul	3.27	4.68	83.37	15.71
Aug	9.36	12.68	70.00	29.10
Sep	14.76	17.56	62.76	27.62
Oct	22.37	18.45	53.08	26.18
Nov	17.35	16.64	60.63	27.79
Dec	14.38	17.21	66.24	27.79

In order to assess the influence of surface fluxes, the mean winter (JFM) Qnet and wind stress curl were calculated in a region to the south of the GS from

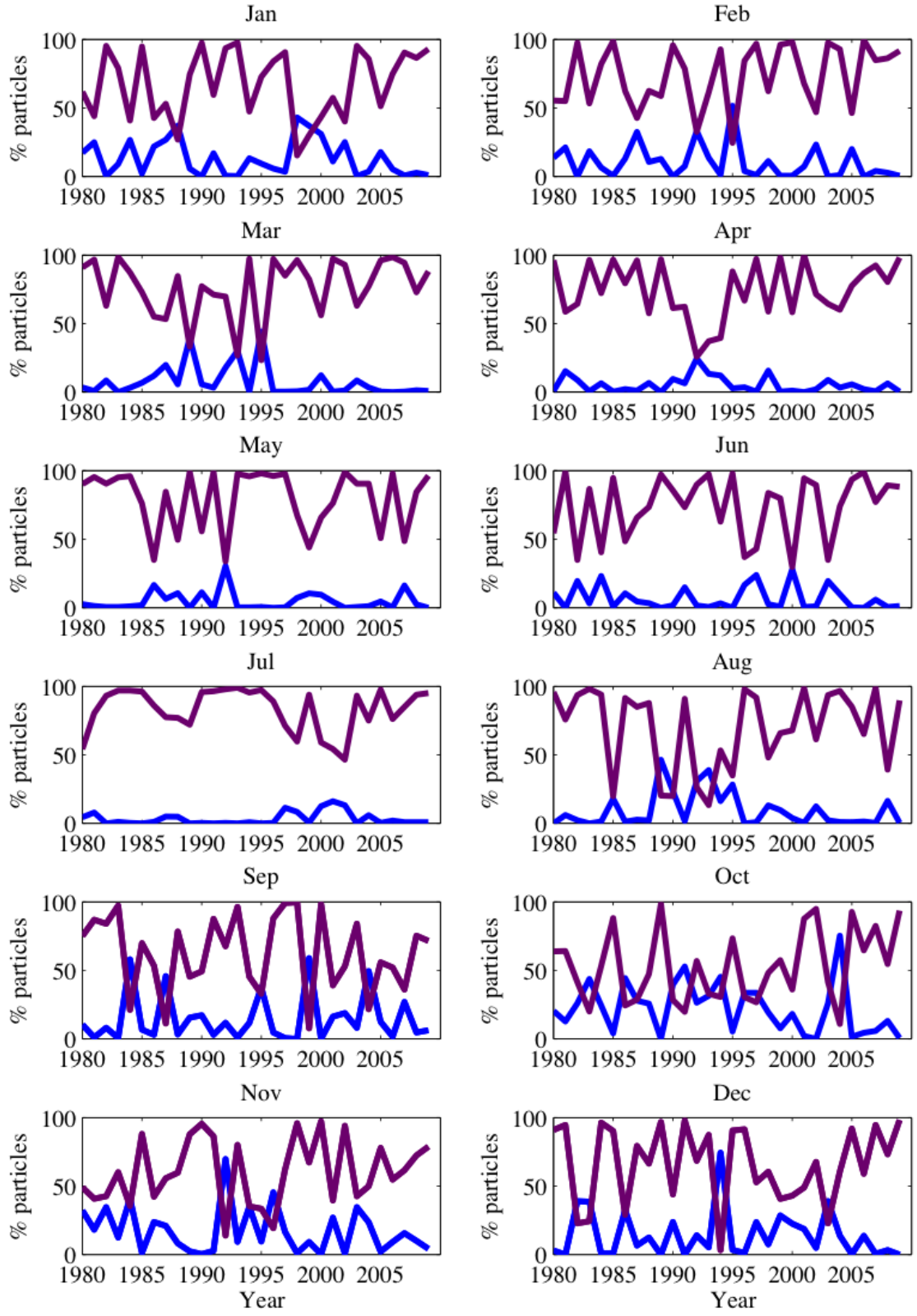

Figure 5.7: Percentage of trajectories residing in the SR (purple) and SPG (blue) when released at $10m$ in the Florida Straits and travelling in the flow field for 12 months for each release month over the period 1980-2009.

$25 - 35^oN$, $50 - 80^oW$, which is shown from 1980-2010 in Figure 5.8a and Figure 5.8c. This region is chosen as when averaged over this region they were found to have an effect on the transport of the GS and, potentially, the strength of the SR in Chapter 4. The average Qnet (Figure 5.8a) varies from up to 180 W m^{-2}, i.e. a large heat loss, in 1987 to a heat loss minimum of -85 W m^{-2} in 1989. In Figure 5.8b, the average wind stress curl is at a minimum in 1985 (-1.8x10^{-7} N m^{-3}) and reaches a maximum in 1983 (-0.7x10^{-7} N m^{-3}). As discussed in Chapter 4, the Qnet and wind stress curl exhibit some covariance (r = -0.09), but this is not always the case.

The mean wind stress along the GS core is also calculated as this will influence the Ekman transport, which is southwestward in the mean at this latitude (see Chapter 4) and could control the amount of near-surface particles entering the SR. In order to account for the tilt of the GS and the meridional shift of its path, a small region was chosen near 70^oW (i.e. where meridional shifts and mesoscale activity is reduced compared to further east, see Chapter 3), to calculate the mean angle of the GS during the winter. Specifically, the meridional (v) and zonal (u) surface velocities are averaged over a box from $36 - 38^o$N, $69 - 71^o$W for each winter (JFM) from 1978-2010. These are used to calculate the angle (θ) of the GS using $\theta = \tan^{-1}(v/u)$. The mean θ over the 33-year period is used to calculate the alongstream wind stress using the following:

$$\tau_{GS} = \tau_u \cos(\theta) + \tau_v \cos(90 - \theta) \tag{5.1}$$

where τ_{GS} is the alongstream wind stress of the GS and τ_u and τ_v are the zonal and meridional components respectively. Figure 5.8b reveals that the average alongstream wind stress varies from up to 0.09N m^{-2} in 1985 and just above 0 in 1990. Additionally, the mean winter (JFM) Ekman transport along 50^oN across the basin is also analysed, shown in Figure 5.8d, which is southward at this latitude (mean is equal to $-3.8Sv$). It also fluctuates interannually with a minimum close to $0Sv$ in 2010 and a maximum of $-7.5Sv$ in 1990. A stronger southward Ekman transport at this latitude could lead to reduced flow across it and, therefore, to the SPG near the surface (i.e. $10m$ release) as this is the southern limit for this defined

region.

The variation in Qnet can be related to the NAO index (Figure 5.8e), r = 0.3, where a positive NAO can lead to a weaker Qnet over this region (e.g. in 1989) while a negative NAO leads to a greater Qnet (e.g. 2010). However, this is not always the case, which could be related to the region under investigation. Additionally, the NAO appears to have minimal impact on the wind stress curl over this region (r = 0.1). However, the NAO index is significantly correlated to the winter wind stress over the GS (r = -0.53) and to the winter Ekman transport at 50^oN (r = -0.63). The reduced Westerlies during negative NAO periods leads to a reduced southward Ekman transport at 50^oN (*Marshall et al.*, 2001). This is clearly visible during the winter of 2010 (Figure 5.8d and Figure 5.8e).

To investigate if the amount of near-surface GS water that resides in the SR or SPG after 1 year is influenced by the winter forcing and Ekman transport seen in Figure 5.8a-d, each monthly release (for 30 years) is correlated with the Qnet, wind stress, wind stress curl and Ekman transport. This is shown in Table 5.2 with all release months being correlated with the average winter (JFM) forcing/transport of the same year with the releases in September-December also correlated with the winter forcing/transport of the following year. This is because the trajectories released later in the year are more likely to feel the effects of the upcoming winter. Significant, but opposite, correlations exist between the mean winter wind stress curl and the percentage of trajectories travelling in the SR (negative correlation) and the SPG (positive correlation) for the January and February releases. This implies that when a more negative winter wind stress curl exists to the south of the GS a higher percentage of trajectories travel in the SR with fewer trajectories continuing northward into the SPG. This could suggest that greater wind stress curl forcing may lead to a stronger SR. This relationship also exists for the October and December releases with the following winter's wind stress curl forcing.

In order to visualize this, the composite of anomaly of winter (DJF) trajectory density (i.e. the number of trajectories that have passed through each grid cell) for the five strongest (1985, 1990, 2004, 2006 and 2007) and weakest (1983, 1984, 1986, 1995 and 2005) winters of wind stress curl forcing (see Figure 5.8b) is shown

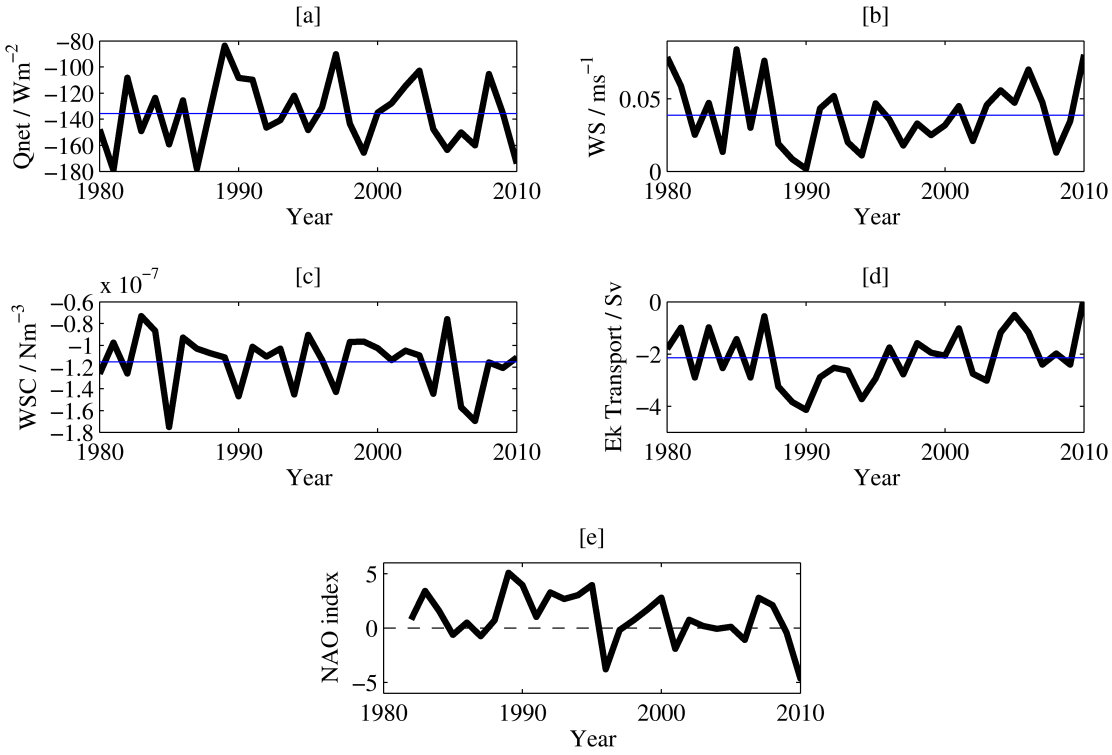

Figure 5.8: Winter (JFM) surface heat flux (W m^{-2}) (Qnet) averaged over the Sargasso Sea region from $25-35^oN, 50-80^oW$ [a], along GS wind stress (m s^{-1}) (WS) averaged over a smaller region from $36-38^o$N, $69-71^o$W [b], wind stress curl (N m^{-3}) (WSC) avergaed over the Sargasso Sea region [c] and the mean winter (JFM) Ekman (Ek) transport (Sv) at 50^oN across the basin [c] over the period 1980-2010 in the ORCA12 hindcast, the blue line denotes the mean in each panel. The winter (djfm) NAO index found online at [https://climatedataguide.ucar.edu/climate-data/hurrell-north-atlantic-oscillation-nao-index-station-based], which is based on the difference of normalized sea level pressure between Lisbon, Portugal and Stykkisholmur/Reykjavik, Iceland, [e] is also shown with the dashed line equal to zero.

in Figure 5.9a. It clearly shows that a greater number of trajectories reside in the SR during years of strong wind stress curl forcing with up to 1500 more reaching west of 60^oW compared with years of weak wind stress curl.

Interestingly, the opposite relationship exists with Qnet (Table 5.2) where a greater heat loss (more negative Qnet) leads to greater throughput to the SPG and less to the SR for the same months. However, these results are not significant. This is further highlighted in Figure 5.9b, which shows the composite of anomaly of winter (DJF) trajectory density (i.e. the number of trajectories that have passed through each grid cell) for the five strongest (1981, 1987, 1999, 2005 and 2007) and

Table 5.2: Correlation coefficient of the percentage of trajectories residing in the SR and SPG when released at $10m$ and allowed to travel in the flow field for 12 months, with the average winter (JFM) surface heat flux and wind stress curl (WSC) (in the region $25-35^oN$, $50-80^oW$), the average winter (JFM) wind stress (WS) (in the region $36-38^o$N, $69-71^o$) and the average winter (JFM) Ekman transport (Ek) along 50^oN across the basin. This is calculated for the same release year (0 lag) and for the later releases (September-December) also the following year (1 year lag). Significant, i.e. $p < 0.05$, relationships are highlighted in bold.

Month	Qnet—SR	Qnet—SPG	WS—SR	WS—SPG	WSC—SR	WSC—SPG	Ek—SR	Ek—SPG
Jan	0.24	-0.30	0.10	-0.05	**-0.49**	**0.51**	-0.09	0.14
Feb	0.31	-0.36	-0.20	0.26	**-0.58**	**0.50**	-0.15	0.13
Mar	-0.19	-0.09	0.12	-0.06	-0.17	0.21	0.3	-0.28
Apr	-0.09	-0.03	0.27	-0.15	-0.09	0.14	0.26	-0.14
May	0.27	-0.23	0.03	0.02	-0.04	0.00	0.04	-0.09
Jun	-0.33	**0.38**	0.16	-0.13	-0.02	0.02	0.15	-0.11
Jul	-0.07	0.02	-0.11	0.03	0.06	0.04	-0.15	0.23
Aug	-0.08	0.20	0.21	-0.31	0.14	0.00	0.3	**-0.42**
Sep	0.26	-0.27	-0.06	0.02	0.10	0.06	0.07	0.02
Oct	-0.12	0.16	0.14	-0.10	-0.07	-0.02	0.03	-0.07
Nov	0.15	0.00	-0.21	0.12	-0.06	0.00	-0.1	0.04
Dec	-0.26	0.24	0.27	-0.28	0.03	-0.08	0.19	-0.28
Sep (+1)	0.05	-0.06	-0.13	0.12	0.07	-0.03	0.01	0.1
Oct (+1)	0.15	-0.21	0.00	0.08	-0.29	**0.37**	-0.08	0.13
Nov (+1)	0.09	-0.16	-0.03	0.05	0.04	0.01	-0.12	0.12
Dec (+1)	0.15	-0.17	-0.07	0.09	**-0.43**	**0.40**	-0.08	0.04

weakest (1982, 1989, 1997, 2003 and 2008) winters of Qnet forcing (see Figure 5.8a). No significant correlations exist for the alongstream winter wind stress but there is some indication that more particles reside in the western SR region when there is a greater wind stress. This is revealed in the composite anomaly in Figure 5.9c for the five years of greatest wind stress (1980, 1985, 1987, 2006 and 2010) and five years of weakest wind stress (1984, 1989, 1990, 1994 and 2008). Additionally, the Ekman transport is not significantly correlated to the throughput to the SPG or SR during any monthly release (except for the SPG in August). Further evidence for this is shown in the composite anomaly for the five strongest Ekman transport years (1988, 1989, 1990, 1994 and 1995) and five weakest transport years (1983, 1985, 1987, 2001 and 2005) (Figure 5.9d). As was found earlier, the Ekman transport is significantly correlated to the NAO index (and the wind stress curl forcing is not), which implies that the throughput of near-surface GS water to the SPG or SR is not controlled by the NAO.

To summarise, near the surface, interannual variability exists in the downstream destination of GS water with multi-year periods of greater/less throughput to the SPG and SR evident. However, as opposed to periods of greater through flow to the SPG being counterbalanced by less flow to the SR on seasonal timescales, the greater flow to the SPG occurs alongside less flow to the SR and the AC on in-

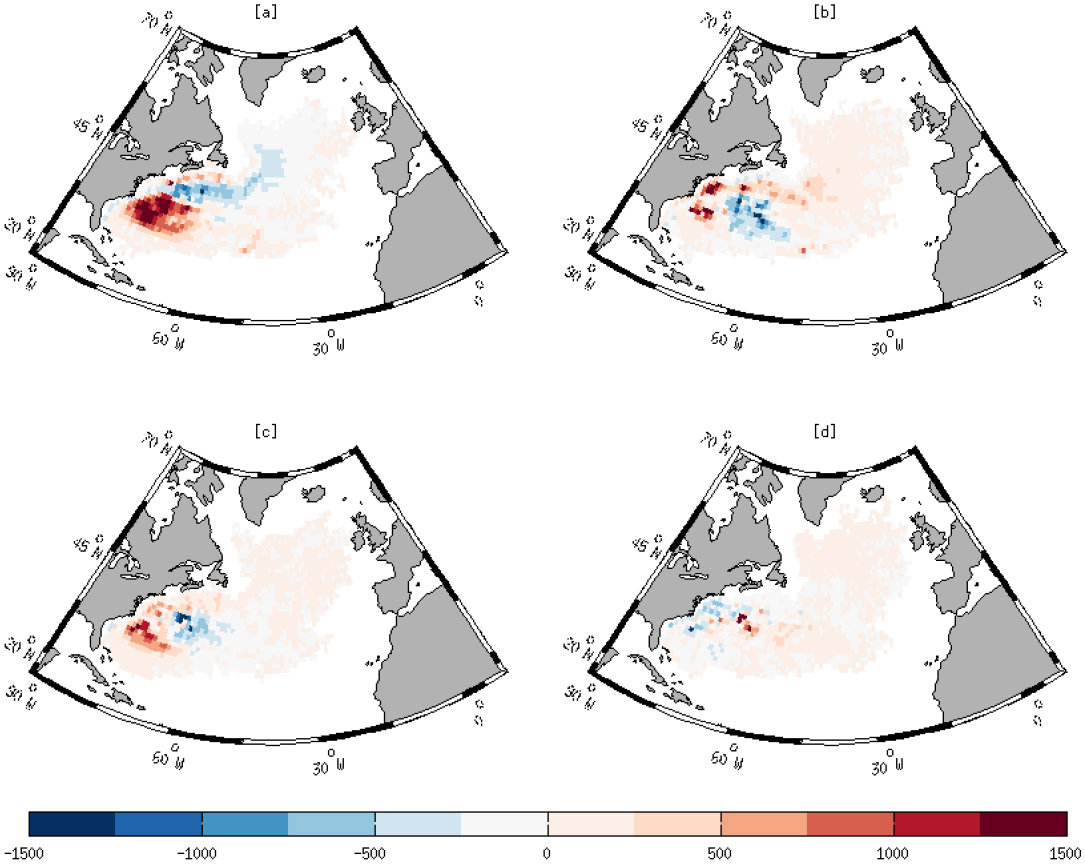

Figure 5.9: Composite anomaly of winter (DJF) trajectory density (number particles per grid box averaged over 1^o grid boxes) for the 5 years of strongest and weakest winter (JFM) wind stress curl [a], Qnet winter (JFM) forcing [b], winter (JFM) wind stress [c] and and winter (JFM) Ekman transport [d], for trajectories released at $10m$ in the Florida Straits and allowed to travel in the flow field for 1 year.

terannual timescales. This implies that the interannual variability in trajectories travelling in the AC is greater than that seen seasonally. Greater variability is seen on monthly timescales, especially in winter, which was found to be influenced by winter forcing. Specifically, the number of trajectories travelling to the SR and SPG is significantly correlated to the wind stress curl averaged over the Sargasso Sea region to the south of the GS. A greater wind stress curl leads to a greater (smaller) proportion of trajectories residing in the SR (SPG), which provides evidence that the SR is intensified during these years. By Sverdrup relations, mass transport is proportional to the wind stress curl so a greater (i.e. more negative) wind stress curl would increase the strength of the southern recirculation. Contrastingly, no significant correlation is found between these two GS pathways and

Qnet, alongstream wind stress or the Ekman transport, which suggests that the wind stress curl is a more important factor in influencing the proportion of trajectories travelling to the SR and SPG during the winter. This opposes that found in Chapter 4, which found a westward intensified SR occurred alongside periods of greater GS transport that coincided with winters of greater heat loss. This could be due to different periods being examined (i.e. at the end of winter as opposed to the winter average or could also be related to a particular region of large Qnet being more important than a widespread heat loss. Despite this, the finding that winters of strong wind stress curl over the SR region can induce an intensification in the SR is unprecedented and may have an impact on the overall throughput to the SPG on interannual timescales.

5.5 Subsurface interannual variability

Similar to the previous section, here the interannual variability of GS pathways is quantified at the subsurface, i.e. when released at $200m$. In particular, the SPG- and STG-bound pathways are examined in terms of the progression of trajectory latitude, longitude, depth, density, temperature and salinity over time in order to establish when and how the two pathways separate. Additionally, the subsurface GS pathways are analysed on decadal timescales with particular emphasis on the SPG pathway. Several mechanisms are examined for the variability in subsurface throughput to the SPG via the GS with the implications to the hydrography of the SPG also discussed.

5.5.1 Variability of Gulf Stream pathways

The interannual variability in the downstream destination of GS water at $200m$ is displayed in Figure 5.10. The year-to-year variability is less than that seen near the surface (Figure 5.6) but the range in interannual variability is still of a similar magnitude. This is due to decadal variations in the throughput of GS water to the SPG at this depth. For example, a period of increasing throughput to the SPG exists from 1982 (22%) to 1992, where it reaches a maximum of 58%, before

declining to 19% by 2009. This is mostly counteracted by a decrease followed by an increase in trajectories residing in the SR. However, during the period of high throughput to the SPG, in addition to a decline in flow to the SR, there is also less flow in the NR, AC and remaining in the GS. This surge of GS water to the SPG during the 1990s could be related to a prolonged period of positive winter NAO and is further investigated later. Additionally, at this depth interannual variability exists for trajectories residing in the Slope Water after being recirculated to the north (NR). This percentage also exhibits more decadal variability with the percentage remaining low during the late-1980s to mid-1990s (2%) before increasing again (5%) during the late-1990s to 2000s. The trajectories residing in the AC is less variable at this release depth compared to 10m (Figure 5.6).

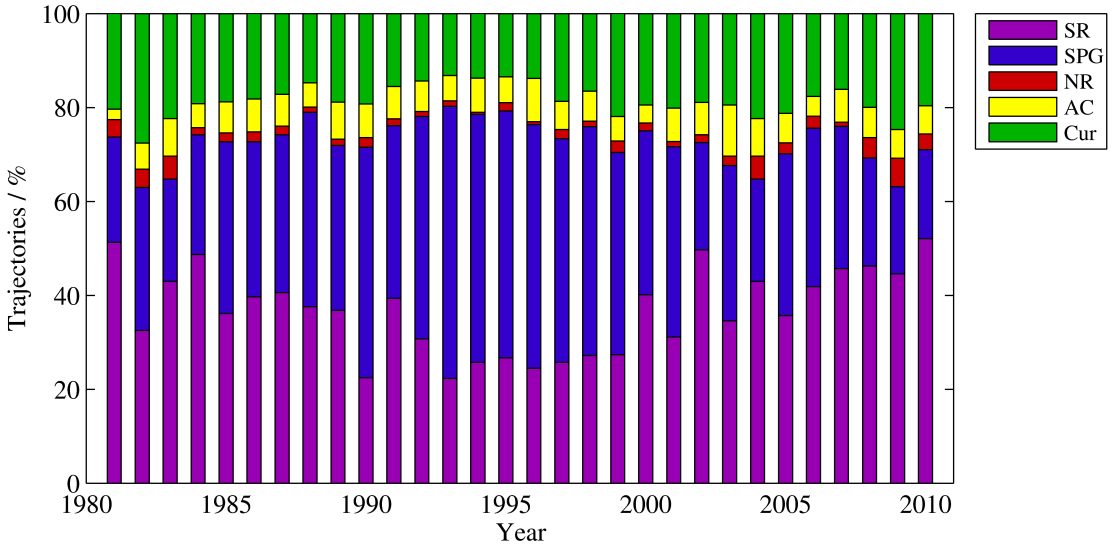

Figure 5.10: Downstream destination of Gulf Stream water after bifurcation (%) at different release years when initiated in the Florida Straits and allowed to travel for 12 months when released at $200m$ and averaged over all months. Particles may enter the SPG, the SR, the NR, the AC or remain in the main Gulf Stream current (Cur).

5.5.2 Subtropical gyre and subpolar gyre pathways

In order to distinguish the pathways of trajectories travelling to the SPG from those that remain in the STG, the average latitude and longitude for each of these pathways for all releases at $200m$, is revealed in Figure 5.11a. The STG-bound trajectories are comprised of all those that do not travel to the SPG, i.e. those residing in the SR, NR, AC and Cur. It shows that, on average, trajectories travelling to the SPG reach a greater latitude, by definition $> 50^oN$, and a more eastward longitude ($< 35^oW$) compared to those remaining in the STG where the maximum latitude and longitude reached are about 40^oN and 45^oW respectively. There is also some evidence that the SPG-bound trajectories take a more northerly path before the GS turns northward at about 50^oW with the SPG and STG pathway bifurcation point occurring as far west as 72^oW. This can also be seen in Figure 5.11b, which shows the mean latitude with age for both pathways. The bifurcation point here occurs at about 30 days. This suggests that the trajectories travelling to the SPG reach a more northerly latitude, and therefore a denser isopycnal, fairly soon after separation from the coast at Cape Hatteras. This can be seen more clearly in Figure 5.12, which focuses on the longitude band $75 - 65^oW$ in Figure 5.12a and the time period 20-50 days in Figures 5.12b-f. Figure 5.12b reveals that after the bifurcation point at 30 days, the pathways begin to diverge until those trajectories travelling to the SPG are about 0.5^o further north of those remaining in the STG by 50 days, just one month after the bifurcation point.

There are also divergences in the depth, temperature, salinity and density between the two pathways, which will now each be discussed in turn. Initially, all trajectories deepen slightly (Figure 5.11c) until about 25 days where those remaining in the STG continue to deepen to about $230m$ before levelling out at 70 days where the depth remains similar, on average, for the duration of the run. Contrastingly, those travelling to the SPG begin to shoal after 25 days where they reach about $150m$ after 1 year. This is further highlighted in Figure 5.12c, which shows the trajectories diverging by about $30m$ from 25-50 days.

The average density of trajectories remaining in the STG remains at a similar value throughout the run (Figure 5.11d) but those travelling to the SPG are seen

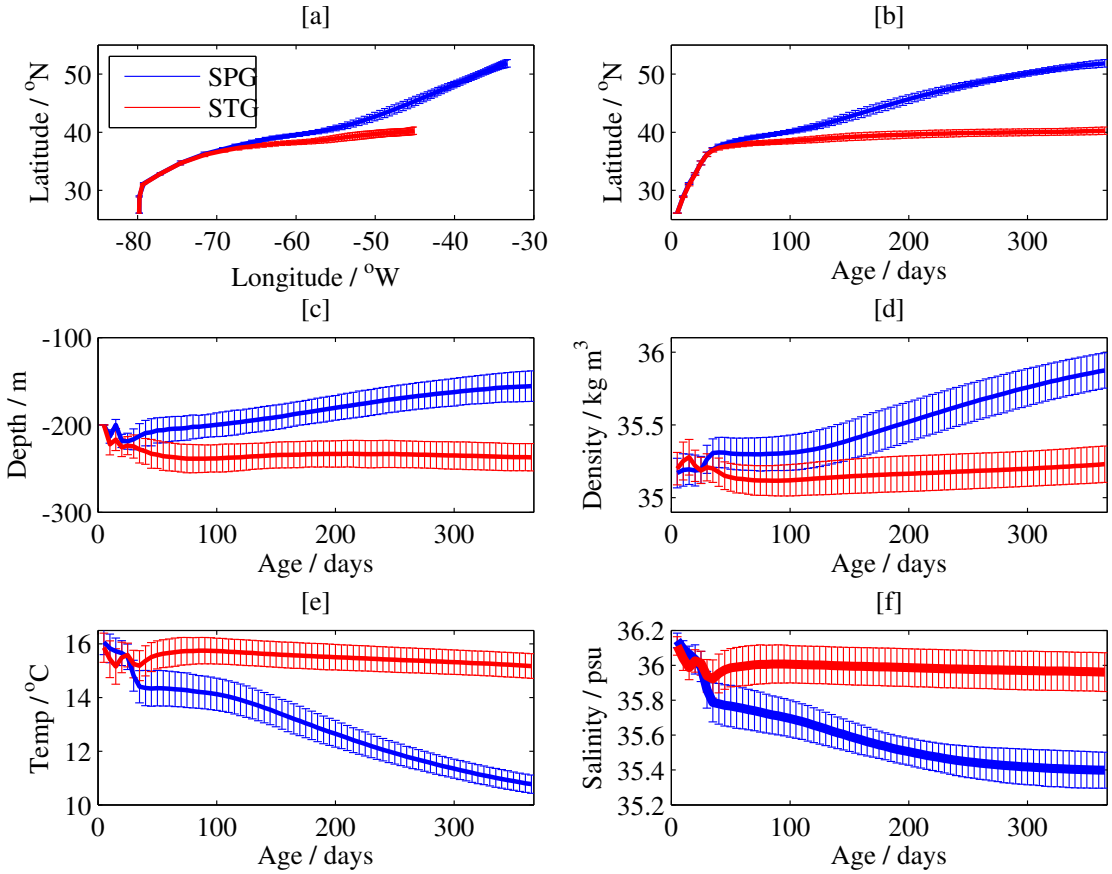

Figure 5.11: Average latitude (^oN) with average longitude (^oW) [a], and average latitude (^oN) [b], depth (m) [c], density (kg m^3) [d] temperature (^oC) [e] and salinity (psu) [f] with age (days) for trajectories travelling to the SPG or remaining in the STG after 1 year when released at $200m$ in the Florida Straits. Trajectories are averaged over all monthly and yearly releases with STG trajectories composed of all those not travelling to the SPG, i.e. southern recirculation, northern recirculation, the Azores Current or remaining in the main current. Error bars are the standard deviation of the annual average at each 5-day interval.

to become denser after 25 days. From this point, they continue to increase their density by up to 0.6 kg m^3 as they reach the SPG. This occurs alongside a reduction in temperature of up to 5^oC (Figure 5.11e) and a freshening of up to $0.6psu$ (Figure 5.11f) between 25 and 365 days. These trends suggest that the trajectories residing on the northern flank of the GS immediately after separation and, therefore, a denser isopycnal, are more likely to travel to the SPG. Conversely, those that reside on the southern flank of the GS, i.e. a less dense isopycnal, are more likely to remain within the STG. This is further highlighted in Figure 5.13, which shows the mean density in 2008, used as an example year, along 70^oW with the location of the SPG- and STG-bound trajectories overlaid for the first 100 days. The star

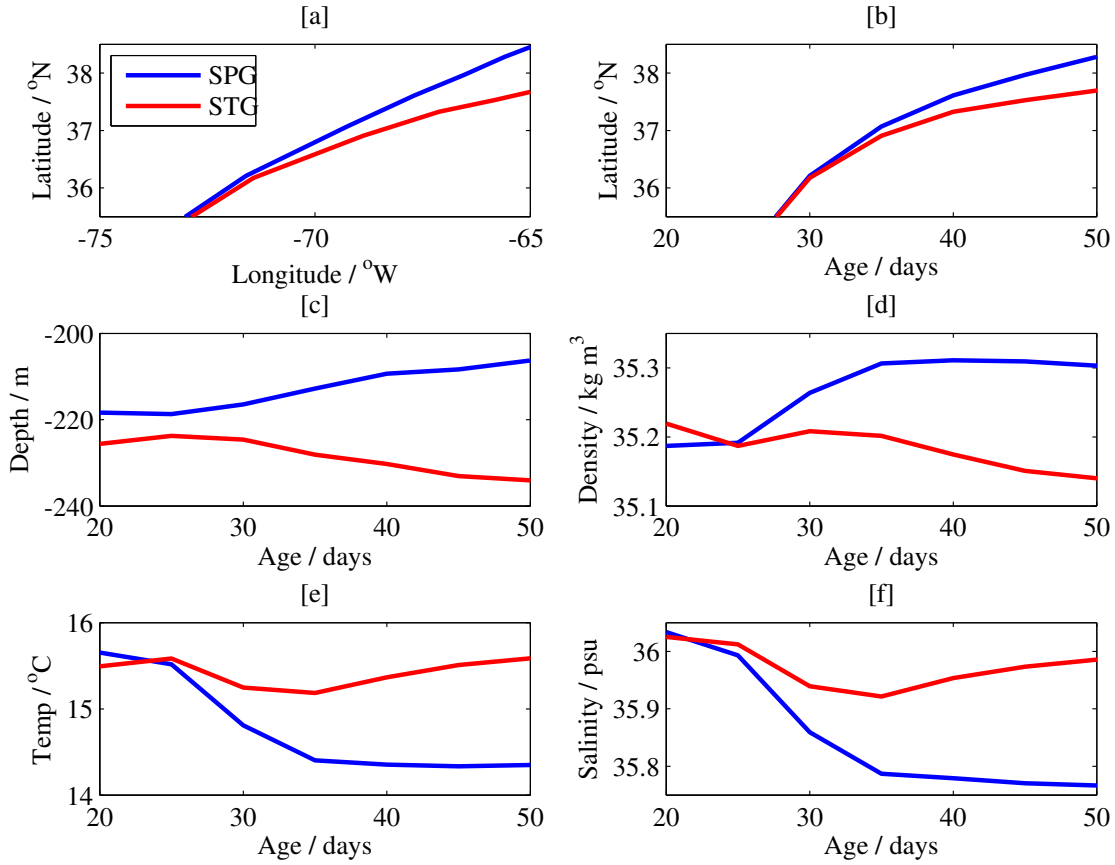

Figure 5.12: As seen in Figure 5.11 but zoomed in to the so-called bifurcation point at $75 - 65^{o}W$ in [a] and $20 - 50$ days in [b, c, d, e, f].

markers highlight the location of trajectories after 40 days, which by this point clearly shows that those travelling to the SPG are on a denser isopycnal, which is up to $10m$ shallower and nearly 0.5^{o} further north than those remaining in the STG.

5.5.3 Decadal variability of subpolar gyre-bound trajectories

The variability of the subsurface pathway to the SPG for each month is revealed in Figure 5.14a. Similar to that seen in Figure 5.10 when examining the annual average, the percentage of trajectories reaching the SPG exhibits some decadal variability where a steady increase occurs from the 1980s to the mid-1990s, which is then followed by a decline until 2009. When investigating individual monthly releases the maximum and minimum values are more extreme than when analysing

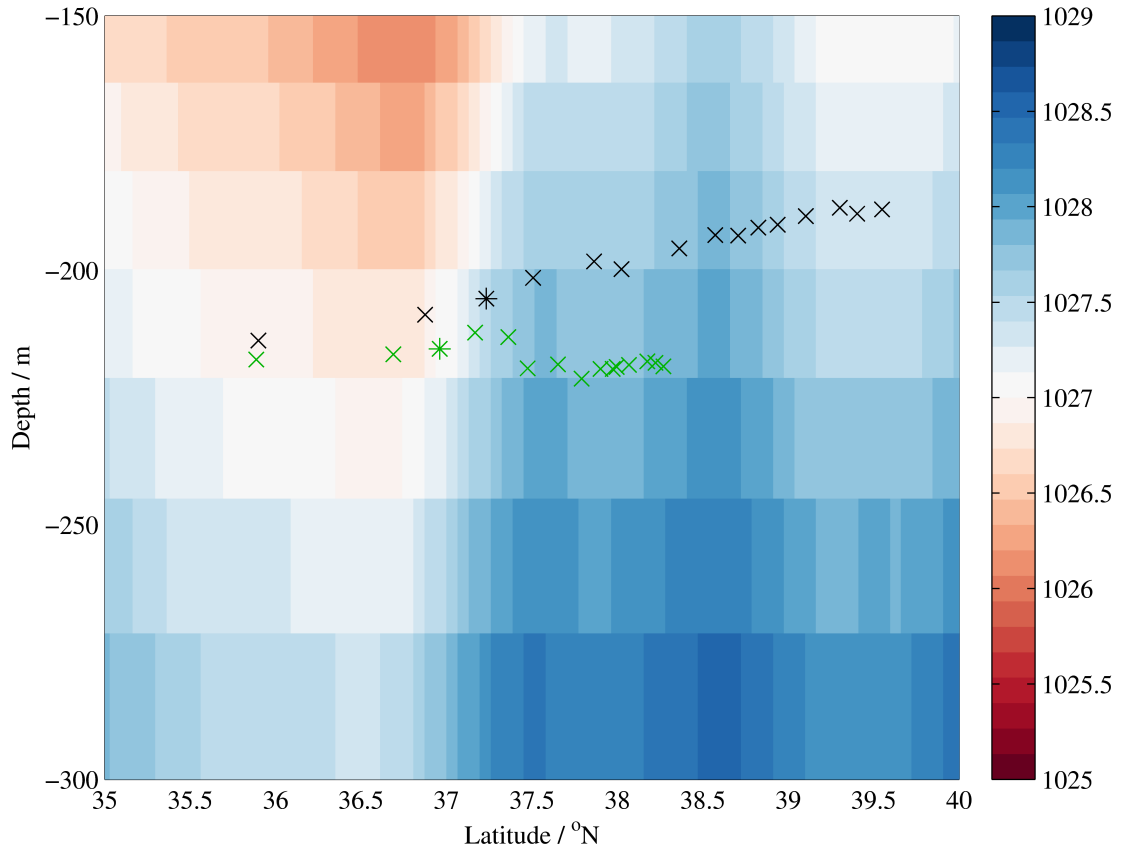

Figure 5.13: Mean density (kg m^3) along 70^oW from $35-40^oN$ and $150-300m$ in 2008 with the location of the SPG- (black x) and STG-bound (green x) trajectories from 25-100 days. The star (*) markers highlight the location of trajectories after 40 days.

the annual average, which highlights the considerable variability across a wide range of timescales. For example, a maximum of 80% of trajectory throughput to the SPG occurs in October 1992, which compares with the annual average of 58% in 1992. Regardless of this, there is a clear decadal fluctuation, which sees a greater throughput to the SPG during the 1990s and a reduced throughput during the 2000s. This could be related to the winter NAO pattern, which is displayed in Figure 5.14b alongside the winter (DJF) average throughput to the SPG. For example, the positive phase dominates the 1980s until 1995, which was followed by a more neutral period that was punctuated with several sharp NAO negative years (e.g. in 1996 and 2010). The percentage of trajectories reaching the SPG when released in winter (DJF) is significantly correlated (to the 95% confidence interval) with the NAO index at a 3-year lag (r = 0.48). This suggests that the persistently positive NAO period could have led to a temporary surge of GS waters into the

SPG region.

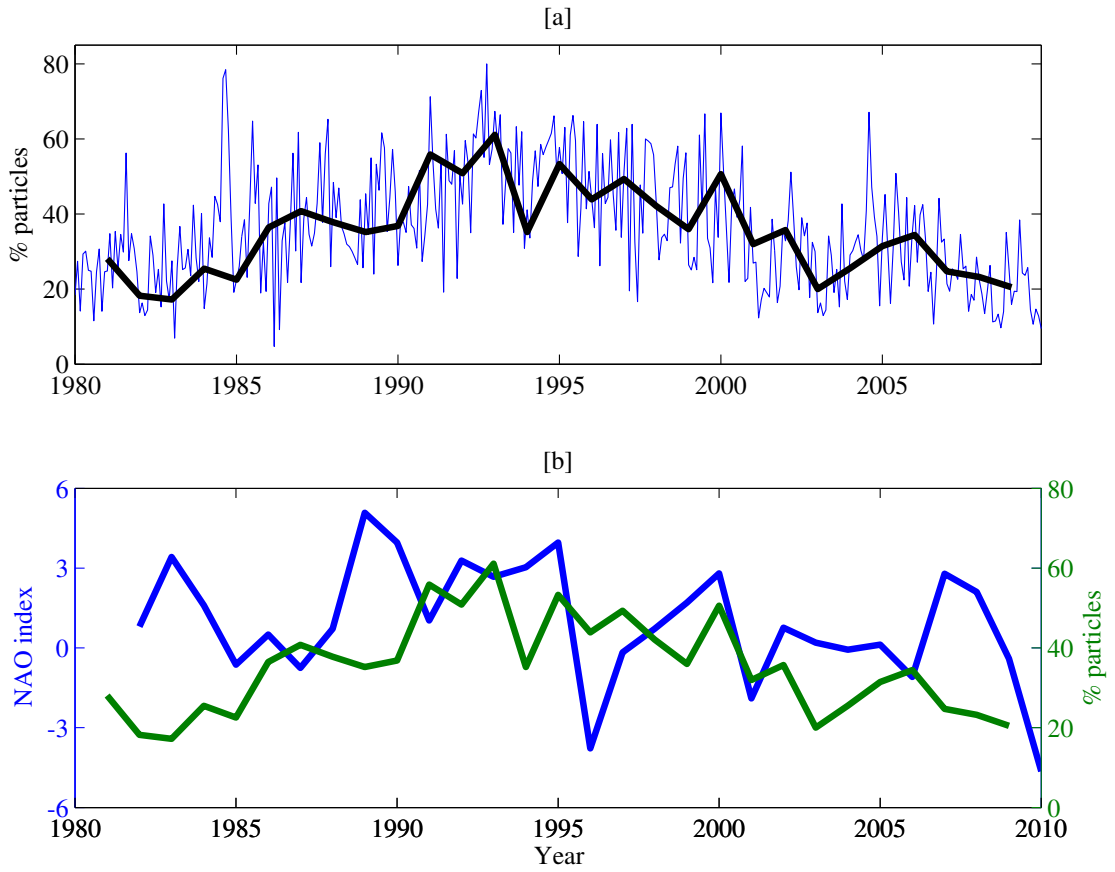

Figure 5.14: Trajectories residing in the SPG (%) for every month (blue line) and averaged over the winter (DJF), from 1980-2009, when released at 200m in the Florida Straits and travelling in the flow field for 12 months [a]. The winter (DJF) average is also plotted alongside the winter NAO index (from Figure 5.7c) over the same period.

There is much literature on how the NAO influences the SPG with clear distinctions between the eastern and western halves, the former is not important here so the western half will be the main focus. During positive NAO winters, there is a greater heat loss over the Labrador Sea due to strengthened westerlies, which intensifies deep convection and leads to a greater formation of LSW (*Hurrell et al.*, 2003). This causes anomalously cold and fresh anomalies to prevail at intermediate levels in the western SPG (*Sarafanov*, 2009). However, after prolonged periods of positive NAO, models have shown that the increased deep water formation has led to an intensification of the AMOC (*Häkkinen*, 1999; *Eden and Willebrand*, 2001; *Dong and Sutton*, 2005; *De Coëtlogon et al.*, 2006; *Lohmann et al.*, 2009; *Robson et al.*, 2012). This has been found to cause increased northward transport in

the upper ocean at a lag of 4-5 years (*Robson et al.*, 2012; *Stepanov and Haines*, 2014), which leads to an anomalously warm western SPG (*Robson et al.*, 2012). This occurred after the period of persistently positive NAO from the late-1980s to mid-1990s with an immediate cooling and freshening followed by a warming, which peaked in the mid-1990s (*Zhang*, 2008; *Robson et al.*, 2012). These AMOC changes are seen in reanalyses and models (*Böning et al.*, 2006; *Grist et al.*, 2010). Here, there is evidence that this result is also reproduced in ORCA12.

In order to establish why there was a greater throughput to the SPG and less throughput to the STG during this period, Figure 5.15 examines the average pathways of the trajectories travelling to the SPG during the 1990s and 2000s. Figure 5.15a and Figure 5.15b reveal very little difference in the average latitude between the two decades. During the 1990s, the pathway was slightly further north from about 140-250 days but this is likely due to the fact that the trajectories are reaching the SPG more quickly compared with that during the 2000s. However, Figure 5.16 shows the anomalous surface speeds during the 1990s compared to the 2000s, which reveals that a positive anomaly exists on the shoreward side of the GS from about $32-37^oN$, $80-70^oW$. This could suggest that the GS is in a more northward position, after separation, during the 1990s, which may have encouraged a greater proportion of trajectories to take a more northward pathway. This northward shift may have been caused by any individual mechanism, or more likely a combination of the mechanisms discussed in Chapter 1.3.2. For example, as a delayed response to the positive NAO or as a direct response to a northward shift in the position of the line of zero wind stress curl (*Heywood et al.*, 1994).

The difference in the average trajectory depth between the two decades is seen in Figure 5.15c. As seen in Figure 5.11c, when travelling to the SPG the trajectories begin to shoal from about 25 days, i.e. at the same bifurcation point as that seen in Figure 5.12. When there is a greater through flow to the SPG during the 1990s, the trajectories follow a deeper pathway after this point with trajectories arriving up to $40m$ deeper, on average, than in the 2000s. Overall, during the 1990s, more trajectories reached a greater depth, and therefore a denser isopycnal, after separation from the coast at Cape Hatteras, which enabled an increased flow

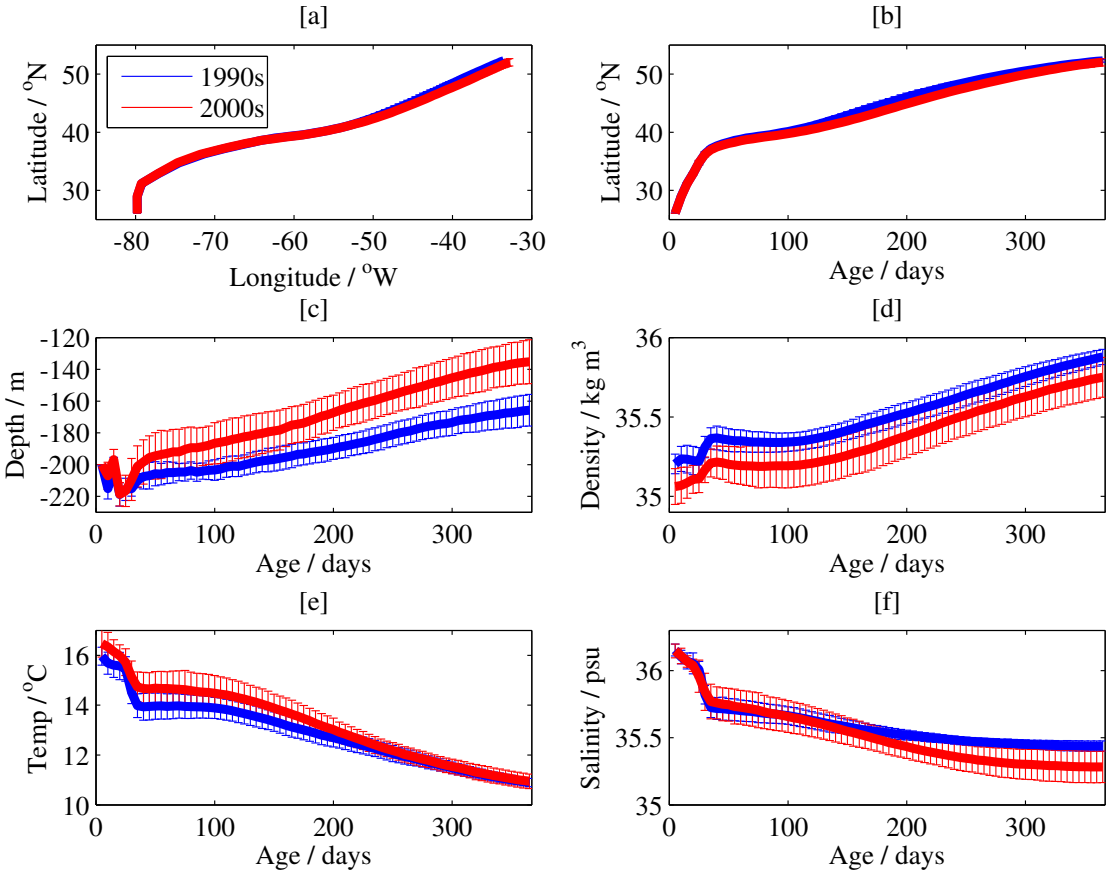

Figure 5.15: Average latitude (^oN) with average longitude (^oW) [a], and average latitude (^oN) [b], depth (m) [c], density (kg m^3) [d], temperature (^oC) [e] and salinity (psu) [f] with age for trajectories travelling to the SPG after 1 year during the 1990s and 2000s when released at $200m$ in the Florida Straits. Error bars are the standard deviation of the annual average at each 5-day interval.

to the SPG.

This is confirmed in Figure 5.15d, which shows that the trajectories travel on a denser (up to $0.2kg\ m^3$) pathway during the 1990s. From 25-200 days, this is likely related to a lower temperature (Figure 5.15e) of up to 1^oC cooler for the mean pathway during the 1990s. However, the temperature during the two periods is similar after this. Contrastingly, the salinity prior to 150 days is similar during both periods but after this begins to diverge with a more saline path during the 1990s (Figure 5.15f). The difference in trajectory density is likely due to the competing effects of temperature and salinity with temperature being dominant from 25-150 days and salinity dominating after this. Interestingly, Figure 5.15d reveals that the trajectories released in the 1990s also begin on a denser isopycnal (by up to

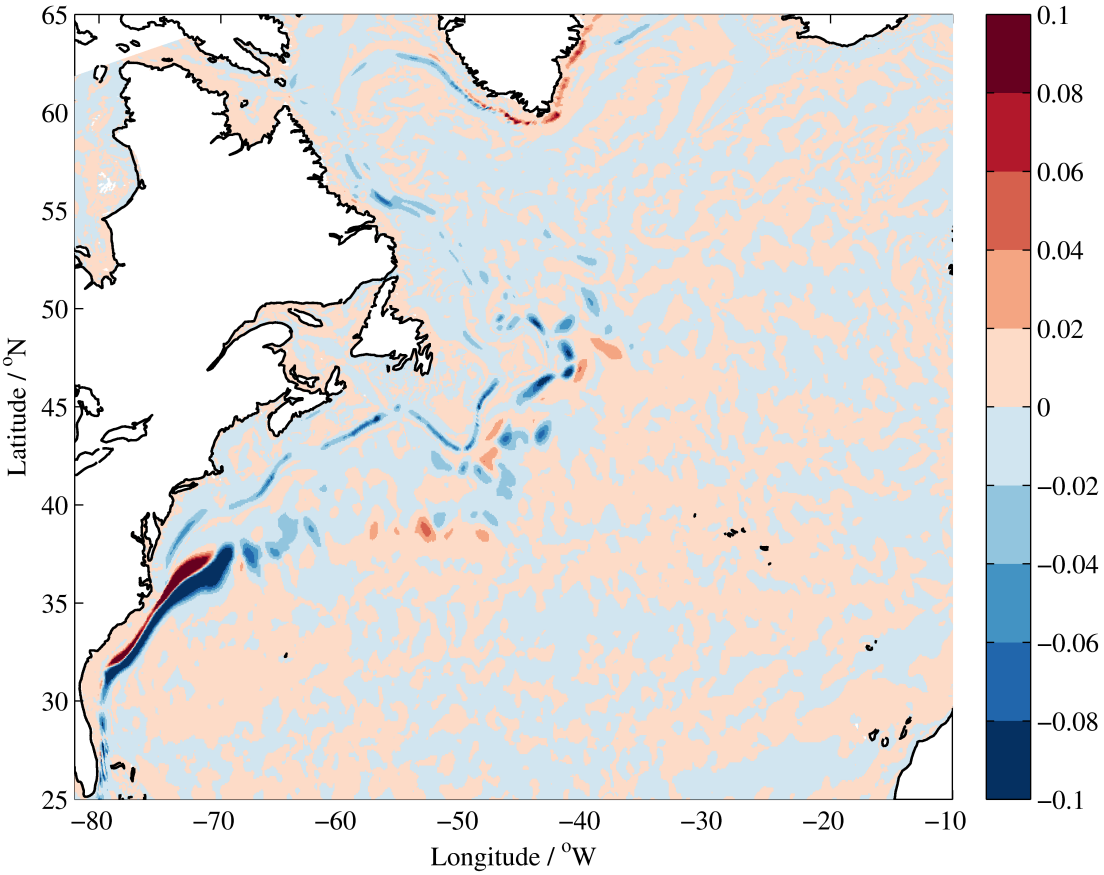

Figure 5.16: Surface speed (m s^{-1}) composite anomaly for 1990s minus 2000s in the ORCA12 hindcast.

0.2 kg m^3) when released in the Florida Straits. This is further highlighted in Figure 5.17, which shows the composite anomaly for temperature in the Florida Straits for the 1990s minus the 2000s. During the 1990s, a negative anomaly of up to 2^oC is evident at the subsurface in the Florida Straits, which extends into the subsurface GS path at this latitude (26^oN). Figure 5.18 shows the mean starting density (Figure 5.18a), temperature (Figure 5.18b) and salinity (Figure 5.18c) of trajectories averaged for each year. It shows that the temperature is $1-2^oC$ cooler during the 1990s, which led to the trajectories starting on a denser isopycnal (by about $0.2kg\ m^3$) compared to during the 2000s. The decadal change in salinity is not as consistent as the change in temperature so the denser isopycnal at the release location is mostly due to cooler temperatures. This could also explain the greater throughput to the SPG during this decade as, as was established earlier, trajectories residing on a denser isopycnal are more likely to be able to reach the

northward side of the GS and travel directly to the SPG, where they continue to cool and increase their density.

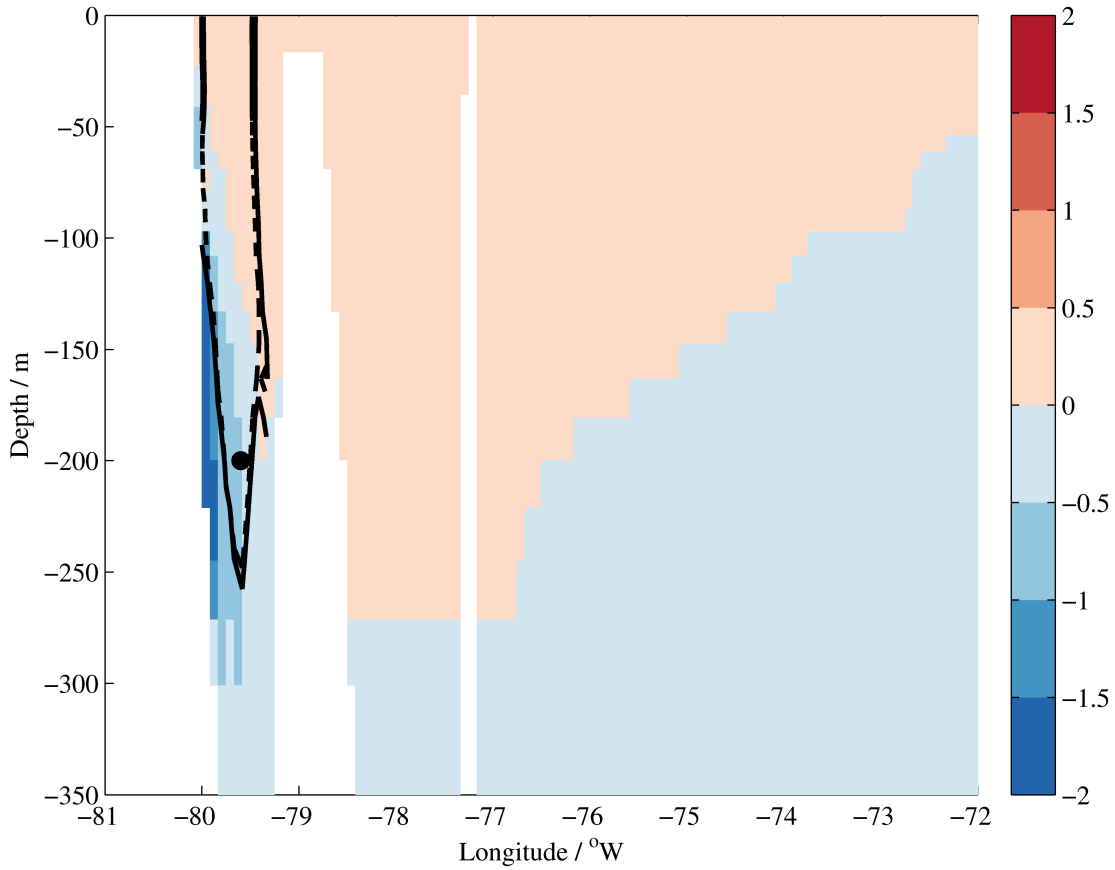

Figure 5.17: Temperature composite anomaly for the 1990s minus the 2000s at 26^oN in the ORCA12 hindcast. The solid black line is the average location of the 1 m s^{-1} meridional velocity contour during the 1990s while the dashed black line represents this during the 2000s. The black marker represents the release location at $200m$.

In addition to this, it has been shown that a PV barrier exists across the GS core, which is associated with a large density shear and has been found to inhibit intergyre exchange near the surface (*Bower et al.*, 1985; *Rypina et al.*, 2011). However, this was found to weaken with depth, which may allow a greater intergyre exchange at the subsurface (*Rypina et al.*, 2011). This is investigated in Figure 5.19 that shows the PV across 45^oN (Figure 5.19a) and 40^oN (Figure 5.19b) at $200m$, which is where the trajectories travelling to the SPG begin to turn northward. During the 1990s the PV at this depth is less than that seen during the 2000s at both latitudes. However, this is mostly due to the existence of a greater PV barrier during the 2000s as, during the 1990s, the PV is closer to the mean. This

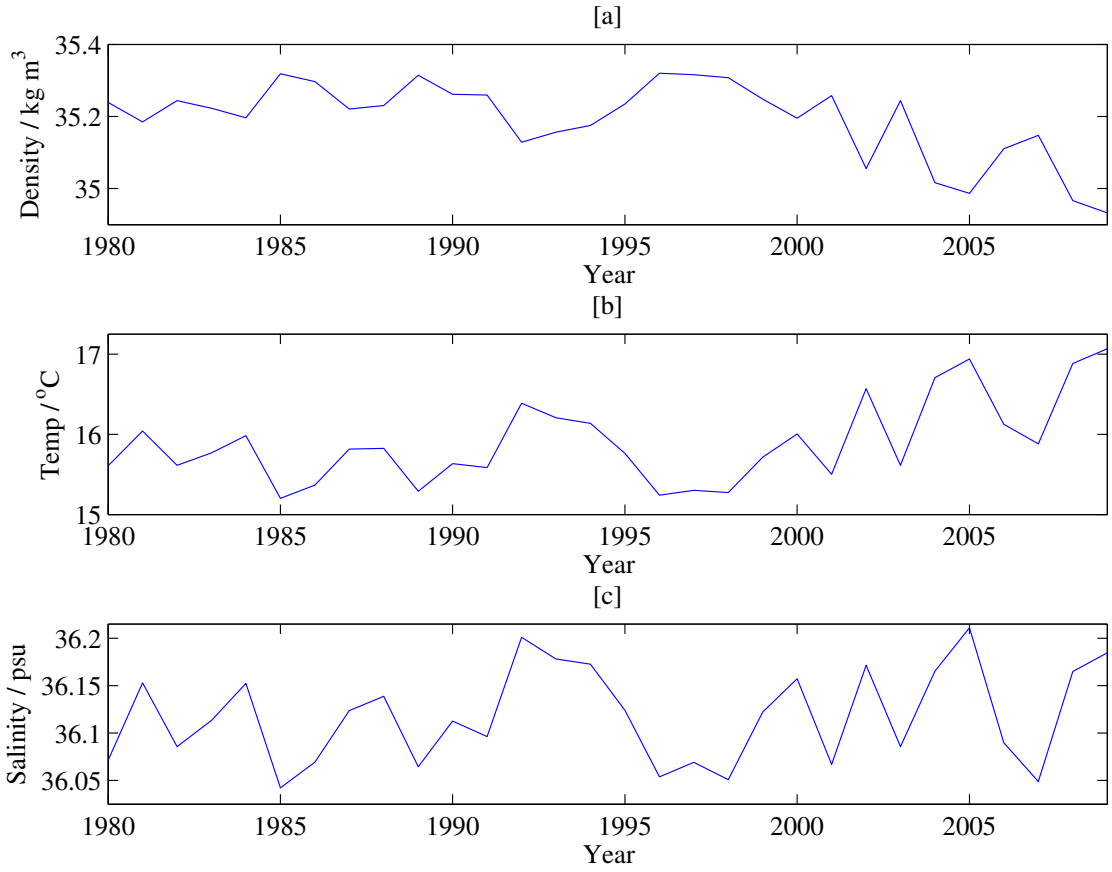

Figure 5.18: Mean density (kg m^3) [a], temperature (^oC) [b] and salinity (psu) [c] at $200m$ for each year at the release location (in the Florida Straits at 26^oN).

mechanism may have enabled a greater through flow to the SPG during the 1990s compared with the 2000s. *Bower et al.* (1985) found that the "PV barrier" was strong west of 60^oW but a "blending" region existed further east where energetic eddies dominate and act to mix high PV waters. This may suggest that during the 1990s there is greater EKE that reduces the barrier and enables greater through flow.

An example of monthly trajectory maps from the two decades, i.e. October 1992 and 2009, is displayed in Figure 5.20a. These releases were selected as they are from the years that exhibit the greatest and least throughput to the SPG respectively. For the 1992 release the red trajectories extend further into the SPG in all directions, compared to the blue trajectories for 2009, but with a particular emphasis in the western SPG.

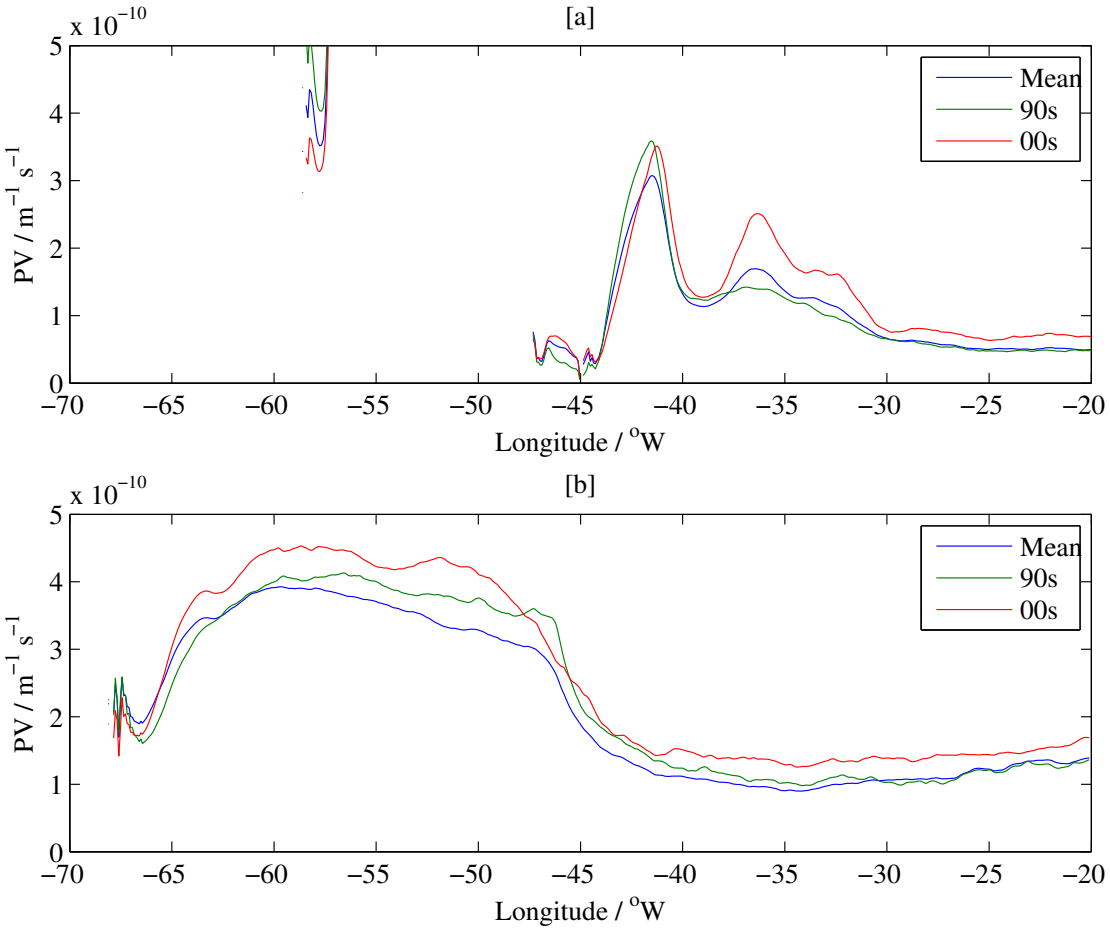

Figure 5.19: Potential vorticity (m^{-1} s^{-1}) along 45^oN [a] and 40^oN [b] at $200m$, shown as a mean from 1978-2010, and averaged over the 1990s and 2000s in ORCA12 hindcast.

In order to gain more quantitative information from this, the trajectory density is obtained by spatially averaging the number of trajectories passing through each grid cell on a 1^o grid. This is time-averaged over the high throughput period (1990s) and the low throughput period (2000s) with the difference taken between them (high-low) to give a composite anomaly. This is shown in Figure 5.20b, which reveals a positive anomaly in much of the area north of about 45^oN. Contrastingly, a negative anomaly exists over much of the STG, notably to the immediate south of the GS core. This provides further evidence that during the 1990s, more subsurface GS trajectories travel north in the NAC as opposed to recirculating in the STG. Specifically, up to 250 more particles per grid cell flow into the western SPG during the earlier period with the greatest anomalies existing in the western SPG region from $50 - 55^oN$, $45 - 35^oW$.

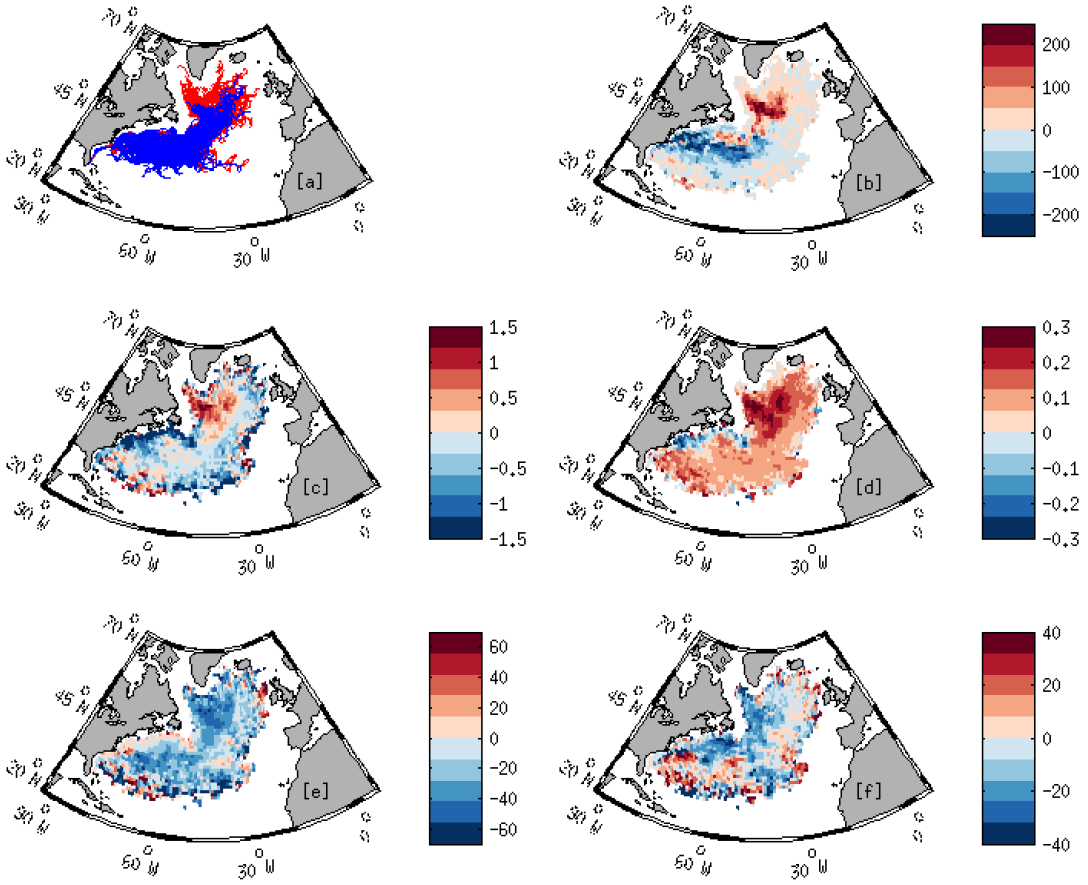

Figure 5.20: Trajectories of particles released at $200m$ in October 1992 (red) and 2009 (blue) [a] and the composite anomaly for 1990s minus 2000s for particles released at $200m$ for the trajectory density (number particles per grid box) [b], temperature (^oC) [c], salinity (psu) [d], depth (m) [e] and age (days) [f] averaged over 1^o grid boxes. All particles have been allowed to travel in the flow field for 1 year.

Figure 5.20c is the composite anomaly for the temperature recorded by the trajectories and shows a warm anomaly of up to 1.5^oC in the western SPG. This contrasts with that seen in Figure 5.15e that reveals a similar average temperature between the two periods after about 200 days. However, this is averaged across the entire SPG where the warm anomalies in the west are counterbalanced by cold anomalies in the east. In addition to this, the salinity composite anomaly in Figure 5.20d shows anomalously saline waters, up to $0.2psu$, exist over much of the North Atlantic during the earlier period. However, the western SPG exhibits a greater anomaly compared the rest of the SPG ($0.3psu$), which closely follows the anomalies seen in Figure 5.20b of the trajectory density. This could imply that

the anomalously warm and saline waters seen in this region are as a consequence of the greater influx of GS waters.

The composite anomaly for the trajectory depth can be seen in Figure 5.20e, which shows that the greater proportion of GS waters arriving in the western SPG are up to $60m$ deeper during the 1990s compared with the 2000s. Figure 5.20f reveals that the trajectories arriving at this location are also up to 40 days younger during this period. Overall, a greater throughput of GS waters occurs to the western SPG during the 1990s, which arrive at a deeper level and also more quickly than that seen during the 2000s. This may have led to anomalously warm and saline conditions in this region.

Further evidence for this is revealed in Figure 5.21, which shows the annual average of trajectories residing in the SPG after travelling in the GS for 1 year (Figure 5.21a), the average winter (JFM) surface heat flux in the western SPG box (Figure 5.21b) and the anomalous temperature (as an annual average) recorded within the same box at the surface and as recorded by the trajectories released at $200m$ (Figure 5.21c). The last panel shows that an anomalous warming of up to 1.1^oC occurred between 1992 and 2001, which is followed by an anomalous cooling of up to -1.5^oC until 2010. This pattern closely follows the percentage of GS trajectories reaching the SPG (Figure 5.21a) but with a lag of two years (r=0.67 and is significant to the 99% confidence interval). The peak is about three years earlier than that found in the climate model used by *Robson et al.* (2012), which may be due to the enhanced EKE in ORCA12. Additionally, there is evidence of enhanced EKE in the late-1980s to 1995 in ORCA12 from $45-55^oN$, $55-30^oW$ (*Marzocchi et al.*, 2015) that could be representative of the real ocean. This may have assisted in the weakening of the PV barrier during this period and enabled greater intergyre exchange.

There are some years where a high heat loss (Figure 5.21b) may have led to an anomalously cool western SPG, e.g. 1990 and 2008. However, the overall trend is unlikely to have caused the anomalously warm temperatures during the 1990s, which provides further evidence that the warming was caused by increased throughput of subtropical waters to the SPG.

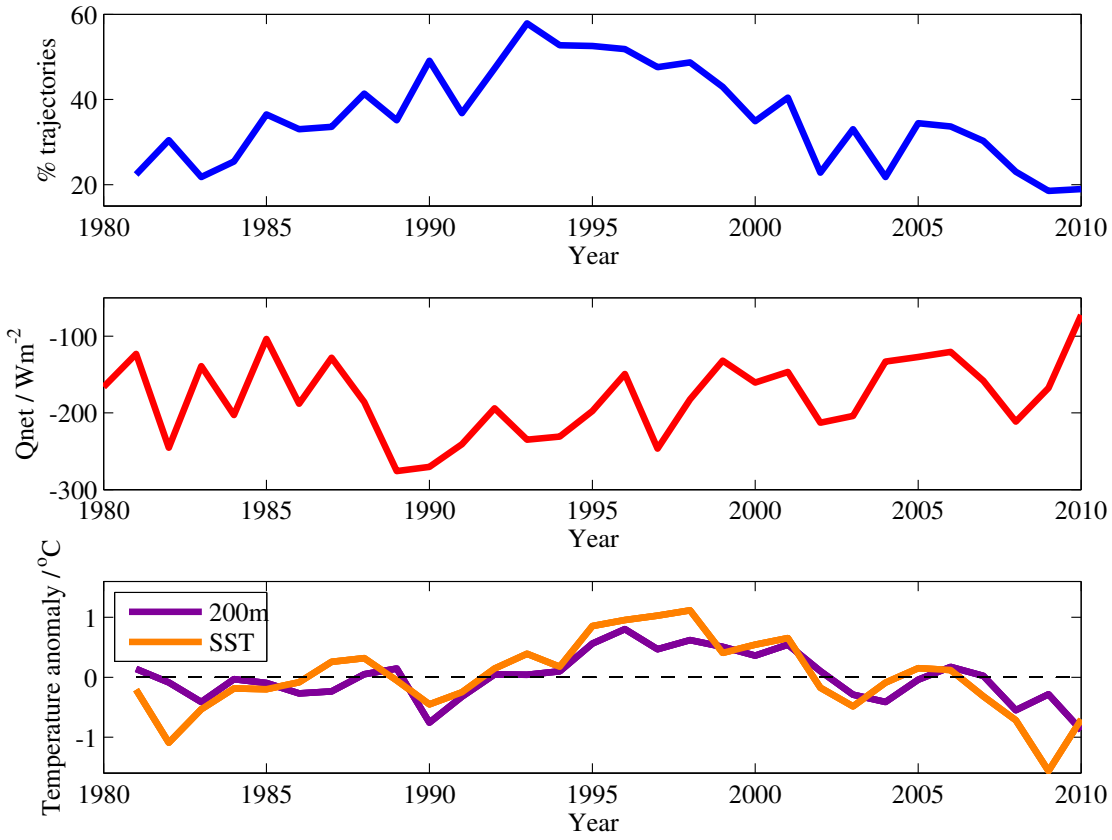

Figure 5.21: Trajectories residing in the SPG (%) shown as an annual average, from 1980-2009, when released at $200m$ in the Florida Straits and travelling in the flow field for 12 months [a], winter (JFM) surface heat flux (Qnet) (W m^{-2}) averaged in a box in the western subpolar gyre $50-55^{o}N$, $45-35^{o}W$, [b] and the anomalous temperature at the surface and as recorded by the trajectories released at $200m$ averaged over the western SPG box [c].

As opposed to the high year-to-year variability of trajectories travelling to the SPG or SR at the surface (Chapter 5.4), a decadal cycle is visible at the subsurface with an enhanced throughput to the SPG occurring during the 1990s followed by a decline during the 2000s. Compared with trajectories remaining in the STG after travelling in the flow field for 1 year, those reaching the SPG were found to take a more northerly pathway soon after separation from the coast at Cape Hatters. The bifurcation point where the two pathways diverge occurs at about 30 days. This is accompanied by a divergence in the density with those travelling to the SPG doing so on a denser pathway from about 25 days. This provides further evidence that trajectories residing on a denser isopycnal are more likely to travel to the SPG. The intensified throughput to the SPG during the 1990s may have been due to the prolonged period of positive NAO since the late-1980s. The increased LSW outflow

during positive NAO winters (*Hurrell et al.*, 2003) has been found to lead to an intensification of the AMOC, which causes enhanced northward flow in the upper ocean, i.e. a strengthened GS. This finding is also found in reanalyses and models (*Böning et al.*, 2006; *Frankignoul et al.*, 2001; *Grist et al.*, 2010). In addition to this, the greater throughput to the SPG could be related to more trajectories residing on a denser isopycnal, which coincides with a more northward GS path during this period and the fact that the trajectories begin on a denser pathway compared to during the 2000s. Furthermore, the weaker PV barrier at 40^oN and 45^oN, i.e. where the GS begins to turn northwards, during the 1990s may have also enabled a greater throughput to the SPG. The intensified AMOC during the 1990s was likely to be the main mechanism leading to an increased flow to the SPG as was found in other studies. However, it appears that the other mechanisms facilitated an even greater throughput to this region at different stages along the GS path, i.e. a denser start, followed by a more northerly GS path and a weaker PV barrier further to the east. Regardless of this, the increased throughput led to a warming of up to 1.5^oC in the western SPG during the 1990s.

5.6 Discussion

Trajectory analysis has been performed to investigate the Lagrangian pathways of the GS with considerable variability found at different depths and on seasonal and interannual timescales. The four main pathways analysed were the NAC to the SPG, the AC and the recirculation to the south and to the north. The main findings will each be discussed in turn but the key points are as follows:

1. A direct pathway to the SPG exists when released at $200m$ in the main GS core on timescales as short as 4 months.

2. Trajectories residing on a denser isopycnal are more likely to reach the SPG, which was found to be important in determining the seasonal variability of GS pathways.

3. Near the surface, an enhanced throughput to the SR is significantly correlated with a greater wind stress curl during the winter.

4. The prolonged period of positive NAO from the late-1980s to the mid-1990s led to an intensification of the AMOC, which initiated an increased throughput to the SPG via a subsurface pathway during the 1990s.

5. The increased throughput may have also been enhanced by trajectories starting on a denser isopycnal, a more northward, deeper and, therefore, denser pathway after separation and a weaker PV barrier further to the east.

The two most favoured pathways at all depths and on different timescales are the SR and the SPG. However, an enhanced throughput to the SPG occurs with greater depth with a maximum of 36% of trajectories reaching the SPG when released at $200m$. This implies that trajectories residing on a denser isopycnal are more likely to travel to the SPG. The existence of an intergyre subsurface pathway agrees with prior findings (*Burkholder and Lozier*, 2011, 2014; *Foukal and Lozier*, 2016). Here, GS waters have been found to reach the SPG on timescales as short as 4 months when released in the main GS core. This is much shorter than has been found in previous studies that focus on intergyre exchange (i.e. 2-5 years) when trajectories are released across the entire STG. Here, a more direct, faster pathway has been revealed using the subsurface GS as a conduit.

Substantial seasonal variability was found to exist near the surface with the starting density, i.e. at the release location, being crucial in determining the amount of throughput to the SPG. The greatest amount of seasonal variability occurs at $100m$, which is due to the seasonal cycle in thermocline depth altering the density at the release location. For example, it was found in section 5.2 that particles residing on a denser isopycnal have a greater chance of reaching the SPG, so the shallower thermocline and, therefore, denser isopycnal at $100m$ during the summer may have led to the greater throughput to the SPG e.g. 35% in August. At greater depths, no seasonal cycle exists as it is too deep to feel the effects of the seasonal variation in density changes experienced at the surface.

Near the surface (at $10m$), there is considerable interannual variability in the proportion of trajectories travelling in the SR, the most favoured pathway at this depth. This is counterbalanced by a combination of increases or decreases in the

number of trajectories residing in the SPG or AC. Greater variability exists on individual monthly timescales, especially when examining releases during the winter, which was found to be related to winter forcing. Specifically, the number of trajectories travelling to the SR is significantly greater when a stronger wind stress curl exists, averaged over the Sargasso Sea region to the south of the GS, during the winter. This could imply that a stronger SR exists when a more negative wind stress curl exists over the Sargasso Sea, which, by extension, would lead to a reduced throughput to the SPG near the surface. Contrastingly, no significant correlation is found with winter Qnet forcing, wind stress and Ekman transport with the SPG and SR pathways. This implies that, during the winter, wind stress curl is a more important factor in determining the distribution of surface trajectories travelling in the SPG and SR.

Chapter 4 found an intensified westward component in the SR after severe winters, i.e. anomalous heat loss, which opposes that found here. However, this was found at the end of winter in April rather than during the winter and could be related to particular regions of enhanced heat loss during these particular winters as opposed to a high Qnet over the entire SR region. Additionally, the focus of Chapter 4 were the years of intensified GS transport, which were associated with anomalous heat loss as opposed to the direct influence of Qnet on the SR.

A greater throughput to the SPG was found to occur at the subsurface. Compared to trajectories remaining in the STG, SPG-bound trajectories were found to take a more northerly pathway soon after separation from the coast at Cape Hatteras with the bifurcation point, i.e. where the pathways begin to diverge, occurring at 25 days. This may have enabled them to follow a cooler, fresher and denser path, which provides further evidence that trajectories residing on a denser isopycnal are more likely to reach the SPG.

The greater throughput to the SPG during the 1990s may have been due to the prolonged period of positive NAO since the late-1980s. During positive NAO winters, the stronger westerlies over the Labrador Sea initiates anomalous heat loss and greater deep water formation (*Hurrell et al.*, 1995). This leads to an increased outflow of LSW and models have shown that after consecutive years of

positive NAO, there is an intensification of the AMOC (*Häkkinen*, 1999; *Eden and Willebrand*, 2001; *Dong and Sutton*, 2005; *De Coëtlogon et al.*, 2006; *Lohmann et al.*, 2009; *Robson et al.*, 2012). The increased deep water outflow would then initiate an intensification of the northward flow of the upper ocean (*Böning et al.*, 2006; *Grist et al.*, 2010; *Robson et al.*, 2012). This was found using the ORCA12 by *Marzocchi et al.* (2015) using Eulerian estimates, which is also reproduced here using Lagrangian techniques.

The increased northward flow of warm subtropical water into the SPG during the 1990s led to an anomalously warm western SPG of up to 1.5^oC compared to the weakened flow in the 2000s. This result was also found in EN3 observations and in a climate model used by at a lag of about 4 years *Robson et al.* (2012). However, the peak in temperature anomalies occurs 2 years earlier in ORCA12 (r=0.67 at a lag of 2 years), compared with the climate model, which could be related to the eddy-resolving resolution that enables a faster propagation of anomalies (*Marzocchi et al.*, 2015). The peak in temperature increase coincided with the strongly negative NAO winter of 1995/96, which saw relaxed southward Ekman currents, but after this the NAO was relatively neutral (*Lohmann et al.*, 2009). Although this was likely to have contributed, the most important role was related to the increase in meridional transport at the southern boundary since the late-1980s (*Lohmann et al.*, 2009; *Robson et al.*, 2012).

Additionally, during periods of positive NAO, a northward shift in the GS path is consistent with Sverdrup theory (*Frankignoul et al.*, 2001; *Visbeck et al.*, 2003). Evidence of a more northerly path during the 1990s is seen in Figure 5.18, which could be explained by the positive NAO into the mid-1990s. Contrastingly, observations show that the GS path is forced further south when the AMOC is strong, but ocean-only models have been found to show the opposite (*Joyce and Zhang*, 2010), which is seen here in the ORCA12 hindcast.

Other mechanisms were also found to be acting to enhance the flow to the SPG. First, the release location in the Florida Straits was found to be up to 2^oC cooler during the 1990s compared to during the 2000s, which led to the trajectories beginning on a denser isopycnal. As was found earlier, trajectories residing on a denser

isopycnal are more likely to travel directly to the SPG. The more northerly GS path may have also enabled a greater number of trajectories to travel in the northern flank of the GS. This, combined with a deeper pathway during the 1990s, enabled trajectories to travel on a denser isopycnal, which increased the likelihood of reaching the SPG. Furthermore, further to the east where the GS turns northward as the NAC, there was a weakening in the PV during the 1990s compared with the 2000s, which may have enabled a greater through flow to the SPG. Although an increased through flow to the SPG is consistent with an intensified AMOC, forced by strong buoyancy fluxes over the Labrador Sea, these additional factors may have allowed an even greater number of trajectories to enter the SPG.

To conclude, the results found in this chapter build on previous findings that use a Lagrangian framework to investigate the interconnectivity of the STG and SPG. The greater connectivity at the subsurface is also reproduced but here, there is evidence of a more direct and fast pathway to the SPG via the GS. An enhanced throughput to the SPG was also found to occur when trajectories reside on a denser isopycnal on seasonal and interannual timescales. The increased flow of subtropical waters into the SPG during the 1990s, via an intensification of the AMOC, found in reanalyses and in models using Eulerian estimates was also reproduced here using a Lagrangian framework, which is unprecedented. Further mechanisms were also highlighted, i.e. a more northward GS path, a denser starting location and a weakening of the PV barrier further east, that may have acted to further enhance the throughput to the SPG during this decade.

Chapter 6

Conclusions

6.1 Summary

Understanding the mechanisms that induce changes in the path and transport of the GS is important as they have implications further downstream. Namely, changes to the GS path over the North Atlantic could initiate changes in the position and strength of the storm track (*Joyce et al.*, 2000) and affect the weather of western Europe. The work presented in this thesis provides new insights into the importance of air-sea fluxes in inducing changes in the path and transport of the GS. The main findings will each be summarised in turn but the key findings are as follows:

1. Density changes were found to be important in controlling interannual upper GS transport variability, with strong heat losses during the winter of 1976/77 found to induce the greatest increase in GS transport from the previous year over the period 1970-2014.

2. Using ORCA12, increases in end-of-winter GS transport from the previous year were found to be associated with large heat losses over the western STG, deeper mixed layers further to the east, a strengthened southern recirculation gyre and strengthened temperature gradients to the north.

3. Momentum and buoyancy fluxes were found to significantly control GS pathways, directly, near the surface and, indirectly, for deeper pathways. The increased flow to the SPG during the 1990s, via the deeper pathway, is also reproduced here using Lagrangian techniques.

Chapter 3 examined different methods to quantify the interannual variability of the GS path and transport. Utilising the SST field in AVHRR and ORCA12, the most effective method at capturing latitudinal variability of the GS to the west of 70^oW is the 21^oC surface isotherm as the maximum SST gradient commonly coincided with the edges of eddies. However, due to the large seasonal migration of the 21^oC isotherm (larger than the seasonal migration of the GS path), it is not always accurate on monthly timescales. Additionally, the agreement between the methods is reduced further to the east, which is related to the increase in mesoscale activity further downstream. Furthermore, there is a low correspondence on interannual timescales between AVHRR and ORCA12 at all longitudes. This is due a combination of factors, including their different horizontal resolution and the greater mesoscale variability in ORCA12. These factors create difficulty in accurately estimating the GS path in ORCA12. However, full depth transport can be calculated in models and observational products that contain current velocities (e.g. GODAS) and this has the effect of filtering out a lot of high frequency variability. Using the latitude of greatest transport along 70^oW proved to be the most accurate method to define the GS core at this location and it also eliminates the need to account for seasonal and mesoscale variability. This method (in GODAS) produced some common features of interannual variability with the 21^oC isotherm method (in AVHRR), e.g. the GS is anomalously north since 2007.

In addition to using current velocities, the transport can also be estimated using the thermal wind relation to calculate the baroclinic transport using the meridional density gradients. The upper $(0-1000m)$ baroclinic transport of the GS, i.e. where the largest density changes occur due to air-sea fluxes, was found to be significantly correlated with the total upper transport in both observations (GODAS) and model (ORCA12). This implies that density changes are important in controlling interannual transport variations of the GS at 70^oW. Density changes were found to strongly impact the baroclinic transport, and therefore the total transport, in the upper $1000m$ during the winter of 1976/77, whereby anomalously strong heat losses led to a high STMW formation, low PV and the largest transport observed during the 1970s. Furthermore, the increase in transport (60.5%) from the previous year was the greatest seen throughout the period 1970-2014, which closely

matches the finding of *Worthington* (1977) who found a transport increase of 50%. Contrastingly, no major change in the baroclinic transport was evident during the winter of 2013/14 but a change in the structure of the NAC at 30^oW was induced by considerable heat loss over the central SPG. This led to the greatest cold anomaly observed in this region since 1986 and is referred to as the Cold Blob, which persisted through 2014/15 and may have led to the greatest transport in the NAC since 1998 during early 2015. This was a rare event as heat content changes in this region are dominated by changes in ocean heat transport as opposed to air-sea exchange (*Grist et al.*, 2010).

Chapter 4 utilised the ORCA12 hindcast in order to explore the extent to which localised buoyancy forcing over the western STG impacts the full-depth transport of the GS as it enables a more thorough investigation into the associated mechanisms. The availability of the model SSH field enables the absolute (barotropic and baroclinic) geostrophic currents to be calculated. The considerable variability of mesoscale activity and the westward counter-currents, the southern recirculation and the Slope Water current, creates difficulties in setting latitudinal limits. Thus, the most accurate measure to capture GS transport variability is obtained using the eastward-only velocities and integrated from 30^oN to the coast. Quantifying the contributions from the barotropic and baroclinic components is challenging as density changes, and therefore changes in the steric height field via thermal expansion or contraction, will contribute to the change in SSH. In spite of this, the majority ($> 88\%$) of the SSH changes, and therefore overall transport changes, at 70^oW were found to be due to density changes, with only a minor role being played by processes such as mass convergence by fluctuations in the wind and JEBAR.

Increases in the end of winter transport from year-to-year are associated with anomalous heat losses (of more than -100W m^{-2}) and deeper mixed layers (up to 200m) over the Sargasso Sea, which is consistent with observed changes during 1976/77 (Chapter 3). This implies that the pre-winter ocean condition influences how much anomalously strong surface heat fluxes deepen the MLD and strengthen geostrophic transport in the upper ocean. The prevailing meteorological conditions facilitated the arrival of CAOs, which resulted in the strong heat losses during these

years. The deeper mixed layers at 54^{o}W led to a strengthening of the meridional temperature gradients at greater depths in the GS core, which is consistent with a what was found by *Worthington* (1977). This may have created a stronger baroclinic flow, which drives a stronger recirculation, also consistent with *Worthington* (1976) and *Huang* (1990). The years of increased transport were characterised by a stronger, westward-intensified, southern recirculation, which may be contributing to the greater transports at 70^oW. Additionally, anomalous cooling, of up to 4^oC, occurs in the Slope Water, which strengthens the meridional temperature gradients on the northern flank of the GS, consistent with (*Zheng et al.*, 1984). This induced a strengthening of the geostrophic current and therefore, the total transport. Overall, this highlights the role of buoyancy forcing, via multiple mechanisms, in setting interannual GS transport variations.

In order to further investigate the variability of the southern recirculation, and other GS pathways, trajectory analysis was performed using ORCA12 in Chapter 5. Considerable variability was found at a range of timescales, from seasonal to decadal. In general, at greater depth (and density) there is a greater chance that particles will reach the SPG as opposed to recirculating in the STG. Specifically, a greater percentage of trajectories (36%) reach the SPG when released at the subsurface ($200m$) in the Florida Straits, which is consistent with prior findings (*Foukal and Lozier*, 2016). However, here, a more direct, faster pathway (as short as 4 months) has been revealed. Differences in density at the release location or near separation are important in determining whether trajectories travel to the SPG or remain in the STG. For example, variations in the depth of the thermocline in the Florida Straits affected the release density (at a fixed depth) on seasonal timescales. Meanwhile, a northward shift in the GS path enables more particles to come into contact with colder, denser water on interannual timescales.

Near the surface, trajectories are also influenced by surface fluxes. A strengthened southern recirculation was correlated with a greater wind stress curl during the winter but no significant relationships were identified with the surface heat flux, wind stress or the Ekman transport. At the subsurface, the increased throughput to the SPG during the 1990s is also associated, indirectly, with air-sea fluxes.

The prolonged period of positive NAO from the late-1980s to the mid-1990s led to stronger Westerlies and anomalous heat loss over the Labrador Sea, which initiated deep convection and LSW formation. Models have shown that this led to an intensification of the AMOC (*Häkkinen*, 1999; *Eden and Willebrand*, 2001; *Dong and Sutton*, 2005; *De Coëtlogon et al.*, 2006; *Lohmann et al.*, 2009), which initiated the intensification of the upper limb of the AMOC and, therefore, the GS (*Grist et al.*, 2010; *Robson et al.*, 2012). Here, this is shown for the first time using a Lagrangian approach. In this thesis it has been shown that the increased flow to the SPG appeared to lead to anomalous warming of up to 1.5^oC in the western SPG, which is also consistent with the aforementioned Eulerian studies. However, the maximum correlation was found at a lag of two years, which is sooner than that found in climate models, e.g. 4 years (*Robson et al.*, 2012), which may be due to the inclusion of an eddy field in ORCA12 due to higher resolution. This advection of warm GS water may have had a considerable impact on the surface heat fluxes and therefore, the North Atlantic storm track and the winters of western Europe if the atmospheric conditions are conducive to being ocean-forced (*Yamamoto et al.*, 2015). Hence, the throughput of GS waters to the SPG may exert considerable influence on European climate variability.

To conclude, this thesis has provided new insights into the importance of air-sea fluxes in forcing GS transport and the variability of its pathways. Due to the considerable level of air-sea interaction in this region, and the prevailing atmospheric circulation, the forced variability may initiate changes to the climate system further downstream.

6.2 Further Work

There are many avenues for potential future research surrounding the mechanisms controlling the GS. Chapter 3.2 highlighted the discrepancies that exist on GS path and transport variability and may be due to the variety of indicators used to represent its path. For example, the latitude of the maximum SST gradient and the 21^oC isotherm were found to differ by up to 1^o at 73^oW. Further work needs to be done to critically evaluate the different methods or metrics for defining the GS path

to ascertain which of these can be used effectively. A comprehensive study could be undertaken to quantify and statistically evaluate the spatial range of the latitudinal variability of the GS along its separated path, i.e. from $75 - 50^oW$, using different path definitions. Along with the maximum SST gradient and the 21^oC surface isotherm, existing methods include the 15^oC isotherm at 200 m (*Tracey and Watts*, 1986; *Joyce and Zhang*, 2010; *Chaudhuri et al.*, 2011; *Davis et al.*, 2013), the 12^oC isotherm at 400 m (*Chaudhuri et al.*, 2011), the maximum SSH gradient or a SSH contour (*Kelly and Gille*, 1990; *Kelly et al.*, 1999; *Frankignoul et al.*, 2001; *Flatau et al.*, 2003; *Joyce and Zhang*, 2010; *Kelly et al.*, 2010; *Lillibridge and Mariano*, 2012; *Ezer et al.*, 2013; *Pérez-Hernández and Joyce*, 2014)], EKE (*Fratantoni*, 2001; *Volkov*, 2005) and Sea Surface Salinity (*Lillibridge and Mariano*, 2012). A range of observational products are available for this purpose, which includes, but is not limited to, AVHRR, GODAS, AVISO and SMOS. Furthermore, the utilisation of the ORCA12 hindcast would enable a direct comparison between all methods on a range of timescales. Drifters could also be employed to create an index for the GS path, which are available in both observations (ARGO) and in ORCA12.

The difficulty of estimating an accurate GS transport in ORCA12, even further to the west at 70^oW where the GS has a narrow core, was evident in Chapter 3.5 and Chapter 4. This was due to the occurrence of mesoscale activity, i.e. meanders and eddies, and two westward counter-currents on either side of the GS, i.e. the southern recirculation and the Slope Water Current. The inability of being able to define fixed latitudinal limits to capture the total GS transport was found to be due to the variability of these processes. Further work to create an index that measures the strength and latitudinal location of the recirculations to produce variable latitudinal limits would improve the accuracy of GS transport estimation. Additionally, the identification of eddies is vital to ensure that the return flow is included to compensate the outward flow, or to eliminate eddy transports entirely. This method may also be implemented further downstream, where mesoscale activity exceeds that further to the west (*Krauss et al.*, 1990). This would enable the variability of GS transport to be captured accurately on a range of time scales and at different longitudes.

The use of trajectory analysis in Chapter 5 enabled the quantification of GS pathways and their variability on different timescales. At the surface, the along-stream temperature evolution of a trajectory is predominantly related to the buoyancy fluxes that it encounters. This could be important for determining the strength and location of the North Atlantic storm track. Trajectory analysis could be utilised on a smaller scale to investigate the evolution of individual trajectory depth, temperature, salinity and density. Using ORCA12, or another high-resolution ocean circulation model, years of particularly strong or weak heat loss could be identified along trajectories initiated in the GS. Combined with changes in temperature, this would enable the estimation of how much heat is carried to the SPG from the subtropics. Furthermore, the calculation of heat content in the model SPG would enable the quantification of the advection contribution using the trajectory-derived results. The initiation of thousands of trajectories from different locations and release depths would enable regions to be identified where temperature changes and heat fluxes are important. Additionally, during the period of greater throughput to the SPG in the 1990s (Chapter 5), the trajectories were found to be up to $40m$ deeper, on average, on arrival to the western SPG. The investigation of the evolution of trajectory depth may also provide information on when and how this change occurs and if it is conducive to variations in GS pathways. Finally, process experiments could be conducted using a model to isolate the various physical processes, e.g. wind stress, wind stress curl, buoyancy forcing, Ekman transport etc., causing the interannual variability in GS pathways. These experiments could also be used to investigate if particular regions are important, e.g. the western STG.

Bibliography

Alexander, M. A., and J. D. Scott, Surface flux variability over the North Pacific and North Atlantic oceans, *Journal of climate*, *10*(11), 2963–2978, 1997.

Anderson, D., and R. Corry, Ocean response to low frequency wind forcing with application to the seasonal variation in the Florida Straits—Gulf Stream transport, *Progress in Oceanography*, *14*, 7–40, 1985.

Antonov, J., R. Locarnini, T. Boyer, A. Mishonov, and H. Garcia, World Ocean Atlas 2005, vol. 2, Salinity, NOAA Atlas NESDIS, vol. 62, edited by S, 2006.

Arakawa, A., Design of the UCLA general circulation model, 1972.

Bane, J. M., and K. E. Osgood, Wintertime air-sea interaction processes across the Gulf Stream, *Journal of Geophysical Research: Oceans (1978–2012)*, *94*(C8), 10,755–10,772, 1989.

Baringer, M. O., and J. C. Larsen, Sixteen years of Florida Current transport at 27 N, *Geophysical Research Letters*, *28*(16), 3179–3182, 2001.

Behringer, D., and Y. Xue, Evaluation of the global ocean data assimilation system at NCEP: The Pacific Ocean, in *Proc. Eighth Symp. on Integrated Observing and Assimilation Systems for Atmosphere, Oceans, and Land Surface*, 2004.

Bisagni, J. J., A. Gangopadhyay, and A. Sanchez-Franks, Secular change and interannual variability of the Gulf Stream position, 1993–2013, 70 °- 55 ° W, *Deep Sea Research Part I: Oceanographic Research Papers*, *125*, 1–10, 2017.

Bjerknes, J., Atlantic air-sea interaction, *Advances in geophysics*, *10*, 1–82, 1964.

Blaker, A. T., J. J.-M. Hirschi, G. McCarthy, B. Sinha, S. Taws, R. Marsh, A. Coward, and B. de Cuevas, Historical analogues of the recent extreme minima observed in the Atlantic meridional overturning circulation at 26 ° N, *Climate dynamics*, *44*(1-2), 457–473, 2015.

Blanke, B., and S. Raynaud, Kinematics of the Pacific equatorial undercurrent: An Eulerian and Lagrangian approach from GCM results, *Journal of Physical Oceanography*, *27*(6), 1038–1053, 1997.

Böning, C. W., M. Scheinert, J. Dengg, A. Biastoch, and A. Funk, Decadal variability of subpolar gyre transport and its reverberation in the North Atlantic overturning, *Geophysical Research Letters*, *33*(21), 2006.

Bower, A. S., and H. D. Hunt, Lagrangian observations of the deep western boundary current in the North Atlantic Ocean. Part II: The Gulf Stream–deep western boundary current crossover, *Journal of physical oceanography*, *30*(5), 784–804, 2000.

Bower, A. S., and W.-J. von Appen, Interannual variability in the pathways of the North Atlantic current over the Mid-Atlantic Ridge and the impact of topography, *Journal of Physical Oceanography*, *38*(1), 104–120, 2008.

Bower, A. S., H. T. Rossby, and J. L. Lillibridge, The Gulf Stream—barrier or blender?, *Journal of Physical Oceanography*, *15*(1), 24–32, 1985.

Brambilla, E., and L. D. Talley, Surface drifter exchange between the North Atlantic subtropical and subpolar gyres, *Journal of Geophysical Research: Oceans (1978–2012)*, *111*(C7), 2006.

Brayshaw, D. J., B. Hoskins, and M. Blackburn, The basic ingredients of the North Atlantic storm track. Part II: Sea surface temperatures, *Journal of the Atmospheric Sciences*, *68*(8), 1784–1805, 2011.

Bretherton, C. S., M. Widmann, V. P. Dymnikov, J. M. Wallace, and I. Bladé, The effective number of spatial degrees of freedom of a time-varying field, *Journal of climate*, *12*(7), 1990–2009, 1999.

Brodeau, L., B. Barnier, A.-M. Treguier, T. Penduff, and S. Gulev, An ERA40-based atmospheric forcing for global ocean circulation models, *Ocean Modelling*, *31*(3), 88–104, 2010.

Bryan, F. O., M. W. Hecht, and R. D. Smith, Resolution convergence and sensitivity studies with North Atlantic circulation models. Part I: The western boundary current system, *Ocean Modelling*, *16*(3), 141–159, 2007.

Buchan, J., J. J.-M. Hirschi, A. T. Blaker, and B. Sinha, North Atlantic SST anomalies and the cold North European weather events of winter 2009/10 and December 2010, *Monthly Weather Review*, *142*(2), 922–932, 2014.

Buckley, M. W., R. M. Ponte, G. Forget, and P. Heimbach, Low-frequency SST and upper-ocean heat content variability in the North Atlantic, *Journal of Climate*, *27*(13), 4996–5018, 2014.

Burkholder, K. C., and M. S. Lozier, Subtropical to subpolar pathways in the North Atlantic: Deductions from Lagrangian trajectories, *Journal of Geophysical Research: Oceans (1978–2012)*, *116*(C7), 2011.

Burkholder, K. C., and M. S. Lozier, Tracing the pathways of the upper limb of the North Atlantic Meridional Overturning Circulation, *Geophysical Research Letters*, *41*(12), 4254–4260, 2014.

Chassignet, E. P., and Z. D. Garraffo, Viscosity parameterization and the Gulf Stream separation, *Tech. rep.*, MIAMI UNIV FL INST OF MARINE AND ATMOSPHERIC SCIENCES, 2001.

Chassignet, E. P., and X. Xu, Impact of horizontal resolution (1/12 ° to 1/50 °) on Gulf Stream separation, penetration, and variability, *Journal of Physical Oceanography*, (2017), 2017.

Chaudhuri, A. H., A. Gangopadhyay, and J. J. Bisagni, Interannual variability of Gulf Stream warm-core rings in response to the North Atlantic Oscillation, *Continental Shelf Research*, *29*(7), 856–869, 2009.

Chaudhuri, A. H., A. Gangopadhyay, and J. J. Bisagni, Response of the Gulf Stream transport to characteristic high and low phases of the North Atlantic Oscillation, *Ocean Modelling*, *39*(3–4), 220 – 232, doi:http://dx.doi.org/10.1016/j.ocemod.2011.04.005, 2011.

Curry, R. G., and M. S. McCartney, Ocean gyre circulation changes associated with the North Atlantic Oscillation*, *Journal of Physical Oceanography*, *31*(12), 3374–3400, 2001.

Cushman-Roisin, B., On the role of heat flux in the gulf stream-sargasso sea subtropical gyre system, *Journal of physical oceanography*, *17*(12), 2189–2202, 1987.

Davis, X. J., R. A. Weller, S. Bigorre, and A. J. Plueddemann, Local oceanic response to atmospheric forcing in the Gulf Stream region, *Deep-Sea Research II*, *91*, 71–83, 2013.

De Coëtlogon, G., C. Frankignoul, M. Bentsen, C. Delon, H. Haak, S. Masina, and A. Pardaens, Gulf Stream variability in five oceanic general circulation models, *Journal of physical oceanography*, *36*(11), 2119–2135, 2006.

Dengg, J., A. Beckmann, and R. Gerdes, The gulf stream separation problem, in *The warmwatersphere of the North Atlantic Ocean (W Krauss, ed)*, pp. 253–290, 1996.

DiNezio, P. N., L. J. Gramer, W. E. Johns, C. S. Meinen, and M. O. Baringer, Observed interannual variability of the Florida Current: Wind forcing and the North Atlantic Oscillation, *Journal of Physical Oceanography*, *39*(3), 721–736, 2009.

Dong, B., and R. T. Sutton, Mechanism of interdecadal thermohaline circulation variability in a coupled ocean–atmosphere GCM, *Journal of climate*, *18*(8), 1117–1135, 2005.

Dong, S., and K. A. Kelly, Heat budget in the Gulf Stream region: The importance of heat storage and advection, *Journal of physical oceanography*, *34*(5), 1214–1231, 2004.

Dong, S., S. L. Hautala, and K. A. Kelly, Interannual variations in upper-ocean heat content and heat transport convergence in the western North Atlantic, *Journal of Physical Oceanography*, *37*(11), 2682–2697, 2007.

Drinkwater, K., R. Myers, R. Pettipas, and T. Wright, Climatic data for the northwest Atlantic: The positon of the shelf/slope front and the northern boundary of the Gulf Stream between 50W and 75W, 1973-1992, *Canada Data Report of Fisheries and Ocean Sciences*, *125*, 103, 1994.

Duchez, A., et al., A new index for the Atlantic Meridional Overturning Circulation at 26° N, *Journal of Climate*, *27*(17), 6439–6455, 2014.

Duchez, A., et al., Drivers of exceptionally cold North Atlantic Ocean temperatures and their link to the 2015 European heat wave, *Environmental Research Letters*, *11*(7), 074,004, 2016.

Eden, C., and J. Willebrand, Mechanism of interannual to decadal variability of the North Atlantic circulation, *Journal of Climate*, *14*(10), 2266–2280, 2001.

Ezer, T., Revisiting the problem of the Gulf Stream separation: on the representation of topography in ocean models with different types of vertical grids, *Ocean Modelling*, *104*, 15–27, 2016.

Ezer, T., A modeling study of the role that bottom topography plays in Gulf Stream dynamics and in influencing the tilt of mean sea level along the US East Coast, *Ocean Dynamics*, *67*(5), 651–664, 2017.

Ezer, T., and G. L. Mellor, A numerical study of the variability and the separation of the Gulf Stream, induced by surface atmospheric forcing and lateral boundary flows, *Journal of physical oceanography*, *22*(6), 660–682, 1992.

Ezer, T., L. P. Atkinson, W. B. Corlett, and J. L. Blanco, Gulf Stream's induced sea level rise and variability along the US mid-Atlantic coast, *Journal of Geophysical Research: Oceans*, 2013.

Flatau, M. K., L. Talley, and P. P. Niiler, The North Atlantic Oscillation, surface current velocities, and SST changes in the subpolar North Atlantic, *Journal of Climate*, *16*(14), 2355–2369, 2003.

Fofonoff, N., Steady flow in a frictionless homogeneous ocean, *J. mar. Res*, *13*, 254–262, 1954.

Foukal, N. P., and M. S. Lozier, No inter-gyre pathway for sea-surface temperature anomalies in the North Atlantic, *Nature communications*, *7*, 2016.

Frankignoul, C., P. Müller, and E. Zorita, A simple model of the decadal response of the ocean to stochastic wind forcing, *Journal of Physical Oceanography*, *27*(8), 1533–1546, 1997.

Frankignoul, C., G. de Coëtlogon, T. M. Joyce, and S. Dong, Gulf Stream Variability and Ocean-Atmosphere Interactions*, *Journal of physical Oceanography*, *31*(12), 3516–3529, 2001.

Fratantoni, D. M., North Atlantic surface circulation during the 1990's observed with satellite-tracked drifters, *Journal of Geophysical Research: Oceans (1978–2012)*, *106*(C10), 22,067–22,093, 2001.

Fuglister, F. C., *Cyclonic rings formed by the Gulf Stream 1965-66*, Woods Hole Oceanographic Institution, 1972.

Gangopadhyay, A., A. H. Chaudhuri, and A. H. Taylor, On the Nature of Temporal Variability of the Gulf Stream Path from 75° to 55° W, *Earth Interactions*, *20*(9), 1–17, 2016.

Gangopadhyay, P. C., A., and D. R. Watts, Test of the Parsons-Veronis hypothesis on the separation of the Gulf Stream, *Journal of Physical Oceanography*, *22*, 1286–1301, 1992.

Gawarkiewicz, G. G., R. E. Todd, A. J. Plueddemann, M. Andres, and J. P. Manning, Direct interaction between the Gulf Stream and the shelfbreak south of New England, *Scientific Reports*, *2*(553), 1–6, 2012.

Gerdes, R., and C. Köberle, On the influence of DSOW in a numerical model of the North Atlantic general circulation, *Journal of physical oceanography*, *25*(11), 2624–2642, 1995.

Good, S. A., M. J. Martin, and N. A. Rayner, EN4: Quality controlled ocean temperature and salinity profiles and monthly objective analyses with uncertainty estimates, *Journal of Geophysical Research: Oceans*, *118*(12), 6704–6716, 2013.

Grist, J. P., S. A. Josey, R. Marsh, S. A. Good, A. C. Coward, B. A. De Cuevas, S. G. Alderson, A. L. New, and G. Madec, The roles of surface heat flux and ocean heat transport convergence in determining Atlantic Ocean temperature variability, *Ocean dynamics*, *60*(4), 771–790, 2010.

Grist, J. P., S. A. Josey, Z. L. Jacobs, R. Marsh, B. Sinha, and E. Sebille, Extreme air–sea interaction over the North Atlantic subpolar gyre during the winter of 2013–2014 and its sub-surface legacy, *Climate dynamics*, *46*(11-12), 4027–4045, 2016.

Grossman, R. L., and A. K. Betts, Air–sea interaction during an extreme cold air outbreak from the eastern coast of the United States, *Monthly Weather Review*, *118*(2), 324–342, 1990.

Häkkinen, S., Variability of the simulated meridional heat transport in the North Atlantic for the period 1951–1993, *Journal of Geophysical Research: Oceans*, *104*(C5), 10,991–11,007, 1999.

Häkkinen, S., and P. B. Rhines, Decline of subpolar North Atlantic circulation during the 1990s, *Science*, *304*(5670), 555–559, 2004.

Hakkinen, S., and P. B. Rhines, Shifting surface currents in the northern North Atlantic Ocean, *Journal of Geophysical Research: Oceans (1978–2012)*, *114*(C4), 2009.

Häkkinen, S., P. B. Rhines, and D. L. Worthen, Warm and saline events embedded in the meridional circulation of the northern North Atlantic, *Journal of Geophysical Research: Oceans*, *116*(C3), 2011.

Halkin, D., and T. Rossby, The structure and transport of the Gulf Stream at 73 W, *Journal of Physical Oceanography*, *15*(11), 1439–1452, 1985.

Hall, M. M., and N. P. Fofonoff, Downstream development of the Gulf Stream from 68 to 55 W, *Journal of Physical Oceanography*, *23*(2), 225–249, 1993.

Halliwell, G. R., and C. N. Mooers, The space-time structure and variability of the shelf water-slope water and Gulf Stream surface temperature fronts and associated warm-core eddies, *Journal of Geophysical Research: Oceans*, *84*(C12), 7707–7725, 1979.

Hameed, S., and S. Piontkovski, The dominant influence of the Icelandic Low on the position of the Gulf Stream northwall, *Geophysical research letters*, *31*(9), 2004.

Hand, R., N. Keenlyside, N.-E. Omrani, and M. Latif, Simulated response to inter-annual SST variations in the Gulf Stream region, *Climate dynamics*, *42*(3-4), 715–731, 2014.

Heywood, K. J., E. L. McDonagh, and M. A. White, Eddy kinetic energy of the North Atlantic subpolar gyre from satellite altimetry, *Journal of Geophysical Research: Oceans*, *99*(C11), 22,525–22,539, 1994.

Hogg, N. G., On the transport of the Gulf Stream between Cape Hatteras and the Grand Banks, *Deep Sea Research Part A. Oceanographic Research Papers*, *39*(7), 1231–1246, 1992.

Hogg, N. G., and W. E. Johns, Western boundary currents, *Reviews of Geophysics*, *33*(S2), 1311–1334, 1995.

Holland, W., D. Harrison, and A. Semtner, Eddy-resolving numerical models of large-scale ocean circulation, in *Eddies in marine science*, pp. 379–403, Springer, 1983.

Hoskins, B. J., and P. J. Valdes, On the existence of storm-tracks, *Journal of the atmospheric sciences*, *47*(15), 1854–1864, 1990.

Huang, R. X., Does atmospheric cooling drive the Gulf Stream recirculation?, *Journal of Physical Oceanography*, *20*(5), 750–757, 1990.

Hurrell, J. W., Y. Kushnir, G. Ottersen, and M. Visbeck, *An overview of the North Atlantic oscillation*, 1–35 pp., Wiley Online Library, 2003.

Hurrell, J. W., et al., Decadal trends in the North Atlantic Oscillation: regional temperatures and precipitation, *Science-AAAS-Weekly Paper Edition*, *269*(5224), 676–678, 1995.

Jiang, S., F.-F. Jin, and M. Ghil, Multiple equilibria, periodic, and aperiodic solutions in a wind-driven, double-gyre, shallow-water model, *Journal of Physical Oceanography*, *25*(5), 764–786, 1995.

Johns, W., T. Shay, J. Bane, and D. Watts, Gulf Stream structure, transport, and recirculation near 68 W, *Journal of Geophysical Research: Oceans (1978–2012)*, *100*(C1), 817–838, 1995.

Joyce, T. M., and R. Zhang, On the path of the Gulf Stream and the Atlantic Meridional overturning circulation, *Journal of Climate*, *23*(11), 3146–3154, 2010.

Joyce, T. M., C. Deser, and M. A. Spall, The relation between decadal variability of subtropical mode water and the North Atlantic Oscillation*, *Journal of Climate*, *13*(14), 2550–2569, 2000.

Joyce, T. M., Y.-O. Kwon, and L. Yu, On the relationship between synoptic wintertime atmospheric variability and path shifts in the Gulf Stream and the Kuroshio Extension, *Journal of Climate*, *22*(12), 3177–3192, 2009.

Kalnay, E., et al., The NCEP/NCAR reanalysis 40-year project, *Bull. Am. Meteorol. Soc*, *77*(3), 437–471, 1996.

Kelly, K. A., and S. T. Gille, Gulf Stream surface transport and statistics at 69 W from the Geosat altimeter, *Journal of Geophysical Research: Oceans (1978–2012)*, *95*(C3), 3149–3161, 1990.

Kelly, K. A., M. J. Caruso, S. Singh, and B. Qiu, Observations of atmosphere-ocean coupling in midlatitude western boundary currents, *Journal of Geophysical Research: Oceans (1978–2012)*, *101*(C3), 6295–6312, 1996.

Kelly, K. A., S. Singh, and R. X. Huang, Seasonal Variations of Sea Surface Height in the Gulf Stream Region*, *Journal of physical oceanography*, *29*(3), 313–327, 1999.

Kelly, K. A., R. J. Small, R. Samelson, B. Qiu, T. M. Joyce, Y.-O. Kwon, and M. F. Cronin, Western boundary currents and frontal air-sea interaction: Gulf Stream and Kuroshio Extension, *Journal of Climate*, *23*(21), 5644–5667, 2010.

Knauss, J. A., A note on the transport of the Gulf Stream, *Deep-Sea Res.*, *16*, 117–123, 1969.

Krauss, W., R. Käse, and H.-H. Hinrichsen, The branching of the Gulf Stream southeast of the Grand Banks, *Journal of Geophysical Research: Oceans*, *95*(C8), 13,089–13,103, 1990.

Kwon, Y.-O., and T. M. Joyce, Northern Hemisphere winter atmospheric transient eddy heat fluxes and the Gulf Stream and Kuroshio–Oyashio Extension variability, *Journal of Climate*, *26*(24), 9839–9859, 2013.

Kwon, Y.-O., M. A. Alexander, N. A. Bond, C. Frankignoul, H. Nakamura, B. Qiu, and L. A. Thompson, Role of the Gulf Stream and Kuroshio-Oyashio systems in large-scale atmosphere-ocean interaction: A review, *Journal of Climate*, *23*(12), 3249–3281, 2010.

Lee, T., and P. Cornillon, Temporal variation of meandering intensity and domain-wide lateral oscillations of the Gulf Stream, *Journal of Geophysical Research: Oceans (1978–2012)*, *100*(C7), 13,603–13,613, 1995.

Leetmaa, A., Effects of the winter of 1976-1977 on the northwestern Sargasso Sea, *Science*, *198*(4313), 188–189, 1977.

Lillibridge, J. L., and A. J. Mariano, A statistical analysis of Gulf Stream variability from 18+ years of altimetry data, *Deep Sea Research Part II: Topical Studies in Oceanography*, 2012.

Locarnini, R., A. Mishonov, J. Antonov, T. Boyer, H. Garcia, O. Baranova, M. Zweng, and D. Johnson, World Ocean Atlas 2005, vol. 1, Temperature, NOAA Atlas NESDIS, vol. 61, edited by S, 2006.

Lohmann, K., H. Drange, and M. Bentsen, A possible mechanism for the strong weakening of the North Atlantic subpolar gyre in the mid-1990s, *Geophysical Research Letters*, *36*(15), 2009.

Lozier, M. S., and S. C. Riser, Potential vorticity sources and sinks in a quasi-geostrophic ocean: beyond western boundary currents, *Journal of physical oceanography*, *20*(10), 1608–1627, 1990.

Ma, X., P. Chang, R. Saravanan, D. Wu, X. Lin, L. Wu, and X. Wan, Winter extreme flux events in the Kuroshio and Gulf Stream extension regions and relationship with modes of North Pacific and Atlantic variability, *Journal of Climate*, *28*(12), 4950–4970, 2015.

Madec, G., and M. Imbard, A global ocean mesh to overcome the North Pole singularity, *Climate Dynamics*, *12*(6), 381–388, 1996.

Madec, G., et al., NEMO ocean engine, 2015.

Marchese, P. J., Variability in the Gulf Stream recirculation gyre, *Journal of Geophysical Research: Oceans*, *104*(C12), 29,549–29,560, 1999.

Marsh, R., S. A. Josey, B. A. de Cuevas, L. J. Redbourn, and G. D. Quartly, Mechanisms for recent warming of the North Atlantic: Insights gained with an eddy-permitting model, *Journal of Geophysical Research: Oceans*, *113*(C4), 2008.

Marshall, J., H. Johnson, and J. Goodman, A study of the interaction of the North Atlantic Oscillation with ocean circulation, *Journal of Climate*, *14*(7), 1399–1421, 2001.

Marzocchi, A., J. J.-M. Hirschi, N. P. Holliday, S. A. Cunningham, A. T. Blaker, and A. C. Coward, The North Atlantic subpolar circulation in an eddy-resolving global ocean model, *Journal of Marine Systems*, *142*, 126–143, 2015.

Matthews, T., C. Murphy, R. L. Wilby, and S. Harrigan, Stormiest winter on record for Ireland and UK, *Nature Climate Change*, *4*(9), 738, 2014.

McCartney, M. S., and L. D. Talley, The subpolar mode water of the North Atlantic Ocean, *Journal of Physical Oceanography*, *12*(11), 1169–1188, 1982.

McDougall, T. J., and P. M. Barker, Getting started with TEOS-10 and the Gibbs Seawater (GSW) oceanographic toolbox, *SCOR/IAPSO WG*, *127*, 1–28, 2011.

McDowell, S., P. Rhines, and T. Keffer, North Atlantic potential vorticity and its relation to the general circulation, *Journal of Physical Oceanography*, *12*(12), 1417–1436, 1982.

Meinen, C. S., and D. S. Luther, Structure, transport, and vertical coherence of the Gulf Stream from the Straits of Florida to the Southeast Newfoundland Ridge, *Deep Sea Research Part I: Oceanographic Research Papers*, *112*, 137–154, 2016.

Meinen, C. S., M. O. Baringer, and R. F. Garcia, Florida Current transport variability: An analysis of annual and longer-period signals, *Deep Sea Research Part I: Oceanographic Research Papers*, *57*(7), 835–846, 2010.

Mensa, J. A., Z. Garraffo, A. Griffa, T. M. Özgökmen, A. Haza, and M. Veneziani, Seasonality of the submesoscale dynamics in the Gulf Stream region, *Ocean Dynamics*, *63*(8), 923–941, 2013.

Minobe, S., A. Kuwano-Yoshida, N. Komori, S.-P. Xie, and R. J. Small, Influence of the Gulf Stream on the troposphere, *Nature*, *452*(7184), 206, 2008.

Minobe, S., M. Miyashita, A. Kuwano-Yoshida, H. Tokinaga, and S.-P. Xie, Atmospheric response to the gulf stream: seasonal variations*, *Journal of Climate*, *23*(13), 3699–3719, 2010.

Moat, B., et al., Major variations in subtropical North Atlantic heat transport at short (5 day) timescales and their causes, *Journal of Geophysical Research: Oceans*, *121*(5), 3237–3249, 2016.

Molinari, R. L., Annual and decadal variability in the western subtropical North Atlantic: signal characteristics and sampling methodologies, *Progress in Oceanography*, *62*(1), 33–66, 2004.

Munk, W. H., On the wind-driven ocean circulation, *Journal of meteorology*, *7*(2), 80–93, 1950.

Nakamura, H., T. Sampe, Y. Tanimoto, and A. Shimpo, Observed associations among storm tracks, jet streams and midlatitude oceanic fronts, *Earth's Climate*, pp. 329–345, 2004.

Nakamura, H., T. Sampe, A. Goto, W. Ohfuchi, and S.-P. Xie, On the importance of midlatitude oceanic frontal zones for the mean state and dominant variability in the tropospheric circulation, *Geophysical Research Letters*, *35*(15), 2008.

New, A. L., in communication, 2017.

O'Reilly, C. H., S. Minobe, and A. Kuwano-Yoshida, The influence of the Gulf Stream on wintertime European blocking, *Climate Dynamics*, *47*(5-6), 1545–1567, 2016.

O'Reilly, C. H., S. Minobe, A. Kuwano-Yoshida, and T. Woollings, The Gulf Stream influence on wintertime North Atlantic jet variability, *Quarterly Journal of the Royal Meteorological Society*, *143*(702), 173–183, 2017.

Palmer, T., Record-breaking winters and global climate change, *Science*, *344*(6186), 803–804, 2014.

Parfitt, R., A. Czaja, S. Minobe, and A. Kuwano-Yoshida, The atmospheric frontal response to SST perturbations in the Gulf Stream region, *Geophysical Research Letters*, *43*(5), 2299–2306, 2016.

Peña-Molino, B., and T. M. Joyce, Variability in the Slope Water and its relation to the Gulf Stream path, *Geophysical Research Letters*, *35*(3), 2008.

Pérez-Hernández, M. D., and T. M. Joyce, Two Modes of Gulf Stream Variability Revealed in the Last Two Decades of Satellite Altimeter Data., *Journal of Physical Oceanography*, *44*(1), 2014.

Pickart, R. S., and W. M. Smethie Jr, How does the deep western boundary current cross the Gulf Stream?, *Journal of Physical Oceanography*, *23*(12), 2602–2616, 1993.

Pierini, S., A comparative analysis of Kuroshio Extension indices from a modeling perspective, *Journal of Climate*, *28*(14), 5873–5881, 2015.

Popova, E., A. Yool, Y. Aksenov, and A. Coward, Role of advection in Arctic Ocean lower trophic dynamics: A modeling perspective, *Journal of Geophysical Research: Oceans*, *118*(3), 1571–1586, 2013.

Qiu, B., Determining the mean Gulf Stream and its recirculations through combining hydrographic and altimetric data, *Journal of Geophysical Research: Oceans*, *99*(C1), 951–962, 1994.

Qiu, B., and R. X. Huang, Ventilation of the North Atlantic and North Pacific: subduction versus obduction, *Journal of Physical Oceanography*, *25*(10), 2374–2390, 1995.

Rasmussen, L. L., G. Gawarkiewicz, W. B. Owens, and M. S. Lozier, Slope water, Gulf Stream, and seasonal influences on southern Mid-Atlantic Bight circulation during the fall-winter transition, *Journal of Geophysical Research: Oceans*, *110*(C2), 2005.

Rayner, D., et al., Monitoring the Atlantic meridional overturning circulation, *Deep Sea Research Part II: Topical Studies in Oceanography*, *58*(17), 1744–1753, 2011.

Read, J., R. Pollard, P. Miller, and A. Dale, Circulation and variability of the North Atlantic Current in the vicinity of the Mid-Atlantic Ridge, *Deep Sea Research Part I: Oceanographic Research Papers*, *57*(3), 307–318, 2010.

Reverdin, G., North Atlantic subpolar gyre surface variability (1895-2009), *Journal of climate*, *23*(17), 4571–4584, 2010.

Reynolds, R. W., T. M. Smith, C. Liu, D. B. Chelton, K. S. Casey, and M. G. Schlax, Daily high-resolution-blended analyses for sea surface temperature, *Journal of Climate*, *20*(22), 5473–5496, 2007.

Rhein, M., D. Kieke, S. Hüttl-Kabus, A. Roessler, C. Mertens, R. Meissner, B. Klein, C. W. Böning, and I. Yashayaev, Deep water formation, the subpolar gyre, and the meridional overturning circulation in the subpolar North Atlantic, *Deep Sea Research Part II: Topical Studies in Oceanography*, *58*(17), 1819–1832, 2011.

Richardson, P., Average velocity and transport of the Gulf Stream near 55W, *Journal of Marine Research*, *43*(1), 83–111, 1985.

Rienecker, M. M., et al., MERRA: NASA's modern-era retrospective analysis for research and applications, *Journal of climate*, *24*(14), 3624–3648, 2011.

Riser, S. C., and M. S. Lozier, Rethinking the Gulf stream., *Scientific American*, *308*(2), 50, 2013.

Robson, J., R. Sutton, K. Lohmann, D. Smith, and M. D. Palmer, Causes of the rapid warming of the North Atlantic Ocean in the mid-1990s, *Journal of Climate*, *25*(12), 4116–4134, 2012.

Rossby, T., The North Atlantic Current and surrounding waters: At the crossroads, *Reviews of Geophysics*, *34*(4), 463–481, 1996.

Rossby, T., On gyre interactions, *Deep Sea Research Part II: Topical Studies in Oceanography*, *46*(1), 139–164, 1999.

Rossby, T., and R. Benway, Slow variations in mean path of the Gulf Stream east of Cape Hatteras, *Geophysical Research Letters*, *27*(1), 117–120, 2000.

Rossby, T., and E. Gottlieb, The Oleander Project: Monitoring the variability of the Gulf Stream and adjacent waters between New Jersey and Bermuda, *Bulletin of the American Meteorological Society*, *79*(1), 5–18, 1998.

Rossby, T., G. Siedler, and W. Zenk, The Volunteer Observing Ship and future ocean monitoring, *Bulletin of the American Meteorological Society*, *76*(1), 5–11, 1995.

Rossby, T., C. Flagg, and K. Donohue, Interannual variations in upper-ocean transport by the Gulf Stream and adjacent waters between New Jersey and Bermuda, *Journal of Marine Research*, *63*(1), 203–226, 2005.

Rossby, T., C. Flagg, and K. Donohue, On the variability of Gulf Stream transport from seasonal to decadal timescales, *Journal of Marine Research*, *68*(3-4), 3–4, 2010.

Rossby, T., C. Flagg, K. Donohue, A. Sanchez-Franks, and J. Lillibridge, On the long-term stability of Gulf Stream transport based on 20 years of direct measurements, *Geophysical Research Letters*, 2013.

Rypina, I. I., L. J. Pratt, and M. S. Lozier, Near-surface transport pathways in the North Atlantic Ocean: looking for throughput from the subtropical to the subpolar gyre, *Journal of Physical Oceanography*, *41*(5), 911–925, 2011.

Saba, V. S., et al., Enhanced warming of the Northwest Atlantic Ocean under climate change, *Journal of Geophysical Research: Oceans*, *121*(1), 118–132, 2016.

Sanchez-Franks, A., S. Hameed, and R. E. Wilson, The Icelandic Low as a predictor of the gulf stream north wall position, *Journal of Physical Oceanography*, *46*(3), 817–826, 2016.

Sarafanov, A., On the effect of the North Atlantic Oscillation on temperature and salinity of the subpolar North Atlantic intermediate and deep waters, *ICES Journal of Marine Science*, *66*(7), 1448–1454, 2009.

Sasaki, Y. N., and N. Schneider, Interannual to decadal Gulf Stream variability in an eddy-resolving ocean model, *Ocean Modelling*, *39*(3), 209–219, 2011.

Sato, O. T., and T. Rossby, Seasonal and low frequency variations in dynamic height anomaly and transport of the Gulf Stream, *Deep Sea Research Part I: Oceanographic Research Papers*, *42*(1), 149–164, 1995.

Scaife, A. A., D. Copsey, C. Gordon, C. Harris, T. Hinton, S. Keeley, A. O'Neill, M. Roberts, and K. Williams, Improved Atlantic winter blocking in a climate model, *Geophysical Research Letters*, *38*(23), 2011.

Schmeits, M. J., and H. A. Dijkstra, Bimodal behavior of the Kuroshio and the Gulf Stream, *Journal of physical oceanography*, *31*(12), 3435–3456, 2001.

Schmitz Jr, W. J., On the World Ocean Circulation. Volume 1. Some Global Features/North Atlantic Circulation., *Tech. rep.*, DTIC Document, 1996.

Schoonover, J., W. K. Dewar, N. Wienders, and B. Deremble, Local Sensitivities of the Gulf Stream Separation, *Journal of Physical Oceanography*, *47*(2), 353–373, 2017.

Seager, R., D. S. Battisti, J. Yin, N. Gordon, N. Naik, A. C. Clement, and M. A. Cane, Is the Gulf Stream responsible for Europe's mild winters?, *Quarterly Journal of the Royal Meteorological Society*, *128*(586), 2563–2586, 2002.

Silverthorne, K. E., and J. M. Toole, Quasi-Lagrangian observations of the upper ocean response to wintertime forcing in the Gulf Stream, *Deep Sea Research Part II: Topical Studies in Oceanography*, *91*, 25–34, 2013.

Spall, M. A., Dynamics of the Gulf Stream/deep western boundary current crossover. Part I: Entrainment and recirculation, *Journal of physical oceanography*, *26*(10), 2152–2168, 1996.

Stepanov, V., and K. Haines, Mechanisms for AMOC variability simulated by the NEMO model, *Ocean Science*, *10*(4), 645–656, 2014.

Stommel, H., The westward intensification of wind-driven ocean currents, *Eos, Transactions American Geophysical Union*, *29*(2), 202–206, 1948.

Straneo, F., and P. Heimbach, North Atlantic warming and the retreat of Greenland's outlet glaciers, *Nature*, *504*(7478), 36, 2013.

Sturges, W., and B. Hong, Gulf Stream transport variability at periods of decades, *Journal of physical oceanography*, *31*(5), 1304–1312, 2001.

Sverdrup, H. U., Wind-driven currents in a baroclinic ocean; with application to the equatorial currents of the eastern Pacific, *Proceedings of the National Academy of Sciences*, *33*(11), 318–326, 1947.

Talley, L., and M. Raymer, Eighteen degree water variability, *J. Mar. Res*, *40*, 757–775, 1982.

Taylor, A. H., and A. Gangopadhyay, A simple model of interannual displacements of the Gulf Stream, *Journal of Geophysical Research: Oceans (1978–2012)*, *106*(C7), 13,849–13,860, 2001.

Taylor, A. H., and J. A. Stephens, The North Atlantic oscillation and the latitude of the Gulf Stream, *Tellus A*, *50*(1), 134–142, 1998.

Thompson, J. D., and W. Schmitz Jr, A limited-area model of the Gulf Stream: Design, initial experiments, and model-data intercomparison, *Tech. rep.*, DTIC Document, 1989.

Timmermann, R., H. Goosse, G. Madec, T. Fichefet, C. Ethe, and V. Duliere, On the representation of high latitude processes in the ORCA-LIM global coupled sea ice–ocean model, *Ocean Modelling*, *8*(1), 175–201, 2005.

Tracey, K. L., and D. R. Watts, On Gulf Stream meander characteristics near Cape Hatteras, *Journal of Geophysical Research: Oceans (1978–2012)*, *91*(C6), 7587–7602, 1986.

Vannière, B., A. Czaja, H. Dacre, and T. Woollings, A "Cold Path" for the Gulf Stream–Troposphere Connection, *Journal of Climate*, *30*(4), 1363–1379, 2017.

Veronis, G., MODEL OF WORLD OCEAN CIRCULATION. 1. WIND-DRIVEN, 2-LAYER, *Journal of Marine Research*, *31*(3), 228–288, 1973.

Visbeck, M., E. P. Chassignet, R. G. Curry, T. L. Delworth, R. R. Dickson, and G. Krahmann, The ocean's response to North Atlantic Oscillation variability, *The North Atlantic Oscillation: climatic significance and environmental impact*, pp. 113–145, 2003.

Volkov, D. L., Interannual variability of the altimetry-derived eddy field and surface circulation in the extratropical North Atlantic Ocean in 1993-2001, *Journal of physical oceanography*, *35*(4), 405–426, 2005.

Walsh, J. E., A. S. Phillips, D. H. Portis, and W. L. Chapman, Extreme cold outbreaks in the United States and Europe, 1948–99, *Journal of Climate*, *14*(12), 2642–2658, 2001.

Wang, L., and C. J. Koblinsky, Annual variability of the subtropical recirculations in the North Atlantic and North Pacific: A TOPEX/Poseidon study, *Journal of physical oceanography*, *26*(11), 2462–2479, 1996.

Warren, B. A., Insensitivity of subtropical mode water characteristics to meteorological fluctuations, in *Deep Sea Research and Oceanographic Abstracts*, vol. 19, pp. 1–19, Elsevier, 1972.

Watts, D. R., and W. E. Johns, Gulf Stream meanders: Observations on propagation and growth, *Journal of Geophysical Research: Oceans*, *87*(C12), 9467–9476, 1982.

White, M. A., and K. J. Heywood, Seasonal and interannual changes in the North Atlantic subpolar gyre from Geosat and TOPEX/POSEIDON altimetry, *Journal of Geophysical Research: Oceans*, *100*(C12), 24,931–24,941, 1995.

Worthington, L., The 18 water in the Sargasso Sea, *Deep Sea Research (1953)*, *5*(2-4), 297–305, 1958.

Worthington, L., Intensification of the Gulf Stream after the winter of 1976-77, 1977.

Worthington, L. V., Negative oceanic heat flux as a cause of water-mass formation, *Journal of Physical Oceanography*, *2*(3), 205–211, 1972.

Worthington, L. V., On the north Atlantic circulation, *Johns Hopkins Oceanographic Studies*, *6*, 1976.

Xue, H., and J. M. Bane Jr, A numerical investigation of the Gulf Stream and its meanders in response to cold air outbreaks, *Journal of physical oceanography*, *27*(12), 2606–2629, 1997.

Xue, H., J. M. Bane Jr, and L. M. Goodman, Modification of the Gulf Stream through strong air-sea interactions in winter: Observations and numerical simulations, *Journal of physical oceanography*, *25*(4), 533–557, 1995.

Yamamoto, A., J. B. Palter, M. S. Lozier, M. S. Bourqui, and S. J. Leadbetter, Ocean versus atmosphere control on western European wintertime temperature variability, *Climate dynamics*, *45*(11-12), 3593–3607, 2015.

Yasuda, T., and K. Hanawa, Decadal changes in the mode waters in the midlatitude North Pacific, *Journal of Physical Oceanography*, *27*(6), 858–870, 1997.

Yeager, S. G., and M. Jochum, The connection between Labrador Sea buoyancy loss, deep western boundary current strength, and Gulf Stream path in an ocean circulation model, *Ocean Modelling*, *30*(2), 207–224, 2009.

Zhang, R., Coherent surface-subsurface fingerprint of the Atlantic meridional overturning circulation, *Geophysical Research Letters*, *35*(20), 2008.

Zhang, R., and G. K. Vallis, Impact of great salinity anomalies on the low-frequency variability of the North Atlantic climate, *Journal of climate*, *19*(3), 470–482, 2006.

Zhang, R., and G. K. Vallis, The role of bottom vortex stretching on the path of the North Atlantic western boundary current and on the northern recirculation gyre, *Journal of Physical Oceanography*, *37*(8), 2053–2080, 2007.

Zheng, Q., V. Klemas, and N. E. Huang, Dynamics of the slope water off New England and its influence on the Gulf Stream as inferred from satellite IR data, *Remote Sensing of Environment*, *15*(2), 135–153, 1984.